

Doctoral Thesis

**Study on Nano-Engineering of High-Capacity Anode
Materials for High-Power Energy Storage System**

Sinho Choi

Department of Energy Engineering
(Battery Science and Technology)

Graduate school of UNIST

2015

Study on Nano-Engineering of High-Capacity Anode Materials for High-Power Energy Storage System

Sinho Choi

Department of Energy Engineering
(Battery Science and Technology)

Graduate school of UNIST

Study on Nano-Engineering of High-Capacity Anode Materials for High-Power Energy Storage System

A dissertation
submitted to the Graduate School of UNIST
in partial fulfillment of the
requirements for the degree of
Doctor of Philosophy.

Sinho Choi

6. 18. 2015

Approved by



Advisor

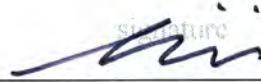
Prof. Soojin Park

Study on Nano-Engineering of High-Capacity Anode Materials for High-Power Energy Storage System

Sinho Choi

This certifies that the dissertation of S.Choi is approved.

6. 18. 2015



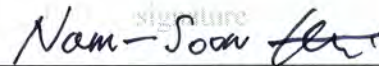
Advisor : Prof. Soojin Park



Committee Member : Prof. Jaephil Cho



Committee Member : Prof. Sang-Young Lee



Committee Member : Prof. Nam-Soon Choi



Committee Member : Dr. Minchul Jang

Abstract

Nano-engineering and nanotechnology issue in various industry fields such as semiconductor, chemistry, energy solution, material science, and medicine. A definition of nanotechnology includes quantum mechanics, molecular chemistry, biology, and atomic level behaviors. Also, nanostructured materials (e.g., nanoparticle, nanorod, nanotube, nanowire, hollow, and yolk-shell) improve properties of materials for performance enhancement of devices. These nanomaterials have been synthesized using bottom-up and top-down approaches. In the early 2000s, many researchers garnered information and experiences about the nanotechnology that led to innovation and progress in industry and academy of science. As a result, many electronic devices were developed for a convenience of our life. Especially, significant advances of devices lead to the development of another new device with more improved performances including faster processing ability, longer working time, light weight, and easy transportation.

In this regard, gradual development of energy storage system must need to satisfy this demand for new electric device (e.g. electric vehicle (EV), energy storage system (ESS), even drone) As one of the powerful energy storage systems, lithium-ion batteries (LIBs) are critically important to operate portable electronic devices. However, they cannot meet requirements for more advanced applications, like electric vehicles and energy storage systems due to limitations of conventional cathode/anode materials in high power and high energy density. To overcome these limitations, several strategies have been developed, including nanostructured design of electrode materials, coating of active materials with electrically conductive layers, and control of electrode architectures.

Herein, we study on a simple, cost effective and unique synthesis method of various shaped functional materials by nano-engineering process in an each chapter. Also, we conduct research about a mechanism of reaction, key for synthesizing good materials, change of chemical reaction in experiment. So, the developed materials appear outstanding properties such as structural stability, chemical stability in electrochemical test, and mainly used energy storage system like LIBs.

In chapter III, we demonstrate a simple route for fabricating trench-type copper patterns by combining a photo-lithography with a wet etching process. Nanostructured CuO was grown on the patterned Cu current collectors via a simple solution immersion process. And silicon nanoparticles were filled into the patterned Cu current collectors. The strongly immobilized CuO on the patterned Cu exhibited high electrochemical performance, including a high reversible capacity and a high rate capability.

In chapter IV, we demonstrate multi-scale patterned electrodes that provide surface-area enhancement and strong adhesion between electrode materials and current collector. The combination of multi-scale structured current collector and active materials (cathode and anode) enables us to make high-performance Li-ion batteries (LIBs). When LiFePO_4 (LFP) cathode and $\text{Li}_4\text{Ti}_5\text{O}_{12}$ (LTO) anode materials are combined with patterned current collectors, their electrochemical performances are significantly improved, including a high rate capability (LFP : 100 mAhg^{-1} , LTO : 60 mAhg^{-1} at 100 C rate) and highly stable cycling. Moreover, we successfully fabricate full cell system consisting of patterned LFP cathode and patterned LTO anode, exhibiting high-power battery performances. We extend this idea to Si anode that exhibits a large volume change during lithiation/delithiation process. The patterned Si electrodes show significantly enhanced electrochemical performances, including a high specific capacity (825 mAhg^{-1}) at high rate of 5 C and a stable cycling retention.

In chapter V, Chemical reduction of micro-assembled $\text{CNT@TiO}_2\text{@SiO}_2$ leads to the formation of titanium silicide-containing Si nanotubular structures. The Si-based nanotube anodes

exhibit a high capacity ($>1850 \text{ mAh g}^{-1}$) and an excellent cycling performance (capacity retention of $>99\%$ after 80 cycles).

In chapter VI, we revisit the metallothermic reduction process to synthesize shape-preserving macro-/nano-porous Si particles via aluminothermic and subsequent magnesiothermic reaction of porous silica particles. This process enables us to control the specific capacity and volume expansion of shape-preserving porous Si-based anodes. Two step metallothermic reactions have several advantages including a successful synthesis of shape-preserving Si particles, tunable specific capacity of as-synthesized Si anode, accommodation of a large volume change of Si by porous nature and alumina layers, and a scalable synthesis (hundreds of gram per batch). An optimized macroporous Si/Al₂O₃ composite anode exhibits a reversible capacity of $\sim 1500 \text{ mAh g}^{-1}$ after 100 cycles at 0.2 C and a volume expansion of $\sim 34\%$ even after 100 cycles.

In chapter VII, we report a redox-transmetalation reaction-based route for the large-scale synthesis of mesoporous germanium particles from germanium oxide at temperatures of $420 \sim 600 \text{ }^\circ\text{C}$. We could confirm that a unique redox-transmetalation reaction occurs between Zn⁰ and Ge⁴⁺ at approximately $420 \text{ }^\circ\text{C}$ using temperature-dependent in situ X-ray absorption fine structure analysis. This reaction has several advantages, which include (i) the successful synthesis of germanium particles at a low temperature ($\sim 450 \text{ }^\circ\text{C}$), (ii) the accommodation of large volume changes, owing to the mesoporous structure of the germanium particles, and (iii) the ability to synthesize the particles in a cost-effective and scalable manner, as inexpensive metal oxides are used as the starting materials. The optimized mesoporous germanium anode exhibits a reversible capacity of $\sim 1400 \text{ mA h g}^{-1}$ after 300 cycles at a rate of 0.5 C (corresponding to the capacity retention of 99.5%), as well as stable cycling in a full cell containing a LiCoO₂ cathode with a high energy density.

In chapter VIII, we report a unique synthesis of redox-responsive assembled carbon-sheathed germanium coaxial nanowire heterostructures without a need of metal catalyst. In our approach, germanium nanowires are grown by reduction of germanium oxide particles and subsequent self-catalytic growth mechanism during thermal decomposition of natural gas, and simultaneously, carbon sheath layers are uniformly coated on the germanium nanowire surface. This process is a simple (one-step process), reproducible, easy size-controllable and cost-effective (mass production) process which total mass of metal oxides can be transformed into nanowires. Furthermore, the germanium nanowires exhibit outstanding electrochemical performance including capacity retention of $\sim 96\%$ after 1000 cycles at 1C rate as lithium-ion battery anode.

Contents

Contents	I
List of Figures	VI
List of Tables	XI
Nomenclature	XII
Chapter I. Nano-Engineering and Nanotechnology	1
1.1. Introduction: Progress of Nano-engineering (Nanotechnology) in Industry	1
1.2. Various Approaches of Nano-engineering	3
1.2.1. Bottom-Up Approach	3
1.2.2. Top-Down Approach	5
1.2.3. General Approaches for Industry	7
1.3. Recent Progress of Nano-engineering in Applications	8
1.3.1. Advanced Semiconductor Device	8
1.3.2. Development of Li-Ion Batteries	10
1.3.3. Various Applications	13
1.4. References	15
Chapter II. Main Components of Lithium-Ion Batteries	17
2.1. Introduction: Li-Ion Rechargeable Batteries for electric Energy Storage System (ESS)	17
2.1.1. History of Li-Ion Batteries	20
2.1.2. Theory of Li-Ion Batteries	21
2.2. Composition Materials in Li-Ion Batteries	25
2.2.1. Cathode	25
2.2.2. Anode	28
2.2.2.1. Carbon-based Materials.....	28
2.2.2.2. Alloy/de-alloy Materials.....	29

2.2.2.2.1.	Silicon (Si)	29
2.2.2.2.2.	Germanium (Ge)	30
2.2.2.3.	Conversion Materials	30
2.2.3.	Separator	33
2.2.4.	Electrolyte	33
2.2.5.	Current Collector.....	33
2.3.	Next Generation Li-Ion Batteries	34
2.3.1.	New designed Li-Ion Batteries	34
2.3.2.	Flexible Li-Ion Batteries	36
2.4.	References	38
 Chapter III. Patterning of Electrodes for Mechanically Robust and Bendable Lithium-ion Batteries		43
3.1.	Introduction	43
3.2.	Experimental	44
3.2.1.	Fabrication of micro patterned copper substrates.....	44
3.3.	Result and discussion	46
3.3.1.	A synthesis of CuO nano-flake electrodes	46
3.3.2.	Mechanical properties of Cu electrodes for bendable electrode	49
3.3.3.	Electrochemical properties of CuO electrodes	54
3.4.	Conclusion	58
3.5.	References	59
 Chapter IV. High-Power Li-Ion Batteries Using Multi-scale Lithographic Patterning of Electrodes		61
4.1.	Introduction	61
4.2.	Experimental	63

4.2.1.	Fabrication of patterned current collectors	63
4.2.2.	LiFePO ₄ synthesis	63
4.2.3.	Anode materials	63
4.2.4.	Characterization	63
4.2.5.	Electrochemical test	64
4.3.	Result and discussion	66
4.3.1.	Characterization of the patterned electrodes	66
4.3.2.	Study on effects of the patterned electrodes	69
4.3.3.	Positive effects of the patterning compared to other conditions	73
4.3.4.	Applying patterned electrode to anode materials	76
4.4.	Conclusion	81
4.5.	References	82
Chapter V. Micro-assembled Si / Titanium Silicide Nanotube Anodes for High-Performance Lithium-ion Batteries		85
5.1.	Introduction	85
5.2.	Experimental	86
5.2.1.	Synthesis of CNT@Si and Si, Si@Ti _x Si _y nanotube structure	86
5.2.2.	Characterization of materials	86
5.2.3.	Electrochemical test	86
5.3.	Result and discussion	87
5.3.1.	Morphologies of Si-based nanotube materials	87
5.3.2.	Characterization of Si-based nanotube with titanium	94
5.4.	Conclusion	101
5.5.	References	102
Chapter VI. Metallothermic reduction for macroporous Si: compromise between capacity and volume expansion for practical Li-ion battery		105

6.1. Introduction	105
6.2. Experimental.....	107
6.2.1. Synthesis of micro-/nanoporous Si particles	107
6.2.2. Characterization of porous Si particles	107
6.2.3. Electrochemical properties of shape-preserving porous Si anodes	107
6.3. Result and discussion.....	108
6.3.1. One-step reduction process of macroporous SiO ₂ particles.....	108
6.3.2. Two-step reduction process of macroporous SiO ₂ particles.....	112
6.3.3. Electrochemical properties of Si anodes synthesized via two-step reduction process.....	115
6.3.4. Analysis of macro porous Si electrodes after cycling	118
6.4. Conclusion	122
6.5. References	123
Chapter VII. Cost-effective Scalable Synthesis of Mesoporous Germanium Particles via Zincothermic Reaction for High-performance Energy Storage Devices.....	126
7.1. Introduction	126
7.2. Experimental	128
7.2.1. Synthesis of hollow germanium oxide material	128
7.2.2. Physical Characterization	128
7.2.3. X-ray absorption spectroscopy	128
7.2.4. Electrochemical test	129
7.3. Result and discussion	130
7.3.1. In-situ study of redox-transmetalation reaction between GeO ₂ and Zn	130
7.3.2. Synthesis of mesoporous Ge particles from bulk GeO ₂ particles	135
7.3.3. Electrochemical properties of mesoporous Ge anode	140
7.3.4. Discussion of electrochemical properties of Ge electrode.....	146
7.4. Conclusion	149

7.5. References	150
-----------------------	-----

**Chapter VIII. Redox-Resposinve Assembly of Carbon-Sheathed Germanium Coaxial Nanowire
Heterostructures** 153

8.1. Introduction.....	153
------------------------	-----

8.2. Experimental.....	155
------------------------	-----

8.2.1. Fabrication of germanium oxide film.....	155
---	-----

8.2.2. Synthesis of Carbon sheathed GeNWs heterostructures.....	155
---	-----

8.2.3. Physical Characterization	155
--	-----

8.2.4. Electrochemical test.....	155
----------------------------------	-----

8.3. Result and discussion.....	157
---------------------------------	-----

8.3.1. Redox responsive reaction and nanowire growth process.....	157
---	-----

8.3.2. Redox responsive reaction mechanism using another metal oxide and hydrocarbon gas	164
---	-----

8.3.3. Effect of carbon sheathed Ge nanowires in application.....	167
---	-----

8.4. Conclusion	171
-----------------------	-----

8.5. References	172
-----------------------	-----

Publication list.....	174
------------------------------	------------

Patent list.....	176
-------------------------	------------

Acknowledgment.....	178
----------------------------	------------

List of Figures

Figure 1. 1	Schematic illustration of nanotechnology in nature and in industry	2
Figure 1. 2	Examples showing various bottom-up approaches	4
Figure 1. 3	Various examples showing top-down approaches	6
Figure 1. 4	Development of semiconductors using nanotechnology	9
Figure 1. 5	Advanced LIBs developed using nanotechnology	11
Figure 1. 6	Challenges in the development of nano-enabled LIBs	12
Figure 1. 7	Various applications with nanotechnology in complex material, medicine, energy and sensor	14
Figure 2. 1	Comparison of different battery technologies in terms of volumetric and gravimetric energy density	19
Figure 2. 2	Scheme of typical lithium-ion battery system	22
Figure 2. 3	Cyclic voltammetry profiles of LIBs components.....	23
Figure 2. 4	Operational principle of SEI formation in the electrode of LiCoO ₂ /C combination...	24
Figure 2. 5	Representative cathode in LIBs: its microstructure, mechanism, electrochemical performances	27
Figure 2. 6	Electrochemical properties of several anode materials for LIBs	32
Figure 2. 7	Fabrication Li-ion battery electrode.....	35
Figure 2. 8	Recent flexible Li-ion batteries	37
Figure 3. 1	A schematic illustration showing the CuO nano-flakes grown on the trench-type patterned Cu foils.....	45
Figure 3. 2	A growth of CuO nano-flakes structure on the patterned Cu foils	47
Figure 3. 3	Three-dimensional hierarchical CuO nano-flakes grown on the flat Cu foil.....	48
Figure 3. 4	SEM images of CuO nano-flakes anchored to the Cu foils after rolling-up test.....	50
Figure 3. 5	Morphologies of CuO nano-flakes after bending test of different direction with pattern direction.....	51
Figure 3. 6	SEM images showing CuO nano-flakes materials on different type Cu current collector after bending test.....	52
Figure 3. 7	A coverage of CuO nano-flakes materials on Cu current collectors after the bending test.....	53
Figure 3. 8	The electrochemical performances of CuO nano-flakes anode on the patterned Cu current collectors.....	56

Figure 3. 9 The rate capabilities of CuO nano-flakes anodes on a flat Cu current collector in the range of 0.1 – 10 C rates.....57

Figure 3. 10 The SEM images of CuO nano-flakes anodes on the patterned Cu current collectors after 100 cycles57

Figure 4. 1 Top: the schematic illustration showing a fabrication process of multi scale patterned current collector. Magnified SEM image shows nano scale patterns on the surface of the aluminum metal foils. Bottom: morphology of patterned Al foil.....65

Figure 4. 2 The SEM images of Al patterns with various shapes67

Figure 4. 3 An adhesion test of patterned and non-patterned LiFePO₄ electrodes.....68

Figure 4. 4 The peel-off test of the patterned and non-patterned LiFePO₄ electrodes.....68

Figure 4. 5 a) The schematic illustration showing the electric pathways of the patterned electrodes. The composite electrodes were loaded on a patterned metal current collector. The composite electrode mass is sectioned into three different regions from the viewpoint of electric pathway. The voltage profiles of LFP electrodes showing rate capabilities of b) the non-patterned electrode and the patterned electrodes with c) 3 μm depth and d) 12 μm depth. e) The deviation of plateau potential from the ideal value (3.45 V) during discharge at various C rates and a fixed charge rate of 0.2C. f) The capacity retention of the patterned (red) and non-patterned (black) electrodes at various discharge rate and a fixed charge rate of 0.2C.....71

Figure 4. 6 The characterization of co-pre LiFePO₄ cathode materials.....72

Figure 4. 7 The characterization of the etched (nanostructured) Al foils obtained by RIE process.....74

Figure 4. 8 The cross-sectional SEM images of co-LFP electrodes with a) a low loading level (10 μm thickness, loading mass of ~1.5 mg cm⁻²) and b) a high loading level (80 μm thickness, loading mass of ~8.2 mg cm⁻²) on the patterned Al current collectors. The plots of C-rate values versus specific capacities at c) low loading and d) high loading level of co-LFP electrodes75

Figure 4. 9 The characterization of Li₄Ti₅O₁₂ (LTO) anode materials.....77

Figure 4. 10 The electrochemical tests of the patterned LTO electrodes.....77

Figure 4. 11 The electrochemical tests of full cell system using LiFePO₄ / Li₄Ti₅O₁₂ electrodes (cathode loading mass of ≈ 2.87 mg cm⁻², N/P ratio=1.1:1).77

Figure 4. 12 The electrochemical tests of the patterned and non-patterned Si electrodes.....79

Figure 4. 13 The characterization of Si electrodes on the non-patterned Cu foils.....80

Figure 5. 1	Top: schematic illustration showing the synthetic process of Si-coated CNTs. Bottom: morphologies of Si-coated CNTs.....	89
Figure 5. 2	Control of SiO ₂ layer thickness by volumetric ratio of NH ₄ OH and TEOS.....	90
Figure 5. 3	XRD patterns of as-synthesized CNT@SiC@Si prepared by a magnesiothermic reduction of SiO ₂ -coated CNTs.....	90
Figure 5. 4	Top: schematic illustration showing the synthetic process of Si nanotube. Bottom : morphologies of Si nanotube.....	92
Figure 5. 5	Electrochemical performances of CNT@SiC@Si three-component and silicon nanotube electrodes.....	93
Figure 5. 6	(a) SEM images and (b) EDAX profile of carbon-coated Si nanotubes.....	93
Figure 5. 7	Top: schematic illustration showing the synthetic process of micro-assembled Ti _x Si _y @Si nanotubes. Bottom: characterization of micro-assembled Ti _x Si _y @Si nanotube.....	96
Figure 5. 8	SEM images of (a) TiO ₂ -coated CNT and (c) micro-assembled CNT@TiO ₂ @SiO ₂ particles. EDAX profiles and elemental contents of (b) TiO ₂ -coated CNT and (d) micro-assembled CNT@TiO ₂ @SiO ₂ particles.....	97
Figure 5. 9	XRD patterns of as-synthesized CNT@TiC/Ti _x Si _y @Si prepared by magnesiothermic reduction of TiO ₂ /SiO ₂ double layer coated CNTs.....	97
Figure 5. 10	Electrochemical properties of carbon-coated CNT@TiC/Ti _x Si _y @Si electrodes	98
Figure 5. 11	(a) SEM image and (b) EDAX profile of carbon-coated Ti _x Si _y @Si nanotubes	98
Figure 5. 12	Electrochemical performances of Si nanotube and Ti _x Si _y @Si nanotube electrodes...	100
Figure 6. 1	Top: schematic illustration showing the synthetic process of macroporous Si/Al ₂ O ₃ composite (Si-Al-5-5) material. Bottom: characterization of macroporous Si/Al ₂ O ₃ composite (Si-Al-5-5) material	109
Figure 6. 2	Low-magnified SEM images showing (a) macroporous silica and (b) as-synthesized porous Si/Al ₂ O ₃ composite. In the inset of Figure 6. 2, XRD pattern shows that the porous silica is a crystalline material with a cristobalite structure.....	110
Figure 6. 3	SEM images of (a) macroporous silica and (b) Si particles prepared by magnesiothermic reaction of the porous silica.....	110
Figure 6. 4	SEM images of as-synthesized porous Si/Al ₂ O ₃ composite materials obtained by two-different etching conditions.....	111
Figure 6. 5	Characterizations of Si/Al ₂ O ₃ composite (Si-Al-7-3) synthesized by two-step metallothermic reaction.....	113
Figure 6. 6	SEM images and elemental analysis of three-different macroporous Si/Al ₂ O ₃ composites	114

Figure 6. 7	Raman spectrum of carbon-coated Si-Al-7-3 composite indicates characteristic of amorphous carbon layer (with D/G ratio of 2.6)	114
Figure 6. 8	Electrochemical performances of macroporous Si/Al ₂ O ₃ composite electrodes with four different Al ₂ O ₃ contents	116
Figure 6. 9	The dQ/dV plots of three composite electrodes at the first cycle	116
Figure 6. 10	Electrochemical performances of carbon-coated non-porous Si electrodes obtained by magnesiothermic reaction.....	117
Figure 6. 11	Cross-sectional SEM images of composite electrodes (Si-Al-5-5 (a, d), Si-Al-7-3 (b, e), and Si-Al-9-1 (c, f)) before (a-c) electrochemical test and after 100 cycles (d-f)	119
Figure 6. 12	(a) Cross-sectional SEM images of Si-Al-7-3 particles after 100 cycles. (b) Magnified image of Si-Al-7-3 (yellow box seen in Figure 6. 12a) showing mesoporous structure. EDS mapping analyses of sample seen in Figure 6. 12b showing (c) inner Si part (magenta) and (d) outer Al layer (cyan)	120
Figure 6. 13	Cross-sectional SEM images of carbon-coated non-porous Si electrode prepared from magnesiothermic reaction (a) before and (b) after 100 cycles	120
Figure 6. 14	Electrochemical performances of full cell consisting of Si-Al-7-3/LiCoO ₂	121
Figure 7. 1	(a) Schematic illustration of the method for synthesizing mesoporous Ge materials via a unique redox-transmetalation process. (b) SEM images of the synthesized GeO ₂ particles showing their ellipsoidal structure. Inset is a HRTEM image of GeO ₂ particles showing their hollow structure. (c) XRD pattern of the as-synthesized hollow GeO ₂ particles. Radial distribution functions of (d) the Ge K-edge k ³ and (e) the Zn K-edge k ³ -weighted XAFS spectra as functions of the temperature.....	131
Figure 7. 2	(a) Normalized Ge and (b) Zn K-edge XANES spectra as function of temperature...	132
Figure 7. 3	Characterization of hollow Ge particles synthesized by the ZRR process	134
Figure 7. 4	(a) SEM image of bulk GeO ₂ powder and (b) its magnification show that large secondary particles (10-20 μm) are irregularly stacked by primary particles (200-500 nm in size) and tiny pores are formed in the stacked regions of primary particles. (c) XRD pattern of the bulk GeO ₂ particles shows that the GeO ₂ has a trigonal crystalline phase.....	137
Figure 7. 5	XRD pattern of as-synthesized mesoporous Ge particles synthesized by ZRR reaction of bulk GeO ₂ and Zn vapor at 550 °C for 3h	137
Figure 7. 6	Characterization of the mesoporous Ge particles synthesized from bulk GeO ₂ by the ZRR process at 600 °C.....	138
Figure 7. 7	Characterization of mesoporous Ge materials obtained by two different ZRR temperatures.....	139

Figure 7. 8	Electrochemical performances of the electrodes formed using the hollow Ge and z600-Ge particles.....	142
Figure 7. 9	Characterization of commercially available Ge particles (c-Ge)	143
Figure 7. 10	Electrochemical performances of z700-Ge and z800-Ge electrodes.....	144
Figure 7. 11	Characterization of Ge particles (m-Ge) obtained by a magnesiothermic reaction of bulk GeO ₂ and Mg vapor.....	145
Figure 7. 12	(a) C 1s and F 1s XPS spectra of the mesoporous z-Ge electrode after 300 cycles. (c) Reaction mechanism showing the formation of the C-F bond and LiF	147
Figure 7. 13	Cross-sectional SEM images of the z600-Ge electrode	148
Figure 7. 14	Cross-sectional SEM images of the commercial-Ge electrode	148
Figure 8. 1	Synthesis process of c-GeNWs and their characterization.....	156
Figure 8. 2	A new class of nanowire growth mechanism.....	159
Figure 8. 3	Characterization of c-GeNWs synthesized by hydrogen/carbon-assisted chemical reduction	160
Figure 8. 4	Characterization of the original bulk GeO ₂ powder.....	161
Figure 8. 5	Characterization of as-synthesized c-GeNWs.....	161
Figure 8. 6	TEM images of Ge nanowires synthesized at various flow rates of acetylene gas at 900°C for 20min.....	162
Figure 8. 7	TEM images of Ge nanowires at various reaction times at 900 °C under a fixed flow rate.....	162
Figure 8. 8	TEM images of Ge nanowires at various reaction temperature at a fixed flow rate of acetylene gas for 20min.....	163
Figure 8. 9	SEM images and XRD patterns of reduced Ge and GeO ₂ obtained by thermal decomposition of various nature gases at 900 °C for 20min.....	165
Figure 8. 10	General approach for synthesizing other metal nanowires.....	166
Figure 8. 11	Anti-oxidation test of c-GeNWs and GeNPs in 3wt% H ₂ O ₂ solution for 1h.....	168
Figure 8. 12	Thermal oxidation tests of c-GeNWs and GeNPs at 550 oC for 2h in air.....	169
Figure 8. 13	Anti-oxidation and electrochemical properties of c-GeNWs and Ge.....	170

List of Tables

Table 2.1 The specifications of various battery systems	18
Table 2.2 Properties of cathodematerials for LIBs	26
Table 2.3 Most common anode materials used for LIBs	31

Nomenclature

3D: Three dimensional	ICP-MS: inductively coupled plasma mass spectrometry
AFM : atomic force microscopy	LCO: lithium cobalt oxide, LiCoO_2
Al: aluminum	LFP: lithium iron phosphate, LiFePO_4
Al_2O_3 : alumina	LIBs: lithium-ion batteries
ALD: Atomic layer deposition	LiPF_6 : lithium hexafluorophosphate
CH_4 : methane gas	LMO: lithium manganese oxides, LiMn_2O_4
C_2H_2 : acetylene gas	LTO: lithium titanium oxide, $\text{Li}_4\text{Ti}_5\text{O}_{12}$
C_2H_4 : ethylene gas	Mg: magnesium
$\text{C}_6\text{H}_5\text{CH}_3$: toluene	NCA: $\text{Li}(\text{Ni}_x\text{Co}_y\text{Al}_z)\text{O}_2$
C.E. or CE: coulomb efficiencies	NCM: $\text{Li}(\text{Ni}_x\text{Co}_y\text{Mn}_z)\text{O}_2$
CMC: sodium carboxymethyl cellulose	Ni-MH: nickel metal hydride
CNTs: carbon nanotubes	NIL: nano imprint lithography
Cu: copper	NPE: nanostructured polymer electrolyte
CuO: copper oxide	NMP: N-methyl-2-pyrrolidone
CuCl_2 : copper chloride	OCV: open-circuit voltage
CTAB: cetyltrimethylammonium bromide	PAA: Polyacrylic acid
CV: cyclic voltammogram	PVdF: polyvinylidene fluoride
CVD: chemical vapor deposition	RT: room temperature
DEC: diethylene carbonate	RFID: Radio-frequency identification
DMC: dimethyl carbonate	RIE: Reactive-ion etching
EC: ethylene carbonate	Si: silicon
EDS: energy-dispersive X-ray	SEM: scanning electron microscopy
EIS: electrochemical impedance spectroscopy	SEI: solid electrolyte interface
EMC: ethyl methyl carbonate	Ti: titanium
ESS: energy storage system	TEM: Transmission electron microscopy
EV or EVs: electric vehicles	VLS: vapour-liquid-solid
FEC: fluoroethylene carbonate	XAFS: X-ray absorption fine structure
FFT: fast-fourier transform	XANES: X-ray absorption near edge structure
FIB: focused-ion-beam instrument	XRD: X-Ray Diffraction
Ge: germanium	XPS: X-ray photoelectron spectroscopy
H_2 : hydrogen	Zn: zinc
HCl : hydrochloric acid	
H_2SO_4 : sulfuric acid	

Chapter I. Nano-Engineering and Nanotechnology

1.1 Introduction: Progress of Nano-engineering(Nanotechnology) in Industry

Nano-engineering is the practice of engineering on the nanoscale. Origin of nano-engineering derives its name from the nanometer, a unit of measurement is one billionth of a meter. Nano-engineering is largely a synonym for nanotechnology. So, nano-engineering is delicate manipulation of matter on an atomic, molecular, and super-molecular scale.¹

The earliest, wide meaning of nano-engineering referred to particular technological goal of precisely fabricating atoms and molecules for production of macro-scale products, and also now referred to as molecular-technology. A more generalized description of nano-engineering defines nanoscale effects, which includes the fact that quantum mechanical effects are important at this quantum scale. Therefore, the definition was shifted from a particular technological goal to a research category inclusive of all types of research and technologies that deal with the special properties of matter that occur below the given size threshold. The application fields of nano-engineering as defined by size is so very broad, including fields of science as diverse as surface modification engineering, material engineering, organic chemistry, molecular biology, semiconductor physics, photo-electronic science, micro-fabrication, etc.² The associated research and applications are diverse, ranging from extensions of conventional device physics to completely new approaches based on molecular level, from synthesis of new materials with nano-size to direct control of particular properties of nanomaterials on the atomic scale. So, recently, many scientists currently research and develop many new materials and devices with excellent demonstrations of advances applied nano engineering in vast range of applications, such as medicine, biomaterials, materials science, physics, electronics, functional materials and energy production.

Among several suitable examples, one of them is synthesis process of nanoparticle. The shape and size of certain types of metal nanoparticles often appeared outstanding properties which do not happen in macro scale of materials such as plasmon effect and quantum confinement effect.³ The other one is synthesis of carbon based materials like carbon nanotube, graphene, and fullerene (C₆₀).⁴ These carbon materials with enhanced properties of higher electrical conductivity, mechanical strength apply semiconductor devices like field effect transistor (FET), transparent electrode, photo-detector, instead of silicon materials in semiconductor market. Another one is DNA nanotechnology which is the utilization of the inherent properties of nucleic acids like DNA to create useful materials and proteins that self-assemble to generate functional materials could be used as a novel approach for the large-scale production of programmable nanomaterials.⁵

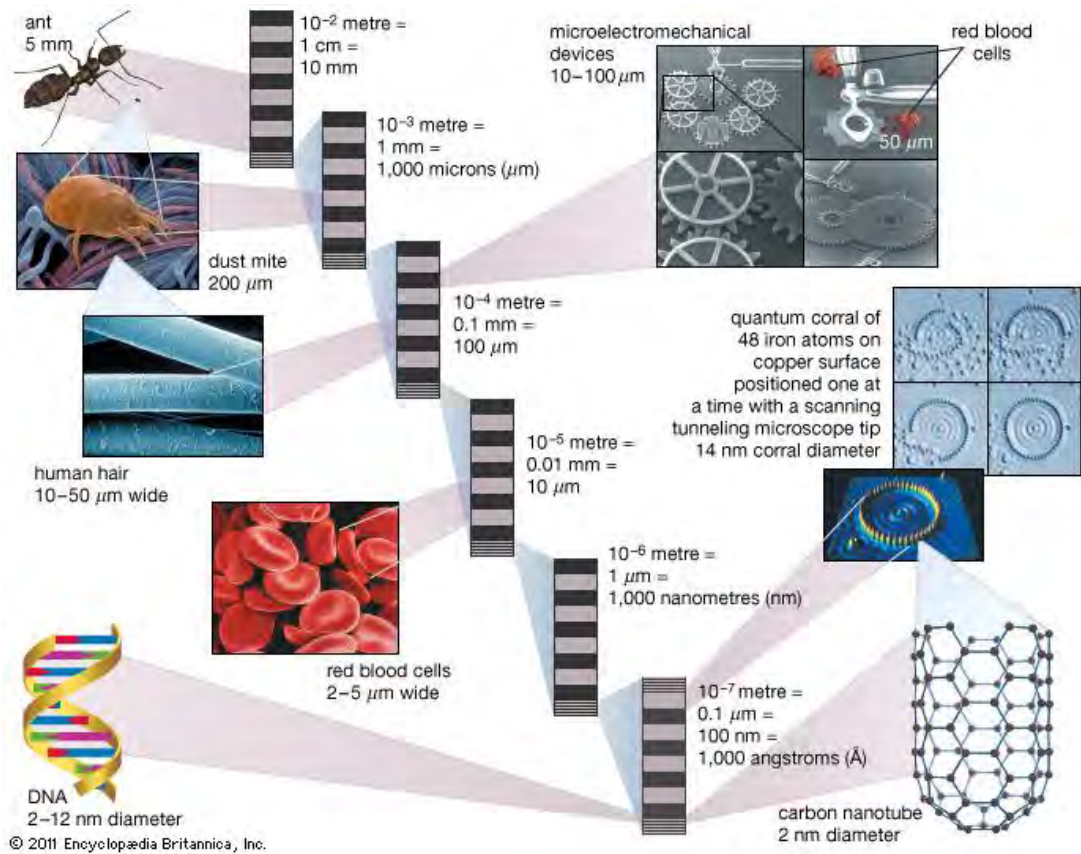


Figure 1.1 Schematic illustration of nanotechnology in nature and in industry.

1.2 Various Approaches of Nano-engineering

Science and technology of nano-engineering about materials includes subfields which study or develop the synthesis of nanomaterials having unique properties arising from their nanoscale dimensions and fabrication process for nanomaterials with smaller scale and equipment for nano-engineering.⁶ These approach enable fabrication of various materials having enhanced properties led to high performance devices. Nanomaterials can also be used for bulk applications; most present commercial applications of nanotechnology are of this flavor. Nanostructure on surface of nano-pillars can be used in solar cells and significantly reduce the cost of traditional silicon solar cells. Development of semiconductor nanoparticles-incorporating applications enables quantum mechanics to be used in the next generation products, such as display technology, lighting, solar cells and biological imaging. Typical method of various approach of nano-engineering is a bottom-up and top-down process. The bottom-up method is assembly of each various small size components under molecular level or atomic level need to fine control for fabrication. The other top-down method is to carve using etching, removing, dissolving with nano-sized templates and masks.

1.2.1 Bottom-Up Approach

Bottom-up approach defines assembly method to arrange smaller components/elements into special structure or template like assembly of model with blocks. This approach aims at designing molecules with well-defined shape from the field of classical chemical synthesis (inorganic and organic synthesis). This bottom-up technique builds or grows larger structures as atom-by-atom or as molecule-by-molecule. These techniques include chemical synthesis of self-assembly with block copolymer that is suitable method for self-assembled pattern on thin films. Another variation of the bottom-up approach is molecular beam epitaxy (MBE).⁷ MBE allows scientists to lay down atomically precise layers of atoms and, in the process, build up complex structures. Important for research on semiconductors, MBE is also widely used to make samples and devices for the newly emerging field of spintronics. The similar method like MBE is atomic-layer deposition (ALD) in CVD method of the normally used method. Another technology using a scanning probe is dip-pen nanolithography (DPN).⁸ DPN uses an AFM tip as a solid-state substrate (likes Au), and molecules with a chemical affinity for the solid-state substrate as ink. Capillary transport of molecules from the AFM tip to the solid substrate is used in DPN to directly write patterns consisting of a relatively small collection of molecules in sub-micrometer dimensions. This technique fits into the various sub-field of nanolithography for nanoelectromechanical systems (NEMS), nanoscale coating process, and surface modification engineering.

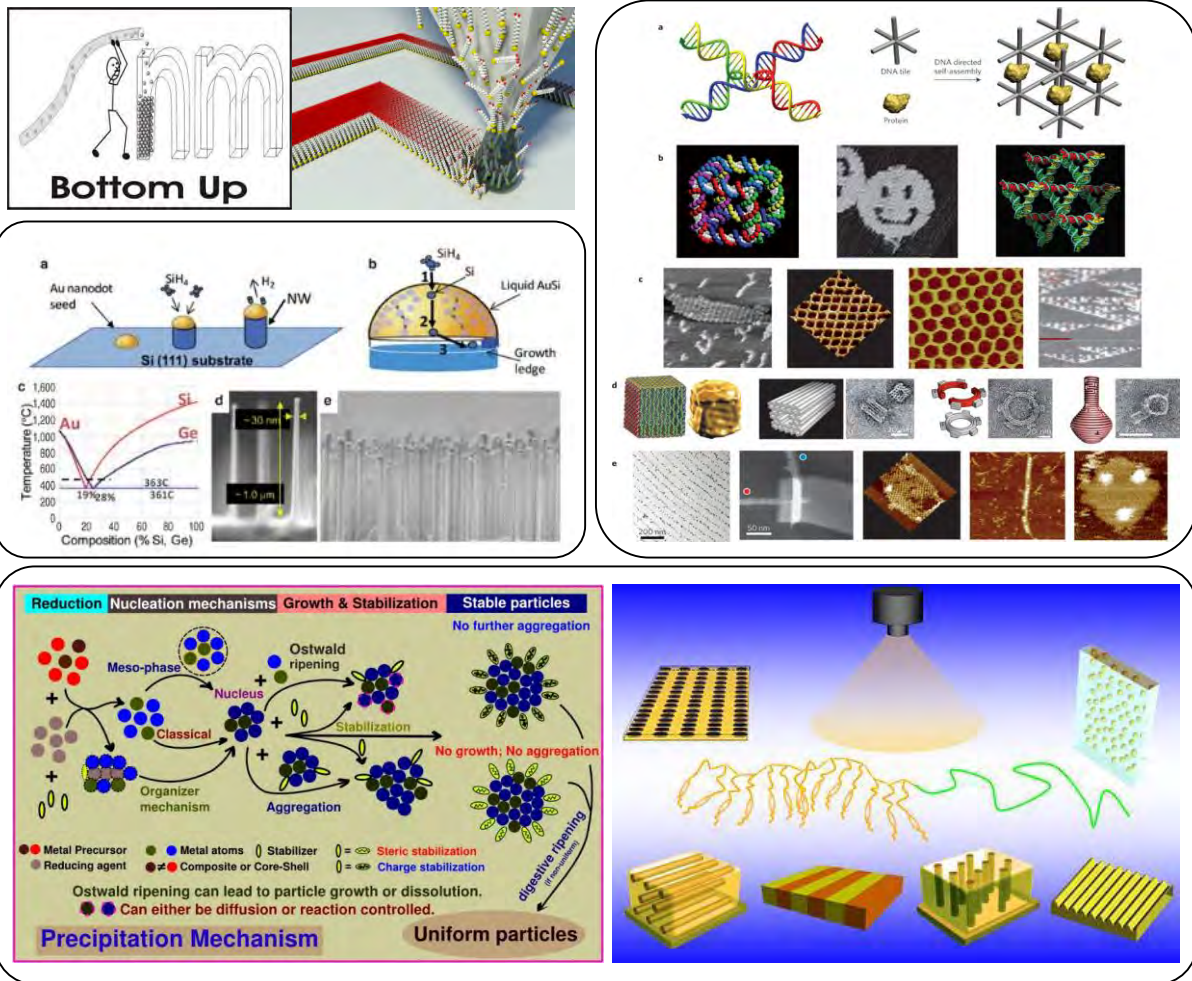


Figure 1.2 Examples showing various bottom-up approaches

1.2.2 Top-Down Approaches

Fabrication of precisely ordered nanostructures is essential for nano-engineering. The ability to fabricate on the nanometer scale guarantees a continuation in the miniaturization of functional devices, a large inherent surface/volume ratio, and short diffusion distances. New advanced fabrication technologies have enabled the lateral dimensions of devices to be shrunk well below 100 nm. Lithography dominates as the most critical procedure for successfully defining structures with such dimensions. Photo-lithographic methods share the same operational principle.⁹ Exposure of an appropriate material to electromagnetic radiation (UV or X-ray) introduces a latent image into the material as a result of a set of chemical changes in its molecular structure. This latent image is subsequently developed into 1D or 2D relief structures through selective etching. X-ray lithography has been used to create submicron size features.¹⁰ Moreover, interference lithography, using interactions between two or more coherent laser beams, and zone-plate array lithography in which array of Fresnel zone plates focus the X-ray beam source and directly pattern on the resist surface without a mask, have been developed to create submicron features in an inexpensive way.¹¹ Exposure is usually patterned either by interposing a mask between the source of radiation and the material or by scanning a focused spot of the source across the surface of the material. When masks are used, the lithographic process yields a 2D replica of the pattern on the mask. Focused ion beam lithography (FIB)¹² and electron beam lithography¹³ are both well suited for generating patterns on the submicron scale.

A shadow-mask evaporation method has also been used to define submicron single layer material patterns.¹⁴ In this approach, the shadow mask, a perforated ultrathin silicon nitride membrane with various submicron size apertures, is in contact with the substrate surface during deposition. The combination of shadow mask and scanning probe methods such as atomic force microscope (AFM) and scanning tunneling microscope (STM) provide improved manipulation of the pattern structures. With scanning probes, a sharp tip (<50 nm) induces a local change in a resist or causes localized deposition of a material. Methods that involve scanning or writing can generate arbitrary 2D patterns and therefore can be used for master writing. Advantages of scanning probe methods include resolution that, for AFM and STM methods, approaches the atomic level, the ability to generate features with nearly arbitrary geometries, and the capability to pattern over surface topography that deviates significantly from planarity.¹⁵ These methods are serial techniques, however, and have writing speeds that are typically limited by the mechanical resonances of the tips and the piezoelectric elements that maintain constant separation between the tip and the sample surface. An alternative high-throughput lithographic method is nanoimprint lithography (NIL), where patterns are defined by a compression molding and a pattern transfer.¹⁶ In this approach, a mold having nanometer length-scale features is first compressed onto a thin resist film deposited on a substrate. A thickness contrast created in the molded resist enables an anisotropic etching process and pattern transfer.

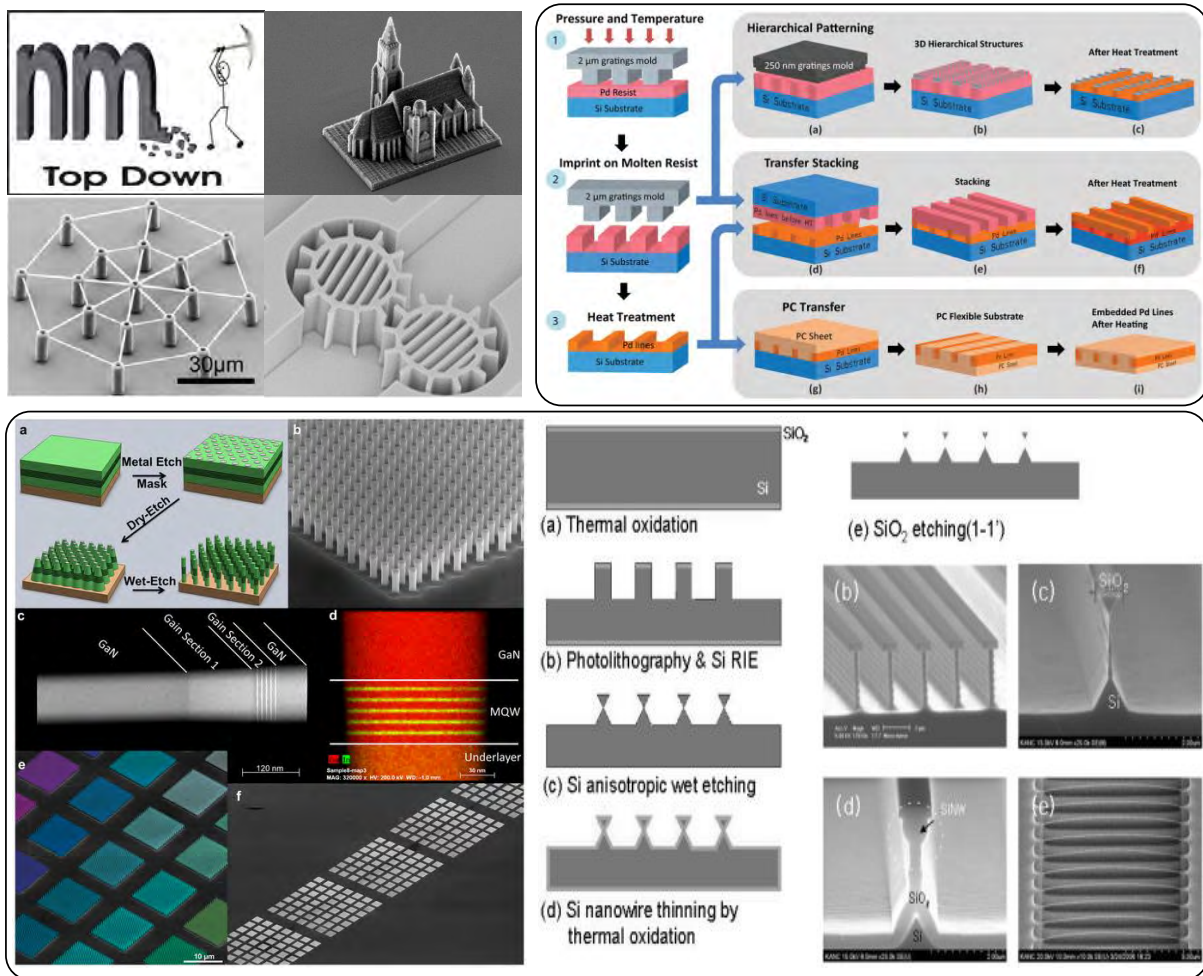


Figure 1.3 Various examples showing top-down approaches

1.2.3. General Approaches for Industry

Nano-engineering is useful process for synthesis of nanomaterials and nanostructuring. For applications for industry fields, various nano-engineering processes must be simple, easy to tunable, and production in a large scale. Especially, synthesis of nanoparticles (e.g., titanium oxide, zinc oxide, silver, gold, etc.) for anti-reflection, anti-fingerprint, super-hydrophobic properties, passivation layer, anti-aging, and various patterning in circuits using a simple wet-synthesis process, sol-gel process, solvothermal process, and hot injection process. These methods have big advantages including cost effective, possibility for mass production, and uniform quality of nanomaterials.

In addition, block copolymer nanostructures by self-assembly method with 10 to 100 nm dimensions are useful as nanoscale membranes, templates for fabrication of nano-objects such as metal, ceramic nano-dots and wires, as 1-, 2- and 3D photonic crystals, and as nanopatterns for fabrication of high density information storage media. Because the block copolymers have also been utilized not only as surfactants but also to spatially pattern the particles.¹⁷

Also, a new approach excluding commonly method (top down, bottom up) needs to develop more enhanced devices.

1.3 Recent Progress of Nano-Engineering in Applications

The early 2000s have shown the beginnings of the applications of nanotechnology in commercial products, although most applications are limited to apply to the bulk material passive using nanomaterials. Examples include titanium dioxide and zinc oxide nanoparticles for anti-reflection, anti-fingerprint, super-hydrophobic properties, passivation layer, anti-aging in cosmetics, coating layer and some food products, silver nanoparticles for various patterning of circuit likes electric board, touch screen in food packaging, clothing, disinfectants and household appliances; carbon nanotubes for stain-resistant textiles; and cerium oxide as a fuel catalyst.¹⁸ Nanotechnology is being used in developing countries to help treat disease and prevent health issues. Nanotechnology is also being applied to or developed for application to a variety of industrial and purification processes. Purification and environmental clean-up applications include the desalination of water, water filtration, wastewater treatment, groundwater treatment, and other nano-remediation. In industry, applications may include construction materials, military goods, and nano-machining of nano-wires, nano-rods, few layers of graphene, etc.¹⁹

1.3.1. Advanced Semiconductor Device

Nano-engineering technology is already in use in many electronic applications with semiconductor chips to provide smaller, faster, and more portable systems that can manage many commands and store larger amounts of information. According to the Moore's law, the number of transistors in a dense integrated circuit has doubled approximately every two years. Nano transistors that are faster, more powerful, and increasingly energy-efficient can operated many commands on on a single tiny chip. Magnetic random access memory (mRAM) enabled by nanometer-scale magnetic tunnel junctions that can quickly and effectively save even encrypted important data. A display for many new TVs, laptop computers, mobile phones, digital cameras, and other devices incorporate nano-structured polymer thin films known as organic light-emitting diodes, or OLEDs instead cathode ray tube display (CRT), liquid crystal display (LCD). The OLED screens offer brighter images in a flat format, as well as wider viewing angles, lighter weight, better picture density, lower power consumption, and longer lifetimes. And also, these OLED screens enable new designed electronic devices including curved, transparent display because of used polymer properties with flexibility and transparency. Other application products include flash memory chips for portable devices, anti-fingerprint/antibacterial coatings on mouse/keyboard/cell phone casings; conductive inks for printed electronics for RFID/smart cards/smart packaging, and flexible displays for e-book readers.

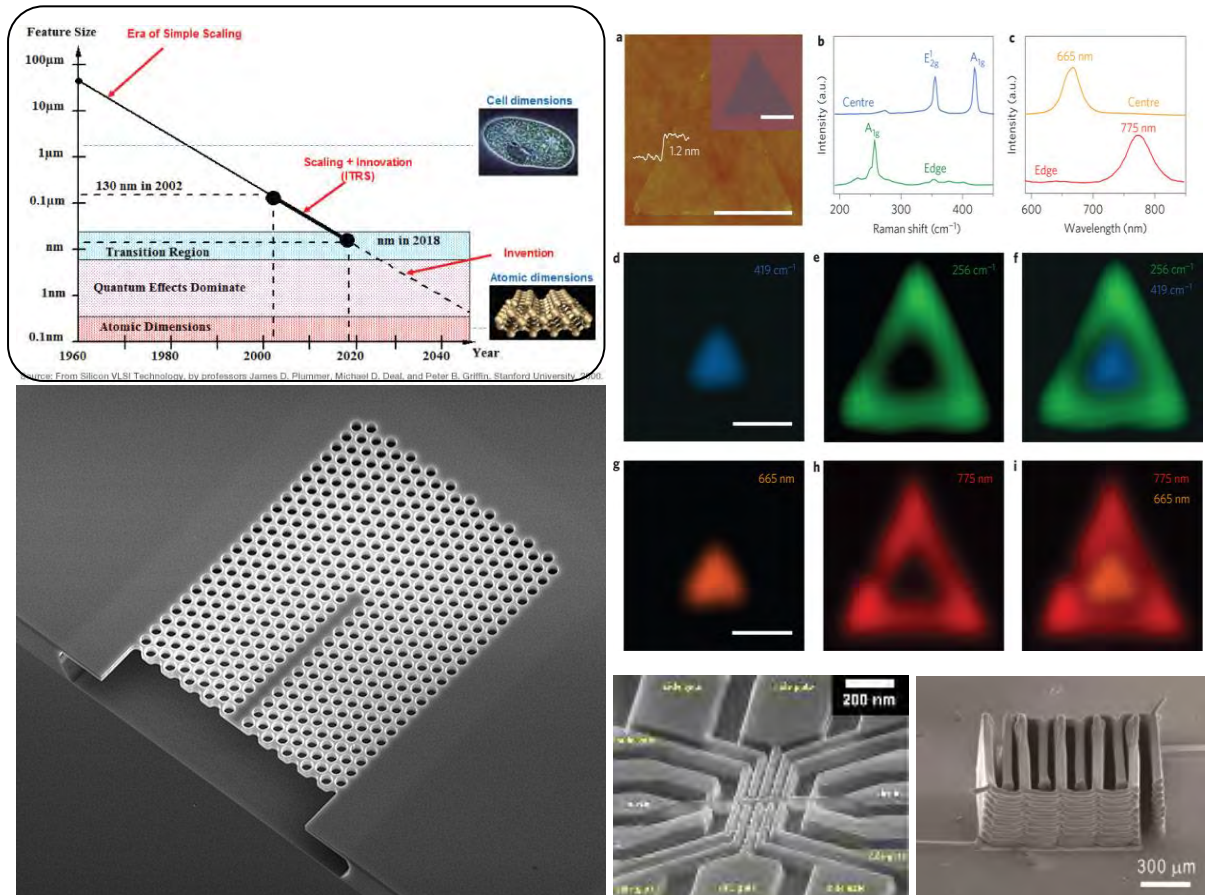


Figure 1.4 Development of semiconductors using nanotechnology.

1.3.2. Development of Li-Ion Batteries

Nanotechnology has the potential to deliver the next generation LIBs with improved performance, durability and safety at an acceptable cost. A typical LIB consists of three main components: an anode (generally made of graphite and other conductive additives), a cathode (generally, a layered transition metal oxide) and electrolyte through which lithium ions shuttles between the cathode and anode during charging and discharging cycles.

Both anode and cathode are made of materials that have the ability to be easily intercalated with lithium ions. The electrodes also should have high electrical conductivity so that the LIB can have high charging rates. Faster intercalation of Li ions can be facilitated by using nanosized materials for electrodes, which offer high surface areas and short diffusion paths, and hence faster storage and delivery of energy. Similarly, nanosizing the anode materials can make the anode to have short mass and charge pathways (i.e allow easier transport of both lithium ions and electrons), resulting in high reverse capacity and deliver at a faster rate. Nanostructured materials like silicon nanowires, silicon thin films, carbon nanotubes, graphene, tin-filled carbon nanotubes, tin, germanium, etc., are currently being explored as anode materials for the next generation LIBs.²⁰

Nanostructuring of solid electrolytes has proven to improve the lithium ion conductivity, for example, when the conventional bulk lithium thiophosphate electrolyte was made nanoporous, it could conduct lithium ions 1000 times faster.²¹ Nanostructured polymer electrolyte (NPE), which ensures safety. Main advantage of using this benign electrolyte is that it allows the use of lithium metal as anodes (instead of carbon based anodes) and contribute to the increase of energy density of the battery.²² Separators with nanoporous structures can prevent the spreading of dendrites by acting as a mechanical barrier without hindering the ion-transport during charging and discharging cycles.²³

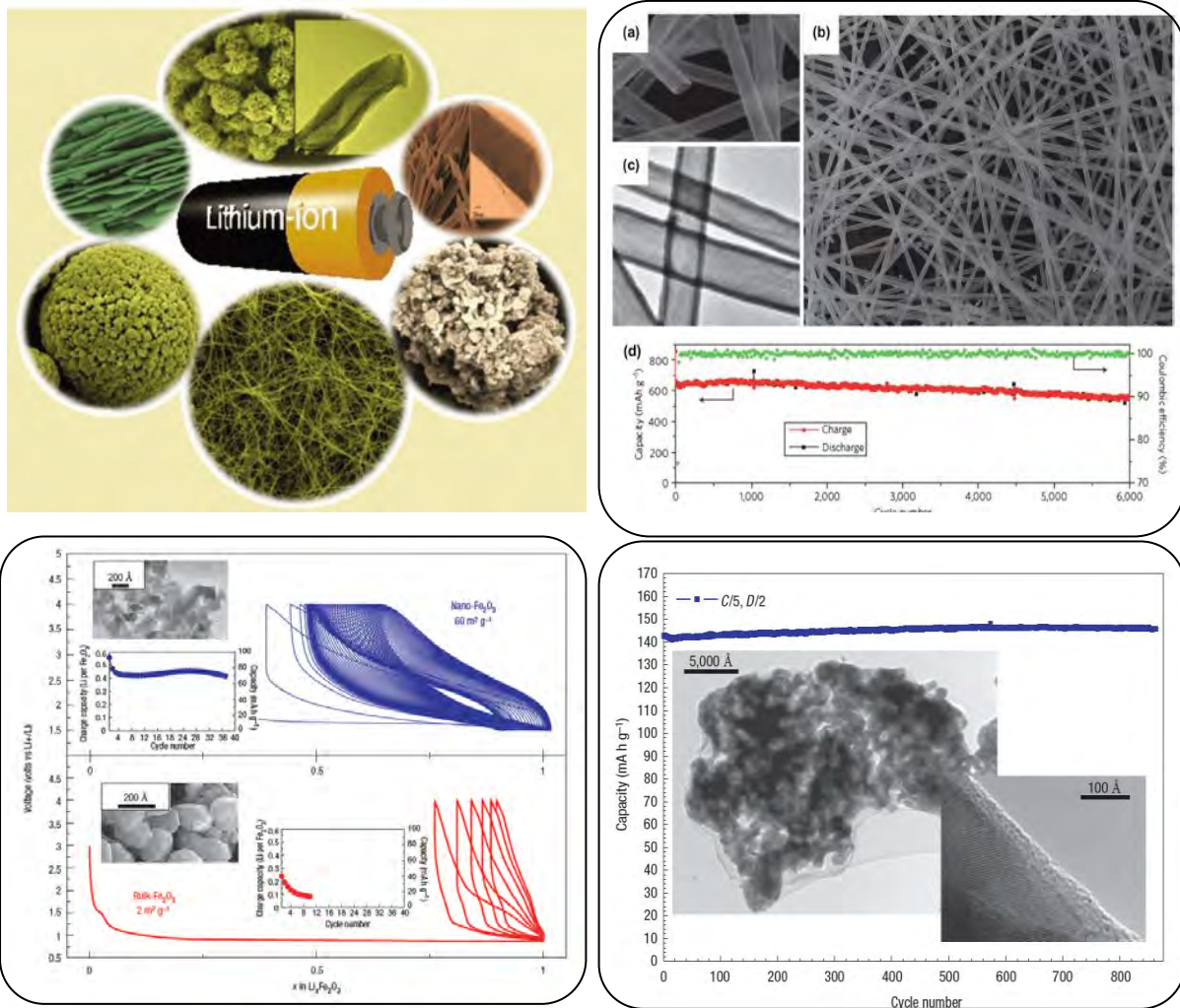


Figure 1.5 Advanced LIBs developed using nanotechnology.^{24,25}

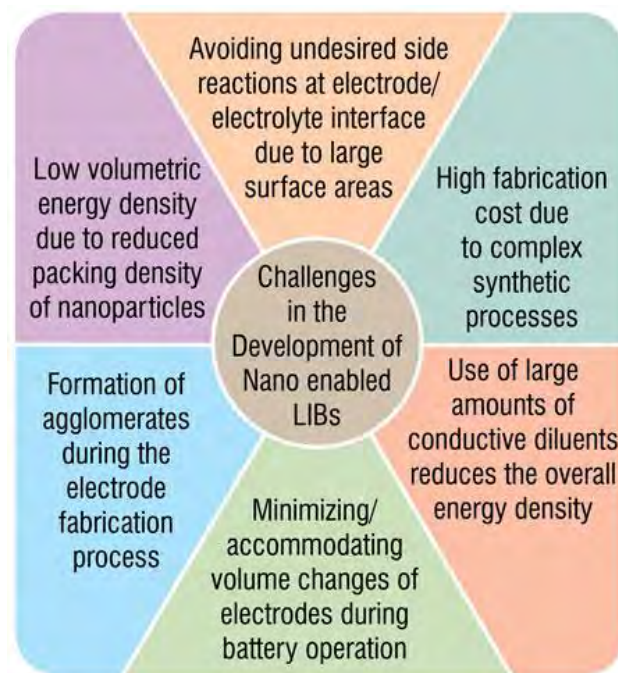


Figure 1.6 Challenges in the development of nano-enabled LIBs. Various strategies like (i) decreasing the particle size to nano-range (ii) employing hollow nanostructures (iii) making nano composites or nano-coatings with carbon and/or inert components, etc., are being used to achieve high capacity and stable cycle-life of electrodes.

1.3.3. Various Applications

During last 20 years, nanotechnology is helping to considerably improve, even revolutionize, many technology and industry sectors: information technology, energy, environmental science, medicine, homeland security, food safety, and transportation, among many others. Described below is a sampling of the rapidly growing list of benefits and applications of nanotechnology. Using nanotechnology, materials can effectively be made to be stronger, lighter, more durable, more reactive, more sieve-like, or better electrical conductors, among many other traits.

For example, polymer composite materials for baseball bats, tennis rackets, motorcycle helmets, automobile bumpers, luggage, and power tool. And surface treatments of fabrics help them resist wrinkling, staining, and bacterial growth, and provide lightweight ballistic energy deflection. Another part, thin films on eyeglasses, computer and camera displays, windows, and other surfaces can make them water-repellent, antireflective, self-cleaning, resistant to ultraviolet or infrared light, antifogging, antimicrobial, scratch-resistant, or electrically conductive. The nanomaterials in cosmetic products provide greater clarity or coverage; cleansing; absorption; personalization; and antioxidant, anti-microbial, and other health properties in sunscreens, cleansers, complexion treatments, creams and lotions, shampoos, and specialized makeup.

Nano-engineered materials in the food industry include nanocomposites in food containers to minimize carbon dioxide leakage out of carbonated beverages, or reduce oxygen inflow, moisture outflow, or the growth of bacteria in order to keep food fresher and safer, longer. Nano-sensors built into plastic packaging can warn against spoiled food. Nanosensors are being developed to detect salmonella, pesticides, and other contaminants on food before packaging and distribution.

Nano-engineered materials in automotive products include high-power rechargeable battery systems such as thermoelectric materials for temperature control, lower-rolling-resistance tires, thin-film smart solar panels, and fuel additives and improved catalytic converters for cleaner exhaust. Nano-engineered materials make superior household products such as degreasers and stain removers; environmental sensors, alert systems, air purifiers and filters; antibacterial cleansers; and specialized paints and sealing products. Nanostructured ceramic coatings exhibit much greater toughness than conventional wear-resistant coatings for machine parts. Nanoparticles are used increasingly in catalysis to boost chemical reactions. This reduces the quantity of catalytic materials necessary to produce desired results, saving money and reducing pollutants. Two big applications are in petroleum refining and in automotive catalytic converters.

In addition to contributing to building and maintaining lighter, smarter, more efficient, and “greener” vehicles, aircraft, and ships, nanotechnology offers various means to improve the transportation infrastructure

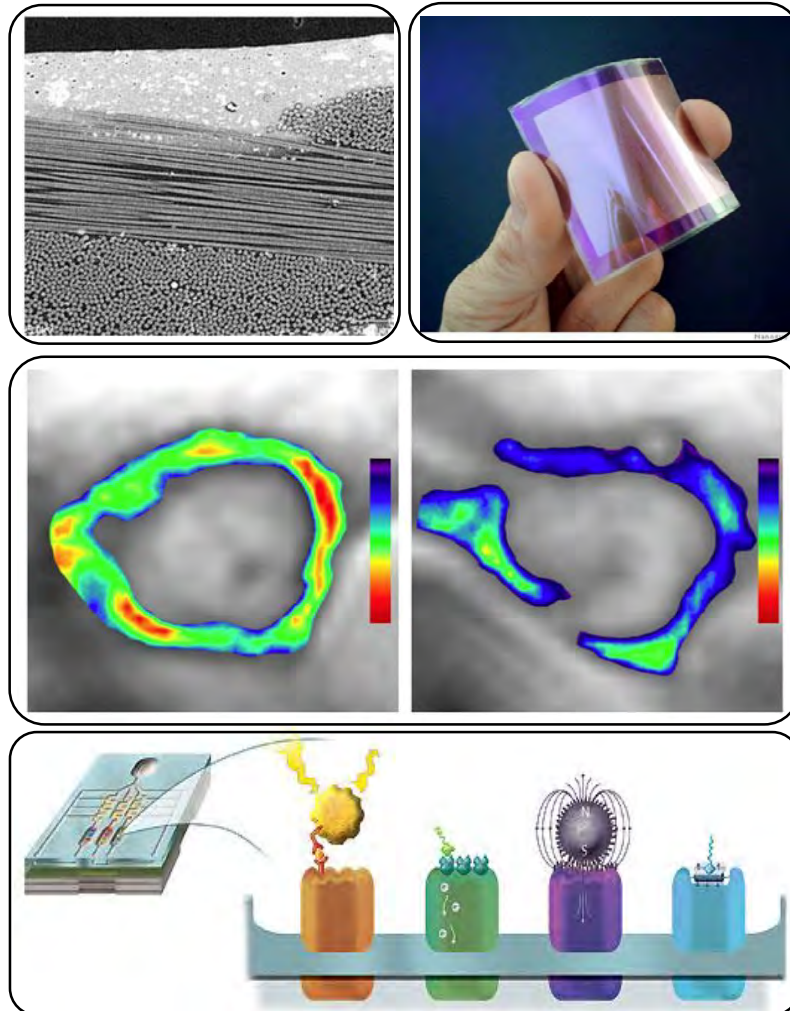


Figure 1.7
and sensor.

Various applications with nanotechnology in complex material, medicine, energy

1.4 References

1. Drexler, K. E., Nanosystems: molecular machinery, manufacturing, and computation. *John Wiley & Sons, Inc.* **1992**.
2. Saini, R.; Saini, S.; Sharma, S., Nanotechnology: the future medicine. *Journal of cutaneous and aesthetic surgery* **2010**, *3* (1), 32.
3. Lu, Z.; Lockwood, D.; Baribeau, J.-M., Quantum confinement and light emission in SiO₂/Si superlattices. *Nature* **1995**, *378* (6554), 258-260.
4. Huertas-Hernando, D.; Guinea, F.; Brataas, A., Spin-orbit coupling in curved graphene, fullerenes, nanotubes, and nanotube caps. *Physical Review B* **2006**, *74* (15), 155426.
5. Nguyen, P. Q.; Botyanszki, Z.; Tay, P. K. R.; Joshi, N. S., Programmable biofilm-based materials from engineered curly nanofibres. *Nat. Commun.* **2014**, *5*, 4945.
6. Narayan, R. J.; Kumta, P. N.; Sfeir, C.; Lee, D.-H.; Choi, D.; Olton, D., Nanostructured ceramics in medical devices: applications and prospects. *Jom* **2004**, *56* (10), 38-43.
7. Panish, M. B., Molecular beam epitaxy. *Science* **1980**, *208* (4446), 916-922.
8. Piner, R. D.; Zhu, J.; Xu, F.; Hong, S.; Mirkin, C. A., "Dip-pen" nanolithography. *science* **1999**, *283* (5402), 661-663.
9. Moreau, W. M., Semiconductor Lithography: Principals and Materials. Plenum, New York, **1988**.
10. Smith, H. I.; Schattenburg, M.; Hector, S.; Ferrera, J.; Moon, E.; Yang, I.; Burkhardt, M., X-ray nanolithography: Extension to the limits of the lithographic process. *Microelectronic engineering* **1996**, *32* (1), 143-158.
11. Choi, J.; Jeong, H.; Pflug, D.; Akinwande, A.; Smith, H., Fabrication of 0.1 μm gate aperture Mo-tip field-emitter arrays using interferometric lithography. *Applied physics letters* **1999**, *74* (20), 3050-3052.
12. Morimoto, H.; Sasaki, Y.; Saitoh, K.; Watakabe, Y.; Kato, T., Focused ion beam lithography and its application to submicron devices. *Microelectronic engineering* **1986**, *4* (3), 163-179.
13. Chou, S. Y.; Wei, M. S.; Krauss, P. R.; Fischer, P. B., Single-domain magnetic pillar array of 35 nm diameter and 65 Gbits/in. ² density for ultrahigh density quantum magnetic storage. *Journal of Applied Physics* **1994**, *76* (10), 6673-6675.
14. Lüthi, R.; Schlittler, R. R.; Brugger, J.; Vettiger, P.; Welland, M. E.; Gimzewski, J. K., Parallel nanodevice fabrication using a combination of shadow mask and scanning probe methods. *Applied Physics Letters* **1999**, *75* (9), 1314-1316.
15. Minne, S.; Manalis, S.; Atalar, A.; Quate, C., Contact imaging in the atomic force microscope using a higher order flexural mode combined with a new sensor. *Applied physics letters* **1996**, *68* (10), 1427-1429.

16. Chou, S. Y.; Krauss, P. R.; Renstrom, P. J., 25-nanometer resolution. *Science* **272** **1996**, 272 (5258), 85-87.
17. Förster, S.; Antonietti, M., Amphiphilic block copolymers in structure-controlled nanomaterial hybrids. *Advanced materials* **1998**, *10* (3), 195-217.
18. Kulkarni, P.; Baron, P. A.; Willeke, K., Aerosol measurement: principles, techniques, and applications. *John Wiley & Sons*: **2011**.
19. Jayasena, B.; Subbiah, S., A novel mechanical cleavage method for synthesizing few-layer graphenes. *Nanoscale Res. Lett* **2011**, *6* (1), 95-101.
20. van Schalkwijk, W.; Scrosati, B., Advances in lithium-ion batteries. *Springer Science & Business Media*: 2002.
21. Liu, Z.; Fu, W.; Payzant, E. A.; Yu, X.; Wu, Z.; Dudney, N. J.; Kiggans, J.; Hong, K.; Rondinone, A. J.; Liang, C., Anomalous high ionic conductivity of nanoporous β -Li₃PS₄. *Journal of the American Chemical Society* **2013**, *135* (3), 975-978.
22. Croy, J. R.; Abouimrane, A.; Zhang, Z., Next-generation lithium-ion batteries: The promise of near-term advancements. *MRS Bulletin* **2014**, *39* (05), 407-415.
23. Tu, Z.; Kambe, Y.; Lu, Y.; Archer, L. A., Nanoporous Polymer-Ceramic Composite Electrolytes for Lithium Metal Batteries. *Advanced Energy Materials* **2014**, *4* (2).
24. Aricò, A. S.; Bruce, P.; Scrosati, B.; Tarascon, J.-M.; Van Schalkwijk, W., Nanostructured materials for advanced energy conversion and storage devices. *Nature materials* **2005**, *4* (5), 366-377.
25. Wu, H.; Chan, G.; Choi, J. W.; Yao, Y.; McDowell, M. T.; Lee, S. W.; Jackson, A.; Yang, Y.; Hu, L.; Cui, Y., Stable cycling of double-walled silicon nanotube battery anodes through solid-electrolyte interphase control. *Nature nanotechnology* **2012**, *7* (5), 310-315.

Chapter II. Main Components of Lithium-Ion Batteries

2.1 Introduction : Li - Ion Rechargeable Batteries for Electric Energy Storage System (ESS)

Today, major battery systems are the rechargeable lead acid system and the primary manganese dioxide-zinc systems. These both systems have a long history and are at an advanced state of technical boundary. Lithium-ion batteries are one of the great successes of modern materials electrochemistry in battery systems (Figure 2.1). Commercially available Li-ion batteries (LIBs) are currently operated at high operation voltage (3.6~3.7V) in cathode, which is generally designed with lithium metal and transition metal oxides, and an anode of carbon materials such as graphite and hard/soft amorphous carbon.^{1,2} The LIBs are poised to challenge these established systems as the demand for higher-performance battery systems continues. Lithium has a low atomic number and a high electrode potential that results in significantly high energy density for the LIBs compared to lead and zinc in the traditional batteries. However, the development for new high-energy lithium systems has been neither simple nor easy. It has required a total systems approach and the development of breakthrough technologies based on new anodes, cathodes, and non-aqueous electrolytes to continue the steady improvement of high energy lithium battery systems. The performance of LIBs depend on the type of cathode materials, and lithium cobalt oxides (LiCoO_2 , LCO) is usually used in mobile and portable device application,³ while lithium manganese oxides (LiMn_2O_4 , LMO) or lithium iron phosphate (LiFePO_4 , LFP) has been applied to electric vehicle (EV) due to plenty resources, and low manufacture cost (Table 2.1).⁴ However, their specific capacity is around 150 mAh/g in the present system. Thus, many researchers study on various approach to cathode another lithium oxide material instead of LCO, LMO, and LFP such as, Li rich cathode materials and the lithium (nickel, manganese, aluminum, cobalt) composited oxide materials, which is still needed to be developed for smaller LIB system with high capacity about > 250 mAh/g. In anode materials parts, the alloying materials likes silicon, tin were developed morphology control and surface modification to use anode parts in battery systems instead of carbon based materials.⁵ however, the development of new anode materials still needs solution about many problems of side reaction during operation of battery systems. So, the development of alternative anode with 500~800 mAh/g is needed to balance the cell when increasing the capacity of cathode materials is considered. Recently, various extended approaches play design of battery and systems for new typed batteries satisfied flexible, wearable, stretchable properties such as cable type battery, system removed one of needs parts like current collector, binder and separator.

Specifications	Lead-Acid	NiCd	NiMH	Li-Ion		
				Cobalt	Manganese	Phosphate
Specific energy density (Wh/kg)	30 – 50	45 – 80	60 – 120	150 – 190	100 – 135	90 – 120
Internal resistance (mΩ/V)	<8.3	17 – 33	33 – 50	21 – 42	6.6 – 20	7.6 – 15.0
Cycle life (80% discharge)	200 – 300	1,000	300 – 500	500 – 1,000	500 – 1,000	1,000 – 2,000
Fast-charge time (hrs.)	8 – 16	1 typical	2 – 4	2 – 4	1 or less	1 or less
Overcharge tolerance	High	Moderate	Low	Low	Low	Low
Self-discharge/month (room temp.)	5 – 15%	20%	30%	<5%	<5%	<5%
Cell voltage	2.0	1.2	1.2	3.6	3.8	3.3
Charge cutoff voltage (V/cell)	2.40 (2.25 float)	Full charge indicated by voltage signature	Full charge indicated by voltage signature	4.2	4.2	3.6
Discharge cutoff volts (V/cell, 1C*)	1.75	1	1	2.5 – 3.0	2.5 – 3.0	2.8
Peak load current**	5C	20C	5C	> 3C	> 30C	> 30C
Peak load current* (best result)	0.2C	1C	0.5C	<1C	< 10C	< 10C
Charge temperature	-20 – 50°C	0 – 45°C	0 – 45°C	0 – 45°C	0 – 45°C	0 – 45°C
Discharge temperature	-20 – 50°C	-20 – 65°C	-20 – 65°C	-20 – 60°C	-20 – 60°C	-20 – 60°C
Maintenance requirement	3 – 6 months (equalization)	30 – 60 days (discharge)	60 – 90 days (discharge)	None	None	None
Safety requirements	Thermally stable	Thermally stable, fuses common		Protection circuit mandatory		
Time durability				>10 years	>10 years	>10 years
In use since	1881	1950	1990	1991	1996	1999
Toxicity	High	High	Low	Low	Low	Low

Source: batteryuniversity.com. The table values are generic, specific batteries may differ.

**C* refers to battery capacity, and this unit is used when specifying charge or discharge rates. For example: 0.5C for a 100 Ah battery = 50 A.

*Peak load current = maximum possible momentary discharge current, which could permanently damage a battery.

Table 2.1 The specifications of various battery systems.

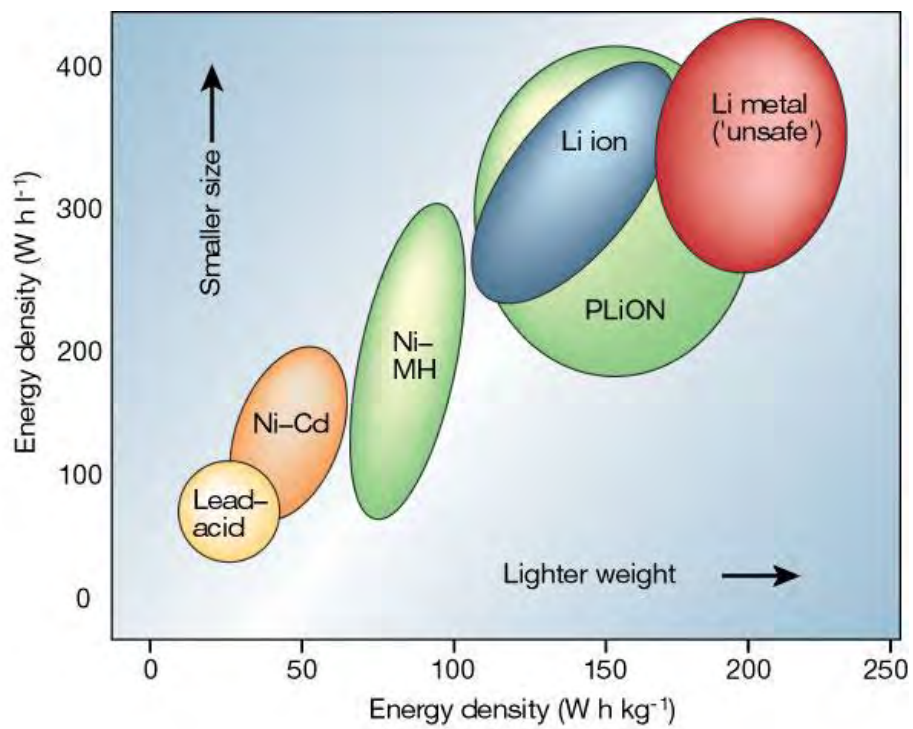


Figure 2.1 Comparison of different battery technologies in terms of volumetric and gravimetric energy density.

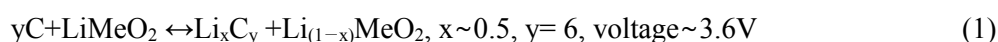
2.2.2 History of Li - Ion Batteries

Lithium (Li) batteries were first designed by M. S. Whittingham who is working for Exxon in the 1970s.⁶ He used titanium sulfide and lithium metal as the electrodes. The lithium batteries with metallic Li electrodes present safety issues, as pure Li metal is a highly reactive element; it burns in normal atmospheric conditions with the water and oxygen.⁷ As a result, research topic was moved to development of Li-batteries which is lithium compounds with not only electrical reactivity of accepting and releasing lithium ions but also stability of environments, instead of metallic lithium. And a graphite⁸ having reaction mechanism of reversible intercalation with Li ion and cathodic oxide materials^{9,10} was discovered in the 1970s by J. O. Besenhard at TU Munich. Also, he proposed its application in lithium cells.¹¹ However, in this lithium cell, an electrolyte decomposition and solvent co-intercalation into graphite were severe early drawbacks for battery cycling life.

In 1979, John Goodenough and Koichi Mizushima demonstrated a rechargeable cell with voltage in the 4 V range using lithium cobalt oxide (LiCoO₂, LCO) materials as the positive electrode and lithium metal as the negative electrode.¹² This innovation of new material provided the positive electrode material in commercial usable Li batteries. The material is a stable positive electrode material which acts as a donor of lithium ions, which means that it can be used with a negative electrode material other than lithium metal. By enabling the use of stable and easy-to-handle negative electrode materials, the material opened a whole new range of possibilities for novel rechargeable battery systems. In 1977, Samar Basu demonstrated electrochemical intercalation of lithium in graphite at the University of Pennsylvania.¹³ This results led to the development of a workable lithium intercalated graphite electrode at Bell Labs (LiC₆)¹⁴ to provide an usable negative electrode instead of the lithium metal electrode in Li battery. In 1980, Rachid Yazami demonstrated the reversible electrochemical intercalation of lithium in graphite.¹⁵ The organic electrolytes available at the time would decompose during charging with a graphite negative electrode, slowing the development of a rechargeable lithium/graphite battery. He used a solid electrolyte to demonstrate that Li could be reversibly intercalated in graphite through an electrochemical mechanism. The graphite electrode discovered by him is currently the most commonly used electrode in commercial lithium ion batteries.^{16,17} In 1985, Akira Yoshino assembled a prototype cell using carbonaceous material into which Li ions could be inserted as one electrode, and LCO, which is stable in air, as the other to improve safety by using materials without Li metal.¹⁸ The LCO enabled industrial-scale production and represents the birth of the current LIBs. In 1989, Goodenough and Arumugam Manthiram of the University of Texas at Austin showed that positive electrodes containing polyanions produce higher voltages than oxides due to the induction effect of the polyanion.¹⁹ The performance and capacity of lithium-ion batteries increases as development progresses. In 1991, Sony Corporation and Asahi Kasei released the first commercial lithium-ion battery using both LCO and graphite electrodes.

2.2.3 Theory of Li - Ion Batteries

Lithium ion batteries are light, compact and work with a voltage as high as 3.6V (three times that of alkaline systems) with a specific energy density ranging between 120Wh kg⁻¹ and 150Wh kg⁻¹ (two to three times those of usual Ni–Cd batteries). In its most conventional structure (Figure 2.2), a common lithium ion battery contains a graphite anode (e.g. mesocarbon microbeads, MCMB), a cathode formed by a lithium metal oxide, (e.g. LiCoO₂), an electrolyte consisting of a solution of a lithium salt (e.g. LiPF₆) in a mixed organic solvent (e.g. ethylene carbonate–dimethyl carbonate, EC–DMC), and imbedded a separator membrane in electrolyte.²⁰ In most common cases, these batteries are based on the C // LiPF₆ in EC–DMC // LiMeO₂ sequence and operate on a process:



This involves the reversible extraction and insertion of Li ions between the two electrodes with a concomitant removal and addition of electrons. Due to the high value of the energy content, LIBs have triggered the growth of the market of popular devices, such as mobile phone, lap-top computer, MP3player and others. At first sight, the electrochemical process which drives the lithium ion battery appears quite simple, apparently consisting of the reversible exchange of lithium ions between the two electrodes. However, in practice the operation of this battery requires the ongoing of key side processes. In Figure 2.3a we can see that the redox process at the graphite anode evolves around 0.05V vs. Li and that of the LiCoO₂ cathode evolves at about 4V vs. Li. The onset of the current in the electrolyte reveals the occurrence of either reductive or oxidative decomposition processes that define its stability domain. The figure shows that the electrolyte domain extends from about 0.8V vs. Li to 4.5V vs. Li and that the graphite anode operates well outside the stability of the electrolyte and the cathode is just at its limit.

This is also clearly visible from Figure 2.3b that shows the voltage ranges of the graphite anode and the LCO cathode in comparison with the stability window of the most common organic liquid electrolytes. We can then conclude that the C/LCO battery is thermodynamically unstable in these electrolytes. However, in practice, the battery operates under a kinetic stability: the initial decomposition of the electrolyte results in the formation of a protective film on the anode surface, this providing the condition to assure the continuation of its charge and discharge processes. More dangerously serious are the oxidative processes at the cathode side. Under proper conditions the battery operates below the oxidative limit of the electrolyte. However, if by unexpected events, such as accidental overcharge, this limit is exceeded, no protecting film is formed on the cathode and the electrolyte continues to oxidize, this greatly contributing to accelerate cell failure. Overall, both anode and cathode decomposition processes imply consumption of active masses and of electrolytes, accompanied by gas evolution led to loss of capacity and safety hazard (Figure 2.4)

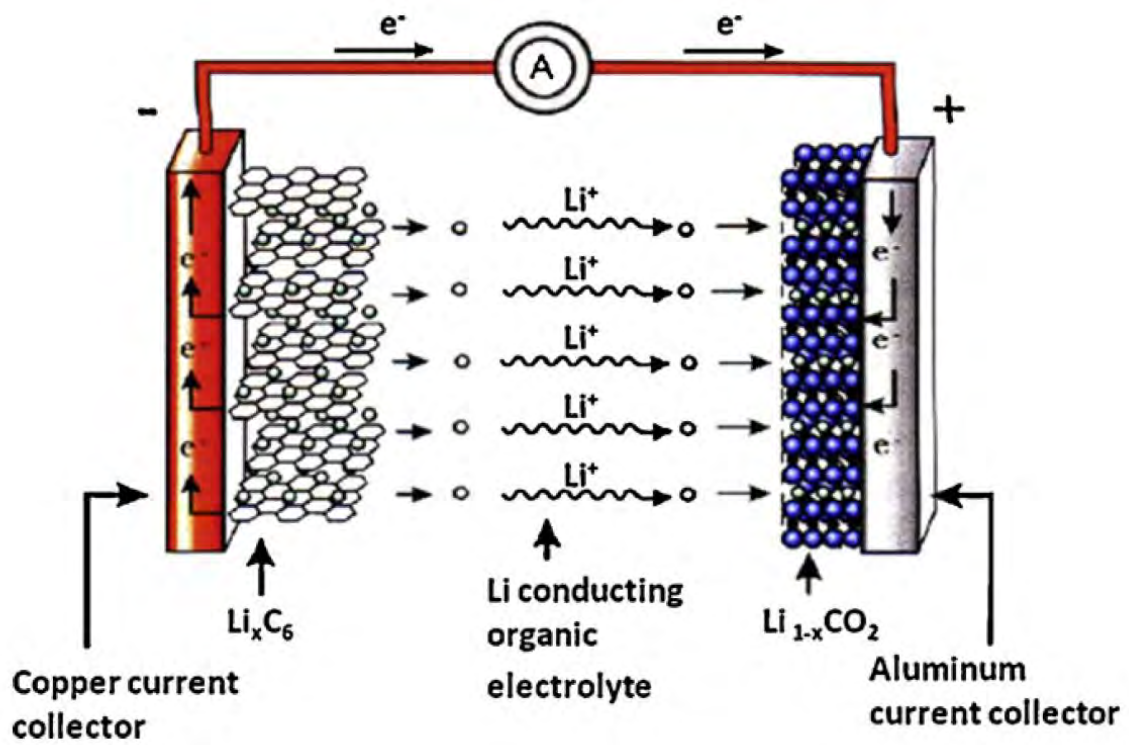


Figure 2. 2 Scheme of typical lithium-ion battery system.

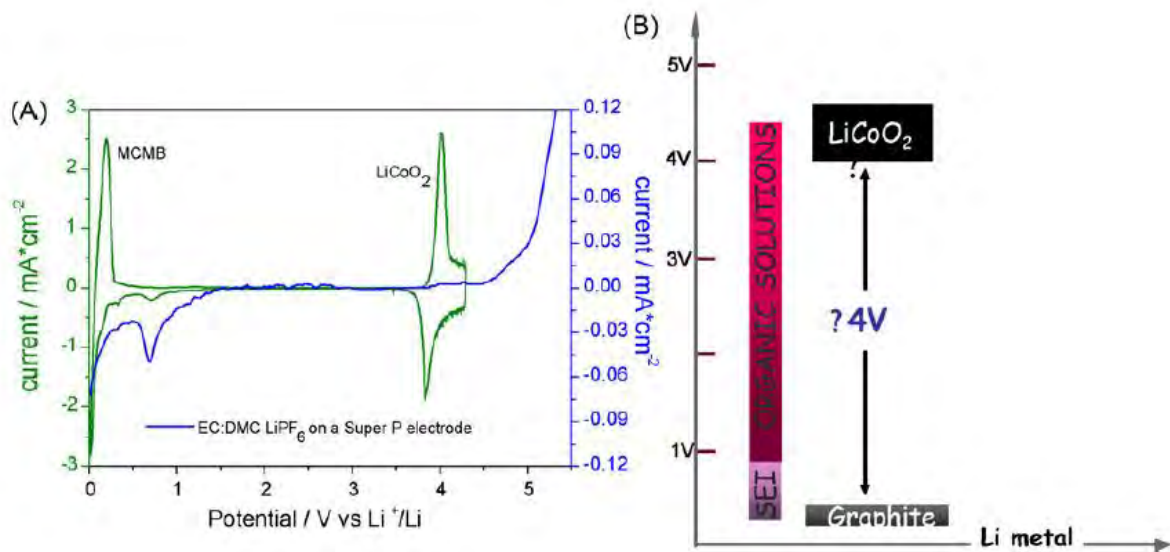


Figure 2.3 Cyclic voltammetry profiles of LIBs components: anode and cathode (green), electrolyte (blue). Counter electrodes: super P carbon, in EC/DMC, LiPF₆. (B) Potential operation ranges of the LiCoO₂/C electrode combination.

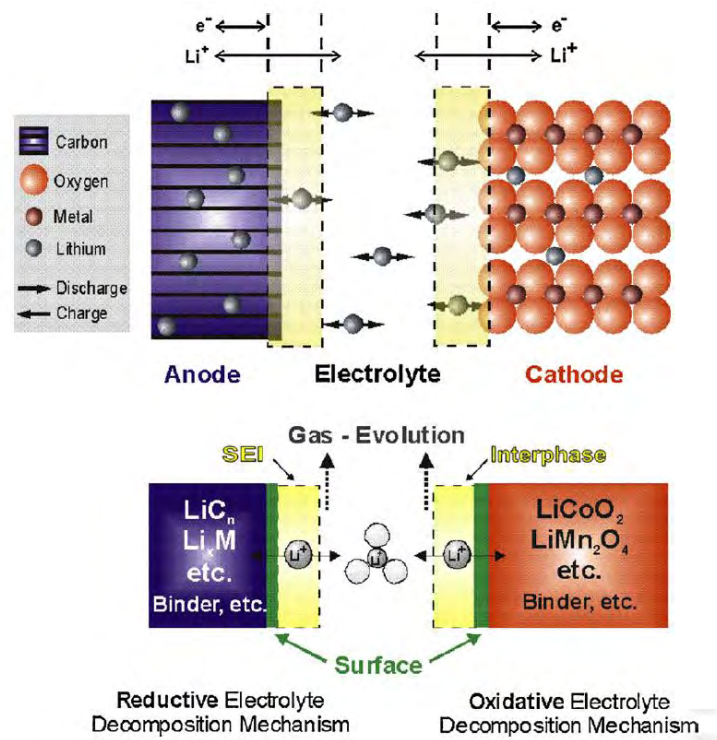


Figure 2. 4 Operational principle of SEI formation in the electrode of LiCoO₂/C combination.

2.2 Composition Materials in Li - Ion Batteries

2.3.2 Cathode

Cathode materials has the important proportion in the LIB material, and they are classified into layered, spinel, and olivine depending on a structure.(Table 2.2) The cathode material most commonly used in lithium ion batteries is LiCoO_2 .²¹ LiCoO_2 forms the $\alpha\text{-NaFeO}_2$ structure, which is a distorted rock-salt structure where the cations order in alternating (111) planes. This ordering results in a trigonal structure and, for LiCoO_2 , planes of lithium ions through which lithiation and delithiation can occur.²² Although LiCoO_2 is a successful cathode material, alternatives are being developed to lower cost and improve stability. Cobalt is less available, and thus more costly, than other transition metals, such as manganese, nickel and iron. In addition, LiCoO_2 is not as stable as other potential electrode materials and can undergo performance degradation or failure when overcharged.²³ The most commonly used a $\text{Li}(\text{Ni},\text{Mn},\text{Co})\text{O}_2$ composition contains equal amounts of the three transition metals such as $\text{Li}(\text{Ni}_{1/3}\text{Mn}_{1/3}\text{Co}_{1/3})\text{O}_2$ having a high capacity, a good rate capability²⁴ and can operate at high voltages. A higher charging voltage increases the capacity, but also leads to more rapid loss of capacity during cycling.²⁵ As with $\text{LiNi}_{1-x}\text{Co}_x\text{O}_2$, cobalt helps to reduce the amount of nickel in the lithium layer and small amounts of cobalt (up to 0.20 ~ 0.25) have been shown to improve capacity.²⁶ Increased cobalt content can also reduce the loss in capacity during cycling.²⁷ The improved performance has been attributed to cobalt increasing the conductivity²⁸ and improving the structural stability²⁹ of the cathode. Although nickel in the lithium layer can be detrimental to lithium transport, it has been shown to stabilize the structure during delithiation and thus improve cycling performance.³⁰ $\text{Li}(\text{Ni},\text{Mn},\text{Co})\text{O}_2$ can be over lithiated, which has been shown to improve electrode performance³¹, especially with low cobalt contents.³² There can be an oxidative loss during the first cycle, which is not recovered during normal cycling.³³

Another promising cathode material is LiMn_2O_4 that forms a spinel structure, in which manganese occupies the octahedral sites and lithium predominantly occupies the tetrahedral sites.³⁴ In this case, the paths for lithiation and delithiation are a 3-dimensional network of channels rather than planes, as in the $\alpha\text{-NaFeO}_2$ structure. LiMn_2O_4 is lower cost and safer than LiCoO_2 ,³⁵ but has a lower capacity as compared to the cathode materials that form the $\alpha\text{-NaFeO}_2$ structure described above.³⁶ One of the challenges in the use of LiMn_2O_4 as a cathode material is that phase changes can occur during cycling.³⁷

Another promising class of cathode materials are phosphates (LiMPO_4) with the olivine structure, in which phosphorous occupies tetrahedral sites, the transition metal (M) occupies octahedral sites and lithium forms one-dimensional chains along the [0 1 0] direction.³⁸ The phosphate most commonly used for the cathode is LiFePO_4 , which delithiates to FePO_4 as the Fe^{2+} is oxidized to Fe^{3+} .³⁹ Some iron ions occupy lithium sites, which results in the formation of lithium ion vacancies to maintain charge neutrality.⁴⁰ There is amiscibility gap between FePO_4 and LiFePO_4 ,⁴¹ so the

delithiation occurs by growth of a two-phase front rather than a continuous change in lithium content.⁴² The formation of a two-phase mixture establishes a fixed activity, which results in a relative flat discharge profile

Material	Capacity (mAh/g)	Density (g/CC)	Energy Density (mAh/CC)	Potential curve	Safety	Cost	Comments
LiCoO₂	160	5.05	808	Flat	Fair	High	Small Size
LiNiO₂	220	4.80	1056	Sloping	Poor	Fair	Impossible
LiNi_{0.8}Co_{0.2}O₂	180	4.85	873	Sloping	Fair	Fair	Small Size
LiNi_{0.8}Co_{0.15}Al_{0.05}O₂	200	4.80	960	Sloping	Fair	Fair	Small Size
LiMn_{0.5}Ni_{0.5}O₂	160	4.70	752	Sloping	Good	Low	
LiMn_{1/3}Ni_{1/3}Co_{1/3}O₂	200	4.70		Sloping	Good	Low	
LiMn_{0.4}Ni_{0.4}Co_{0.2}O₂	200	4.70					
LiMn₂O₄	110	4.20	462	Flat	Good	Low	EV
Li_{1.06}Mg_{0.06}Mn_{1.88}O₄	100	4.20	420	Flat	Good	Low	EV
LiFePO₄	160	3.70	592	Flat	Good	Low	Low conductivity

Table 2.2 Properties of cathode materials for LIBs

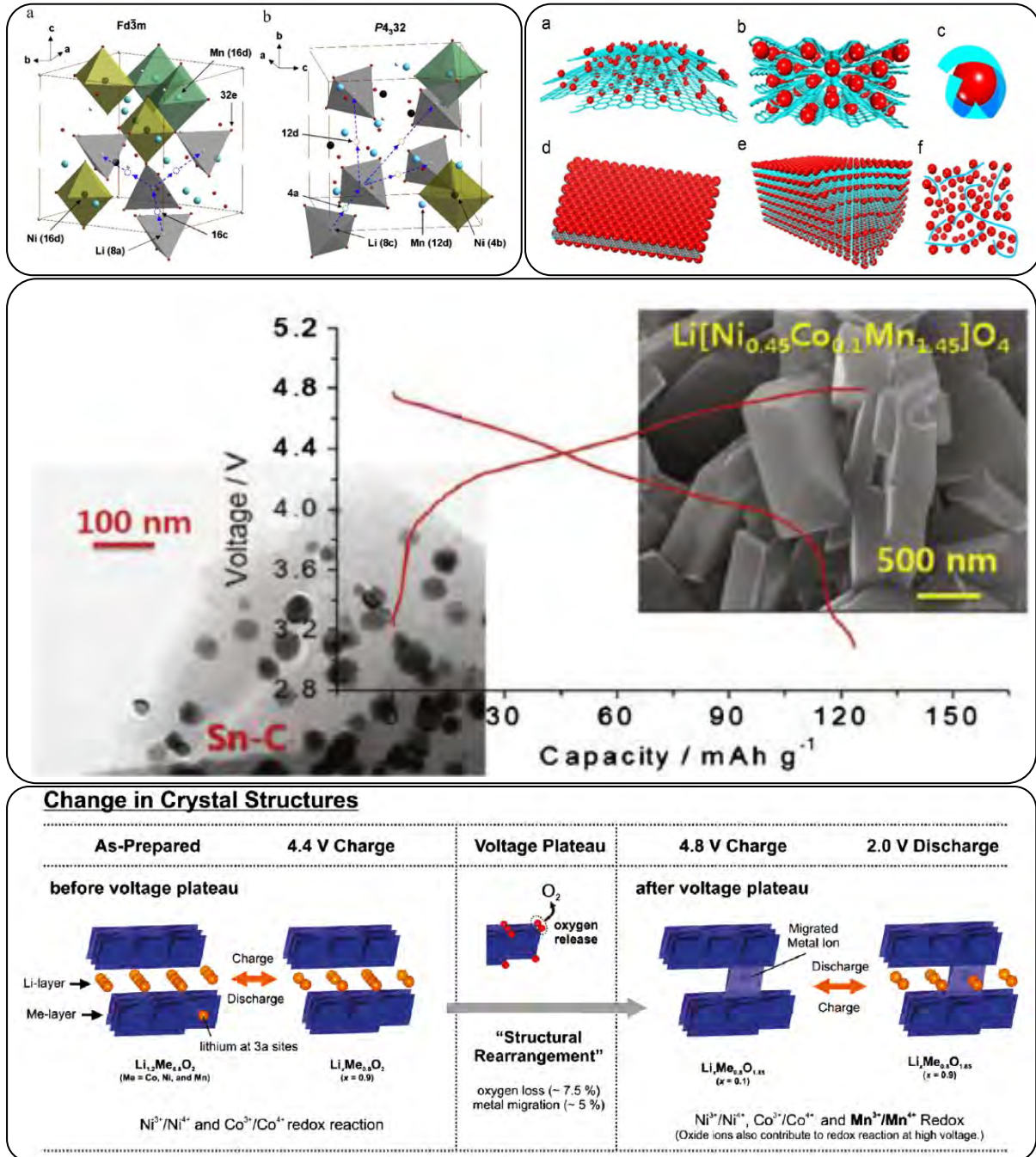


Figure 2.5 Representative cathode in LIBs; its microstructure, mechanism and electrochemical performances.

2.3.3 Anode

We will discuss the state-of-the-art of anode materials for LIBs, with particular emphasis on the recent nanotechnology outcomes and outstanding results. Also, we will classify the discussed innovative anode materials in three main groups, depending on their Li-ion battery performances and reaction mechanism (see Table 2.3):

- 1) Intercalation/de-intercalation materials: carbon based materials (porous carbon, carbon nanotubes (CNT), grapheme), TiO_2 , and $\text{Li}_4\text{Ti}_5\text{O}_{12}$
- 2) Alloy/de-alloy materials: Si, Ge, Sn, Al, Bi,
- 3) Conversion materials: transition metal oxides (Mn_xO_y , NiO, Fe_xO_y , CuO, Cu_2O , MoO_2 etc.), metal sulphides, metal phosphides and metal nitrides (M_xX_y ; here X= S, P, N).

2.1.3.1. Carbon based materials

Carbon-based materials with various consistencies and morphologies have been recognized as appropriate anode materials for LIBs due to their features, such as ease of availability, stability in thermal, chemical and electrochemical environment, low cost, and good lithium intercalation and de-intercalation reversibility.^{17,43} These characteristics are quite important especially when considering that charged electrode materials, either delithiated cathodes or lithiated anodes, have the tendency to violently react with non-aqueous electrolytes at elevated temperatures. However, also at room temperature, side reactions can occur.⁴³ In particular, the LiPF_6 lithium salt has the tendency of reacting with moisture resulting in the formation of HF. The produced HF would, in turn, cause the dissolution of any transition metal in the electrodes and/or the surface erosion of the active materials, therefore leading to capacity decay upon charge-discharge cycling. The final result is the slow degradation of both the active electrode material and the electrolyte as well as the formation of a thick passive layer on the electrode surface during cycling. In particular, when it comes to anode, this layer is known as Solid Electrolyte Interface (SEI). In this regard, the use of carbon coating on the active materials can provide a way to mitigate the mentioned drawbacks. In fact, carbon shows an electrochemical activity towards the electrolyte only at very low potentials, and without any oxidation up to the cutoff voltage of the battery. Furthermore, high resistance to HF corrosion can be expected owing to the very good chemical stability of carbon. Finally, carbon coating can also prevent the surface oxidation of active materials in air, especially at the nanoscale level. In fact, nanostructured active materials present a high surface area which enhances the surface oxidation. For these reasons the carbon coating has the capability to greatly retard any surface degradation during storage and to strongly reduce the capacity fading upon charge-discharge cycling. Some studies reporting the role of carbon coating on anode active materials for Li-ion batteries are here listed. For example, Zhang et al. directly observed the difference in the SEI formation between carbon coated and non-coated graphite anode.⁴⁴ The SEI film for carbon coated natural graphite spheres was found to be quite compact with a

thickness from 60 nm to 150 nm, much thinner than the SEI film found on uncoated graphite spheres, showing thickness from 450 nm to 980 nm. The conclusion was that carbon coating can reduce the decomposition of the electrolyte and it can lead to the formation of a thin SEI on the electrode surface. Furthermore, it has been proved that after carbon coating the graphite surface, any direct contact of graphite with the electrolyte is prevented, therefore the decomposition of propylene carbonate is greatly reduced and the intercalation of electrolyte species (organic carbonates) into graphene layer is prevented.⁴⁵ The role of carbon coating on different kinds of active materials other than graphite has also been studied. For example, He et al. investigated the effect of carbon coating

2.2.2.2. Alloy/de-alloy materials

The next generation of LIBs is expected to fulfil the power demand of high energy consuming devices, to power electric vehicles (EV) and storage systems (ESS) and to be used in stationary applications. Hence, the specific capacity is the fundamental parameter to be considered in novel anode active materials. Materials which can satisfy the requirement of high capacity are, for example, silicon, germanium, silicon monoxide and tin oxide which react with lithium according to an alloy/de-alloy mechanism. Their specific theoretical capacity ranges from 783 mAh g⁻¹ for tin oxide up to 4211 mAh g⁻¹ for silicon.^{46,47} Even though these alloy based materials can provide larger specific capacity than graphite (372 mAh g⁻¹) and LTO (175 mAh g⁻¹), the major drawbacks are the poor cycling life due to the high volume expansion/contraction and the larger irreversible capacity at the initial cycles. In order to overcome these issues, various approaches have been followed: the downsizing from micro to nanoscale particle and the fabrication of composites with both lithium active and inactive material, are the most promising. In the latter case the lithium active/inactive material serves as a conductive buffer matrix between the alloy materials and lithium source.⁴⁸ Nanostructured alloy materials with different morphologies like nanowires and nanotubes have been considered as an implementable path to achieve high capacity with a good rate capability and long cycling life.⁴⁹

2.2.2.2.1 Silicon (Si)

Silicon has both the highest gravimetric capacity (4200 mAh g⁻¹, Li₂₂Si₅) and volumetric capacity (9786 mAh cm⁻³) among the anode material candidates.⁵⁰⁻⁵² In addition, the discharge (lithiation) potential of silicon is almost close to graphite i.e. 0.4 V vs. Li/Li⁺. Finally, Si is the 2nd most abundant element on earth, hence inexpensive and eco-friendly. It is then easily understood why silicon and its derivatives are considered the most promising and interesting materials for the realization of the future generation of LIBs, which justifies the strong academic and industrial interest for their development as anode active materials. The electrochemical lithiation of Si electrodes has been deeply investigated by many groups. It has been clarified that the high specific capacity value is due to the formation of intermetallic Li-Si binary compounds such as Li₁₂Si₇, Li₇Si₃, Li₁₃Si₄, Li₂₂Si₅.⁵²

However, some issues prevent the employment of Si as anode in LIBs. Firstly, the large volume modification ($\sim 400\%$) during the charge/discharge process causes poor cycling life and irreversible capacity. Secondly, the formation of Si compounds at the solid electrolyte interface inhibits the alloy/de-alloy process. In order to understand the exact reason of poor cycling stability of Si as anode in LIBs, many in-situ investigations with different experimental techniques such as XRD, NMR, TEM have been performed.⁵³ These studies evidenced that the electrical contact between the active material and both the conductive carbon and current collector undergoes a drop due to the large volume expansion/contraction of the Si anode, leading to an irreversibility of lithium insertion/extraction. Eventually, these volume changes result in shorter cycling life and capacity fading.

2.2.2.2.2. Germanium (Ge)

A germanium is an extensively studied active anode material owing to its high lithium storage capability (1623 mAh g^{-1}) with $\text{Li}_{22}\text{Ge}_5$ as equivalent stoichiometry and reversible alloy/de-alloy reactions.^{47,54} Even though Ge is considerably more expensive and shows lower capacity than silicon, it has desirable advantages such as high intrinsic electrical conductivity (104 times higher than silicon), higher capacity than graphite anode and a narrow band gap (0.67 eV). Furthermore, it has been reported that the lithium diffusion into Ge is 15 and 400 times faster than in Si at 360°C and at room temperature, respectively. This ensures higher rate capability and more efficient charge transport than in silicon and graphite as well.^{47,55} Ge high power capability is then extremely important in advanced high power density applications such as electric vehicles. However, as discussed for silicon, the practical usage of Ge as active electrode in LIBs is hindered by the dramatic volume change ($\sim 300\%$) during lithium insertion/deinsertion.^{47,56} Ge nanostructures, such as nanoparticles, nanowires and nanotubes can effectively sustain the volume change with better efficiency than bulk and microstructures. Noticeably, improvements have been observed with hybrid composite of Ge nanoparticles using conductive matrices, obtained through simple preparation routes.

2.2.2.3. Conversion materials

In this section we will provide an overview on the transition metal compounds such as oxides, phosphides, sulphides and nitrides (M_xN_y ; $\text{M} = \text{Fe, Co, Cu, Mn, Ni}$ and $\text{N} = \text{O, P, S}$ and N) when utilized as anodes in LIBs. The electrochemical reaction mechanism involving these compounds together with lithium, implies the reduction (oxidation) of the transition metal along with the composition (decomposition) of lithium compounds (Li_xN_y ; here $\text{N} = \text{O, P, S}$ and N). Anodes based on these compounds exhibit high reversible capacities ($500\sim 1000 \text{ mAh g}^{-1}$) owing to the participation of a high number of electrons in the conversion reactions.⁵⁷

Active materials	Theoretical capacity (mAh/g)	Advantages	Common issues
Insertion/de-insertion materials			
A. Carbonaceous		➤ Good working potential	➤ Low coulombic efficiency
a. Hard carbons	200-600	➤ Low cost	➤ High voltages hysteresis
b. CNTs	1116	➤ Safety	➤ High irreversible capacity
c. Graphene	780/1116		
B. Titania		➤ Extreme safety	➤ Low capacity
a. Li ₄ Ti ₅ O ₁₂	175	➤ Good cycle life	➤ Low energy density
b. TiO ₂	330	➤ Low cost	
		➤ High power capability	
Alloy/de-alloy materials			
A. Silicon	4212	➤ \	➤ High irreversible capacity
B. Germanium	1624	➤ High specific capacities	➤ Huge capacity fading
C. Tin	993	➤ High energy density	➤ Poor cycling
D. Antimony	660	➤ Good safety	➤ Huge volume change
E. Tin oxide	790		
F. Silicon monoxide	1600		
Conversion materials			
A. Metal oxide (Fe ₂ O ₃ , Fe ₃ O ₄ , CoO, Co ₃ O ₄ , Cu ₂ O, CuO, RuO ₂ , MoO ₂ , MoO ₃)	500-1200	➤ High capacity ➤ High energy density ➤ Low cost ➤ Environmentally compatibility	➤ Low coulombic efficiency ➤ Unstable SEI formation ➤ High voltages hysteresis ➤ Poor cycle life
B. Metal phosphides/sulfides/nitrides (MX, M=Fe, Mn, Ni, Co X=P, S, N)	500-1800	➤ High capacity ➤ Low operation V ➤ Low polarization than counter oxides	➤ Poor cycle life ➤ High cost of production

Table 2.3 Common anode materials used for LIBs.

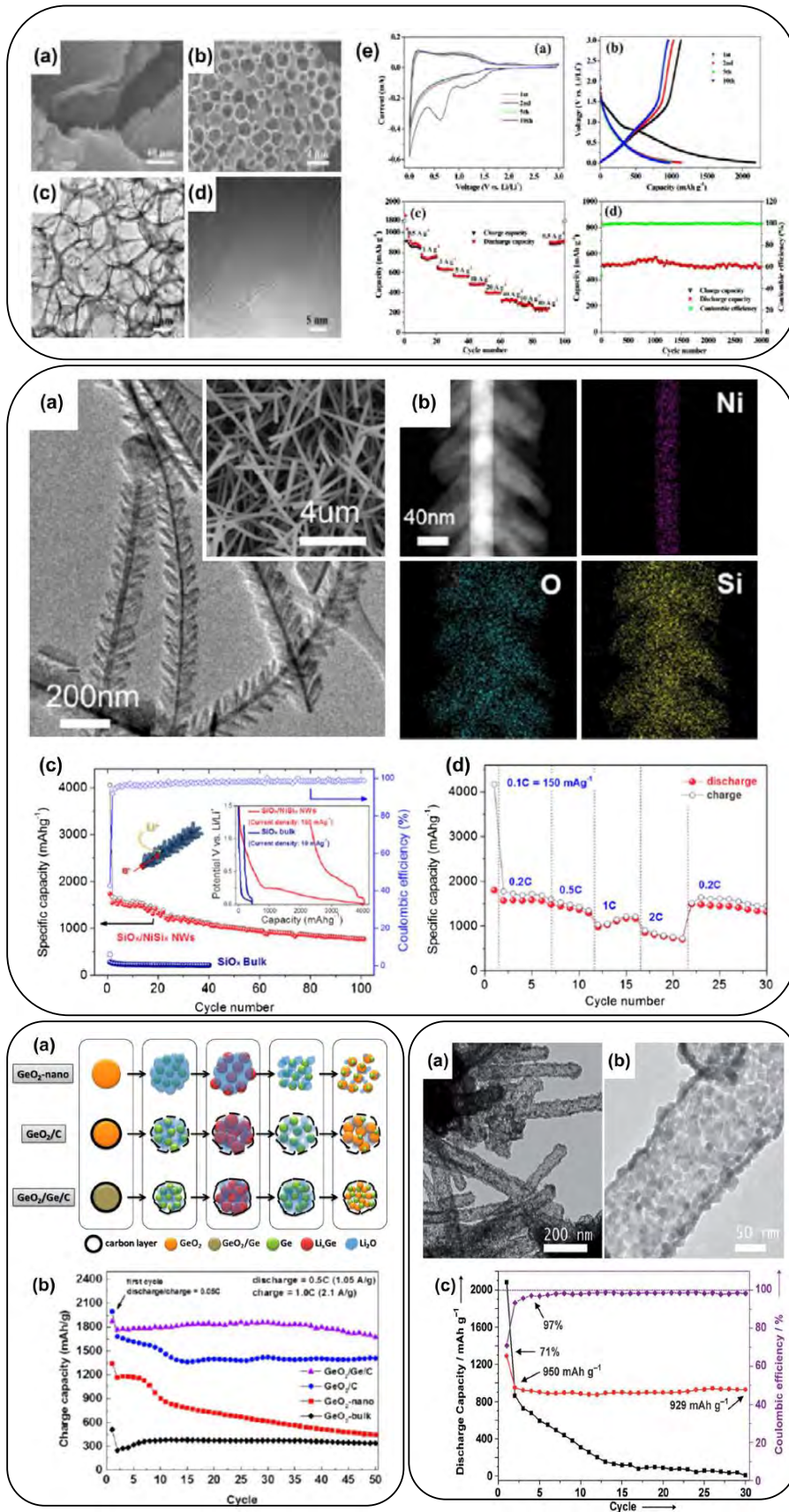


Figure 2.6 Electrochemical properties of Several anode materials for LIBs.

2.3.4 Electrolyte

Electrolyte can be considered as an intermediate allowing a transport of Li ion during charge/discharge process. It consists of co-solvent likes EC and DMC mixed, which is mixed with a low viscosity solvent and a high permittivity solvent, and a Li salt prepared by dissolving a predetermined concentration.⁵⁸ Lithium hexafluorophosphate (LiPF₆) is generally used due to high ionic conductivity and good stability. To stabilize an interface between electrode and electrolyte, the additives is added, and a fluorine-based electrolytes is being used to improve an electrolyte stability with poor flame retardancy.⁵⁹ For the development of advanced electrolyte, it is strongly considered that electrolyte should be designed with i) non-fluorine-based flame retardant property, ii) electrochemical stability within operating voltage range, iii) thermal stability at high temperature during operation, and iv) securing the ion conductivity at low temperature. Additionally, a polymer electrolyte is considered due to little leakage and high stability, but its ion conductivity is low. Therefore, to address this problem, a plasticizer is added to make gel condition which can improve a rate of ionic conductivity in polymer electrolyte.

2.3.5 Separator

Separator has a function to separate cathode and anode electrode for a prevention of electrical contact between the electrodes. Also, it enables Li ion to penetrate through the pores during electrochemical reaction. Depending on how separator is produced, it can be classified into dry- and wet-based process. IT devices adapt a separator from a mixed process, while EV system utilizes one from dry-process due to an excellent high-temperature stability. General separator has a thickness of ~ 20μm, which is porosity film based on polyolefin. Also, the very small pores are produced to pass through Li ions only, and the separator porosity has greatly influenced on the output characteristics of the battery.⁶⁰ For existing small applications, separator is mainly comprised of polyethylene or polypropylene, and the research of increasing porosity has been developed to enhance a cycle-life and high power characteristics. Importantly, separator is critical component to influence on stability in battery, induces rapid thermal shrinkage when batteries are exposed to heat above 150 °C, finally, resulting in an internal short-circuit. Therefore, in order to prevent explosion of the battery, the thermal contraction is also required for cell stability, and the surface coating with inorganic materials has been applied to realize the required thermal property.⁶¹

2.3.6 Current collector

Current collector is thin metal foil which receives electrons from or to external circuit, and is a substrate for electrode slurry coating. An aluminum and copper are generally used in cathode and anode, respectively. The main characteristics of the current collector are surface roughness and thickness. In case of thickness, its value is normally in the range of 8~10 μm, but the thickness under 6 μm is gradually required to meet the growing demand of thinner characteristic in various applications.

2.3 Next Generation Li - Ion Batteries

2.3.1 New designed Li - Ion Batteries

Commercial battery electrodes (anodes and cathodes) are typically created by casting a porous powder composite (a mixture of the active material, a small amount of polymer binder, and a conductive agents such as carbon) onto a metal foil current collector. Electrons are conducted via chains of particles through the composite to the current collector. In contrast, ions move through the liquid or solid electrolyte that fills the pores of the composite. Optimization of both pathways is critical for battery performance. Although this slurry-casted electrode structure works very well, better control of the three-dimensional (3D) architecture would enhance the energy per unit mass and volume of the electrode. (Figure 2. 7)

So, in new electrode, robust physical or chemical bonds formed during cosynthesis or annealing of the active particles with conductive fibers give superior performance during charge / discharge cycling (Figure 2. 7B) However, these fibrous or templated 3D structures are generally difficult to form as a dense body. Another conversion electrodes provide improved density by forming an internal conductive network through electrochemical reaction. Bonding of the conversion particles to a conductive carbon fiber scaffold through high-temperature processing not only prevents capacity loss but also reduces the voltage drop to recharge the battery. (Figure 2. 7C)

New designed electrode was reported an important step toward understanding how optimized battery electrode architectures can maximize the energy per unit volume and weight. (Figure 2. 7D) To further improve access to full capacity, future, thicker electrodes could also include gradients in morphology spanning the thickness of the electrode and the distance from the electrode terminal. Using the battery chemistry itself to drive the formation of the electrode structure is an elegant approach toward such an optimized structure.⁶²

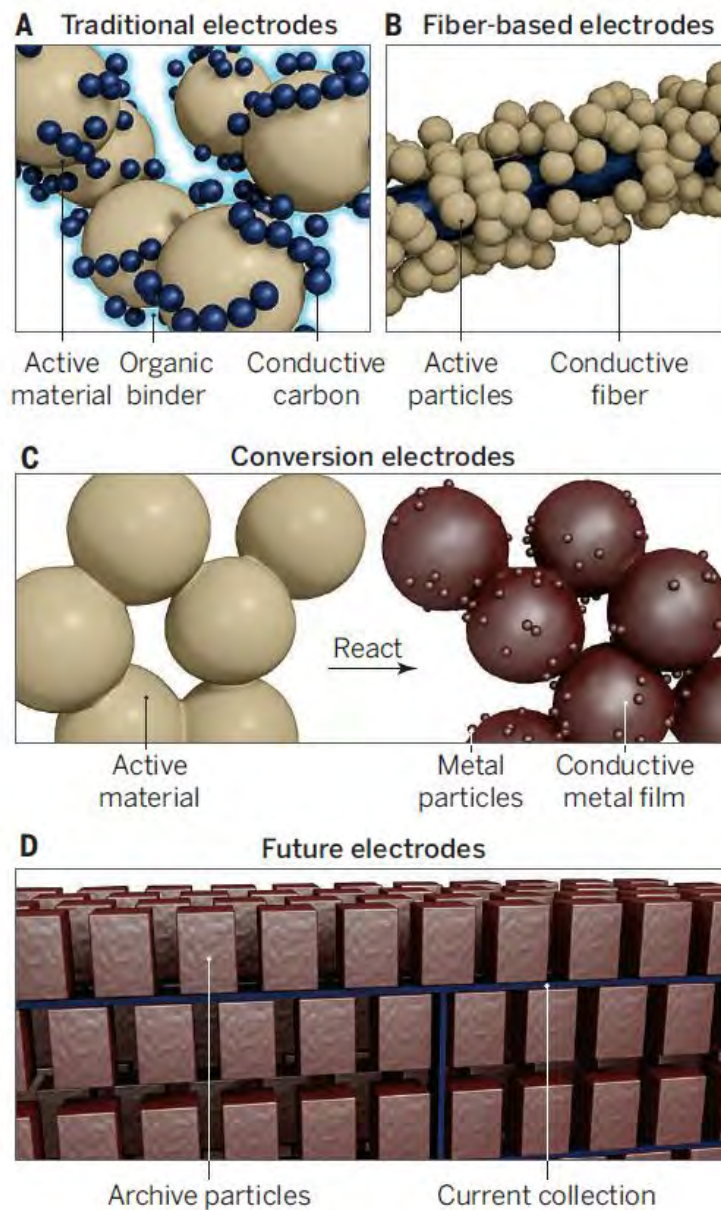


Figure 2.7 Fabricating Li-ion battery electrodes. (A) Traditional electrodes rely on a random arrangement of contacts and may result in parts of the battery not being accessible. (B) Electrodes with physical or chemical bonds connecting the active particles to a conductive fiber perform better, but are difficult to make into a dense structure. (C) The metal coating and nodules provide a conductive pathway for electrons along all interior surfaces. If well formed, it should penetrate the entire volume of the electrode for full access of the stored energy. (D) In a conceptual, completely optimized battery electrode, every active particle is perfectly shaped, sized, and wired to the current collector and to the solid or liquid electrolyte.

2.3.2 Flexible Li-Ion Batteries

In conventional LIBs, graphite as well as lithium-containing transition metal oxides are typically used in the anode and cathode, respectively. Most commonly, both electrodes are fabricated by coating a metal foil current collector with a slurry containing the powdered active materials, conductive carbon and a polymer binder. Even though the powdered particles in the electrode are held in place by a polymeric binder, they can easily be separated from the current collector following repeated deformation. In flexible LIBs, the electrode design (including the active materials and current collector) must allow these components to remain intact following multiple deformations, as well as long-term operation in both unstrained and deformed states.

There are two approaches to developing flexible electrodes: the use of an active material that is intrinsically flexible, or the use of composite electrodes with flexible supports. The availability of electrode chemistry that retains the electrochemical activity under deformation, and is mechanically flexible, is limited. Intrinsically flexible electrodes that are so far known typically use carbon-based materials such as carbon nanotubes (CNTs) or some electroactive polymers. Composite electrodes, in which the active materials are combined using flexible supports, allow a wider variety of active materials to be used; however, the electrode design is more complicated.

The mechanical and electrochemical properties of flexible LIBs depend on how the battery components, i.e., the electrodes, electrolytes, and separators, are combined into a single device. The electrolyte, a key component of LIBs, carries ions from one electrode to the other, avoiding direct electrical contact between the two electrodes. Since it transports ions between the electrodes, the properties of the interface significantly affect the performance. Specifically, with the repeated deformation of a flexible LIB, stable interface contact between the electrode and electrolyte is of critical importance. Electrolytes in LIBs are commonly classified into liquid or solid electrolytes. Each type has different advantages and challenges to overcome in the application to flexible LIBs. This section reviews various approaches for applying electrolytes in flexible LIBs.⁶³

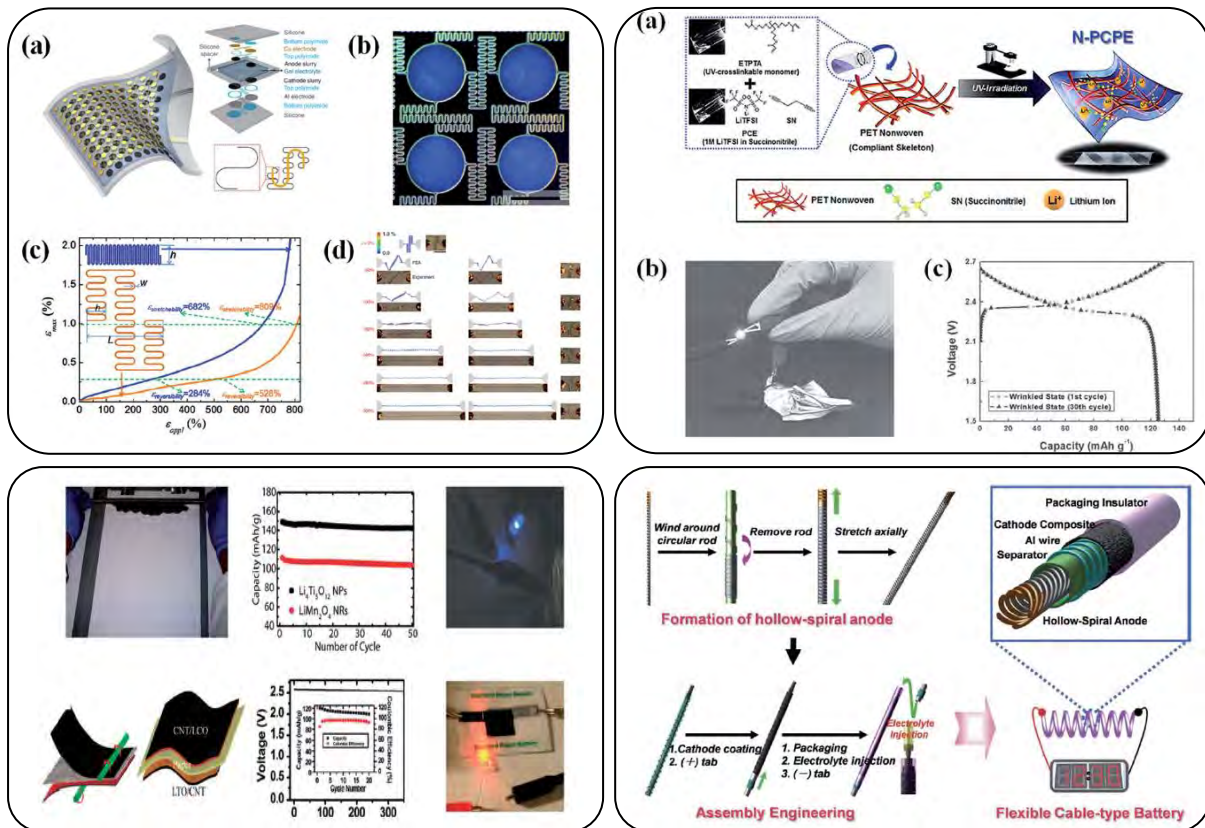


Figure 2. 8 Recent flexible Li-ion batteries.

2.4. References

1. Tarascon, J.-M.; Armand, M., Issues and challenges facing rechargeable lithium batteries. *Nature* **2001**, *414* (6861), 359-367.
2. Aricò, A. S.; Bruce, P.; Scrosati, B.; Tarascon, J.-M.; Van Schalkwijk, W., Nanostructured materials for advanced energy conversion and storage devices. *Nature materials* **2005**, *4* (5), 366-377.
3. Armand, M.; Tarascon, J.-M., Building better batteries. *Nature* **2008**, *451* (7179), 652-657.
4. Terada, N.; Yanagi, T.; Arai, S.; Yoshikawa, M.; Ohta, K.; Nakajima, N.; Yanai, A.; Arai, N., Development of lithium batteries for energy storage and EV applications. *Journal of power sources* **2001**, *100* (1), 80-92.
5. Chan, C. K.; Peng, H.; Liu, G.; McIlwrath, K.; Zhang, X. F.; Huggins, R. A.; Cui, Y., High-performance lithium battery anodes using silicon nanowires. *Nature nanotechnology* **2008**, *3* (1), 31-35.
6. Whittingham, M. S., Electrical energy storage and intercalation chemistry. *Science* **1976**, *192* (4244), 1126-1127.
7. Author, A., XXIV.—On chemical analysis by spectrum-observations. *Quarterly Journal of the Chemical Society of London* **1861**, *13* (3), 270-289.
8. Besenhard, J.; Fritz, H., Cathodic reduction of graphite in organic solutions of alkali and NR 4+ salts. *Journal of Electroanalytical Chemistry and Interfacial Electrochemistry* **1974**, *53* (2), 329-333.
9. Schöllhorn, R.; Kuhlmann, R.; Besenhard, J., Topotactic redox reactions and ion exchange of layered MoO₃ bronzes. *Materials Research Bulletin* **1976**, *11* (1), 83-90.
10. Besenhard, J.; Schöllhorn, R., The discharge reaction mechanism of the MoO₃ electrode in organic electrolytes. *Journal of Power Sources* **1977**, *1* (3), 267-276.
11. Besenhard, J.; Eichinger, G., High energy density lithium cells: Part I. Electrolytes and anodes. *Journal of Electroanalytical Chemistry and Interfacial Electrochemistry* **1976**, *68* (1), 1-18.
12. Mizushima, K.; Jones, P.; Wiseman, P.; Goodenough, J., Li_xCoO₂ (0 < x ≤ 1): A new cathode material for batteries of high energy density. *Solid State Ionics* **1981**, *3*, 171-174.
13. Basu, S.; Zeller, C.; Flanders, P.; Fuerst, C.; Johnson, W.; Fischer, J., Synthesis and properties of lithium-graphite intercalation compounds. *Materials Science and Engineering* **1979**, *38* (3), 275-283.
14. SAMAR, B. Rechargeable battery 1981.
15. Yazami, R.; Touzain, P., A reversible graphite-lithium negative electrode for electrochemical generators. *Journal of Power Sources* **1983**, *9* (3), 365-371.

16. Thackeray, M.; David, W.; Bruce, P.; Goodenough, J., Lithium insertion into manganese spinels. *Materials Research Bulletin* **1983**, *18* (4), 461-472.
17. Nazri, G.-A.; Pistoia, G., *Lithium batteries: science and technology*. Springer Science & Business Media: 2008.
18. Yoshino, A.; Sanechika, K.; Nakajima, T., Secondary battery. Google Patents: 1987.
19. Manthiram, A.; Goodenough, J., Lithium insertion into Fe₂(SO₄)₃ frameworks. *Journal of Power Sources* **1989**, *26* (3), 403-408.
20. van Schalkwijk, W.; Scrosati, B., *Advances in lithium-ion batteries*. Springer Science & Business Media: 2002.
21. Antolini, E., LiCoO₂: formation, structure, lithium and oxygen nonstoichiometry, electrochemical behaviour and transport properties. *Solid State Ionics* **2004**, *170* (3), 159-171.
22. Akimoto, J.; Gotoh, Y.; Oosawa, Y., Synthesis and structure refinement of LiCoO₂ single crystals. *Journal of Solid State Chemistry* **1998**, *141* (1), 298-302.
23. Doh, C.-H.; Kim, D.-H.; Kim, H.-S.; Shin, H.-M.; Jeong, Y.-D.; Moon, S.-I.; Jin, B.-S.; Eom, S. W.; Kim, H.-S.; Kim, K.-W., Thermal and electrochemical behaviour of C/Li_xCoO₂ cell during safety test. *Journal of Power Sources* **2008**, *175* (2), 881-885.
24. Martha, S. K.; Sclar, H.; Framowitz, Z. S.; Kovacheva, D.; Saliyski, N.; Gofer, Y.; Sharon, P.; Golik, E.; Markovsky, B.; Aurbach, D., A comparative study of electrodes comprising nanometric and submicron particles of LiNi_{0.50}Mn_{0.50}O₂, LiNi_{0.33}Mn_{0.33}Co_{0.33}O₂, and LiNi_{0.40}Mn_{0.40}Co_{0.20}O₂ layered compounds. *Journal of Power Sources* **2009**, *189* (1), 248-255.
25. Dahbi, M.; Wikberg, J. M.; Saadoune, I.; Gustafsson, T.; Svedlindh, P.; Edström, K., A delithiated LiNi_{0.65}Co_{0.25}Mn_{0.10}O₂ electrode material: A structural, magnetic and electrochemical study. *Electrochimica Acta* **2009**, *54* (11), 3211-3217.
26. Bang, H.; Kim, D.-H.; Bae, Y. C.; Prakash, J.; Sun, Y.-K., Effects of Metal Ions on the Structural and Thermal Stabilities of Li [Ni_{1-x-y}Co_xMn_y]O₂ (x+y ≤ 0.5) Studied by In Situ High Temperature XRD. *Journal of The Electrochemical Society* **2008**, *155* (12), A952-A958.
27. Xiao, J.; Chernova, N. A.; Whittingham, M. S., Layered mixed transition metal oxide cathodes with reduced cobalt content for lithium ion batteries. *Chemistry of Materials* **2008**, *20* (24), 7454-7464.
28. Oh, S. W.; Myung, S.-T.; Kang, H. B.; Sun, Y.-K., Effects of Co doping on Li [Ni_{0.5}Co_xMn_{1.5-x}]O₄ spinel materials for 5V lithium secondary batteries via Co-precipitation. *Journal of Power Sources* **2009**, *189* (1), 752-756.
29. Wu, H.; Tu, J.; Yuan, Y.; Xiang, J.; Chen, X.; Zhao, X.; Cao, G., Effects of abundant Co doping on the structure and electrochemical characteristics of LiMn_{1.5}Ni_{0.5-x}Co_xO₄.

- Journal of Electroanalytical Chemistry* **2007**, 608 (1), 8-14.
30. Rosciano, F.; Colin, J.-F.; La Mantia, F.; Tran, N.; Novák, P., Electrochemical Stress at High Potential to Investigate Phase Transitions in $\text{Li}_{1-x}(\text{Ni}_{1/3}\text{Mn}_{1/3}\text{Co}_{1/3})\text{O}_2$. *Electrochemical and Solid-State Letters* **2009**, 12 (7), A140-A144.
 31. Tran, N.; Croguennec, L.; Ménétrier, M.; Weill, F.; Biensan, P.; Jordy, C.; Delmas, C., Mechanisms associated with the “plateau” observed at high voltage for the overlithiated $\text{Li}_{1-x}(\text{Ni}_{0.425}\text{Mn}_{0.425}\text{Co}_{0.15})\text{O}_2$ system. *Chemistry of Materials* **2008**, 20 (15), 4815-4825.
 32. Kim, J.-M.; Kumagai, N.; Cho, T.-H., Synthesis, Structure, and Electrochemical Characteristics of Overlithiated $\text{Li}_{1+x}(\text{Ni}_z\text{Co}_{1-2z}\text{Mn}_z)_{1-x}\text{O}_2$ ($z=0.1-0.4$ and $x=0.0-0.1$) Positive Electrodes Prepared by Spray-Drying Method. *Journal of The Electrochemical Society* **2008**, 155 (1), A82-A89.
 33. La Mantia, F.; Rosciano, F.; Tran, N.; Novák, P., Direct evidence of oxygen evolution from $\text{Li}_{1+x}(\text{Ni}_{1/3}\text{Mn}_{1/3}\text{Co}_{1/3})_{1-x}\text{O}_2$ at high potentials. *Journal of Applied Electrochemistry* **2008**, 38 (7), 893-896.
 34. Thackeray, M.; De Kock, A.; David, W., Synthesis and structural characterization of defect spinels in the lithium-manganese-oxide system. *Materials Research Bulletin* **1993**, 28 (10), 1041-1049.
 35. Whittingham, M. S., Lithium batteries and cathode materials. *Chemical reviews* **2004**, 104 (10), 4271-4302.
 36. Takami, N.; Inagaki, H.; Kishi, T.; Harada, Y.; Fujita, Y.; Hoshina, K., Electrochemical kinetics and safety of 2-volt class Li-ion battery system using lithium titanium oxide anode. *Journal of The Electrochemical Society* **2009**, 156 (2), A128-A132.
 37. Liu, Q.; Mao, D.; Chang, C.; Huang, F., Phase conversion and morphology evolution during hydrothermal preparation of orthorhombic LiMnO_2 nanorods for lithium ion battery application. *Journal of Power Sources* **2007**, 173 (1), 538-544.
 38. Padhi, A. K.; Nanjundaswamy, K.; Goodenough, J., Phospho-olivines as positive-electrode materials for rechargeable lithium batteries. *Journal of the electrochemical society* **1997**, 144 (4), 1188-1194.
 39. Padhi, A.; Nanjundaswamy, K.; Masquelier, C.; Okada, S.; Goodenough, J., Effect of structure on the $\text{Fe}^{3+}/\text{Fe}^{2+}$ redox couple in iron phosphates. *Journal of the Electrochemical Society* **1997**, 144 (5), 1609-1613.
 40. Axmann, P.; Stinner, C.; Wohlfahrt-Mehrens, M.; Mauger, A.; Gendron, F.; Julien, C., Nonstoichiometric LiFePO_4 : defects and related properties. *Chemistry of Materials* **2009**, 21 (8), 1636-1644.
 41. Kobayashi, G.; Nishimura, S. i.; Park, M. S.; Kanno, R.; Yashima, M.; Ida, T.; Yamada, A.,

- Isolation of Solid Solution Phases in Size-Controlled Li_xFePO_4 at Room Temperature. *Advanced Functional Materials* **2009**, *19* (3), 395-403.
42. Maccario, M.; Croguennec, L.; Desbat, B.; Couzi, M.; Le Cras, F.; Servant, L., Raman and FTIR Spectroscopy Investigations of Carbon-Coated Li_xFePO_4 Materials. *Journal of the Electrochemical Society* **2008**, *155* (12), A879-A886.
 43. Li, H.; Zhou, H., Enhancing the performances of Li-ion batteries by carbon-coating: present and future. *Chemical communications* **2012**, *48* (9), 1201-1217.
 44. Zhang, H.-L.; Liu, S.-H.; Li, F.; Bai, S.; Liu, C.; Tan, J.; Cheng, H.-M., Electrochemical performance of pyrolytic carbon-coated natural graphite spheres. *Carbon* **2006**, *44* (11), 2212-2218.
 45. Yoshio, M.; Wang, H.; Fukuda, K.; Umeno, T.; Abe, T.; Ogumi, Z., Improvement of natural graphite as a lithium-ion battery anode material, from raw flake to carbon-coated sphere. *Journal of Materials Chemistry* **2004**, *14* (11), 1754-1758.
 46. Reddy, A. L. M.; Gowda, S. R.; Shaijumon, M. M.; Ajayan, P. M., Hybrid nanostructures for energy storage applications. *Advanced materials* **2012**, *24* (37), 5045-5064.
 47. Park, C.-M.; Kim, J.-H.; Kim, H.; Sohn, H.-J., Li-alloy based anode materials for Li secondary batteries. *Chemical Society reviews* **2010**, *39* (8), 3115-3141.
 48. Kasavajjula, U.; Wang, C.; Appleby, A. J., Nano-and bulk-silicon-based insertion anodes for lithium-ion secondary cells. *Journal of Power Sources* **2007**, *163* (2), 1003-1039.
 49. Zhang, H.; Braun, P. V., Three-dimensional metal scaffold supported bicontinuous silicon battery anodes. *Nano letters* **2012**, *12* (6), 2778-2783.
 50. Wu, H.; Cui, Y., Designing nanostructured Si anodes for high energy lithium ion batteries. *Nano Today* **2012**, *7* (5), 414-429.
 51. Magasinski, A.; Dixon, P.; Hertzberg, B.; Kvit, A.; Ayala, J.; Yushin, G., High-performance lithium-ion anodes using a hierarchical bottom-up approach. *Nature materials* **2010**, *9* (4), 353-358.
 52. Szczech, J. R.; Jin, S., Nanostructured silicon for high capacity lithium battery anodes. *Energy & Environmental Science* **2011**, *4* (1), 56-72.
 53. Key, B.; Bhattacharyya, R.; Morcrette, M.; Seznéc, V.; Tarascon, J.-M.; Grey, C. P., Real-time NMR investigations of structural changes in silicon electrodes for lithium-ion batteries. *Journal of the American Chemical Society* **2009**, *131* (26), 9239-9249.
 54. Rudawski, N.; Yates, B.; Holzworth, M.; Jones, K.; Elliman, R.; Volinsky, A., Ion beam-mixed Ge electrodes for high capacity Li rechargeable batteries. *Journal of Power Sources* **2013**, *223*, 336-340.
 55. Chockla, A. M.; Klavetter, K. C.; Mullins, C. B.; Korgel, B. A., Solution-grown germanium nanowire anodes for lithium-ion batteries. *ACS applied materials & interfaces* **2012**, *4* (9),

- 4658-4664.
56. Liu, X. H.; Huang, S.; Picraux, S. T.; Li, J.; Zhu, T.; Huang, J. Y., Reversible nanopore formation in Ge nanowires during lithiation–delithiation cycling: An in situ transmission electron microscopy study. *Nano letters* **2011**, *11* (9), 3991-3997.
 57. Ji, L.; Lin, Z.; Alcoutlabi, M.; Zhang, X., Recent developments in nanostructured anode materials for rechargeable lithium-ion batteries. *Energy & Environmental Science* **2011**, *4* (8), 2682-2699.
 58. Xu, K., Nonaqueous liquid electrolytes for lithium-based rechargeable batteries. *Chemical reviews* **2004**, *104* (10), 4303-4418.
 59. Zhang, S. S., A review on electrolyte additives for lithium-ion batteries. *Journal of Power Sources* **2006**, *162* (2), 1379-1394.
 60. Zhang, S. S., A review on the separators of liquid electrolyte Li-ion batteries. *Journal of Power Sources* **2007**, *164* (1), 351-364.
 61. Kang, S. M.; Ryou, M.-H.; Choi, J. W.; Lee, H., Mussel-and diatom-inspired silica coating on separators yields improved power and safety in Li-ion batteries. *Chemistry of Materials* **2012**, *24* (17), 3481-3485.
 62. Dudney, N. J.; Li, J., Using all energy in a battery. *Science* **2015**, *347* (6218), 131-132.
 63. Gwon, H.; Hong, J.; Kim, H.; Seo, D.-H.; Jeon, S.; Kang, K., Recent progress on flexible lithium rechargeable batteries. *Energy & Environmental Science* **2014**, *7* (2), 538-551.

Chapter III. Patterning of Electrodes for Mechanically Robust and Bendable Lithium-Ion Batteries

3.1. Introduction

Significantly advances in the technologies of numerous portable electronics, like wearable devices, roll-up displays, integrated-circuit smart cards, and radio-frequency identification (RFID) tags, demand has been rapidly growing for the bendable lithium-ion batteries that power device systems.¹⁻⁵ To successfully achieve bendable batteries, an energy density of active material, a mechanical flexibility of electrode, high stability in electrochemical reaction environments, and an electrical conductivity should be carefully considered. Carbon-based materials, such as carbon nanotube (CNT) networks and graphene sheets, have usually been used to make flexible or bendable lithium-ion batteries (LIBs), since these materials exhibited a high mechanical strength, a superior electrical conductivity, and an excellent flexibility. When they were appropriately combined with cathode or anode active materials by employing a pulsed laser deposition, chemical vapor deposition (CVD), electroplating, or infiltration process, a promising electrochemical performance was achieved in bendable LIBs, compared to non-flexible conventional available batteries.¹⁻⁵ However, since the CNTs network and graphene sheets have several functional groups on the surface of the carbon, a serious side reaction takes place during initial cycling, resulting in a poor coulombic efficiency at the first cycle.⁶ From a point of view of practical applications, it may hard to apply to practically usable LIBs due to a significant loss of capacity. An one solution to solve these problems is to fabricate a current collector with patterned surface by employing conventional electrodes, such as copper or aluminum foils, via a lithographic process.⁷ The electrode using patterned current collectors lead to a high surface area enlargement, resulting in a fast charging–discharging process of the battery and an increase of the energy density within the new footprint area. Also, the volume changes of active materials in the confined geometry of patterns may be alleviated by frames of patterns. Here, we demonstrate a simple process for fabricating trench-type copper (Cu) patterned foils by combining photo-lithography with a wet etching process. And then, we prepared three-dimensional hierarchical copper oxides on the surface of patterned Cu foils by a simple solution immersion process. The copper oxides were strongly anchored to the patterned Cu surfaces even after bending, resulting in improved electrochemical properties including a stable cycling retention, a high rate capability, and a high reversible capacity.

3.2. Experimental

3.2.1. Fabrication of Micro Patterned Copper Substrates.

A layer of photoresist (Positive PR, AZ-5214E) was coated by spin-coating process at 2000 rpm for 1min onto a flat Cu substrate (50 μm thick, 99.9%, Good-fellow) and developed after a UV(365nm)-mask illumination standard photolithography process (MA6, SUSS MicroTec) to make trench-type polymer patterns having dimension of 10 μm . Subsequently, the PR-patterned Cu foils were immersed in 20% copper chloride (CuCl_2) aqueous solution for 20 min to make trench-type Cu patterns having depth of 10 μm . After growing copper oxide nanoflakes in a basic ammonia solution, the PR patterns were completely removed by immersing them in acetone.

A schematic illustration of the copper oxide (CuO) nano-flakes grown onto a lithographically patterned electrode is depicted in Figure 3.1. First, trench-type Cu patterns were constructed by photolithography and a wet chemical etching, following a top-down approach. PR patterns were fabricated using a well-known standard photolithography technique (Figure 3.1a).⁸ Subsequently, the PR patterned Cu substrates were immersed in 20% copper chloride (CuCl_2) aqueous solution to etch down the Cu foils (Figure 3.1b). CuCl_2 , iron(III) chloride (FeCl_3), and alkaline etchants have been widely used for Cu materials etching. Among them, the CuCl_2 provides a high etch rate, and the full regeneration of CuCl_2 makes it attractive etchant.⁹ The etching of Cu with CuCl_2 can be expressed by the following chemical equation:¹⁰⁻¹¹



The CuCl_2 attacks the Cu surface while cuprous chloride (CuCl) is formed. Reaction of one copper atom with one Cu^{2+} ion produces two cuprous ions. In the process, the concentration of CuCl_2 and the etching temperature play an important role in giving high and stable etch rate for the Cu etching.¹⁰⁻¹¹ And also, an additional composition of reaction such as surfactant and reducing agent for decreasing by-products acts effect point for etching rate and etched shape. CuO nano-flakes were grown from the patterned Cu surfaces of foils by immersing the Cu foils into an ammonium hydroxide (NH_4OH) basic solution (Figure 3.1c). Subsequent removal of PR led to the fabrication of a strongly anchored CuO anode material to the patterned Cu electrodes (Figure 3.1d).

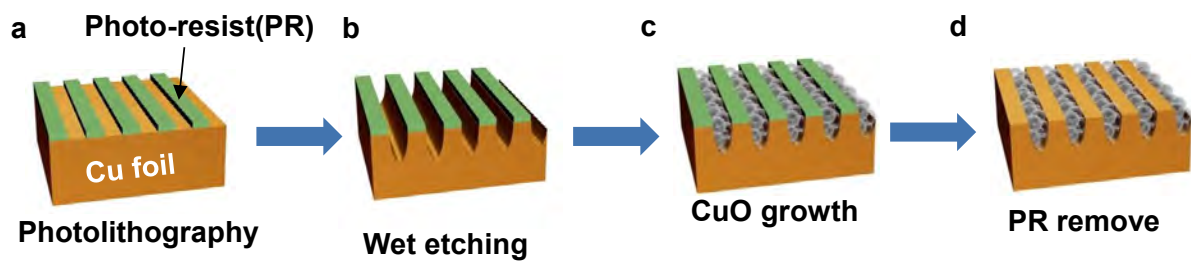


Figure 3. 1 A schematic illustration showing the CuO nano-flakes grown on the trench-type patterned Cu foils. (a) Lithographically patterned PR polymer on the Cu foil; (b) trench-type Cu patterns fabricated via a wet chemical etching process; (c) growth of CuO nano-flakes on open areas of Cu foils in a basic solution; (d) The CuO anchored onto the Cu foils after PR polymer removal.

3.3. Result and discussion

3.3.1. A Synthesis of CuO Nano-Flake Electrodes

Firstly, the patterned Cu electrodes were characterized by scanning electron microscopy (SEM). An average value of pattern width and pattern depth were $\sim 25 \mu\text{m}$ and $\sim 15 \mu\text{m}$, respectively (Figure 3.2a). The patterned Cu foil was immersed in a dilute solution of ammonium hydroxide ($3.3 \times 10^{-2} \text{ M}$, $\text{pH} \approx 10$) at room-temperature for 48 h, followed by rinsing with deionized water several times, and dried in argon(Ar) purge systems for anti-oxidation. Under the conditions, copper hydroxide ($\text{Cu}(\text{OH})_2$) was initially synthesized, and then it was quickly converted into copper oxide (CuO).¹² When this sample was further thermally annealed at $180 \text{ }^\circ\text{C}$ for 3 h under an Ar stream, the $\text{Cu}(\text{OH})_2$ was completely converted into CuO. Figure 3.2b shows the SEM image of CuO grains grown onto the patterned Cu foils. A magnified SEM image (selected area in Figure 3.2b) shows three-dimensional hierarchical CuO nano-flakes with the thickness of 20–30 nm and the length of $\sim 1 \mu\text{m}$ (Figure 3.2c). When this process was applied to a flat Cu foil which is non-patterned foil, a similar CuO nano-flake structure was synthesized (Figure 3.3). Previously, various CuO structures, including nano-wires, tubes, sheets, flakes, and flowers, have been synthesized on the Cu surfaces *via* the Oswald ripening process, by controlling the temperature, reaction time, pH value, and addition of surfactants in the basic aqueous solution.¹³⁻¹⁵

Under the reaction condition values used in this study, $\text{Cu}(\text{OH})_2$ nano-flakes structure were synthesized within 1 h. Immediately after the formation of $\text{Cu}(\text{OH})_2$, it was partially converted to CuO without any changing the morphologies, as seen in the X-ray diffraction (XRD) pattern (Figure 3.2d, top). When the copper foils were immersed in the ammonium hydroxide solution for a long period of time ($\sim 48 \text{ h}$), the pure CuO was successfully synthesized without thermal treatment (Figure 3.2d, bottom). The CuO nano-flake structures grown on the Cu foils were further confirmed by transmission electron microscopy (TEM) (Figure 3.2e). The magnified TEM image shows a highly crystalline structure of the CuO and the growth direction (Figure 3.2f).

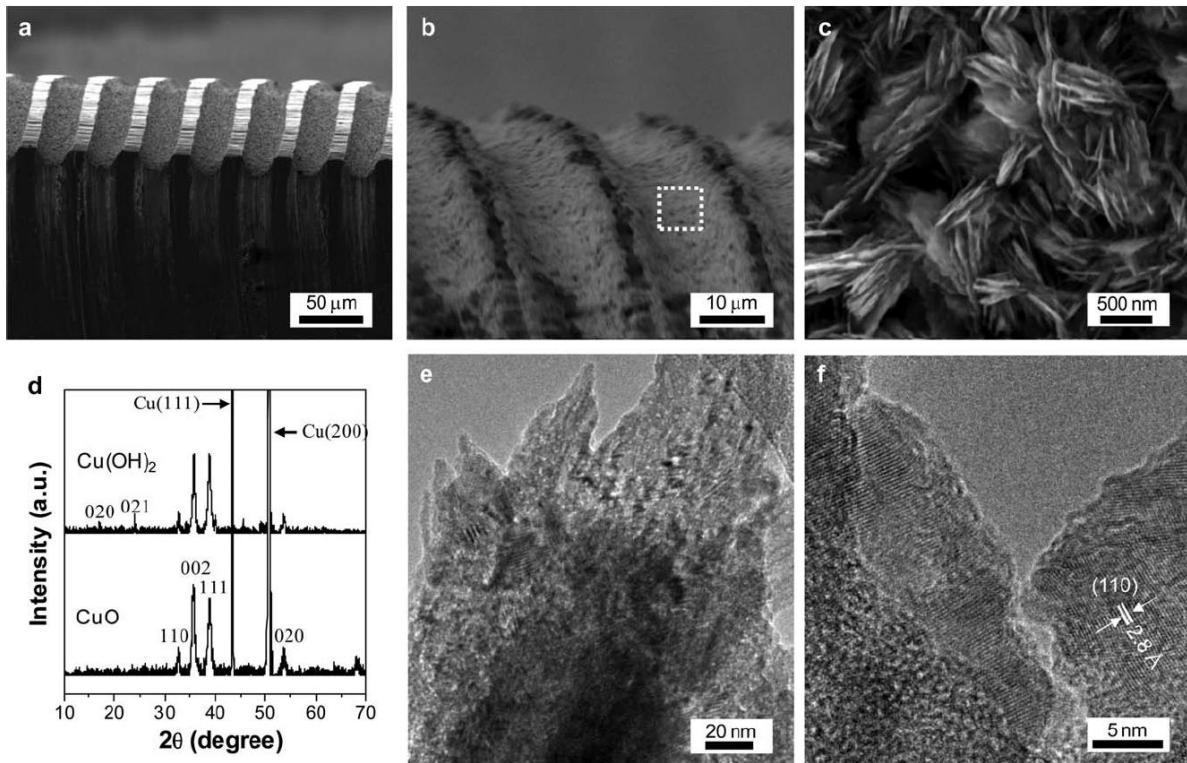


Figure 3. 2 A growth of CuO nano-flakes structure on the patterned Cu foils. (a) The trench-type patterned Cu foils fabricated by photolithography and wet chemical etching, (b) CuO nano-flakes structure grown on open sites of the patterned Cu foils, (c) SEM image magnified in the selected regions seen in (b), (d) XRD patterns obtained from Cu(OH)₂ (top) and CuO (bottom) nano-flakes grown on surface of open sites of the patterned Cu foils, (e) TEM image showing a CuO nano-flake detached from the Cu foils by ultra-sonication, and (f) magnified TEM image showing a highly crystalline plane of CuO nano-flake.

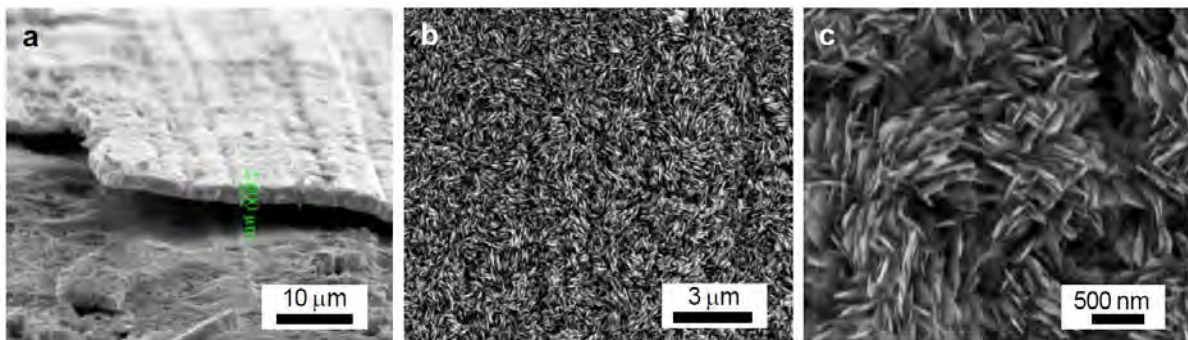


Figure 3. 3 Three-dimensional hierarchical CuO nano-flakes grown on the flat Cu foil. a) SEM image showing thickness of the CuO grown onto the surface of Cu foil, b) SEM image showing CuO nano-flakes in a large area, and c) Magnified SEM image of hierarchical CuO flakes.

3.3.2. Mechanical Properties of Cu Electrodes for Bendable Electrode.

In order to investigate the stability of the CuO structure grown on the Cu substrates, we rolled them up. The CuO nano-flakes on the surface of flat Cu foils were seriously detached from the Cu surface, due to the weak adhesion of brittle CuO to the flat Cu substrate (Figure 3.4a). The magnified SEM image showed that the CuO maintained the morphology of nano-flakes, however, irregular cracks occurred randomly (Figure 3.4b). In contrast, the CuO nano-flakes that were strongly anchored to the patterned Cu substrates showed a significantly reduced cracks after rolling-up test (Figure 3.4c and d). This result suggests that the patterning of surface on Cu substrates may increase the adhesion of CuO nano-flakes to the Cu surfaces in the confined geometry. It should be noted that the rolling-up test was performed on the direction where the etched trenches were parallel to the axis of the roll. When the etched trenches were vertical to the axis of the roll, the CuO electrodes showed so many cracks which are similar as those of a flat electrode (Figure 3.5). But the CuO electrodes using the patterned Cu foil exhibit outstanding adhesion properties of electrode materials to substrates in all of bending test conditions.

Also, we investigated an adhesion property of CuO nano-flakes structure on the just etched Cu foil (no patterned Cu surfaces) and CuO flakes grown on the selected area of a flat Cu foils after bending test. Both samples showed many cracks, resulting in detachment of the CuO nano-flakes from Cu surfaces (Figure 3.6). In particular, when the coverage of CuO materials on patterned Cu surfaces were investigated as a function of bending cycles, loss of the CuO was not observed even during 100 bending cycles, while CuO nano-flakes on a flat Cu foils were significantly detached from the Cu current collector (Figure 3.7a). Photographs showing CuO nano-flakes electrodes before and after bending cycles also confirmed the strong anchoring of the CuO materials to the Cu current collector (Figure 3.7b). From these results, the patterning and etching processes of Cu foils are attributed to a strong adhesion property of the CuO materials to the Cu current collector.

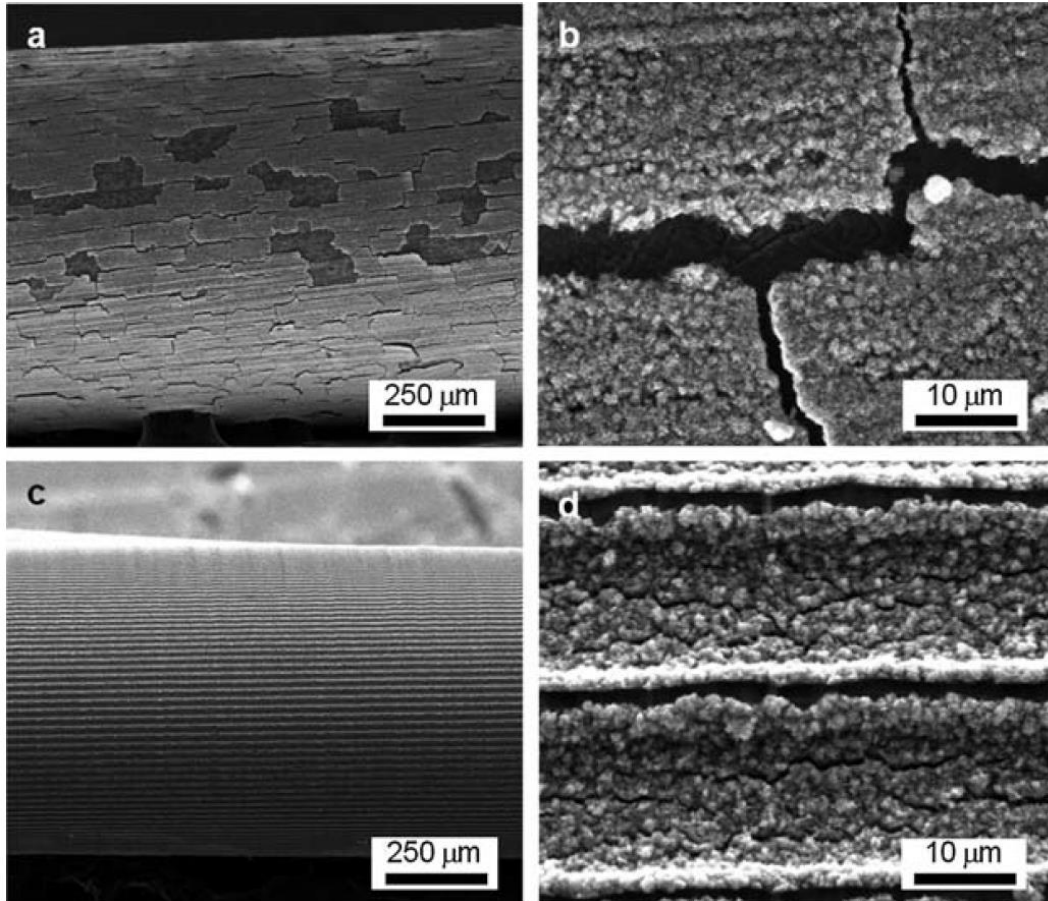


Figure 3. 4 SEM images of CuO nano-flakes anchored to the Cu foils after rolling-up test. (a) CuO nano-flakes film on the flat Cu foils, (b) the magnified SEM image of the CuO nano-flakes film seen in (a) showing randomly distributed cracks, (c) the SEM image of CuO nano-flakes film on the patterned Cu foils, and (d) the magnified image showing the reduced cracks due to the patterning.

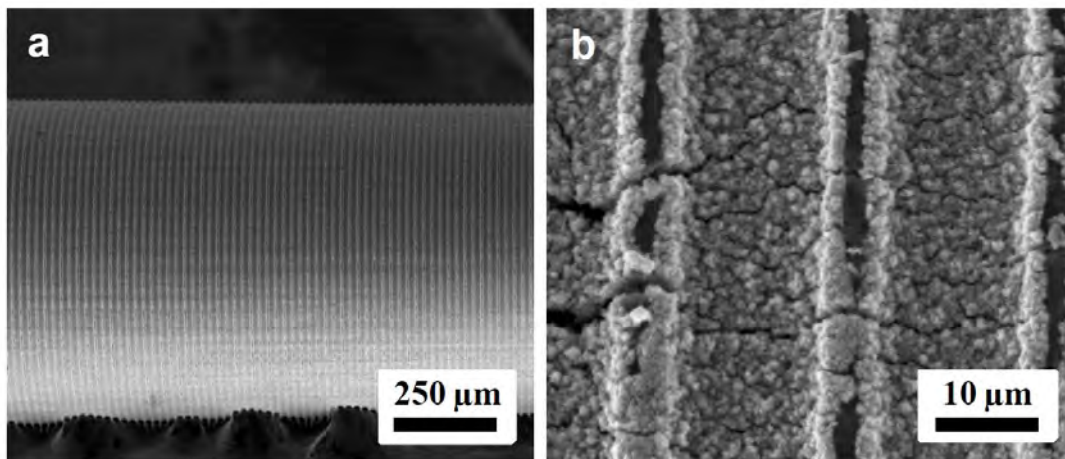


Figure 3. 5 Morphologies of CuO nano-flakes after bending test of different direction with pattern direction. a) SEM image and b) magnified SEM image showing CuO flakes. When the etched trenches pattern were the vertical direction to the axis of the roll, many cracks of CuO flakes formed.

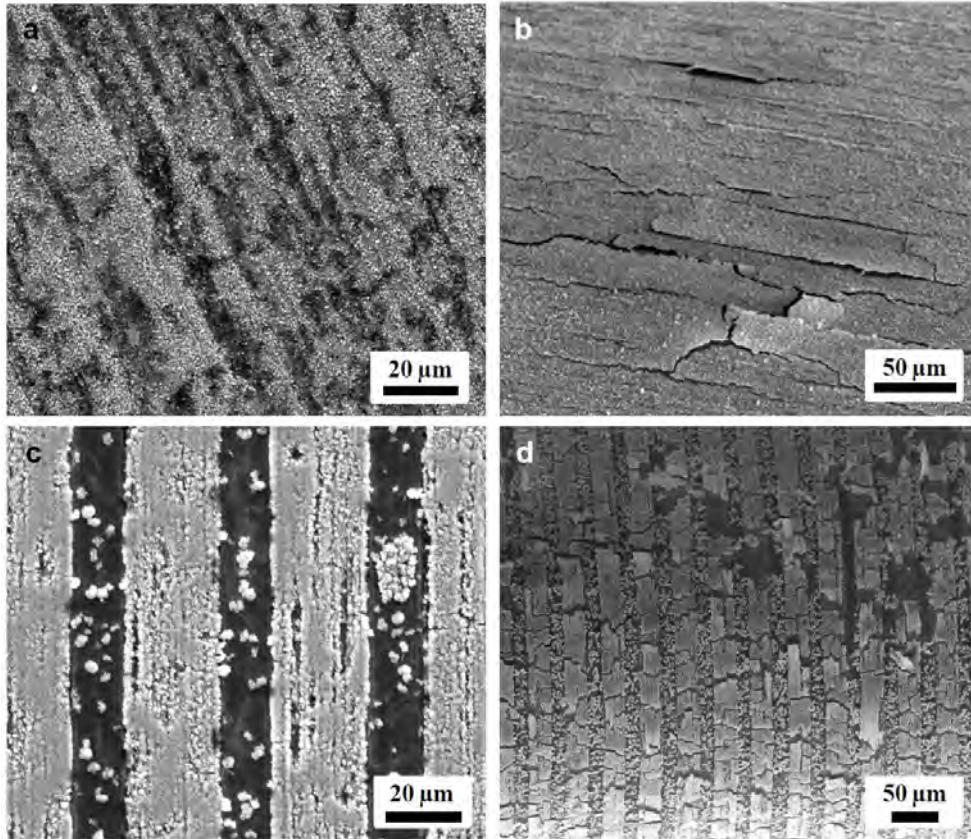


Figure 3. 6 SEM images showing CuO nano-flakes materials on different type Cu current collector after bending test. a) only Etched but no patterned Cu surfaces with roughness property, b) CuO materials detached from the etched Cu foil after bending test, c) CuO flakes grown onto patterned but no etched Cu surfaces, and d) SEM image showing many cracks after bending of the sample seen in c).

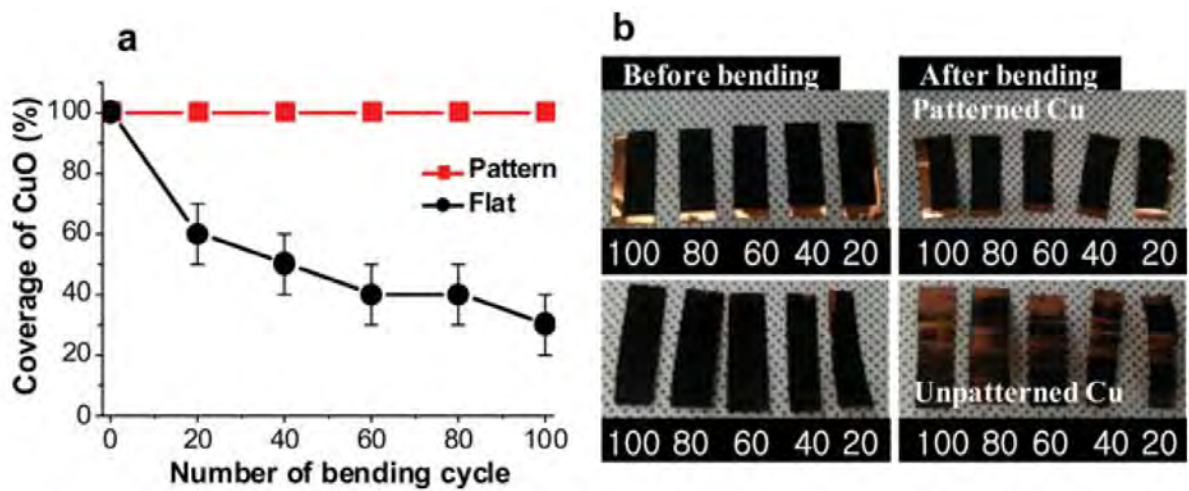


Figure 3. 7 A coverage of CuO nano-flakes materials on Cu current collectors after the bending test. (a) Plot showing coverage of CuO materials as a function of bending cycle (patterned Cu foil vs. flat Cu foil), and (b) photographs showing two type CuO nano-flakes electrodes before and after bending cycles.

3.3.3. Electrochemical Properties of CuO Electrodes.

The CuO nano-flakes grown on the surface of Cu foil electrodes were employed as the anode material in LIBs. Since the CuO nan-flakes electrodes were strongly anchored to the surface of Cu current collector, the binder materials and conducting agent materials (e.g., super P carbon black) were not needed. The electrochemical properties of the CuO nano-flakes electrodes were investigated by galvanostatic charge–discharge measurements. As shown in Figure. 3.8a, the CuO nano-flakes electrodes were rolled up during the cycling. The electrode was rolled up with Teflon rod having diameter of 1 mm, so that the radius of curvature was ~0.5 mm. Figure 3.8b shows voltage profiles of CuO nano-flakes electrodes on the trench type patterned Cu foils at a rate of 0.1C in the range of 0.005–3.0 V. The cycle numbers (1st, 10th, 30th, 50th, and 100th) are assigned in the figure. In the first discharge curve, three distinct potential slopes were seen at 2.25–1.8 V (region I), 1.4–1.0 V (region II), and 1.0–0.01 V (region III), which were attributed to a multi-step electrochemical reaction including the creation of a $\text{Cu}^{\text{II}}_{1-x}\text{Cu}^{\text{I}}_x\text{O}_{1-x/2}$ ($0 \leq x \leq 0.4$) by the reaction of lithium ions and the CuO phase (region I), the formation of Cu_2O phase (region II), and the conversion of Cu_2O into Cu and Li_2O (region III).¹⁶ The initial charge capacity of the CuO electrode is 700 mAh g⁻¹, while its discharge capacity is 1180mAh g⁻¹, corresponding to a coulombic efficiency of 59.3%. The large irreversible capacity loss in the first cycle may be attributed to a decomposition of electrolytes on the surface of the CuO nano-flakes electrode and the formation of lithium oxide, as commonly observed the property in nano-materials with a large surface area.¹⁸⁻²⁰ The cycling performance of the CuO anode was tested at a 0.1C-rate. The CuO anode on the patterned Cu foils showed a high reversible capacity of ~570 mA h g⁻¹ after second cycle, and kept their capacity at ~550 mA h g⁻¹ after 100 cycles (Figure 3.8c). The stable cycling performance can be explained by the fact that the hierarchical nanostructured CuO electrode may alleviate the volume expansion during the lithium insertion–extraction process, and the Cu patterns may enhance the contact of the CuO electrodes. In general, nanostructured materials have a strong impact on the volume change of electrodes, which can better accommodate the structural strains during the cycling of battery operation. As a result, the CuO anodes showed highly stable reversible capacities upon repeated cycling.^{21,22} In addition to the high capacity, the CuO anodes attached to the patterned Cu foils exhibited excellent rate capabilities (Figure 3.8d). The C-rates were gradually increased from 0.1C to 10C. The CuO electrodes delivered high capacities of 470 mA h g⁻¹ (1C), 270 mA h g⁻¹ (5C), and 220mAh g⁻¹ (10C). However, the CuO on the flat Cu foils showed a significantly decreased capacity with increasing C-rates (Figure 3.9). The high-rate capabilities of the CuO electrodes on the patterned Cu foils are mainly attributed to nanostructured CuO materials that provides several advantages, including short diffusion paths for electrons and Li⁺ ions, and a large contact area between active materials of electrode and electrolyte. Moreover, since the CuO nano-flakes material is strongly immobilized on the surface of the patterned Cu current collector, significantly enhanced electronic conduction was provided.²³⁻²⁵ After 100 cycles,

the morphologies of CuO nano-flakes materials on the patterned Cu foils were not observed, due to the aggregation of the particles and the formation of SEI-layers, but the CuO films were still strongly anchored to the patterned Cu foil(Figure 3.10).

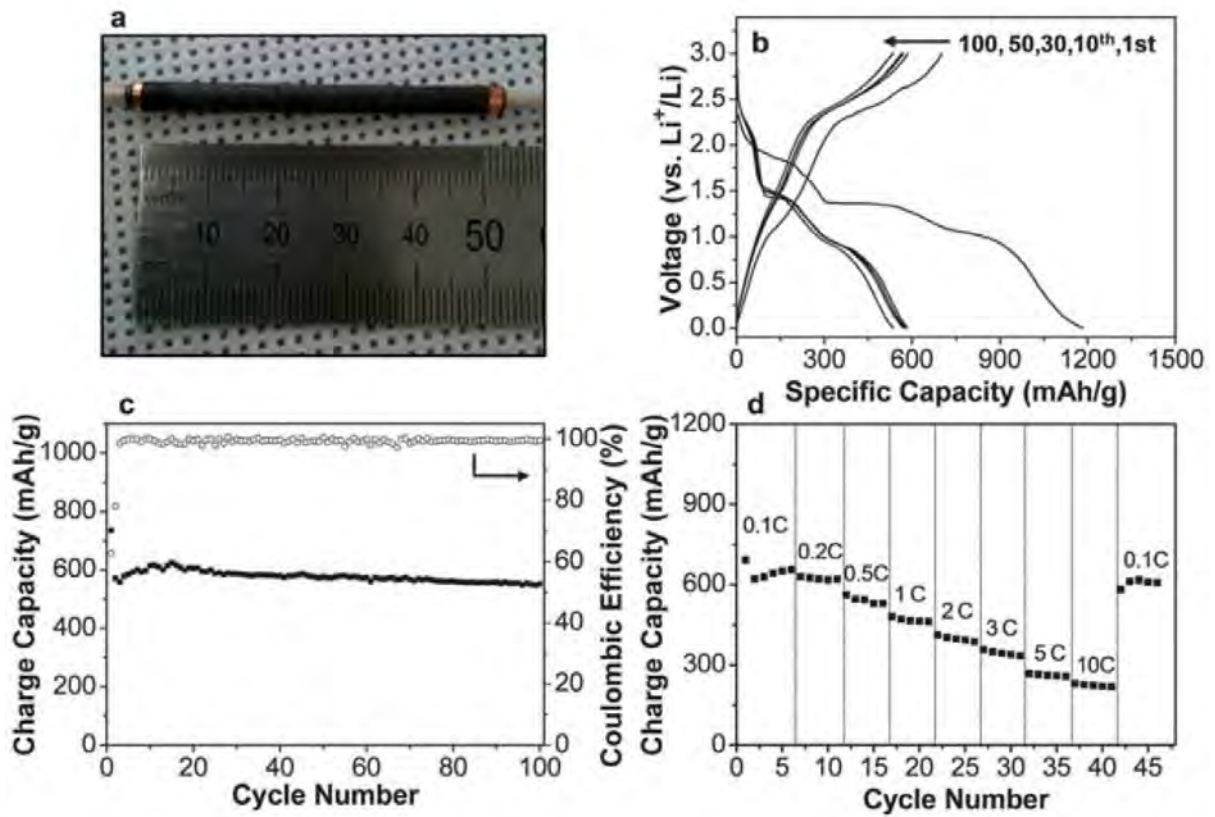


Figure 3. 8 The electrochemical performances of CuO nano-flakes anode on the patterned Cu current collectors. (a) The photograph showing the CuO nano-flakes electrodes after rolling-up, (b) the voltage profiles of the CuO nano-flakes anodes on the patterned Cu foils obtained at a rate of 0.1C in the range of 0.005–3.0 V, (c) the cycling performance of CuO nano-flakes anodes on the patterned Cu foils, and (d) the rate capabilities of CuO nano-flakes anodes on the patterned Cu foils at various C-rates (0.1–10C).

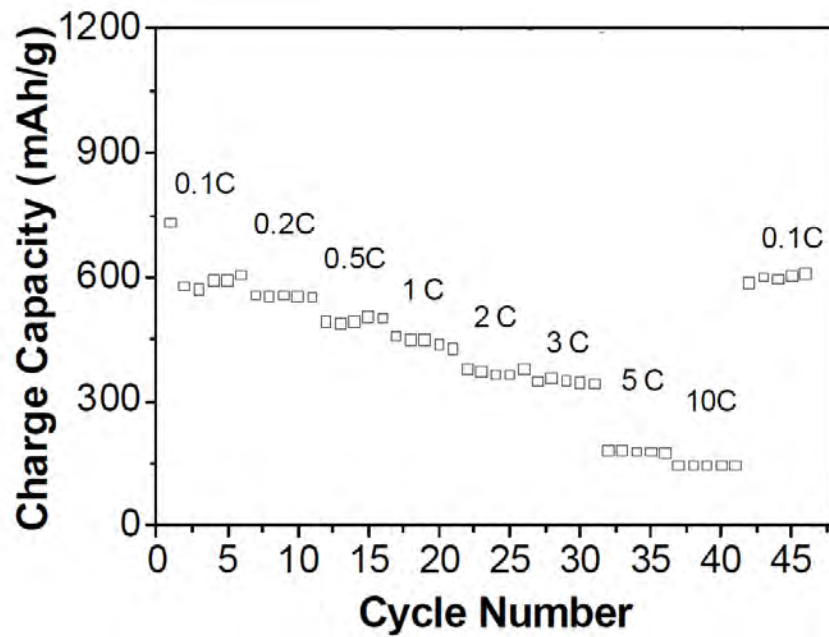


Figure 3. 9 The rate capabilities of CuO nano-flakes anodes on a flat Cu current collector in the range of 0.1 – 10 C rates.

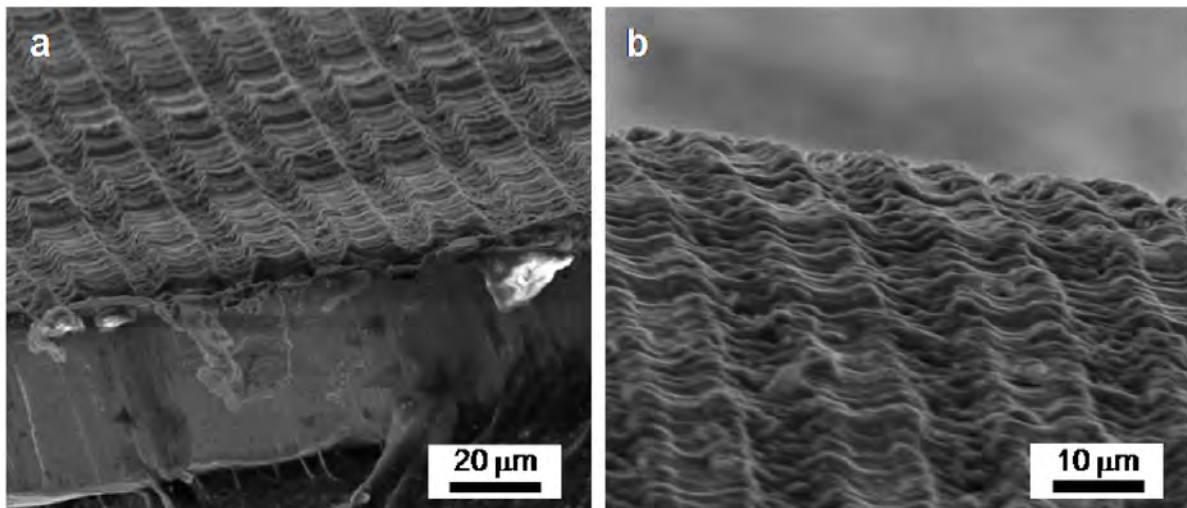


Figure 3. 10 The SEM images of CuO nano-flakes anodes on the patterned Cu current collectors after 100 cycles. a) Tilted view of the SEM image and b) the magnified SEM image. The CuO nano-flakes were aggregated and SEI-layers on the surface of the CuO were formed.

3.4. Conclusion

In summary, we fabricated trench type patterns on Cu foils by combining the conventional photolithography process and the wet chemical etching process. Three-dimensional nanostructured CuO nano-flakes materials were grown on the patterned Cu foils via a solution immersion process. The strong anchoring of the nanostructured CuO materials to the patterned Cu foils remained unchanged even after 100 cycles in bending test, resulting in high electrochemical performances, including a high reversible electrical capacity ($\sim 550 \text{ mA h g}^{-1}$ after 100 cycles) and a high rate capability (220 mA h g^{-1} at a rate of 10C). The use of a patterned current collector opens up a route which can be extended to other anode and cathode materials.

3.5. References

1. Wang, J.-Z.; Chou, S.-L.; Chen, J.; Chew, S.-Y.; Wang, G.-X.; Konstantinov, K.; Wu, J.; Dou, S.-X.; Liu, H. K., Paper-like free-standing polypyrrole and polypyrrole–LiFePO₄ composite films for flexible and bendable rechargeable battery. *Electrochemistry Communications* **2008**, *10* (11), 1781-1784.
2. Hu, L.; Wu, H.; La Mantia, F.; Yang, Y.; Cui, Y., Thin, flexible secondary Li-ion paper batteries. *Acs Nano* **2010**, *4* (10), 5843-5848.
3. Wang, J.-Z.; Zhong, C.; Chou, S.-L.; Liu, H.-K., Flexible free-standing graphene-silicon composite film for lithium-ion batteries. *Electrochemistry Communications* **2010**, *12* (11), 1467-1470.
4. Goyal, A.; Reddy, A. L.; Ajayan, P. M., Flexible Carbon Nanotube–Cu₂O Hybrid Electrodes for Li-Ion Batteries. *Small* **2011**, *7* (12), 1709-1713.
5. Gwon, H.; Kim, H.-S.; Lee, K. U.; Seo, D.-H.; Park, Y. C.; Lee, Y.-S.; Ahn, B. T.; Kang, K., Flexible energy storage devices based on graphene paper. *Energy & Environmental Science* **2011**, *4* (4), 1277-1283.
6. Ko, S.; Lee, J. I.; Yang, H. S.; Park, S.; Jeong, U., Mesoporous CuO Particles Threaded with CNTs for High-Performance Lithium-Ion Battery Anodes. *Advanced materials* **2012**, *24* (32), 4451-4456.
7. Oudenhoven, J. F.; Baggetto, L.; Notten, P. H., All-Solid-State Lithium-Ion Microbatteries: A Review of Various Three-Dimensional Concepts. *Advanced Energy Materials* **2011**, *1* (1), 10-33.
8. Duffy, D. C.; McDonald, J. C.; Schueller, O. J.; Whitesides, G. M., Rapid prototyping of microfluidic systems in poly (dimethylsiloxane). *Analytical chemistry* **1998**, *70* (23), 4974-4984.
9. Georgiadou, M.; Alkire, R., Anisotropic chemical pattern etching of copper foil III. mathematical model. *Journal of the Electrochemical Society* **1994**, *141* (3), 679-689.
10. Allen, D. M., *The Principles and Practice of Photochemical Machining and Photoetching*. Adam Hilger: 1986.
11. S. Gowri, K. S. I., B.A. Shenoi,, Etching of copper and its alloys. *Metal Finishing* **1966**, *64* (12), 54-59.
12. Wen, X.; Zhang, W.; Yang, S., Synthesis of Cu(OH)₂ and CuO nanoribbon arrays on a copper surface. *Langmuir* **2003**, *19* (14), 5898-5903.
13. Oswald, H.; Reller, A.; Schmalle, H.; Dubler, E., Structure of copper (II) hydroxide, Cu(OH)₂. *Acta Crystallographica Section C: Crystal Structure Communications* **1990**, *46* (12), 2279-2284.

14. Wang, H.; Pan, Q.; Zhao, J.; Yin, G.; Zuo, P., Fabrication of CuO film with network-like architectures through solution-immersion and their application in lithium ion batteries. *Journal of power sources* **2007**, *167* (1), 206-211.
15. Zhang, W.; Ding, S.; Yang, Z.; Liu, A.; Qian, Y.; Tang, S.; Yang, S., Growth of novel nanostructured copper oxide (CuO) films on copper foil. *Journal of crystal growth* **2006**, *291* (2), 479-484.
16. Wang, S.; Zhang, J.; Chen, C., Dandelion-like hollow microspheres of CuO as anode material for lithium-ion batteries. *Scripta Materialia* **2007**, *57* (4), 337-340.
17. Liu, B.; Zeng, H. C., Mesoscale organization of CuO nanoribbons: formation of “dandelions”. *Journal of the American Chemical Society* **2004**, *126* (26), 8124-8125.
18. Larcher, D.; Masquelier, C.; Bonnin, D.; Chabre, Y.; Masson, V.; Leriche, J.-B.; Tarascon, J.-M., Effect of Particle Size on Lithium Intercalation into α Fe₂O₃. *Journal of The Electrochemical Society* **2003**, *150* (1), A133-A139.
19. Doi, T.; Fukuda, A.; Iriyama, Y.; Abe, T.; Ogumi, Z.; Nakagawa, K.; Ando, T., Low-temperature synthesis of graphitized nanofibers for reversible lithium-ion insertion/extraction. *Electrochemistry communications* **2005**, *7* (1), 10-13.
20. Wu, G.; Wang, C.; Zhang, X.; Yang, H.; Qi, Z.; Li, W., Lithium insertion into CuO/carbon nanotubes. *Journal of power sources* **1998**, *75* (1), 175-179.
21. Bonino, F.; Brutti, S.; Reale, P.; Scrosati, B.; Gherghel, L.; Wu, J.; Müllen, K., A Disordered Carbon as a Novel Anode Material in Lithium-Ion Cells. *Advanced materials* **2005**, *17* (6), 743-746.
22. Pan, Q.; Jin, H.; Wang, H.; Yin, G., Flower-like CuO film-electrode for lithium ion batteries and the effect of surface morphology on electrochemical performance. *Electrochimica Acta* **2007**, *53* (2), 951-956.
23. Taberna, P.-L.; Mitra, S.; Poizot, P.; Simon, P.; Tarascon, J.-M., High rate capabilities Fe₃O₄-based Cu nano-architected electrodes for lithium-ion battery applications. *Nature materials* **2006**, *5* (7), 567-573.
24. Chan, C. K.; Peng, H.; Liu, G.; McIlwrath, K.; Zhang, X. F.; Huggins, R. A.; Cui, Y., High-performance lithium battery anodes using silicon nanowires. *Nature nanotechnology* **2008**, *3* (1), 31-35.
25. Liu, J.; Li, Y.; Huang, X.; Ding, R.; Hu, Y.; Jiang, J.; Liao, L., Direct growth of SnO₂ nanorod array electrodes for lithium-ion batteries. *Journal of Materials Chemistry* **2009**, *19* (13), 1859-1864.

* Chapter III is reproduced in with a permission of “S. Choi, J. -I. Lee, S. Park, Patterning of electrodes for mechanically robust and bendable lithium-ion. *Journal of Materials Chemistry* 2012”.

Copyright **2012** The Royal Society of Chemistry

Chapter IV. High-Power Li-Ion Batteries Using Multi-Scale Lithographic Patterning of Electrodes

4.1. Introduction

Lithium-ion batteries (LIBs) are a critically important thing for operating portable electronic devices. However, they cannot meet the requirements for more advanced applications, like electric vehicles (EV) and energy storage systems(ESS) due to limitations of the conventional cathode/anode materials in high power and high energy density.¹⁻³ To overcome these limitations, several strategies have been developed, including nanostructured design of active materials and electrodes, coating of active materials with electrically conductive layers, and a control of electrode architectures.⁴⁻⁶ The nanostructured active materials (e.g., porous nanoparticles, nanotubes, nanowires, hollow structures) show significantly improved the electrochemical performances compared to micron-sized particles.⁷⁻¹¹ Since the characteristic time constant (t) for diffusion is proportional to the square of the diffusion length (l), such that $t \sim l^2/D$ (where D is the diffusion constant), reducing the dimension of electrode materials significantly increases the rate of lithium insertion/extraction due to the short distances for Li^+ ion transport within the active material particles.^{4-6, 12} However, because the nano materials have a high surface area, a high surface energy, and tend to aggregate, they cannot effectively shorten the path length for electronic transport.¹³ If the electronic conductive layers (e.g., metal, conductive carbon, conducting polymer) were fully coated on the surface of nano materials, the electronic transport length would be effectively shortened.¹⁴

As another strategy, a reconfiguration of electrodes (from 2D to 3D architecture) can provide an effective ion and electron transport to improve battery performance.¹⁵ 3D architectures, like pillar arrays,^{16, 17} 3D network structures,¹⁸⁻²¹ polymer scaffolds,²² metal foams,²³⁻²⁵ and carbon-based interpenetrating structures,^{26, 27} have been fabricated to an achieve fast charging and/or discharging performance in anode and cathode electrodes.^{28, 29} However, most of them are difficult to use in practical LIBs applications due to the low energy density of active materials in electrodes.

For practical battery applications, the electrode design should meet both the requirements of short ion/electron transport lengths and a high energy density. A lithographic process that allows a rich variety of geometries is one of the attractive methods to design various shaped structures of metal substrates.³⁰⁻³² For example, Peled et al. fabricated a 3D micro-battery using a nickel foam current collector based on a glass micro-channel plate.³⁰ The surface area of the 3D structured substrate was increased by 20–30 times compared to that of a planar device. When a molybdenum oxysulfide cathode was applied to the 3D substrates, the reversible capacity per footprint area of the electrodes was significantly increased by a factor of 20–30, compared to a planar device prepared by the same process. This result is in good agreement with the enhancement of surface area.³⁰ Valvo et al.

fabricated 3D electrode and electrolyte materials to enable stable cycling performance in LIBs.³² Electrochemically prepared metal nano-rods and 3D-structured carbon substrates were combined with various active materials, resulting in enhanced capacities per footprint area compared to systems with 2D flat current collectors. However, the above examples did not meet a high storage electrical capacity (high energy density) and a high rate capability (high power density) due to a limited loading amount of active materials.

Herein, we demonstrate the lithographically patterned electrodes consisting of micro- and nano-scale patterns, in which the multi-scale patterns provide a surface area enhancement and a strong adhesion between active materials and the surface of current collector. The advantages of this concept are explained as follows: (i) an increased contact area between making surface of current collectors by lithographically patterns and composite materials including active materials, conductive agents, and binders, (ii) shorter electric pathways from the surface of current collectors to points of the composite electrode materials and (iii) a strong adhesion of electrode materials to the nano-scale patterns of the patterned current collector that can prevent a delamination of the electrodes. When LiFePO_4 cathode, $\text{Li}_4\text{Ti}_5\text{O}_{12}$ and Si anode materials are applied to the these electrodes using the lithographically patterned current collectors, the excellent electrochemical performances of various active materials are achieved, including a high rate capability (LiFePO_4 : 96 mAhg^{-1} at 100C rate, $\text{Li}_4\text{Ti}_5\text{O}_{12}$: 140 mAhg^{-1} at 10C, Si: 825 mAhg^{-1} at 5C) and highly stable cycling performances. This simple strategy and approach can be extended to other cathode and anode materials for the practical LIBs applications.

4.2. Experimental

4.2.1. Fabrication of Patterned Current Collectors

The lithographically patterned metal foils were prepared from a conventional standard photolithography technique and dry and/or wet etching process. Aluminum (Al) foil (Good-fellow, 99.0%) was coated with a photoresist (AZ9260) at 3000 rpm for 40 s by a spin coater system. To make various shape polymer pattern masks, the photoresist films were exposed to an ultraviolet (UV) intensity of 13 mW cm^{-2} for 25 s and developed by MIF-300 developing solution for 3 min. Subsequently, various shape patterned Al foils were fabricated by a reactive-ion etching (RIE) process in chlorine (Cl_2) gas (at 350W RF power, reaction pressure $<70 \text{ mTorr}$, and etching rates of 100 \AA s^{-1}). Then, the photoresist was removed in acetone by ultra-sonication process. In contrast, the patterning of Cu foil (Good-fellow, 99.9%) was carried out by a wet-etching process. The photoresist-patterned Cu foils were immersed in 30% copper chloride (CuCl_2) aqueous solution to etch down the open site of Cu foils. The photoresist pattern was removed with acetone, rinsed with large amounts of water, and dried with N_2 gas.

4.2.2. LiFePO_4 Synthesis

LiFePO_4 nanoparticles were prepared by the coprecipitation method using solubility product (K_{sp}).³⁹ The solution of iron sulfate heptahydrate ($\text{FeSO}_4 \cdot 7\text{H}_2\text{O}$) as a Fe^{2+} precursor was mixed with 0.684 mL of phosphoric acid, H_3PO_4 (aq). Cetyltrimethylammonium bromide (CTAB) was dissolved in deionized water. The solution, including Fe^{2+} and PO_4^{3-} precursors, was added to the CTAB solution under stirring. Then, lithium hydroxide monohydrate ($\text{LiOH} \cdot \text{H}_2\text{O}$) solution was slowly added to the prepared solution with stirring. This solution was transferred into an autoclave and then heated at 120°C for 5 h in a convection oven. After washing and filtration with deionized water, all prepared samples were dried in a vacuum condition and calcined at 700°C for 6 h with Ar gas flowing.

4.2.3. Anode Materials

$\text{Li}_4\text{Ti}_5\text{O}_{12}$ properties: $\text{Li}_4\text{Ti}_5\text{O}_{12}$ powders were prepared commercial available products by Sud Chemie AG (Germany).

Silicon properties: Si nanoparticles (an average particle size of 100 nm) were purchased from Sigma–Aldrich and used without further purification

4.2.4. Characterization

A morphology of the samples was observed using scanning electron microscopy (SEM, Nano 230, FEI) and the as-synthesized LiFePO_4 powders were measured by an XRD on a Rigaku D/MAX at

2500 V using CuK_α radiation. Three-dimensional measurement of the patterned foils was recorded using phase-shifting interferometry (NV-3000, Nano-system).

4.2.5. Electrochemical Test

The characterization of electrochemical properties about various electrodes was evaluated using coin-type half cells (2016R) at 25°C. The Si anode electrodes for the half-cell test were composed of Si nanoparticles, super-P carbon black, and poly(acrylic acid)/sodium carboxymethyl cellulose (1:1, w/w) binder in a weight ratio of 6:2:2. The electrolyte was 1.3M LiPF_6 with ethylene carbonate (EC)/diethyl carbonate (DEC) [PANAX, 3:7 (v/v)] including 5% fluoroethylene carbonate additive. The half-cells of Si anode electrode were tested galvanostatic charge–discharge measurements between 0.01 and 1.2 V (versus Li/Li^+) at 0.1C and 5C rate. The LTO anode electrodes for the half-cell test were composed of $\text{Li}_4\text{Ti}_5\text{O}_{12}$ powder, super-P carbon black, and polyvinylidene fluoride (PVdF) binder in a weight ratio of 8:1:1. The electrolyte was 1M LiPF_6 with ethylene carbonate (EC)/dimethyl carbonate (DMC) [PANAX, 3:7 (v/v)]. The half cells were tested galvanostatic charge–discharge measurements between 1.0 and 2.5 V (versus Li/Li^+) at various C rates (0.1C–50C). The cathode electrodes for the half-cell test were composed of LiFePO_4 powder, super-P carbon black, and polyvinylidene fluoride (PVdF) binder in a weight ratio of 8:1:1. The electrolyte was 1m LiPF_6 with ethylene carbonate/dimethyl carbonate [PANAX, 3:7 (v/v)]. The half cells were tested galvanostatic charge–discharge measurements between 4.3 and 2.0 V (versus Li/Li^+) at various C rates (0.1C–500C). The electrode materials were coated on the patterned and non-patterned current collectors using a typical slurry coating method. The full-cell tests were combined with $\text{Li}_4\text{Ti}_5\text{O}_{12}$ anode electrode and LiFePO_4 cathode electrode in a N/P ratio of 1.1:1. The electrolyte was 1M LiPF_6 with ethylene carbonate (EC)/dimethyl carbonate (DMC) [PANAX, 3:7 (v/v)]. The full cell was tested galvanostatic charge–discharge measurements between 1.0 and 2.5 V (versus Li/Li^+) at various C rates (0.1C–10C).

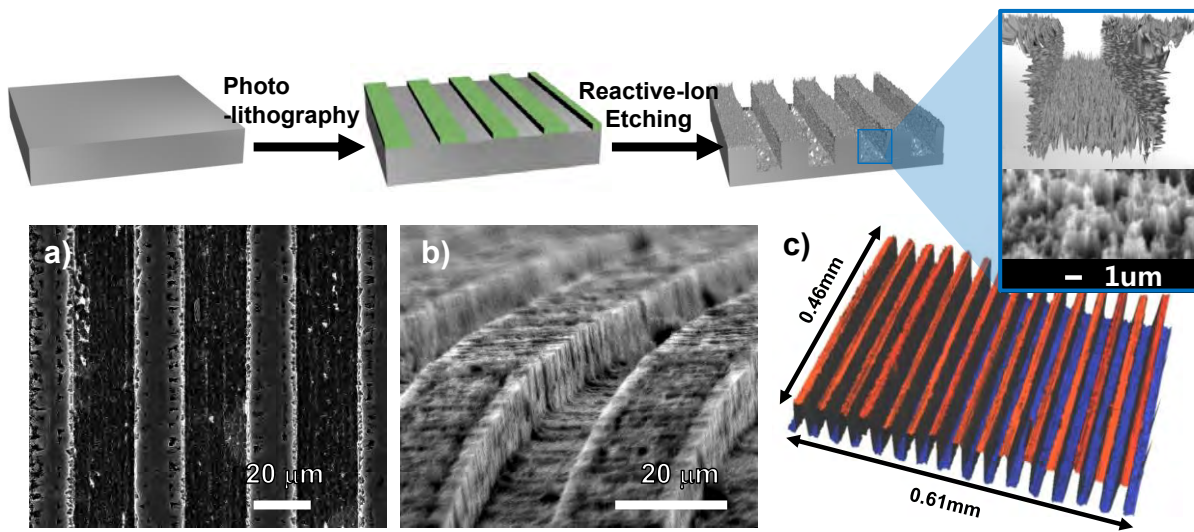


Figure 4. 1 Top: the schematic illustration showing a fabrication process of multi scale patterned current collector. Magnified SEM image shows nano scale patterns on the surface of the aluminum (Al) metal foils. Bottom: a) SEM image (top view) of the patterned Al foil, b) tilting view SEM image of (a), and c) three dimensional image of trench patterned structures on the surface of Al foil in a large area.

4.3. Result and discussion

4.3.1. Characterization of Patterned Electrodes.

A schematic illustration of the fabrication process for micro- and nano- scale patterned metal current collectors is depicted (Images of scheme in Figure 4.1). The patterning process consists of a photolithography process of a guide pattern on the surface of the metal current collectors and a subsequent anisotropic etching process including reactive ion etching (RIE) or wet chemical etching. This method is well known as a standard process for the patterning of semiconductor circuits.³³ When an appropriate etching time is applied to the metal current collectors, micro- and nano-scale patterns that may increase adhesion properties between electrode materials and the surface of current collectors are produced (Figure 4.1, top).³⁴⁻³⁶

Figure 4. 1a shows a SEM image of multi-scale patterned surface of Al foils which were fabricated by the photolithographic patterning and subsequent chlorine RIE process. The fabrication details are described in the experimental section. The tilt-view SEM image shows that the trench-type patterned Al foils have an average width of 20 μm and an average depth of 12 μm (Figure 4. 1b). In addition, we confirmed the characteristics of the patterned Al foils by non-contact-mode phase-shifting interferometry which can characterize a morphology, a surface roughness, and a depth value of structure on surface in a large area (Figure 4. 1c). Moreover, various patterned Al foils including holes, honeycombs, and zig-zag structures can be fabricated by the standard lithographic process (Figure 4.2). Among them, we used the trench-type patterns as representative current collectors and combined them with cathode and anode materials.

First, we investigated the effect of the electrodes using trench type patterned Al foils on an adhesion of active materials and patterned surface of current collectors through flexibility tests such as bending and twisting. When a surface coverage of LiFePO_4 electrodes on patterned Al foils was investigated as a function of bending/twisting cycle, loss of the active materials was not observed, while the electrode materials on a non-patterned Al foil were seriously depleted (70% surface coverage of electrode materials) due to a weak adhesion between the active material and the flat surface of current collector (Figure 4.3). Moreover, the strong adhesion of the patterned electrodes was seen in the peel-off test result using a Scotch-tape method for evaluating the adhesion of a coating to a substrate. The 3M Scotch-tape was attached to an area of the coating on prepared LiFePO_4 (LFP) cathode electrode. The patterned electrode showed a strong adhesion of active materials with the surface of patterned current collector. But the non-patterned electrode was almost pulled off by the tape when the tape was removed. (Figure 4.4).

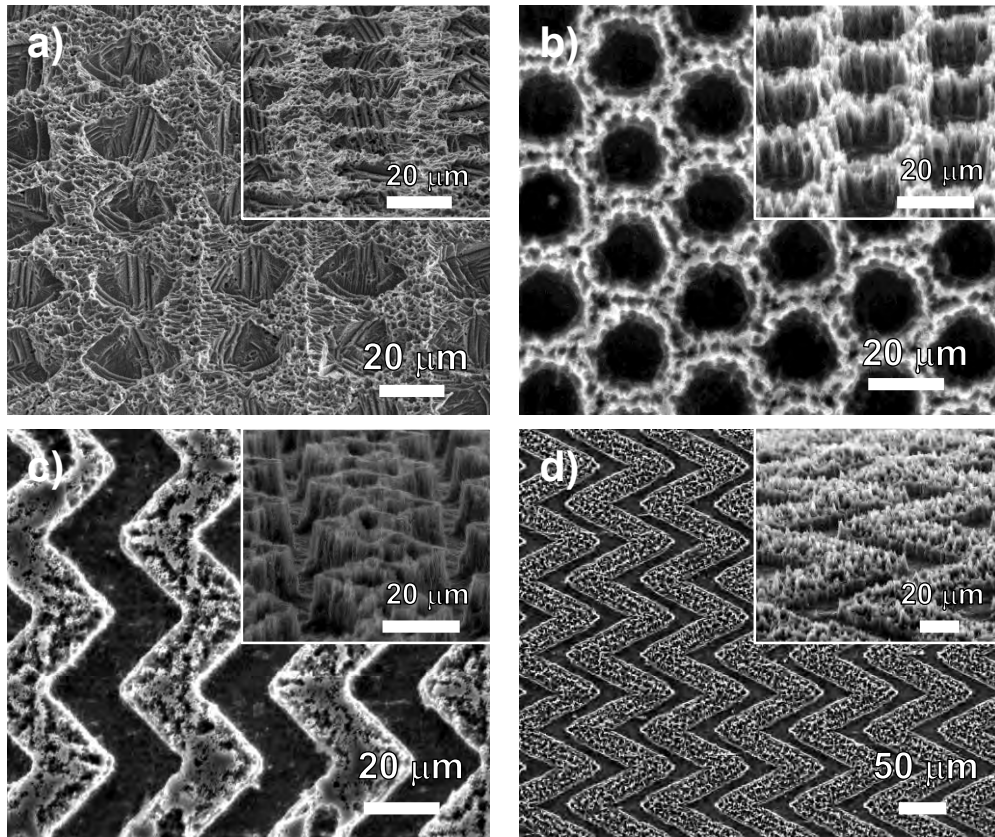


Figure 4. 2 The SEM images of Al patterns with various shapes including (a) mesh pattern, (b) honeycomb pattern, (c) zigzag pattern, and (d) low-magnified zigzag pattern.

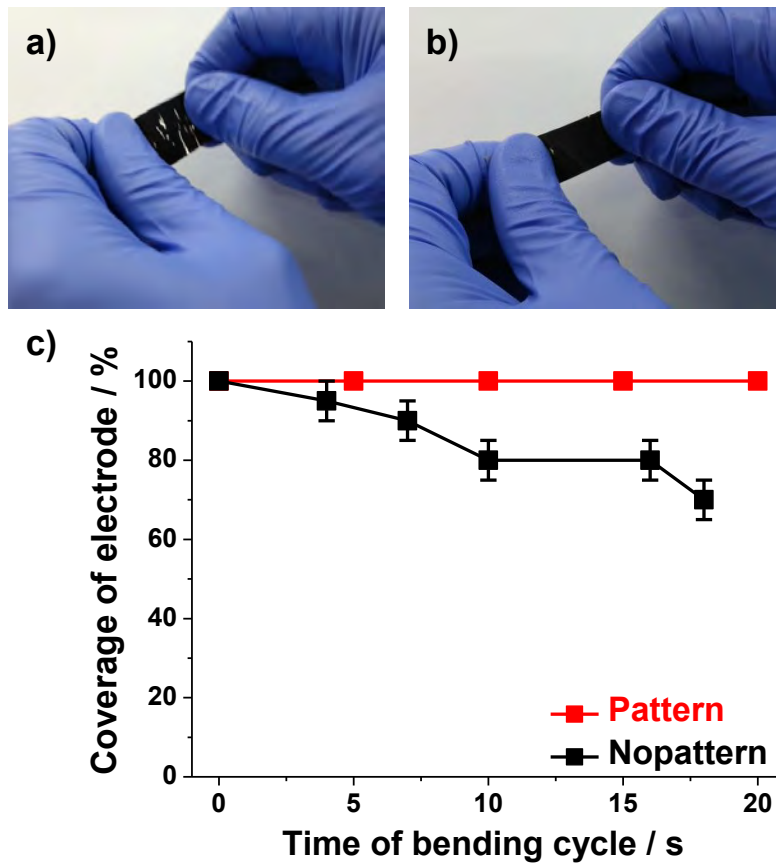


Figure 4. 3 An adhesion test of patterned and non-patterned LiFePO_4 electrodes. The photographs of a) non-patterned electrode and b) patterned electrode after 20 bending and twisting cycles. c) The plot of surface coverage of two electrodes versus bending/twisting cycle. The non-patterned electrodes show a significant detachment of active materials from current collector. We measured the surface coverage using an image analysis program of photographs.



Figure 4. 4 The peel-off test of the patterned and non-patterned LiFePO_4 electrodes. As expected, the LiFePO_4 electrodes on the patterned current collectors were strongly attached to the current collectors, while electrode materials were easily peeled off from non-patterned current collectors.

4.3.2. Study on Effects of Patterned Electrodes

Expected benefits of patterned current collectors are two-fold when they are used in electrochemical cells based on the electro-active materials (Figure 4.5 a). First, the interfacial surface area at which electrode materials make contact with the current collectors increases when the surface is patterned. Consider a line pattern with W as the width of troughs as well as crests and H as the height of crests. An enhancement factor (η) of the surface area can be described by:

$$\begin{aligned} \text{Surface area ratio} &= \text{area of pattern} / \text{area of flat surface} \\ &= (2W + 2H) / (2W) = 1 + H / W = \text{aspect ratio of crest} \end{aligned} \quad (1)$$

$$\eta = (\text{surface area ratio} - 1) = \text{aspect ratio of crest} \quad (2)$$

Therefore, a higher aspect ratio of crests leads to a higher surface area. In this work, W was fixed at 20 μm while H was 3 or 12 μm . Surface area is expected to increase 15% and 60% for $H = 3$ and 12 μm , respectively.

In addition to the interfacial surface area increase, a shorter average length of electronic pathways is another benefit of patterning. The main difference between patterned and non-patterned electrodes, in terms of electronic pathways from the current collector to each point of electrode composites, results from an electro-active mass present in the trough of the pattern (Figure 4.5 a). A portion of the trough mass would be transported via electric shortcuts to the lateral sides of crests of patterns (point α_1 in Figure 4.5 a) instead of the bases of the troughs (point α_2). However, within the electro-active mass of a non-patterned flat current collector, electronic pathways must go through the base of the electrode coating. Therefore, we distinguished the electro-active mass loaded on the patterned current collectors into two parts: the mass in troughs between crests (in-pattern mass) and the mass existing above the level of crests (above-pattern mass). From the viewpoint of electric pathways, the above-pattern mass can be split further into two regions: the on-crest and above-trough regions. Electric pathways of the in-pattern part and the on-crest region of the above-pattern part are described by shortcut lines perpendicular to current collector surface near an electro-active point of interest (points α_1 , α_2 , β_1 , and β_2 in Figure 4.5 a). The points of an above-trough region are connected to the nearby corner point of the pattern (points γ_1 and γ_2 in Figure 4.5 a). Therefore, current lines are concentrated at the corner region.^{37, 38} Based on the schematic description of electric pathways (Figure 4.5 a), average lengths of pathways (λ) were calculated as a function of dimensions of patterns (W and H) and the thickness of above-pattern mass (L): $\lambda = 5.50 \mu\text{m}$ with $H=3 \mu\text{m}$ and $\lambda = 5.40 \mu\text{m}$ with $H=12 \mu\text{m}$ for $L=10 \mu\text{m}$ (Table S1 and calculation section of the Supporting Information). The values of l were estimated at 5.75 and 8.00 μm for the corresponding non-patterned controls respectively when the same masses of composite materials were loaded on non-patterned current collectors. The pathway reduced to 95.6% and 67.4% of the average conduction length of the flat current collectors for the 3

and 12 μm deep patterns, respectively. As the value of L increased, the reduction percentage significantly decreased. With $L = 80 \mu\text{m}$, only 97.2% and 88.0% reduction was observed for the 3 and 12 μm deep patterns, respectively.

Electrochemical lithiation of a cathode material for LIBs was evaluated with our patterned Al current collectors (Figure 4.5 b–f). The LiFePO_4 prepared by co-precipitation (co-LFP) was used as a cathode material (Figure 4.6). To investigate the effects of patterning, two different patterns electrode were compared: 3 or 12 μm deep trench patterns with 40 μm periodicity versus non-patterned (with flat surface) as a control. The same amount of co-LFP materials ($\approx 1.5 \text{ mg}$) was loaded to the patterned and non-patterned current collectors. Lithiation (discharge) kinetics of co-LFP was directly related to depths of patterns of the current collectors. At a low discharge rate (0.1C to 1C), there was no distinguishable difference of capacity between the patterned and non-patterned electrodes, as recorded with capacity of approximately 150 mAh g^{-1} (Figure 4.5 b and c). At high discharge rates, however, the patterned electrodes showed impressively enhanced capacities superior to that of the non-patterned one (Figure 4.5 c).

Also, the enhancement property was more emphasized with the deeper pattern of 12 μm depth (Figure 4.5 d). For example, the patterned electrodes (3 or 12 μm deep) exhibited more than ten times higher capacity compared to the non-patterned electrode at 50C: 110 mAh g^{-1} for patterned electrodes versus 10 mAh g^{-1} for the non-patterned electrode. The specific capacity of 100 mAh g^{-1} at 100C obtained with the patterned electrodes is the highest specific capacity that has ever been reported with practical electrode compositions (here: active materials/binder/carbon black=8:1:1) as far as we know. At ultrafast discharge rates such as 500C, the 12 μm deep patterned electrode even outperformed its shallow counterpart (3 μm deep one) in terms of kinetics. The deeper pattern delivered capacity at 50 mAh g^{-1} with a comparatively small IR drop, while the shallow pattern showed no faradaic plateau only with capacitive discharge (Figure 4.5 e). Capacity retention at a fast rate of 10C was also improved with the patterned current collectors, when compared with their non-patterned counterpart (Figure 4.5 f): 130 mAh g^{-1} for patterned current collector (12 μm deep) versus 5 mA g^{-1} for the non-patterned one. Also, the coulombic efficiency of patterned electrode was 99.8% after 70 cycles (50 cycles at 10C).

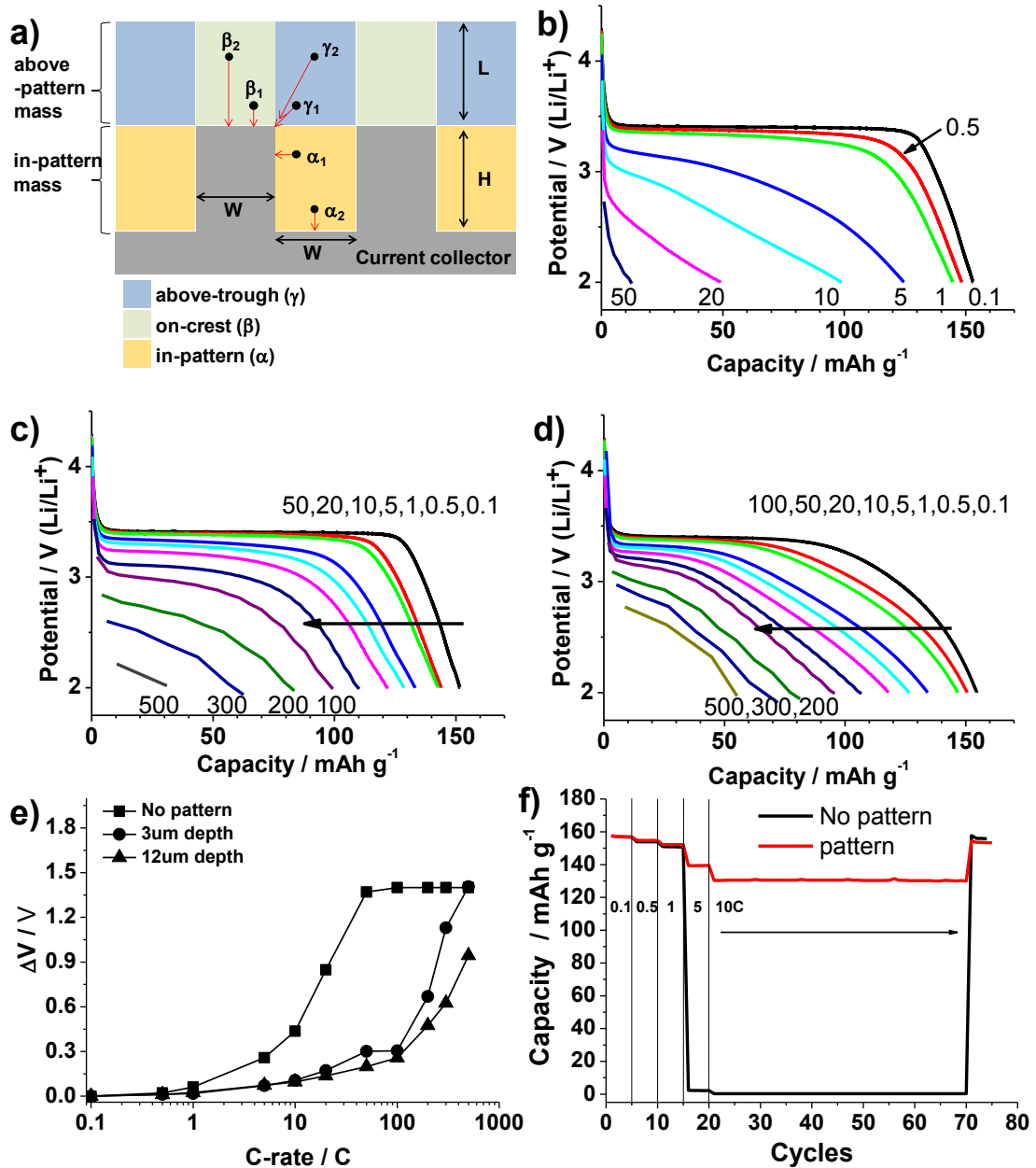


Figure 4.5 a) The schematic illustration showing the electric pathways of the patterned electrodes. The composite electrodes were loaded on a patterned metal current collector. The composite electrode mass is sectioned into three different regions from the viewpoint of electric pathway. The voltage profiles of LFP electrodes showing rate capabilities of b) the non-patterned electrode and the patterned electrodes with c) 3 μ m depth and d) 12 μ m depth. e) The deviation of plateau potential from the ideal value (3.45 V) during discharge at various C rates and a fixed charge rate of 0.2C. f) The capacity retention of the patterned (red) and non-patterned (black) electrodes at various discharge rates and a fixed charge rate of 0.2C.

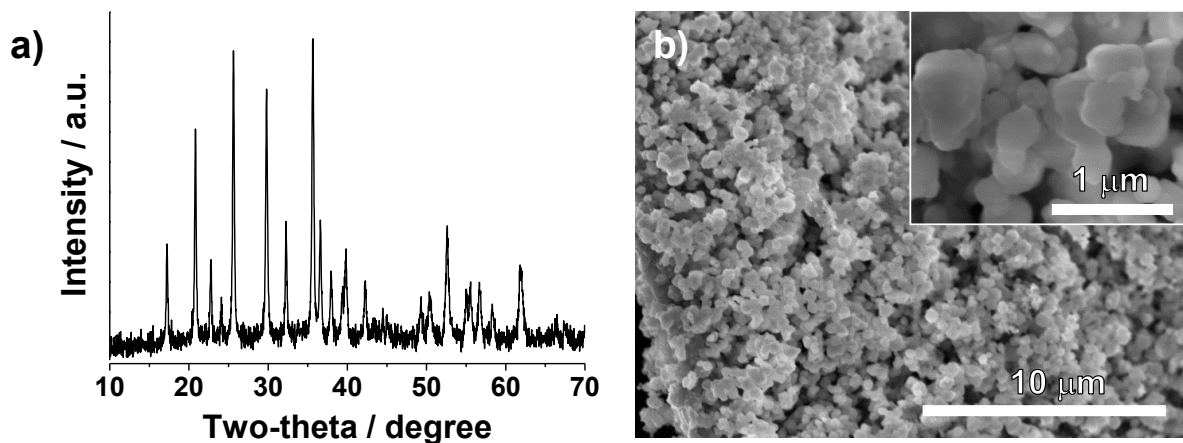


Figure 4. 6 The characterization of co-pre LiFePO_4 cathode materials. (a) The XRD patterns showing pure LiFePO_4 and (b) The SEM images of co-LFP particles showing an average particle size of 500nm.

4.3.3. Positive Effects of Patterning Compared to Other Conditions

Moreover, we investigated the effects of etched Al foils on a high rate property of the co-LFP cathode. A surface nanostructure was created on the surface of Al foil by a reactive ion etching process without polymer pattern. Compared to the electrode using non-patterned Al foils, the co-LFP electrodes on the etched Al current collectors showed remarkably enhanced rate capabilities. The etched electrodes exhibited higher electrical capacity compared to the non-patterned electrode at 20C: $Q_{20}/Q_{0.1} = 55\%$ for the etched current collector versus 30% for the non-patterned one (Q = capacity and subscript = C rate). When power densities per area for the non-patterned and patterned (surface area enhancement of 60 %, compared to non-patterned Al current collectors) LFP electrodes at 20C rate were calculated, 74.9 and 137 mWcm⁻² were obtained, respectively. This result indicates that a strong adhesion property between co-LFP electrodes and the current collectors plays an important role in exhibiting a high rate capability (Figure 4.7).

The patterned current collectors (12 μm deep) containing in-pattern mass with low-loading above-pattern mass (10 μm thick) were compared with the same current collectors containing in-pattern mass with high-loading above-pattern mass (80 μm thick) (Figure 4.8). As expected, the low-loading above-pattern mass showed an improved rate capability as a result of shorter average length of electronic pathways due to the effects of patterning, compared to its high-loading counterparts (Figure 4.8 a and b). The ratio of discharge capacity at 100C to 0.1C was estimated at 13.6% for high-loading above-pattern mass (80 μm thick) versus 61.9% for the low-loading counterpart (10 μm thick). If an infinite amount of above-pattern mass were loaded onto a patterned current collector, no benefits of patterning could be expected because the average length of electric pathways would become identical between the patterned and non-patterned electrodes.

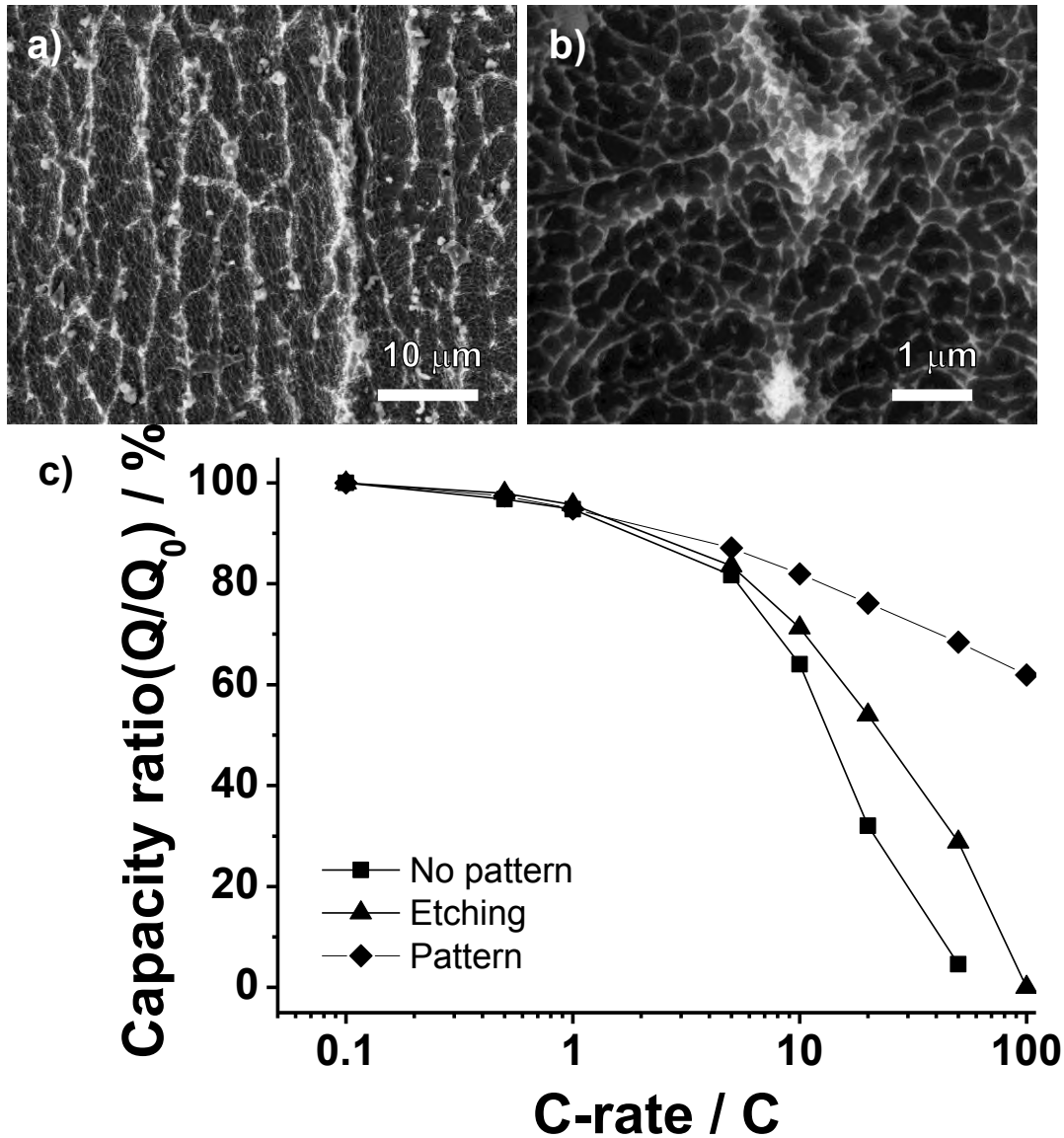


Figure 4. 7 The characterization of the etched (nanostructured) Al foils obtained by RIE process. a) The low-magnified and b) the high-magnified SEM images showing nano-scale patterns (ranging from 200 to 500 nm) on the surface of Al foils. c) The normalization plot of rate performances of co-LFP electrodes on non-patterns (solid square), etched (solid triangle), and lithographically patterned (solid lozenge) Al current collectors.

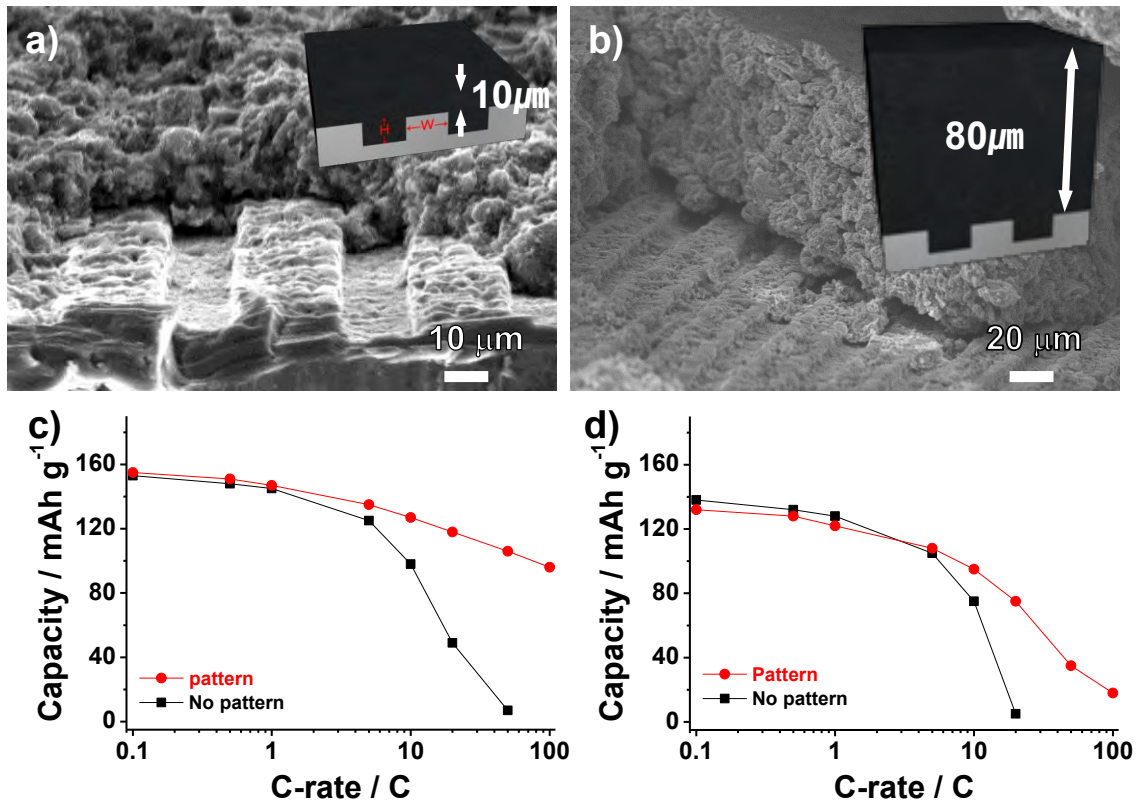


Figure 4. 8 The cross-sectional SEM images of co-LFP electrodes with a) a low loading level (10 μm thickness, loading mass of ~1.5 mg cm⁻²) and b) a high loading level (80 μm thickness, loading mass of ~8.2 mg cm⁻²) on the patterned Al current collectors. Inset represents schematic illustration showing the dimension between co-LFP electrodes and the patterned current collectors. The plots of C-rate values versus specific capacities at c) low loading and d) high loading level of co-LFP electrodes.

4.3.4. Applying Patterned Electrode to Anode Materials

In addition to another active materials, we applied a similar strategy to lithium–titanium-oxide anode materials. Commercially available $\text{Li}_4\text{Ti}_5\text{O}_{12}$ (LTO) particles with an average particle size of 1 μm were used as an anode material (Figure 4.9). Figure 4.10 a shows the first cycle voltage profiles of the patterned LTO electrode and non-patterned LTO electrode at a rate of 0.1C in the range of 1.0 – 2.5 V. The first discharge (lithiation) capacity of the patterned electrode was 174 mAh g^{-1} with an initial coulombic efficiency of 97.7 %, while a specific capacity of the non-patterned electrodes was 173 mA g^{-1} , corresponding to a coulombic efficiency of 94.8 %. Similar to the results of the co-LFP cathode, initial capacity and coulombic efficiency are not much different in the patterned and the non-patterned electrodes. However, high-rate capabilities of both electrodes are quite different (Figure 4.10 b). The high-rate capabilities of patterned LTO electrode was 140 mAh g^{-1} at 10C and 60 mAh g^{-1} even at a high rate of 50C. In contrast, non-patterned LTO electrode did not exhibit usable capacities over 10C rate. Notably, even though the LTO particles were not coated with any conductive layers (e.g., metal, carbon layers, and conductive polymers), the patterned electrodes showed a significant improved electrochemical performance, compared to the non-patterned electrodes. From the point of view of practical battery application, we investigated an effect of patterned electrodes on a full-cell system. We assembled the patterned LFP cathode electrode and the patterned LTO anode electrode, achieving ultra-high rate capabilities. The first cycle capacity of cell with patterned electrode was 150 mAh g^{-1} , while the non-patterned electrode cell was 138 mAh g^{-1} at 0.1C, indicating that the patterning electrodes play an important role in exhibiting a high specific capacity. At a high rate of 10C, a capacity gap between the patterned electrode and the non-patterned one became larger (Figure 4.11a). Moreover, we tested a long term cycling stability property at a fast charging/discharging condition (10C rate corresponding to charging time of 6 min). The patterned electrodes showed approximately 70 mAh g^{-1} even after 1000 cycles, while the non-patterned electrodes showed significantly decayed capacity after tens of cycles (Figure 4.11 b). Notably, the patterned electrodes enabled us to make fast charging and highly stable cycling in LIBs systems.

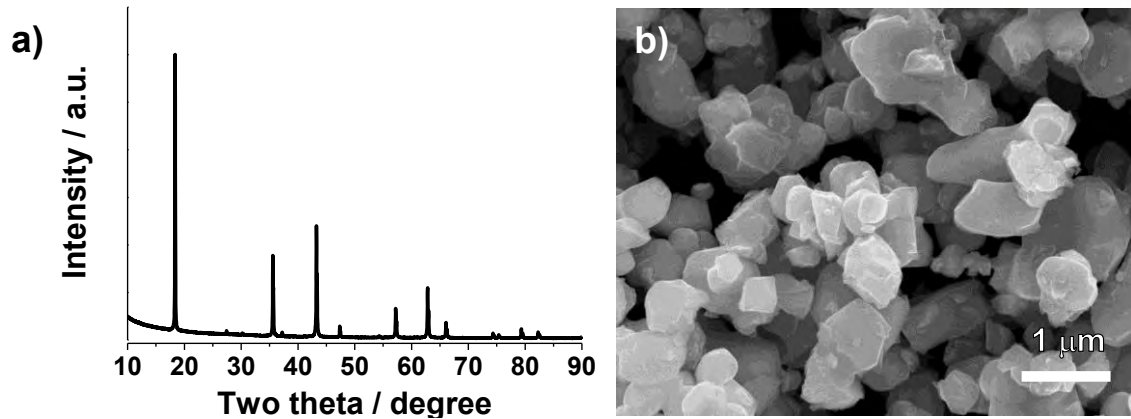


Figure 4. 9 The characterization of $\text{Li}_4\text{Ti}_5\text{O}_{12}$ (LTO) anode materials. (a) The XRD patterns showing pure LTO materials and (b) the SEM images of LTO showing an average particle size of $\sim 1\ \mu\text{m}$.

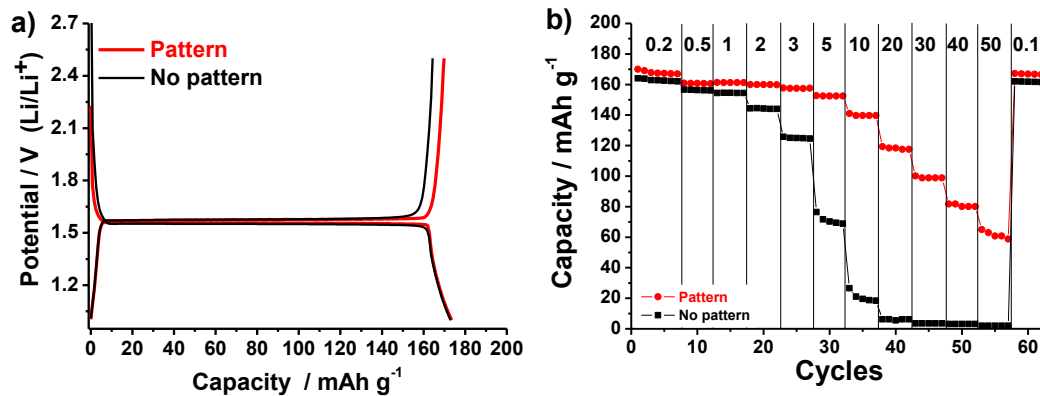


Figure 4. 10 The electrochemical tests of the patterned LTO electrodes. a) The first cycle voltage profiles of the patterned and non-patterned LTO electrodes and b) the rate capabilities of the patterned and non-patterned LTO electrodes at various charge C rates. (a fixed discharge C rate at 0.2C).

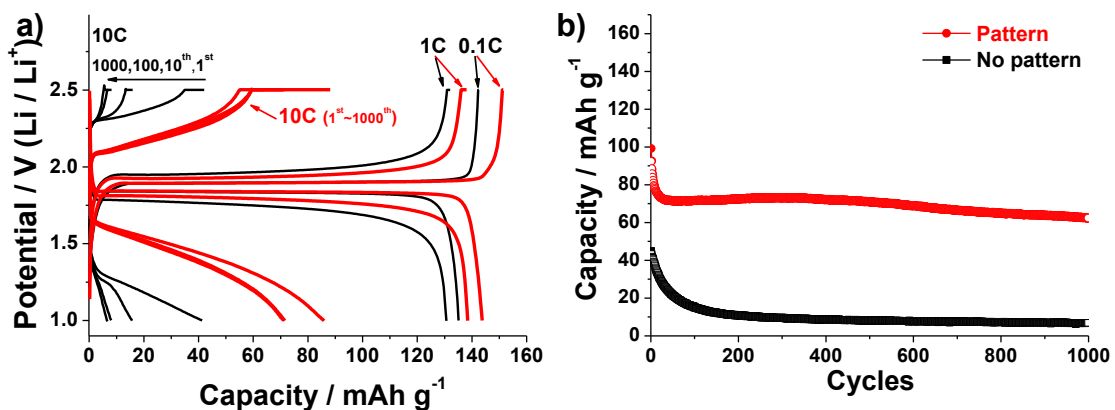


Figure 4. 11 The electrochemical tests of full cell system using $\text{LiFePO}_4 / \text{Li}_4\text{Ti}_5\text{O}_{12}$ electrodes (cathode loading mass of $\approx 2.87\ \text{mg cm}^{-2}$, N/P ratio=1.1:1). a) The voltage profiles at each cycle step and b) the long term cycling performances of the patterned and the non-patterned cell at high C-rate (charge/discharge rate of 10C).

We extended an idea of electrode patterning to the Silicon (Si) anode material in LIBs. Instead of Al foils, we employed Copper (Cu) foils and fabricated trench-type Cu patterns with an average depth of 6 μm and an average width of 20 μm by means of a wet chemical etching process.³⁵ The electrochemical properties of commercially available Si nanoparticles (≈ 100 nm) were evaluated with patterned Cu foils and non-patterned Cu foils (Figure 4.12). It should be noted that the Si nanoparticles without an electrical conductive layer (e.g., metal particles, carbon layer, and conductive polymer) were used to investigate the effects of patterned electrodes on the electrochemical properties and the same loading amount (≈ 1 mg) was applied to the patterned and non-patterned Cu foils.

Figure 4.12 a shows the first cycle voltage profiles of the patterned Si electrode and the non-patterned Si electrode at a rate of 0.1C in the range of 0.005–1.2 V. The first discharge (lithiation) capacity of the patterned electrode was 2660 mAh g^{-1} with an initial coulombic efficiency of 81%, while the first charge and discharge capacity of non-patterned Si electrodes were 2700 and 2160 mAh g^{-1} , respectively, corresponding to a coulombic efficiency of 80%. Similar to the results of the previous LFP and LTO systems, initial electrical capacity and coulombic efficiency are not much different in the patterned and the non-patterned electrodes. However, the cycling performances of both electrodes are quite different (Figure 4.12 b). The patterned Si electrode showed a high specific capacity of 1963 mAh g^{-1} at a rate of 0.1C after 80 cycles corresponding to the capacity retention of 88% compared to initial specific capacity. In contrast, the non-patterned Si electrodes showed a low specific capacity of 621 mAh g^{-1} after 80 cycles. Moreover, the rate capabilities of the patterned electrodes were investigated at various rates (from 0.2C to 5C) between 1.2 and 0.01 V. The patterned Si electrodes exhibited a specific capacity of 825 mAh g^{-1} at a high rate of 5C, compared to that of the 0.2C rate. The excellent electrochemical performances of the patterned Si electrodes can be explained as follows: (i) an increased contact area between surface of current collectors and composite materials including active materials, conductive agents and binders, (ii) shorter electric pathways from the surface of current collector to points of the composite materials and (iii) a strong adhesion of the electrode materials to the patterned current collector that can prevent delamination of the electrodes.

To prove the stability of the Si electrode after 80 cycles, we obtained cross-sectional SEM images of the Si electrode within trench type patterned Cu foils before (Figure 4.12d) and after cycling (inset of Figure 4.12 d). Even after 80 cycles, the Si electrodes on the patterned Cu foils were strongly adhered to the Cu current collector as shown in the magnified SEM image (inset of Figure 4.12d). However, the Si electrode on the non-patterned Cu current collectors was easily delaminated from the Cu current collector (Figure 4.13).

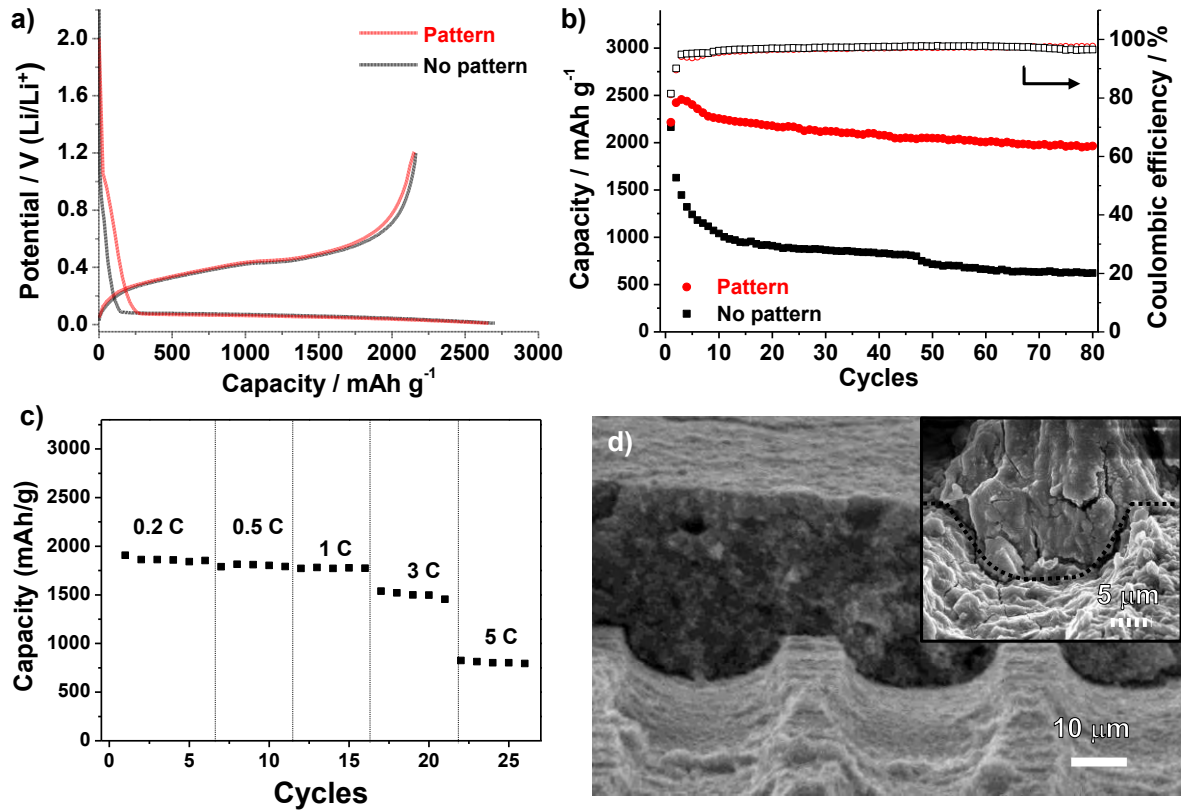


Figure 4. 12 The electrochemical tests of the patterned and non-patterned Si electrodes. a) The first cycle voltage profiles and b) cycling performances of the patterned and the non-patterned Si electrodes at a rate of 0.1C. c) The rate capabilities of the patterned Si electrodes at various C rates. d) The cross-sectional SEM images of the patterned Si electrodes. Inset magnified SEM image shows a strong adhesion of Si electrodes to the patterned Cu foils after 80 cycles.

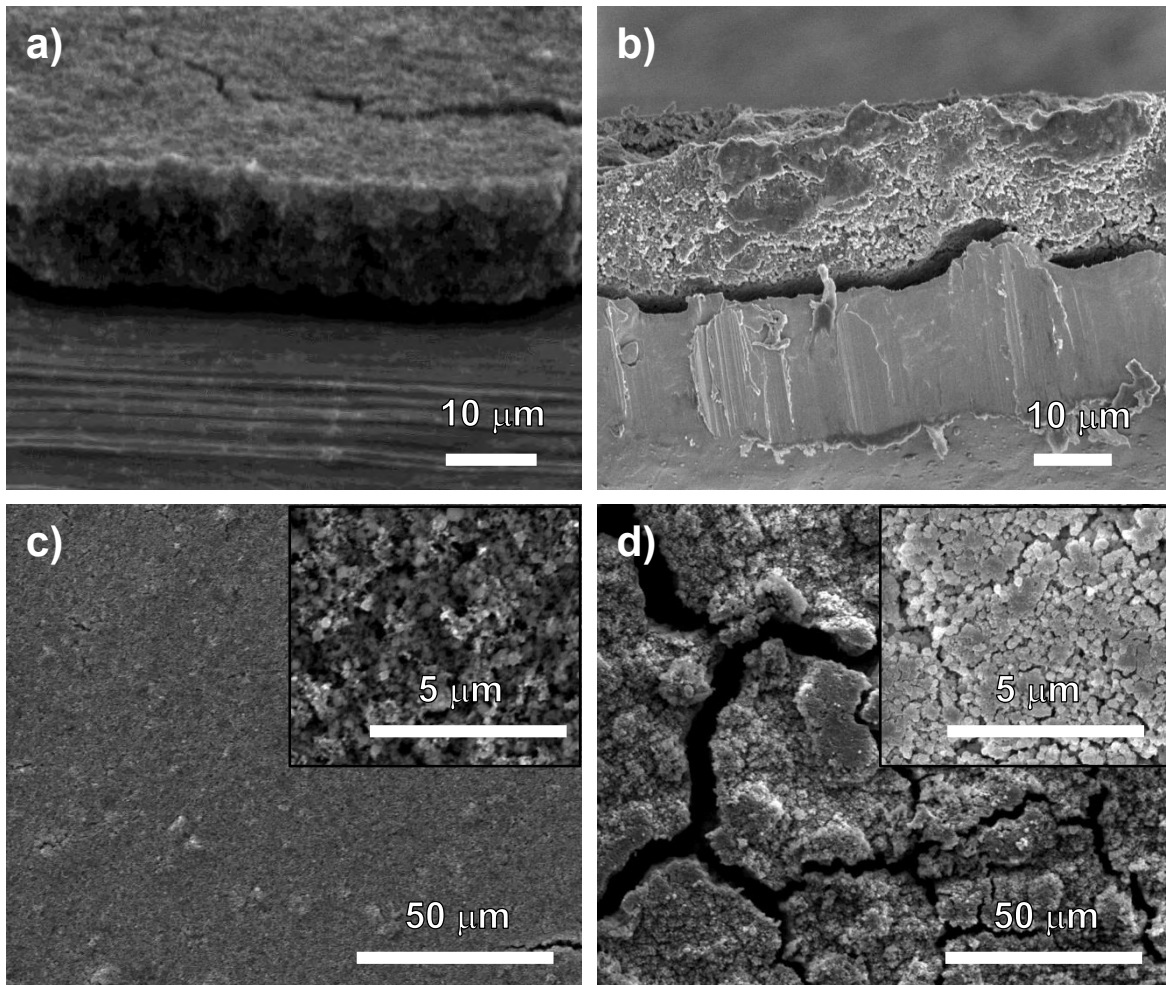


Figure 4. 13 The characterization of Si electrodes on the non-patterned Cu foils. The cross-sectional SEM images of Si electrodes (a) before cycle and (b) after 80 cycles. The Si electrodes are easily delaminated from non-patterned Cu current collectors after cycling. The top-view SEM images of Si electrodes (c) before cycle and (d) after 80 cycles. After cycling, the Si electrodes show numerous cracks due to a large volume change of the electrodes during the lithiation/delithiation process.

4.4. Conclusion

We demonstrated the multi scale patterned electrodes that provide surface-area enhancement and a strong adhesion between various electrode materials and metal current collector. A combination of micro- / nano- scale structured current collector and cathode materials and anode materials exhibited significantly improved electrochemical performances including a highly stable cycling life (energy density for long cycles) and a high rate capability (power density) of LiFePO_4 cathode and $\text{Li}_4\text{Ti}_5\text{O}_{12}$ and Si anodes. Moreover, the full cell system consisting of patterned LFP cathode and patterned LTO anode showed superior rate capabilities and a highly stable long cycling life ($\sim 70 \text{ mAhg}^{-1}$ at rate of 10C discharge/charge even after 1000 cycles). In addition to the electrode materials with a low volume expansion of materials, the Si anode materials having a large volume change also showed significantly improved electrochemical properties on the patterned metal current collectors, including a highly stable cycling life and a high rate capability.

4.5. References

1. Nazri, G. A.; Pistoia, G., *Lithium Batteries: Science and Technology*. Springer: 2004.
2. Armand, M.; Tarascon, J.-M., Building better batteries. *Nature* **2008**, *451* (7179), 652-657.
3. Song, M.-K.; Park, S.; Alamgir, F. M.; Cho, J.; Liu, M., Nanostructured electrodes for lithium-ion and lithium-air batteries: the latest developments, challenges, and perspectives. *Materials Science and Engineering: R: Reports* **2011**, *72* (11), 203-252.
4. Bruce, P. G.; Scrosati, B.; Tarascon, J. M., Nanomaterials for rechargeable lithium batteries. *Angewandte Chemie International Edition* **2008**, *47* (16), 2930-2946.
5. Manthiram, A.; Murugan, A. V.; Sarkar, A.; Muraliganth, T., Nanostructured electrode materials for electrochemical energy storage and conversion. *Energy & Environmental Science* **2008**, *1* (6), 621-638.
6. Liu, C.; Li, F.; Ma, L. P.; Cheng, H. M., Advanced materials for energy storage. *Advanced materials* **2010**, *22* (8), E28-E62.
7. Magasinski, A.; Dixon, P.; Hertzberg, B.; Kvit, A.; Ayala, J.; Yushin, G., High-performance lithium-ion anodes using a hierarchical bottom-up approach. *Nature materials* **2010**, *9* (4), 353-358.
8. Chan, C. K.; Peng, H.; Liu, G.; McIlwrath, K.; Zhang, X. F.; Huggins, R. A.; Cui, Y., High-performance lithium battery anodes using silicon nanowires. *Nat Nano* **2008**, *3* (1), 31-35.
9. Yoo, H.; Lee, J.-I.; Kim, H.; Lee, J.-P.; Cho, J.; Park, S., Helical silicon/silicon oxide core-shell anodes grown onto the surface of bulk silicon. *Nano letters* **2011**, *11* (10), 4324-4328.
10. Park, M.-H.; Kim, M. G.; Joo, J.; Kim, K.; Kim, J.; Ahn, S.; Cui, Y.; Cho, J., Silicon nanotube battery anodes. *Nano Letters* **2009**, *9* (11), 3844-3847.
11. Kim, H.; Han, B.; Choo, J.; Cho, J., Three-dimensional porous silicon particles for use in high-performance lithium secondary batteries. *Angewandte Chemie* **2008**, *120* (52), 10305-10308.
12. Aricò, A. S.; Bruce, P.; Scrosati, B.; Tarascon, J.-M.; Van Schalkwijk, W., Nanostructured materials for advanced energy conversion and storage devices. *Nature materials* **2005**, *4* (5), 366-377.
13. Guo, Y. G.; Hu, J. S.; Wan, L. J., Nanostructured materials for electrochemical energy conversion and storage devices. *Advanced materials* **2008**, *20* (15), 2878-2887.
14. Wang, Y.; Li, H.; He, P.; Hosono, E.; Zhou, H., Nano active materials for lithium-ion batteries. *Nanoscale* **2010**, *2* (8), 1294-1305.
15. Rolison, D. R.; Long, J. W.; Lytle, J. C.; Fischer, A. E.; Rhodes, C. P.; McEvoy, T. M.; Bourg, M. E.; Lubers, A. M., Multifunctional 3D nanoarchitectures for energy storage and conversion. *Chemical Society reviews* **2009**, *38* (1), 226-252.

16. Taberna, P. L.; Mitra, S.; Poizot, P.; Simon, P.; Tarascon, J. M., High rate capabilities Fe₃O₄-based Cu nano-architected electrodes for lithium-ion battery applications. *Nature materials* **2006**, *5* (7), 567-573.
17. Chen, X.; Gerasopoulos, K.; Guo, J.; Brown, A.; Wang, C.; Ghodssi, R.; Culver, J. N., A Patterned 3D Silicon Anode Fabricated by Electrodeposition on a Virus-Structured Current Collector. *Advanced Functional Materials* **2011**, *21* (2), 380-387.
18. Kim, J.-H.; Myung, S.-T.; Sun, Y.-K., Molten salt synthesis of LiNi_{0.5}Mn_{1.5}O₄ spinel for 5 V class cathode material of Li-ion secondary battery. *Electrochimica Acta* **2004**, *49* (2), 219-227.
19. Whitehead, A. H.; Schreiber, M., Current collectors for positive electrodes of lithium-based batteries. *Journal of The Electrochemical Society* **2005**, *152* (11), A2105-A2113.
20. Zhang, H.; Yu, X.; Braun, P. V., Three-dimensional bicontinuous ultrafast-charge and-discharge bulk battery electrodes. *Nature nanotechnology* **2011**, *6* (5), 277-281.
21. Hu, L.; Wu, H.; Gao, Y.; Cao, A.; Li, H.; McDough, J.; Xie, X.; Zhou, M.; Cui, Y., Silicon–Carbon Nanotube Coaxial Sponge as Li-Ion Anodes with High Areal Capacity. *Advanced Energy Materials* **2011**, *1* (4), 523-527.
22. Guo, J.; Wang, C., A polymer scaffold binder structure for high capacity silicon anode of lithium-ion battery. *Chem. Commun.* **2010**, *46* (9), 1428-1430.
23. Yao, M.; Okuno, K.; Iwaki, T.; Kato, M.; Tanase, S.; Emura, K.; Sakai, T., LiFePO₄-based electrode using micro-porous current collector for high power lithium ion battery. *Journal of Power Sources* **2007**, *173* (1), 545-549.
24. Yu, Y.; Chen, C. H.; Shui, J. L.; Xie, S., Nickel-Foam-Supported Reticular CoO–Li₂O Composite Anode Materials for Lithium Ion Batteries. *Angewandte Chemie International Edition* **2005**, *44* (43), 7085-7089.
25. Ji, H.; Zhang, L.; Pettes, M. T.; Li, H.; Chen, S.; Shi, L.; Piner, R.; Ruoff, R. S., Ultrathin graphite foam: a three-dimensional conductive network for battery electrodes. *Nano letters* **2012**, *12* (5), 2446-2451.
26. Ergang, N. S.; Lytle, J. C.; Lee, K. T.; Oh, S. M.; Smyrl, W. H.; Stein, A., Photonic Crystal Structures as a Basis for a Three-Dimensionally Interpenetrating Electrochemical-Cell System. *Advanced materials* **2006**, *18* (13), 1750-1753.
27. Fischer, A. E.; Pettigrew, K. A.; Rolison, D. R.; Stroud, R. M.; Long, J. W., Incorporation of homogeneous, nanoscale MnO₂ within ultraporous carbon structures via self-limiting electroless deposition: implications for electrochemical capacitors. *Nano Letters* **2007**, *7* (2), 281-286.
28. Arthur, T. S.; Bates, D. J.; Cirigliano, N.; Johnson, D. C.; Malati, P.; Mosby, J. M.; Perre, E.; Rawls, M. T.; Prieto, A. L.; Dunn, B., Three-dimensional electrodes and battery

- architectures. *Mrs Bulletin* **2011**, 36 (07), 523-531.
29. Oudenhoven, J. F. M.; Baggetto, L.; Notten, P. H. L., All-Solid-State Lithium-Ion Microbatteries: A Review of Various Three-Dimensional Concepts. *Advanced Energy Materials* **2011**, 1 (1), 10-33.
 30. Golodnitsky, D.; Nathan, M.; Yufit, V.; Strauss, E.; Freedman, K.; Burstein, L.; Gladkikh, A.; Peled, E., Progress in three-dimensional (3D) Li-ion microbatteries. *Solid State Ionics* **2006**, 177 (26), 2811-2819.
 31. Kotobuki, M.; Suzuki, Y.; Munakata, H.; Kanamura, K.; Sato, Y.; Yamamoto, K.; Yoshida, T., Fabrication of three-dimensional battery using ceramic electrolyte with honeycomb structure by sol-gel process. *Journal of The Electrochemical Society* **2010**, 157 (4), A493-A498.
 32. Valvo, M.; Roberts, M.; Oltean, G.; Sun, B.; Rehnlund, D.; Brandell, D.; Nyholm, L.; Gustafsson, T.; Edström, K., Electrochemical elaboration of electrodes and electrolytes for 3D structured batteries. *Journal of Materials Chemistry A* **2013**, 1 (32), 9281-9293.
 33. Duffy, D. C.; McDonald, J. C.; Schueller, O. J. A.; Whitesides, G. M., Rapid Prototyping of Microfluidic Systems in Poly(dimethylsiloxane). *Analytical Chemistry* **1998**, 70 (23), 4974-4984.
 34. Takamura, T.; Uehara, M.; Suzuki, J.; Sekine, K.; Tamura, K., High capacity and long cycle life silicon anode for Li-ion battery. *Journal of power sources* **2006**, 158 (2), 1401-1404.
 35. Xu, W.; Canfield, N. L.; Wang, D.; Xiao, J.; Nie, Z.; Li, X. S.; Bennett, W. D.; Bonham, C. C.; Zhang, J.-G., An approach to make macroporous metal sheets as current collectors for lithium-ion batteries. *Journal of The Electrochemical Society* **2010**, 157 (7), A765-A769.
 36. Choi, S.; Lee, J.-I.; Park, S., Patterning of electrodes for mechanically robust and bendable lithium-ion batteries. *J. Mater. Chem.* **2012**, 22 (42), 22366-22369.
 37. Zadin, V.; Kasemägi, H.; Aabloo, A.; Brandell, D., Modelling electrode material utilization in the trench model 3D-microbattery by finite element analysis. *Journal of Power Sources* **2010**, 195 (18), 6218-6224.
 38. Zadin, V.; Brandell, D., Modelling polymer electrolytes for 3D-microbatteries using finite element analysis. *Electrochimica Acta* **2011**, 57, 237-243.
 39. Lee, M.-H.; Kim, T.-H.; Kim, Y. S.; Song, H.-K., Precipitation revisited: shape control of LiFePO₄ nanoparticles by combinatorial precipitation. *The Journal of Physical Chemistry C* **2011**, 115 (25), 12255-12259.

* Chapter IV is reproduced in with a permission of “S. Choi, T. -H. Kim, J. -I. Lee, J. Kim, H. -K. Song, S. Park, General Approach for High-Power Li-Ion Batteries : Multiscale Lithographic Patterning of Electrodes. *ChemSusChem* 2014”. Copyright **2014** Wiley & Sons, Inc.

Chapter V. Micro-assembled Si / Titanium Silicide Nanotube Anodes for High-performance Lithium-Ion Batteries

5.1. Introduction

Carbonaceous anode materials are most widely used in lithium ion batteries (LIBs), owing to their stable reversible capacity and good cycling performance. However, since the rapid development of electronic devices and electric vehicles which demand a much higher energy and/or power density, the development of alternative anode materials having higher gravimetric and volumetric capacity than carbonaceous materials is urgently required.¹⁻³ Therefore, various high capacity materials (e.g., Al, Si, Ge, Sn, Sb, and Bi, and their alloys) have been intensively studied as promising anode materials in LIBs.⁴⁻⁶ Among them, Si exhibits the highest theoretical gravimetric capacity of 3750 mAh g⁻¹ (10 times higher than that of commercially available natural graphite) at room temperature and moderate electrochemical potential versus Li/Li⁺.⁷ However, the practical application of Si anodes is still hindered due to the rapid capacity fading caused by large volume changes (>300%) during the lithium insertion / extraction process and its low intrinsic electrical conductivity.⁴ Numerous approaches have been developed to accommodate the large volume change of Si by controlling structures (e.g., nanoparticles, nanowires, nanotubes, hollows, etc.) and introducing coating layers such as carbon, metal oxides, and conducting polymers.⁸⁻¹⁰ Nanostructuring of active materials showed enhanced charging and discharging kinetics, high specific capacity, and good cycling performance in LIBs. However, the nanostructured materials suffer from low energy density, surface side reactions, and high cost for practical applications.⁸⁻¹⁰ Appropriate combination of micro- and nanoscale materials is necessary to design high performance anode materials, since micro-sized materials show advantages, like easy processing and increasing energy density, while nanoscale provides enhanced surface kinetics and alleviation of large stress during cycling.^{11,12} According to the spatial locations of nanoscale and microscale materials, several micro-/nanoscale hybrid materials have been reported, including nanoscale coating of microscale active materials,^{11,12} and nanomaterials dispersed in a microscale matrix.¹³⁻¹⁵ One of the simple methods to make micro- or nanostructured materials is to use micro-assembly by employing one-dimensional (1D) templates. As a representative example, 1D carbon-based materials have been used as templates to make secondary target materials.^{16,17}

Here, we present a simple route for synthesizing high performance Si/titanium silicide (Si/Ti_xSi_y) nanotube anode materials using a magnesiothermic reduction process of micro-assembled CNT/silica and CNT/titania/silica particles. During the reduction reaction, various materials are formed at the interface between CNT and Si, and affect the electrochemical performance of the micro-assembled Si-based nanotube anodes. Mechanically robust, electrically conductive titanium silicide-containing Si nanotube electrodes exhibit a significantly improved electrochemical performance.

5.2. Experimental

5.2.1. Synthesis of CNT@Si and Si, Si@Ti_xSi_y Nanotube Structure

Pristine multi-walled carbon nanotubes (MWCNTs, with an average outer diameter of 15 nm) were purified in a concentrated sulfuric acid, producing functional groups (e.g., -COOH, -OH, and C=O) on the CNT surface. The functionalized CNTs were ultrasonically dispersed into a fixed volume mixture of ethanol (200 mL) and NH₄OH (12 mL, 25.0–28.0 wt%) for 30 min, followed by vigorous mechanical agitation for another 15 min to obtain a stable and homogeneous suspension. Afterwards, appropriate amount of tetraethoxysilane (TEOS) was added to achieve the desired volume ratio of TEOS with respect to ethanol, and kept for 6 h under stirring. The whole reaction was carried out at room temperature. After the reaction, the mixture was centrifuged at a moderate speed (3500 rpm). The darkish product was dried in a vacuum to yield silica-coated CNTs (CNT@SiO₂). The CNT@SiO₂ was sintering at 450°C for 1 h under an argon atmosphere to remove water and enhance structure stability of silica shell. As another silica templates, TiO₂ layers were introduced between CNT and SiO₂ to make CNT@TiO₂@SiO₂. 0.2 mL of titanium tetrabutoxide and 0.2 mL of H₂O were refluxed in ethylene glycol/ethanol (16 mL/4 mL) at 80°C for 6 h in the presence of 0.1 g CNT. The CNT@SiO₂ and CNT@TiO₂@SiO₂ particles were transformed to Si based nanotubes via a magnesiothermic reduction process at 700 °C for 3 h. Subsequently, magnesium oxide (MgO) by-products formed during the reduction reaction was removed by 1 M hydrochloric acid (HCl) solution.

5.2.2. Characterization of Materials

The crystal structures of CNT@SiC@Si, Si nanotube and Ti_xSi_y@Si nanotube powders were measured by a XRD on a Rigaku D/MAX at 2500 V using Cu_{Kα} radiation. The transmission electron microscopy (TEM) was used to observe the nanotube using JEM-2100 (JEOL) operating at an accelerating voltage of 200 kV. The surface of Si-based nanotubes were characterized by a scanning electron microscopy (Nano - SEM 230, FEI) operating at 10 kV with a 3 nm thick Pt coating layer.

5.2.3. Electrochemical Test

Electrochemical test was performed using coin-type half cells (2016 R-type) assembled in an argon-filled glove box. CNT@SiC@Si, Si nanotube and Ti_xSi_y@Si nanotube powders as the working electrode and lithium metal as counter electrode were used. The electrode for the cell test was made of Si-based active material (60 wt%), super P carbon black (20 wt%), and poly(acrylic acid)/sodium carboxymethyl cellulose (50 : 50, wt/wt) binder (20 wt%). The electrolyte was LiPF₆ (1.3 M) with ethylene carbonate/diethyl carbonate (EC/DEC = 30/70 (v/v), Panax starlyte, Korea). The coin-type half cells were cycled at a rate of 0.1–5C between 0.01 and 1.2 V. The loading amount of active materials was ~1.5 mg cm⁻² and thickness of electrode was ~30 μm.

5.3. Result and discussion

5.3.1. Morphologies of Si-Based Materials

Multi-walled CNTs having diameters of 10–20 nm can be used as templates or scaffolds to make tubular-shaped inorganic materials, like silica (SiO₂) and titania (TiO₂).¹⁷ Since most inorganic precursors do not wet on the surface of hydrophobic CNTs due to a huge difference of surface energy, the CNT surface should be oxidized in a strong acid to improve the wettability between CNT and inorganic precursors.¹⁸ In this study, we employed tetraethoxysilane (TEOS) as silica precursor to synthesize micro-assembled SiO₂-coated CNTs (CNT@SiO₂). Afterwards, the SiO₂ was transformed into Si via a magnesiothermic reduction process to test the electrochemical properties of the Si-coated CNT (CNT@Si) (schematic illustration in Figure 5. 1).

A transmission electron microscopy (TEM) image of acid-treated CNTs shows that the CNTs have 10–20 nm diameters and lengths of a few micrometers (Figure 5. 1a). When 9 mL of TEOS and 12 mL of NH₄OH were added to ethanol solution in the presence of 0.2 g CNTs, amorphous SiO₂ layers were conformally coated on the CNT surface in the range of 15–20 nm thickness (inset of Figure 5. 1b). Energy dispersive X-ray spectroscopy (EDAX) results indicate that 27 wt% SiO₂ layers are coated on the CNT surface. During the SiO₂ coating, the CNT@SiO₂ is self-assembled to make a micron-scale assembly due to a strong tendency of SiO₂ aggregation during the conversion reaction of TEOS to SiO₂ in the presence of NH₄OH catalyst (Figure 5. 1b). By controlling the relative amount of TEOS to NH₄OH, the thickness of the SiO₂ layer can be tuned (Figure 5. 2).

To synthesize Si-based anode materials for LIBs, the micro-assembled CNT@SiO₂ were converted to CNT@Si using a shape-preserving magnesiothermic reduction process (Figure 5. 1c). The magnified SEM image shows that CNT@Si nanotubes are clearly seen on the outer layer of the micro-assembled particles (inset of Figure 5. 1c). When amorphous SiO₂ reacts with Mg vapor (at well above the melting temperature of Mg) under inert gas, the SiO₂ is transformed into Si with MgO by-products in the following well-known chemical reaction: $2\text{Mg}(\text{g}) + \text{SiO}_2(\text{s}) \rightarrow 2\text{MgO}(\text{s}) + \text{Si}(\text{s})$.¹⁹ Magnesiothermic reaction leads to successful conversion of micro-assembled CNT@SiO₂ to CNT@Si without perturbing the original structures (Figure 5. 1c). The void space of micro-assembled CNT@SiO₂ after reduction reaction led to the formation of porous regions in the micro-assembled CNT@Si. These porous structures may ensure good electrochemical performances of Si-based anodes because empty spaces can lessen the volume change of Si anode materials during the lithiation/delithiation process.²⁰

The XRD pattern of as-synthesized CNT@Si after dissolving MgO by-products is shown in Figure 5. 3. As expected, crystalline Si was prepared by the reduction reaction of CNT@SiO₂. Interestingly, SiC peaks are observed in the final products. Typically, SiC is formed by high temperature reaction (>1000 °C) of carbon and silicon,²¹ but SiC can be produced even at low temperature (<750 °C) with additional heat generation. Recently, Shi et al. reported a low temperature (600–700 °C) synthesis of

crystalline SiC via magnesiothermic reduction of SiO₂ as silicon source and pluronic surfactant as carbon source. The overall reaction can be described as the following reaction: SiO₂(s) + C(s) + 2Mg(g) / SiC(s) + 2MgO(s).²² Similarly, we observed the formation of SiC through magnesiothermic reaction of CNT (as carbon source) and SiO₂ (as Si source) at 700 °C (Figure 5. 3). However, the formation of insulating SiC layers at the interface between Si and CNT may act as side reactions in LIBs. Lipson et al. reported the electrochemical lithiation of crystalline SiC materials and the Li ions trapped in the SiC were not delithiated.²³

In order to prevent the formation of SiC layers, we used two different simple strategies for synthesizing Si particles without SiC during the magnesiothermic reaction. One method is to remove the CNT (carbon source material) after making micro-assembled CNT/SiO₂ particles. The other process is to insert TiO₂ layers between CNT and SiO₂ and subsequently conduct the magnesiothermic reduction process.

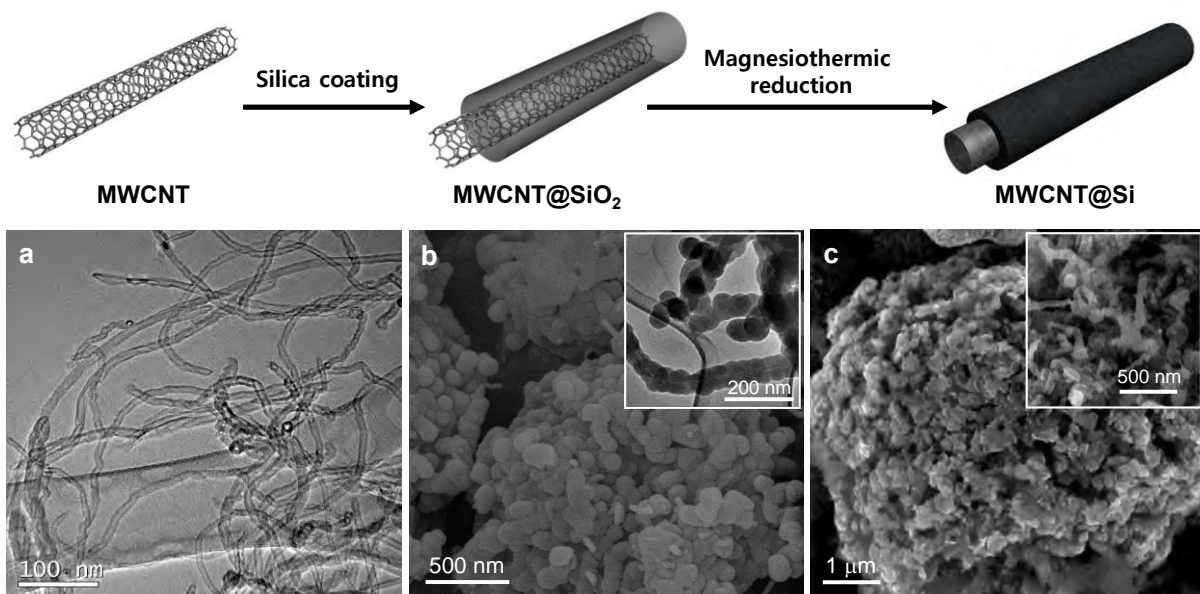


Figure 5. 1 Top: schematic illustration showing the synthetic process of Si-coated CNTs. Bottom: (a) TEM image of oxidized CNTs, (b) SEM image of micro-assembled SiO₂-coated CNTs, and (c) SEM image showing shape-preserving Si-coated CNTs.

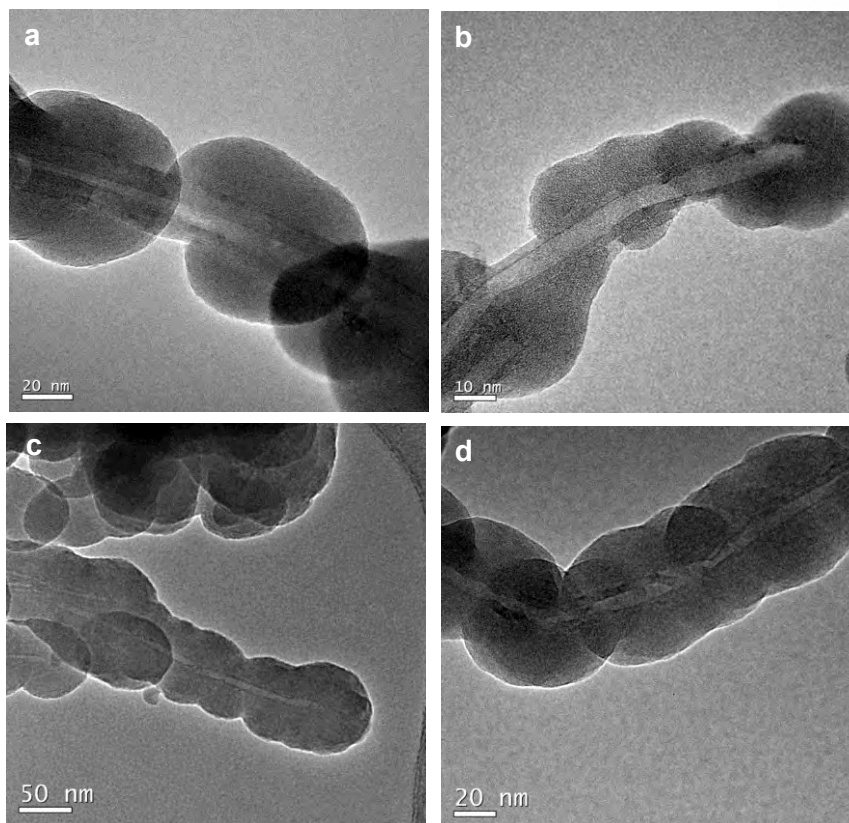


Figure 5. 2 Control of SiO₂ layer thickness by volumetric ratio of NH₄OH and TEOS. (a) NH₄OH /TEOS = 16 mL/9mL, (b) NH₄OH /TEOS = 8mL/9mL, (c) NH₄OH /TEOS = 12 mL/12 mL, and (d) NH₄OH /TEOS = 12 mL/9 mL.

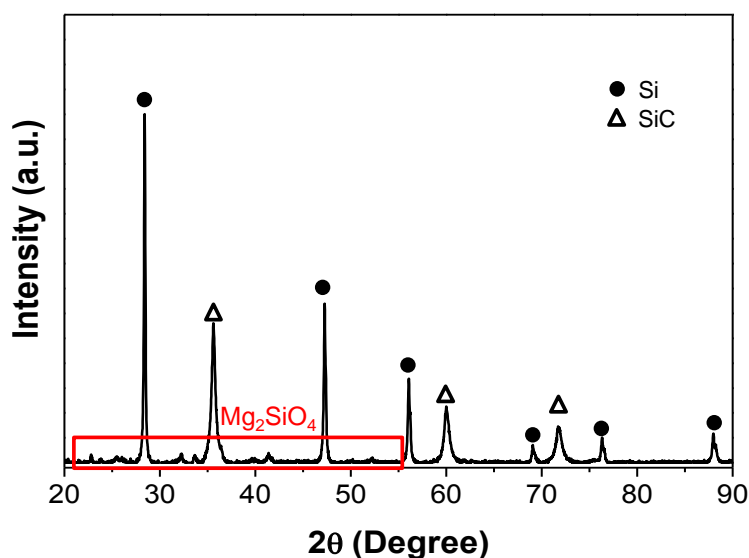


Figure 5. 3 XRD patterns of as-synthesized CNT@SiC@Si prepared by a magnesiothermic reduction of SiO₂-coated CNTs. During the magnesiothermic reaction, SiC was formed at the interface between CNT and Si due to additional reaction of carbon source, CNT, and Si. Solid circle and triangle represent crystalline Si and SiC, respectively. Small peaks represent Mg₂SiO₄ by-products.

As the first process, the SiO₂ coated CNTs were calcined at 600 °C for 1 h in air environment to remove the CNT and to make SiO₂ nanotubes. Afterwards, the SiO₂ nanotubes were transformed into Si via a magnesiothermic reduction process (schematic illustration in Figure 5. 4).

Morphologies of micro-assembled SiO₂ nanotubes after removing CNTs are similar to the pristine CNT@SiO₂ structures seen in Figure 5. 1b (Figure 5. 4a). Subsequent chemical reduction of the SiO₂ nanotubes leads to the formation of shape-preserving micro-assembled Si nanotubes (Figure 5. 4b). As expected, pure crystalline Si was synthesized by the chemical reduction of SiO₂ nanotubes. When we measured the XRD of as-synthesized Si nanotubes after dissolving MgO by-products, XRD patterns of typical crystalline Si were obtained, while SiC peaks were not observed due to the absence of CNTs. Before the electrochemical test of the CNT@SiC@Si electrodes, a typical carbon coating process, which plays an important role in exhibiting stable cycling performance by forming a stable solid–electrolyte interphase (SEI) layer, was conducted.⁴ Thermal decomposition of acetylene gas (at 750 °C for 10 min) was used to coat a carbon layer on the surface of micro-assembled CNT@SiC@Si. The carbon contents of 8 wt% were characterized by elemental analysis. Figure 5. 5a shows the first cycle voltage profiles (discharging (lithiation) and charging (delithiation)) of the carbon-coated CNT@SiC@Si electrodes at a rate of C/10 in the range of 0.01–1.2 V. The first discharge capacity was 1180 mA h g⁻¹ with a fairly low initial coulombic efficiency of 54.2%, even though the carbon layers are introduced on the Si surface (Figure 5. 5a). It may be explained as follows: (i) SiC layers lead to a serious irreversible capacity, as mentioned before; (ii) multi-walled CNTs typically show a huge irreversible capacity; (iii) the use of high temperature (750 °C) during the carbon coating process promotes the formation of SiC layers, resulting in an increase of SiC content. However, after the first cycle, cycling performances are significantly improved due to the formation of stable SEI layers on the carbon-coated Si surface.²⁴ After 50 cycles, highly stable capacity retention of >98% was exhibited (Figure 5. 5c).

To investigate the effect of SiC layers on the electrochemical performances, carbon-coated Si nanotubes without SiC layers were used as anode materials. Morphologies of the carbon coated Si nanotubes are similar to those of SiC@Si particles (Figure 5. 6). Figure 5. 5b shows the voltage curves of the carbon coated Si nanotube anodes during the first cycle at a rate of C/10 in the range of 0.01–1.2 V. The first discharge and charge capacities are 2604 and 1937 mA h g⁻¹, respectively, corresponding to the coulombic efficiency of 74.4% (Figure 5. 5b). As expected, the absence of SiC layers led to a significant enhancement of the coulombic efficiency. Moreover, the Si nanotube electrodes showed a high specific capacity of 1720 mA h g⁻¹ at a rate of C/5 after 50 cycles and a stable cycling performance (>98% after 50 cycles compared to the second cycle at a rate of C/5) (Figure 5. 5d). Since Si nanotube electrodes do not contain CNT and SiC layers (seen in CNT@SiC@Si), a lithium storage capacity of nanostructured Si particles (>1500 mA h g⁻¹) is exhibited.²⁻⁴

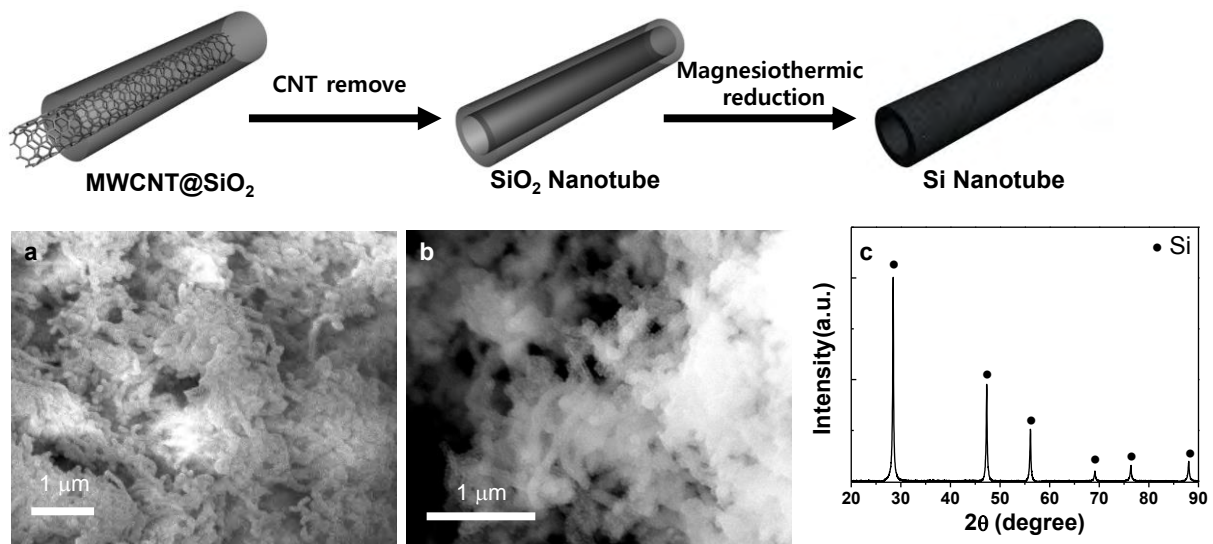


Figure. 5. 4 Top: schematic illustration showing the synthetic process of Si nanotube. Bottom: SEM images of (a) micro-assembled SiO₂ nanotubes and (b) shape-preserving Si nanotubes. (c) XRD pattern of as-synthesized Si nanotubes prepared by a magnesiothermic reduction of SiO₂ nanotubes.

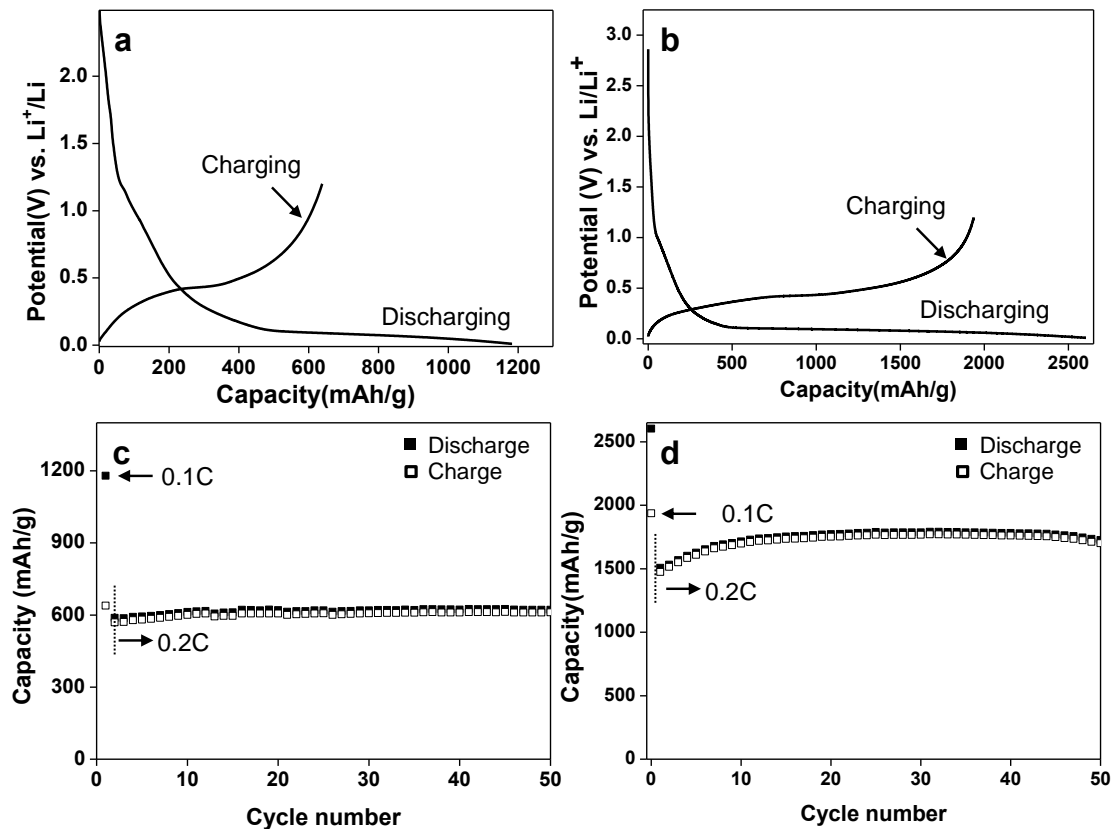


Figure 5. 5 Electrochemical performances of CNT@SiC@Si three-component and silicon nanotube electrodes. The first cycle voltage profiles of (a) carbon-coated CNT@SiC@Si and (b) carbon-coated Si nanotube electrodes were obtained at a rate of $C/10$. The cycle performances of (c) carbon coated CNT@SiC@Si and (d) carbon-coated Si nanotube electrodes were tested at rates of $C/10$ (first cycle) and $C/5$ (second–fiftieth cycles).

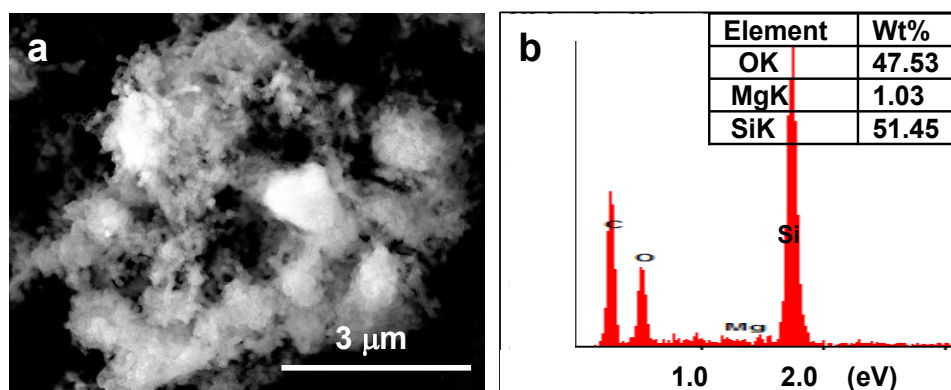


Figure 5. 6 (a) SEM images and (b) EDAX profile of carbon-coated Si nanotubes.

5.3.2. Characterization of Si-Based Nanotube with Titanium

Moreover, we introduced a TiO_2 layer at the interface between CNT and SiO_2 layers to investigate the effect of an additional interfacial layer (TiO_2) on the electrochemical performances of the final Si-based electrodes obtained by chemical reduction (scheme in Figure 5. 7). Firstly, 4 wt% TiO_2 was coated on the CNT surface by controlling the hydrolysis of titanium precursors. A magnified TEM image shows that the amorphous TiO_2 layers were conformally coated on the CNT surface in the range of 2–5 nm thickness (inset of Figure 5. 7a). It should be noted that thin TiO_2 -coated CNT was not aggregated, but subsequent thick SiO_2 coating induced micron-scale assembly (Figure 5. 8). Secondly, after drying the sample, 27 wt% SiO_2 layers (200–400 nm thick) were coated on the surface of TiO_2 -coated CNTs to make micro-assembled $\text{CNT@TiO}_2@\text{SiO}_2$. It should be noted that TiO_2 -coated CNTs should be calcined at 400 °C for 1 h in argon environment before the SiO_2 coating. Otherwise, TiO_2 and SiO_2 phases were mixed together to make $\text{TiO}_2/\text{SiO}_2$ composites. In the final step, the $\text{CNT@TiO}_2@\text{SiO}_2$ reacted with Mg vapor at 700 °C for 3 h to synthesize $\text{CNT@TiC/Ti}_x\text{Si}_y@\text{Si}$ (Figure 5. 9).

Since TiC exhibits high electrical conductivity (0.003–0.008 Ω m) and a high melting point (3160 °C), applications like wear resistant coating materials are desirable.²⁵ From the viewpoint of LIB anodes, the TiC materials are inactive and good electrically conductive materials so that we may expect the improvement of electrochemical properties of the $\text{CNT@TiC/Ti}_x\text{Si}_y@\text{Si}$ electrode. The XRD patterns of the $\text{CNT@TiC/Ti}_x\text{Si}_y@\text{Si}$ showed crystalline Si, TiC, Ti_xSi_y , and small amounts of Mg_2SiO_4 byproducts which may be formed by reaction of MgO and SiO_2 during the magnesiothermic reaction (Figure 5. 9).²⁶

The electrochemical properties of the carbon-coated $\text{CNT@TiC/Ti}_x\text{Si}_y@\text{Si}$ electrodes were comparable to those of carbon-coated CNT@SiC@Si electrodes. The first discharge capacity was 1056 mA h g^{-1} with a low initial coulombic efficiency of 62.9% (Figure 5. 10a). It may be attributed to the presence of CNTs and the formation of Mg_2SiO_4 by-products which can react with lithium ions.²⁵ However, the cycling performances of the carbon-coated $\text{CNT@TiC/Ti}_x\text{Si}_y@\text{Si}$ electrode are highly stable (capacity retention of >99% after 50 cycles compared to the second cycle at a rate of C/5) (Figure 5. 10b). This result suggests that the materials located at the interface between CNT and Si play an important role in determining the electrochemical properties of Si-based anodes.

We revisited the CNT removal process to further increase the initial coulombic efficiency and cycling life of micro-assembled Si-based electrodes. At first, the $\text{CNT@TiO}_2@\text{SiO}_2$ sample was calcined at 600 °C for 1h in air environment to make micro-assembled $\text{TiO}_2@\text{SiO}_2$ nano-tubular structures. Subsequently, the as-synthesized $\text{TiO}_2@\text{SiO}_2$ nanotubes were transformed into $\text{Ti}_x\text{Si}_y@\text{Si}$ nanotubes via a magnesiothermic reduction process (schematic illustration in Figure 5. 7).

The XRD patterns of the $\text{Ti}_x\text{Si}_y@\text{Si}$ -NT after dissolving MgO by-products show that crystalline Si (major component) and Ti_xSi_y (minor components) are detected (Figure 5. 7c). The morphologies of

the $\text{Ti}_x\text{Si}_y@$ Si-NTs are similar to those of Si-NTs (Figure 5. 11). Since the Ti_xSi_y is light-weight, highly electrically conductive, and thermally stable, Ti_xSi_y -containing Si electrodes may exhibit significantly improved electrochemical performances.²⁷ According to the Ellingham diagram, the TiO_2 layer was firstly reduced to Ti followed by the reduction of the SiO_2 layer during the magnesiothermic reduction process.²⁸ In addition, high temperature reaction of Ti and Si produced the Ti_xSi_y (consisting of TiSi_2 , Ti_5Si_3 , and Ti_5Si_4) layer as shown by our previous report.²⁷

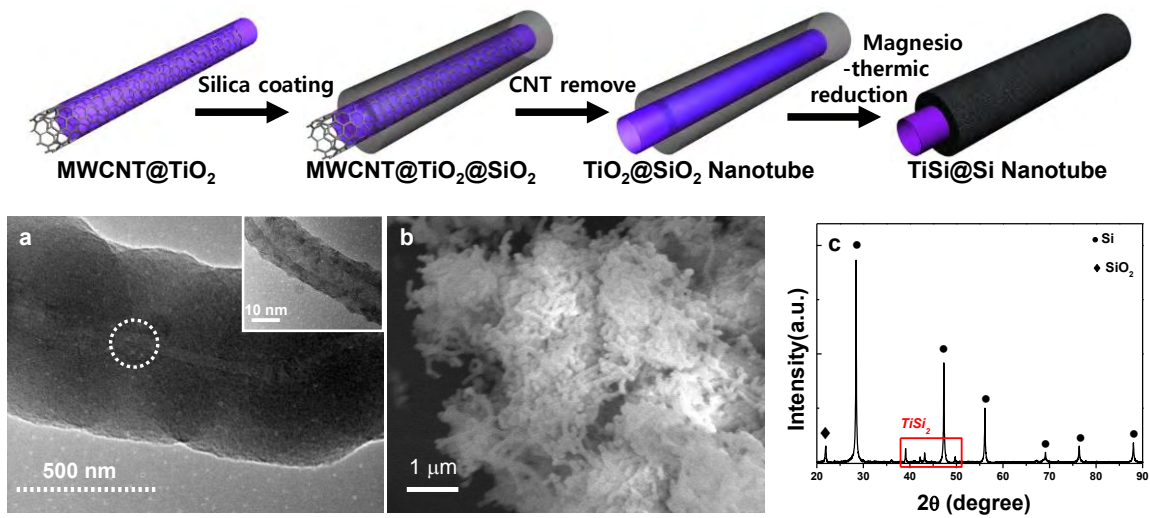


Figure 5. 7 Top: schematic illustration showing the synthetic process of micro-assembled $Ti_xSi_y@Si$ nanotubes. Bottom: (a) TEM image of micro-assembled $TiO_2@SiO_2$ nanotube. In the inset, TiO_2 coating layers on the CNT surface are clearly seen. (b) SEM image showing micro-assembled $Ti_xSi_y@Si$ nanotubes prepared by chemical reduction of $TiO_2@SiO_2$ nanotubes. (c) XRD pattern of synthesized $Ti_xSi_y@Si$ nanotubes.

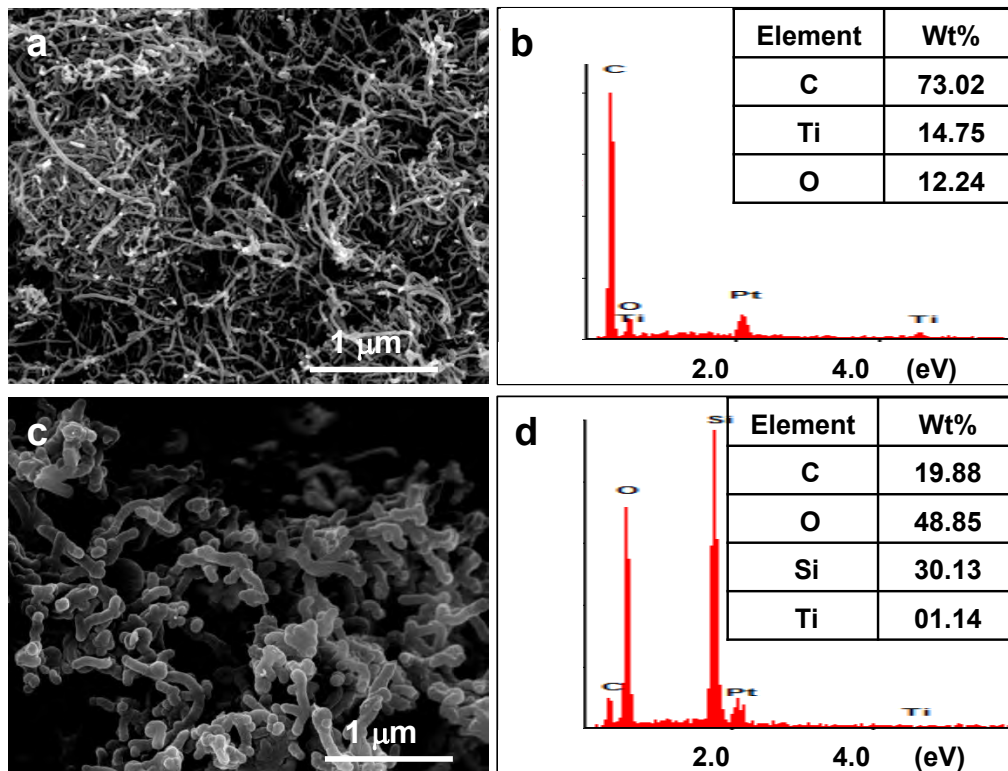


Figure 5. 8 SEM images of (a) TiO₂-coated CNT and (c) micro-assembled CNT@TiO₂@SiO₂ particles. EDAX profiles and elemental contents of (b) TiO₂-coated CNT and (d) micro-assembled CNT@TiO₂@SiO₂ particles.

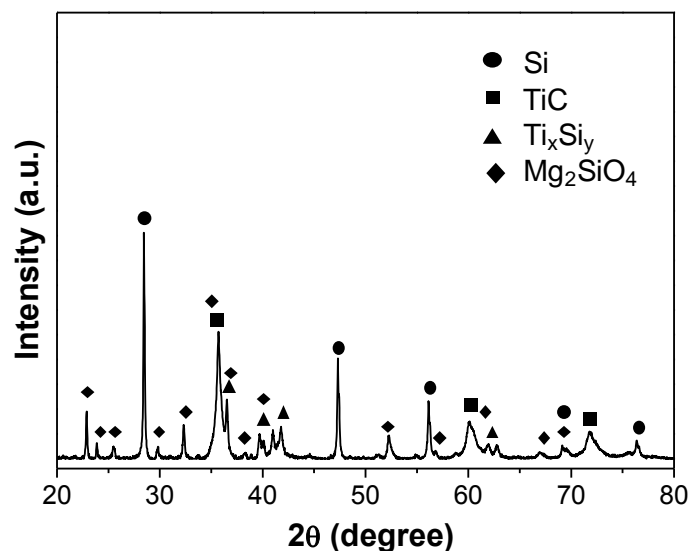


Figure 5. 9 XRD patterns of as-synthesized CNT@TiC/Ti_xSi_y@Si prepared by magnesiothermic reduction of TiO₂/SiO₂ double layer coated CNTs. During magnesiothermic reaction, TiC was formed at the interface between CNT and TiO₂ due to additional reaction of carbon source, CNT, and TiO₂ in addition Ti_xSi_y was formed at the interface between SiO₂ and TiO₂.

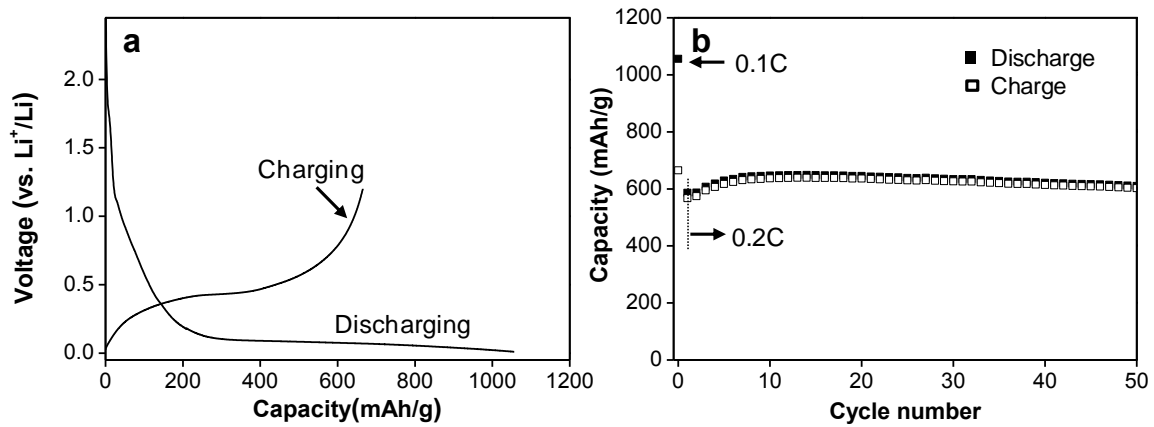


Figure 5. 10 Electrochemical properties of carbon-coated CNT@TiC/Ti_xSi_y@Si electrodes. (a) The first cycle voltage profile and (b) cycling performance of the carbon-coated CNT@TiC/Ti_xSi_y@Si electrodes was obtained in the range of 0.01-1.2 V.

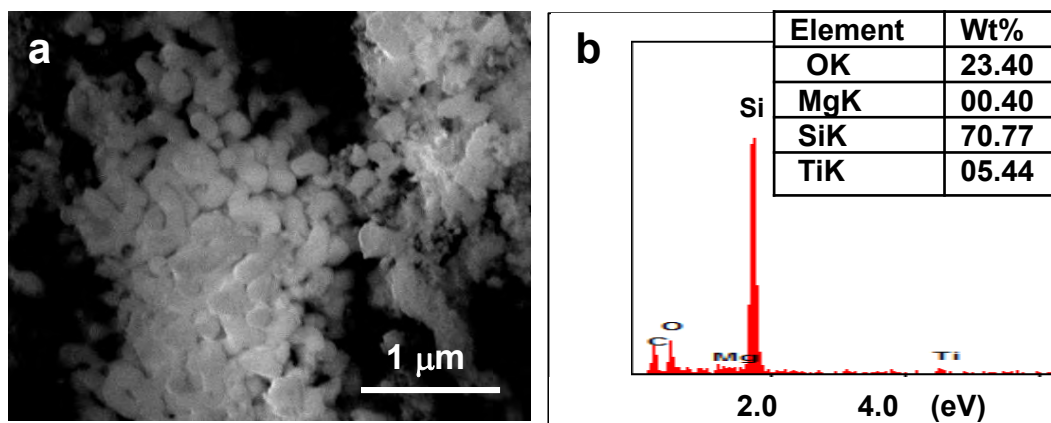


Figure 5. 11 (a) SEM image and (b) EDAX profile of carbon-coated Ti_xSi_y@Si nanotubes.

As expected, carbon-coated $\text{Ti}_x\text{Si}_y@\text{Si}$ nanotube electrodes showed a significantly improved initial coulombic efficiency. Figure 5. 12a shows the first cycle voltage profile obtained at a rate of $C/10$ in the range of 0.01 to 1.2 V. The first discharge and charge capacity are 2450 mA h g^{-1} and 1850 mA h g^{-1} , respectively, corresponding to a coulombic efficiency of 75.5%. Also, highly stable cycling performances (capacity retention of $>99\%$ after 80 cycle, compared to the second cycle) are seen in Figure 5. 12b. These improved electrochemical properties can be explained as follows: (i) the $\text{Ti}_x\text{Si}_y@\text{Si}$ nanotubes can minimize the irreversible capacity at the first cycle due to the absence of SiC, TiC and CNT layers; and (ii) mechanically robust Ti_xSi_y layers can accommodate a large volume expansion of the $\text{Ti}_x\text{Si}_y@\text{Si}$ electrodes during lithiation/delithiation, resulting in the stable cycling life.

Moreover, rate capabilities of the $\text{Ti}_x\text{Si}_y@\text{Si}$ and Si nanotube electrodes were investigated at various rates (from $C/5$ to $5C$) between 1.2 V and 0.01 V with a fixed discharge rate of $C/2$. The Si nanotube electrodes without Ti_xSi_y layers exhibited a capacity retention of 41.1% at a high rate of $5C$, compared to that of the $C/2$ rate. In contrast, the $\text{Ti}_x\text{Si}_y@\text{Si}$ nanotube electrodes showed significantly enhanced rate capabilities. Even at a high rate of $5C$, the capacity retention of the Ti_xSi_y -coated Si was 90.7% (Figure 5. 12c). When the discharge rate is varied at a fixed charge rate, similar results are observed for both electrodes (Figure 5. 12d). The Si nanotube electrodes exhibited a very poor capacity retention at a rate of $2C$, while the $\text{Ti}_x\text{Si}_y@\text{Si}$ nanotube electrode showed significantly enhanced rate capabilities (capacity retention of 58.8% at $2C$ compared to that of $C/2$ rate; Figure 5. 12d). These results suggest that the Ti_xSi_y layers play an important role in exhibiting superior electrochemical properties, including a high specific capacity, highly stable cycling, and an excellent rate capability in LIBs.²⁷

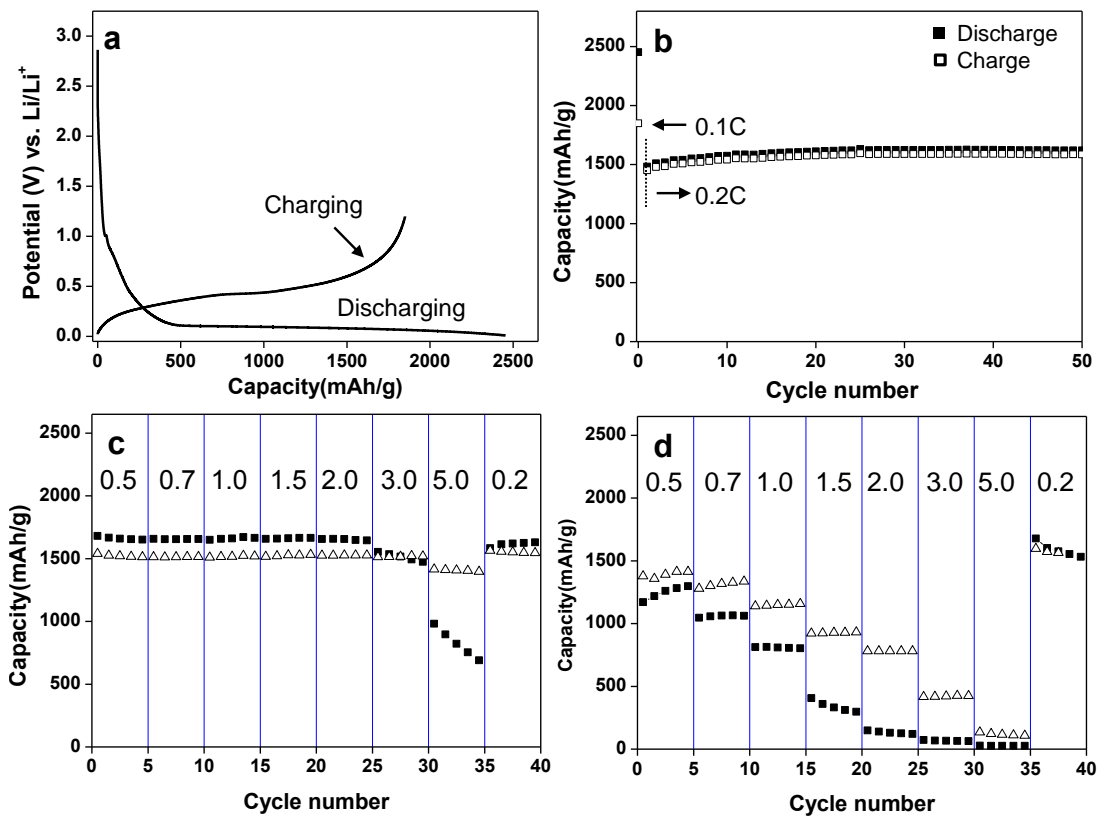


Figure 5. 12 Electrochemical performances of Si nanotube and $Ti_xSi_y@Si$ nanotube electrodes. (a) The first cycle voltage profiles and (b) cycle performance of carboncoated $Ti_xSi_y@Si$ electrodes. (c) Rate capabilities of Si nanotubes (solid squares) and $Ti_xSi_y@Si$ nanotubes (open triangles) electrodes obtained at a fixed discharge rate of $C/5$. (d) Rate capabilities of Si nanotubes (solid squares) and $Ti_xSi_y@Si$ nanotubes (open triangles) electrodes obtained at a fixed charge rate of $C/5$.

5.4. Conclusion

We successfully synthesized micro-assembled Si based nano-tubular structures via a magnesiothermic reduction reaction of SiO₂-coated CNTs and TiO₂/SiO₂-coated CNTs. By controlling the interfacial layer between CNT and SiO₂ layers, electrodes with different lithium storage capacities were fabricated. Interestingly, thermal treatment of TiO₂/SiO₂-coated CNTs before the magnesiothermic reduction process prevented the formation of SiC and TiC layers, resulting in significant enhancement of the initial coulombic efficiency and a reversible capacity. The suitable design of CNT/Si-based anode materials played an important role in determining the electrochemical performances.

5.5. References

1. Tarascon, J.-M.; Armand, M., Issues and challenges facing rechargeable lithium batteries. *Nature* **2001**, *414* (6861), 359-367.
2. Song, M.-K.; Park, S.; Alamgir, F. M.; Cho, J.; Liu, M., Nanostructured electrodes for lithium-ion and lithium-air batteries: the latest developments, challenges, and perspectives. *Materials Science and Engineering: R: Reports* **2011**, *72* (11), 203-252.
3. Liu, C.; Li, F.; Ma, L.-P.; Cheng, H.-M., Advanced Materials for Energy Storage. *Advanced materials* **2010**, *22* (8), E28-E62.
4. Kasavajjula, U.; Wang, C.; Appleby, A. J., Nano-and bulk-silicon-based insertion anodes for lithium-ion secondary cells. *Journal of Power Sources* **2007**, *163* (2), 1003-1039.
5. Zhang, W.-J., A review of the electrochemical performance of alloy anodes for lithium-ion batteries. *Journal of Power Sources* **2011**, *196* (1), 13-24.
6. Hatchard, T.; Dahn, J., In situ XRD and electrochemical study of the reaction of lithium with amorphous silicon. *Journal of The Electrochemical Society* **2004**, *151* (6), A838-A842.
7. Kim, M. G.; Cho, J., Reversible and High-Capacity Nanostructured Electrode Materials for Li-Ion Batteries. *Advanced Functional Materials* **2009**, *19* (10), 1497-1514.
8. Manthiram, A.; Murugan, A. V.; Sarkar, A.; Muraliganth, T., Nanostructured electrode materials for electrochemical energy storage and conversion. *Energy & Environmental Science* **2008**, *1* (6), 621-638.
9. Bruce, P. G.; Scrosati, B.; Tarascon, J. M., Nanomaterials for rechargeable lithium batteries. *Angewandte Chemie International Edition* **2008**, *47* (16), 2930-2946.
10. Zhang, H.-L.; Liu, S.-H.; Li, F.; Bai, S.; Liu, C.; Tan, J.; Cheng, H.-M., Electrochemical performance of pyrolytic carbon-coated natural graphite spheres. *Carbon* **2006**, *44* (11), 2212-2218.
11. Hu, Y. S.; Guo, Y. G.; Dominko, R.; Gaberscek, M.; Jamnik, J.; Maier, J., Improved electrode performance of porous LiFePO₄ using RuO₂ as an oxidic nanoscale interconnect. *Advanced materials* **2007**, *19* (15), 1963-1966.
12. Saint, J.; Morcrette, M.; Larcher, D.; Laffont, L.; Beattie, S.; Pérès, J. P.; Talaga, D.; Couzi, M.; Tarascon, J. M., Towards a fundamental understanding of the improved electrochemical performance of silicon-carbon composites. *Advanced Functional Materials* **2007**, *17* (11), 1765-1774.
13. Hu, Y. S.; Demir-Cakan, R.; Titirici, M. M.; Müller, J. O.; Schlögl, R.; Antonietti, M.; Maier, J., Superior Storage Performance of a Si@ SiO_x/C Nanocomposite as Anode Material for Lithium-Ion Batteries. *Angewandte Chemie International Edition* **2008**, *47* (9), 1645-1649.
14. Lee, J. I.; Lee, K. T.; Cho, J.; Kim, J.; Choi, N. S.; Park, S., Chemical-Assisted Thermal

- Disproportionation of Porous Silicon Monoxide into Silicon-Based Multicomponent Systems. *Angewandte Chemie* **2012**, *124* (11), 2821-2825.
15. Yoo, J. K.; Kim, J.; Jung, Y. S.; Kang, K., Scalable fabrication of silicon nanotubes and their application to energy storage. *Advanced materials* **2012**, *24* (40), 5452-5456.
 16. Cao, F.-F.; Guo, Y.-G.; Wan, L.-J., Better lithium-ion batteries with nanocable-like electrode materials. *Energy & Environmental Science* **2011**, *4* (5), 1634-1642.
 17. Pfeiffer, H.; Tancret, F.; Bichat, M.-P.; Monconduit, L.; Favier, F.; Brousse, T., Air stable copper phosphide (Cu₃P): a possible negative electrode material for lithium batteries. *Electrochemistry communications* **2004**, *6* (3), 263-267.
 18. Bao, Z. H.; Weatherspoon, M. R.; Shian, S.; Cai, Y.; Graham, P. D.; Allan, S. M.; Ahmad, G.; Dickerson, M. B.; Church, B. C.; Kang, Z. T.; Abernathy, H. W.; Summers, C. J.; Liu, M. L.; Sandhage, K. H., Chemical reduction of three-dimensional silica micro-assemblies into microporous silicon replicas. *Nature* **2007**, *446* (7132), 172-175.
 19. Bang, B. M.; Lee, J. I.; Kim, H.; Cho, J.; Park, S., High-Performance Macroporous Bulk Silicon Anodes Synthesized by Template-Free Chemical Etching. *Advanced Energy Materials* **2012**, *2* (7), 878-883.
 20. Sung, I. K.; Mitchell, M.; Kim, D. P.; Kenis, P. J., Tailored Macroporous SiCN and SiC Structures for High-Temperature Fuel Reforming. *Advanced Functional Materials* **2005**, *15* (8), 1336-1342.
 21. Shi, Y.; Zhang, F.; Hu, Y.-S.; Sun, X.; Zhang, Y.; Lee, H. I.; Chen, L.; Stucky, G. D., Low-temperature pseudomorphic transformation of ordered hierarchical macro-mesoporous SiO₂/C nanocomposite to SiC via magnesiothermic reduction. *Journal of the American Chemical Society* **2010**, *132* (16), 5552-5553.
 22. Lipson, A. L.; Chattopadhyay, S.; Karmel, H. J.; Fister, T. T.; Emery, J. D.; Dravid, V. P.; Thackeray, M. M.; Fenter, P. A.; Bedzyk, M. J.; Hersam, M. C., Enhanced lithiation of doped 6H silicon carbide (0001) via high temperature vacuum growth of epitaxial graphene. *The Journal of Physical Chemistry C* **2012**, *116* (39), 20949-20957.
 23. Choi, N.-S.; Yew, K. H.; Lee, K. Y.; Sung, M.; Kim, H.; Kim, S.-S., Effect of fluoroethylene carbonate additive on interfacial properties of silicon thin-film electrode. *Journal of Power Sources* **2006**, *161* (2), 1254-1259.
 24. Radhakrishnan, G.; Robertson, R.; Adams, P.; Cole, R., Integrated TiC coatings for moving MEMS. *Thin Solid Films* **2002**, *420*, 553-564.
 25. Chen, W.; Fan, Z.; Dhanabalan, A.; Chen, C.; Wang, C., Mesoporous silicon anodes prepared by magnesiothermic reduction for lithium ion batteries. *Journal of The Electrochemical Society* **2011**, *158* (9), A1055-A1059.
 26. Park, O.; Lee, J.-I.; Chun, M.-J.; Yeon, J.-T.; Yoo, S.; Choi, S.; Choi, N.-S.; Park, S., High-

performance Si anodes with a highly conductive and thermally stable titanium silicide coating layer. *Rsc Advances* **2013**, 3 (8), 2538-2542.

27. Reed, T. B., *Free Energy of Formation of Binary Compounds*. MIT Press Cambridge, Mass, 1971.

* Chapter V is reproduced in with a permission of “S. Choi, J. C. Lee, O. Park, M.-J. Chun, N.-S. Choi, S. Park, Synthesis of micro-assembled Si/titanium silicide nanotube anodes for high-performance lithium-ion batteries. *Journal of Materials Chemistry A* 2013”. Copyright **2013** The Royal Society of Chemistry

Chapter VI. Metallothermic Reduction for Macroporous Si: Compromise between Capacity and Volume Expansion for Li-Ion batteries

6.1. Introduction

Silicon (Si) has been used as a promising anode material for next-generation rechargeable lithium-ion batteries (LIBs) to replace conventional carbonaceous materials (theoretical capacity of 372 mAh g⁻¹) due to its high storage capacity (3579 mAh g⁻¹ at room temperature), low-cost, relatively low reaction potential (<0.5 V vs. Li/Li⁺), natural abundance in the Earth's crust, and environmental safety.¹⁻⁴ However, there are several critical issues that should be solved in Si-based anode materials.⁵⁻⁷ Firstly, a large volume change (>300%) during the lithiation/delithiation process induces tremendous mechanical stress, resulting in electrical disconnection of electrode materials from the current collector. This leads to a significant capacity fading upon battery operation. Secondly, an intrinsically poor electrical conductivity gives rise to capacity loss and poor rate capability. Thirdly, unstable solid-electrolyte-interphase (SEI) layers are formed on the surface of Si-based electrodes during a repetitive lithiation/delithiation process, resulting in degradation of battery performance.⁸⁻¹⁰

To overcome these problems, significant efforts have been made using the structural design of electrode materials,¹¹⁻¹⁸ introduction of electrically conductive layers,¹⁹⁻²¹ and coating of inorganic materials for stable SEI formation.^{22,23} These nanostructured Si-based electrodes showed significantly improved electrochemical properties, including a high reversible capacity and excellent cycling performance. In particular, the concept of micro-/nano-porous structuring may be one of the most efficient strategies, since the porous region can partially accommodate a large volume change during cycling, and enhance a rate capability of electrodes due to an increasing accessibility of Li ions and electrolytes.^{11,12,14,17,21}

Numerous methods for synthesizing porous Si materials have been described, including a template-based chemical synthesis, metal-assisted chemical etching, and metallothermic reaction.¹¹⁻¹⁸ Among them, the metallothermic reduction process is one of the more effective methods, because it is simple, cost-effective, and a scalable approach to making macro- and/or nano-porous Si particles, depending on the morphologies of silica particles.^{21, 24-26} Since the Ellingham diagram was well defined in 1944, a lot of industries have produced various alkali metals from complex minerals by thermal reduction.^{27,28} For example, Si particles have been synthesized from rice husk (silica source) via a magnesiothermic reaction.^{29,30} When porous Si particles prepared in this way were used as anode materials, most of them showed a significant improvement in cycling performances and rate capabilities, compared to non-porous Si particles.^{14,21,25,26} However, the large volume change of Si electrodes during the lithiation/delithiation process has not been paid attention to, even though it is

one of the critical issues that should be solved for practical LIB applications. That is why there should be a compromise between a reversible capacity and a volume expansion of Si electrodes.

Herein, we revisit the metallothermic reduction process of porous silica particles by combining aluminothermic and magnesiothermic reduction reactions. This process enables us to control the specific capacity and volume expansion of shape-preserving macroporous Si-based anodes. The advantages of this concept are explained as follows: (i) the original porous nature of silica particles is retained after conversion to Si particles, (ii) the specific capacity of an as-synthesized Si anode is easily tunable, (iii) a large volume expansion of Si during lithiation/delithiation is accommodated by macropores and Al₂O₃ layers formed during the metallothermic reaction, and (iv) this process enables us to produce macroporous Si particles in a large scale (hundreds of gram per batch). An optimized macroporous Si/Al₂O₃ composite anode exhibits a reversible capacity of ~1500 mAh g⁻¹ after 100 cycles at C/5 and a volume expansion of ~34% even after 100 cycles.

6.2. Experimental

6.2.1. Synthesis of Micro-/Nanoporous Si Particles

Bare porous silica (Diatomite, EP Minerals company) was uniformly mixed with Al powder (3~5 μm , Angang) in an ethanol solution. The mixture was placed inside an alumina boat and dried in an oven to remove the ethanol at 70°C. Subsequently, the aluminothermic reduction was performed at 900 °C for 3 h under an argon environment to synthesize a shape-preserving macroporous Si/Al₂O₃ composite material. The samples were immersed in 2 M H₃PO₄ at 100 °C for 2 h to remove Al₂O₃ by-products and remaining Al particles. To control the amount of Al₂O₃ in the composites, a second metallothermic reaction, magnesiothermic reaction, was carried out. The as-synthesized Si/Al₂O₃ composite and Mg powder (Sigma-Aldrich) were mixed together, and placed inside a stainless steel vessel whose cap was then closed in an argon-filled glove box. In a typical process, the furnace was heated to 700 °C at a rate of 5 °C min⁻¹ and kept at this temperature for 3 h. The samples were immersed in a 1M HCl solution at 35 °C for 4 h to remove MgO by-products. The carbon coating process of the Si/Al₂O₃ composite was performed by thermal decomposition of acetylene gas at 900 °C for 10 min in a quartz furnace.

6.2.2. Characterization of Porous Si Particles

The morphologies of samples were characterized by scanning electron microscopy (SEM, Hitachi) operating at 10 kV and X-ray diffractometer (XRD, Bruker D8-Advance) operated at 3 kW using CuK α radiation. Raman spectrum was obtained from a JASCO spectrometer (NRS-3000) to characterize the carbon phase in the carbon-coated composite materials.

6.2.3. Electrochemical Properties of Shape-Preserving Porous Si Anodes

Electrochemical properties of the Si-based electrodes were evaluated using coin-type half-cells (2016R) at 25 °C. The Si-based electrodes were composed of Si active materials, super-P carbon black, and poly(acrylic acid)/sodium carboxymethyl cellulose (1:1, w/w) binder in a weight ratio of 7:1:2. The electrolyte was 1.3 M LiPF₆ with ethylene carbonate/diethyl carbonate (PANAX Starlyte, Korea, 3/7 (v/v)) including 10wt% fluoroethylene carbonate additive. The half-cells were tested galvanostatically between 0.01 and 1.2 V (versus Li/Li⁺) at C/20 and C/5 rates. The full cell was formed using the Si/Al₂O₃ as the anode, LiCoO₂ as the cathode, and a 1.3 M LiPF₆ with ethylene carbonate/ethylmethyl carbonate (3/7 (v/v)) including 5 wt% fluoroethylene carbonate additive as electrolytes. The cell was cycled at C/10-C/2 rate within a 2.5-4.2 V voltage limit using WBCS 3000 battery systems.

6.3. Result and discussion

6.3.1. One-Step Reduction Process of Macroporous SiO₂ Particles

A schematic illustration shows the synthetic process of shape-preserving macroporous Si/Al₂O₃ composites via a metallothermic reduction reaction of porous silica (Scheme in Figure 6. 1). Commercially available porous silica (Diatomite) with particle sizes of 5~10 μm reacts with Al vapor (at well above the melting temperature (660 °C) of Al powders) under inert gas, and it leads to the formation of macroporous Si and Al₂O₃ by-products after an aluminothermic reaction.²⁷ A subsequent second chemical reduction of the Si/Al₂O₃ composite with a suitable amount of Mg produces a macroporous Si/Al₂O₃ composite with tunable amounts of Al₂O₃. The Al₂O₃ particles not only act as a shape-preserving layer during the conversion of silica to Si, but also as a buffer layer to accommodate the large volume expansion of the Si anode during cycling.

Porous silica particles (well-known as diatomite) have numerous pores with an average diameter of 500 nm and length ranging from 5 to 10 μm (SEM image of Figure 6. 1a). The bare silica was reacted with Al vapor at 900 °C for 3 h under Ar gas. Immediately after the aluminothermic reaction, the SiO₂ was transformed into Si with Al₂O₃ by-products in the following chemical equation (1):



The aluminothermic reaction of the bare silica led to the shape-preserving macroporous Si/Al₂O₃ composite without perturbing the original SiO₂ structure (Figure 6. 1b). In a low-magnified SEM image, as-synthesized Si/Al₂O₃ particles show macroporous structures without changing the particle size (Figure 6. 2). However, when we used a magnesiothermic reaction that is known as a highly exothermic reaction ($\Delta G^\circ(700^\circ\text{C}) = -256.75 \text{ kJ mol}^{-1}$),^{27,31} the original porous structure of SiO₂ was completely destroyed after making Si particles (Figure 6.3). We have found that a large batch (100-200 g) undergoes a dramatic temperature rise once the magnesiothermic reaction proceeds, resulting in a serious aggregation of Si particles without retaining the porous structures.

The X-ray diffraction (XRD) pattern displays that the as-synthesized Si/Al₂O₃ composite contained a large amount of Al₂O₃ by-products (Bottom of Figure 6. 1c). When the composite materials were dissolved in a 5M HCl or 2M H₃PO₄ etchant at 100 °C, a negligible amount of Al₂O₃ was detected in the XRD pattern (Top of Figure 6. 1c). However, the energy-dispersive X-ray spectroscopy (EDS) analysis indicates that a large amount of amorphous phase Al₂O₃ (50 wt%) is still contained in the Si/Al₂O₃ (denoted as Si-Al-5-5) composite (Figure 6. 4). The EDS mapping of the composite shows that Al₂O₃ layers are uniformly distributed to Si phases (Figure 6. 1d-1g).

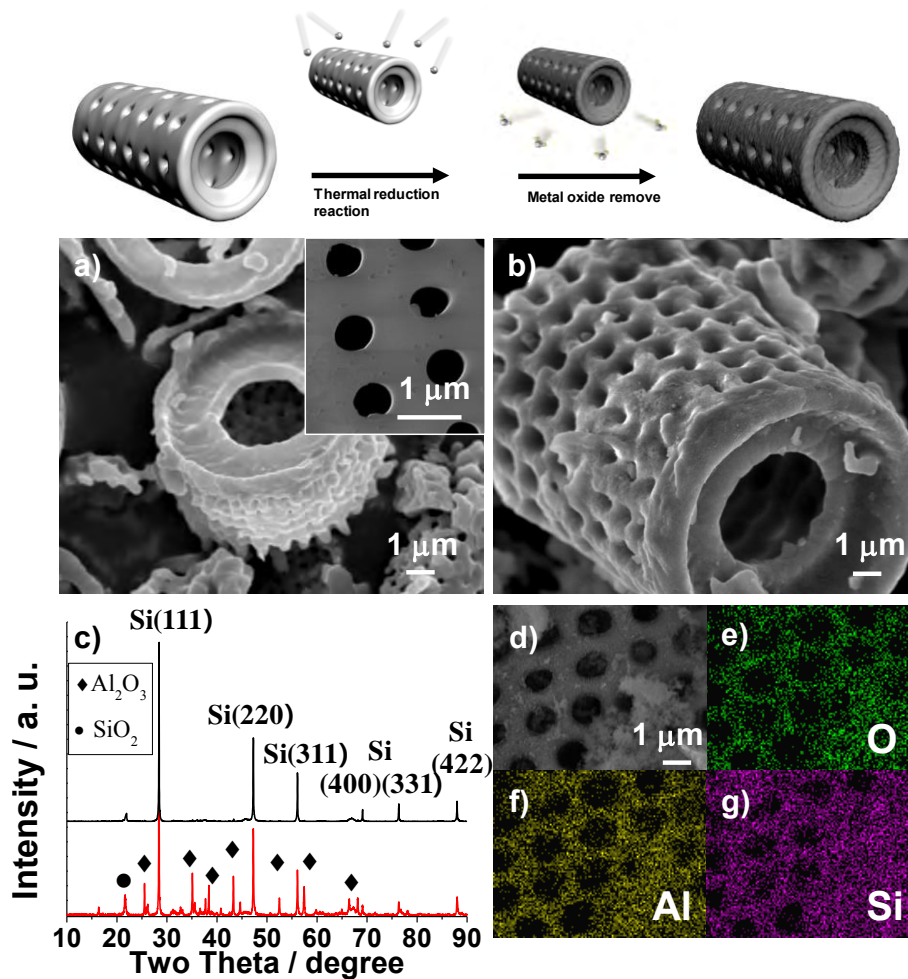


Figure 6. 1 Top: schematic illustration showing the synthetic process of macroporous Si/Al₂O₃ composite (Si-Al-5-5) material. Bottom: (a) SEM image of bare porous silica particles. In the inset, macropores in the side wall of the silica are clearly seen. (b) SEM image of Si-Al-5-5 composite after aluminothermic reduction reaction. (c) XRD pattern of as-synthesized Si-Al-5-5 composite (red) and dissolving-off sample in an etchant. (d) Magnified SEM image showing shape-reserving macroporous Si. EDS mapping results of samples (seen in Figure 6. 1d) indicate that (e) oxygen (green), (f) Al (yellow), and (g) Si (magenta) are uniformly distributed in the Si/Al₂O₃ composite.

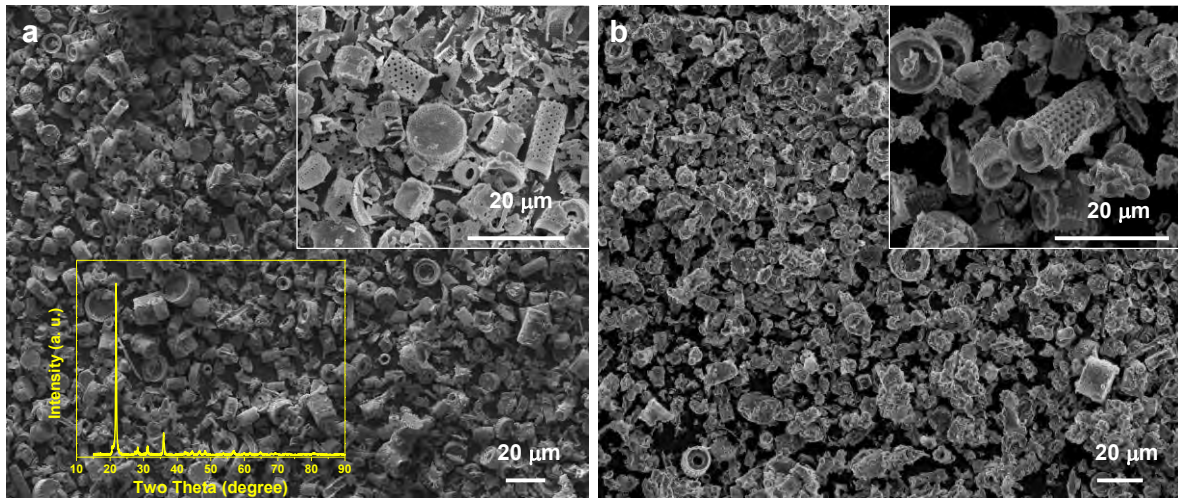


Figure 6. 2 Low-magnified SEM images showing (a) macroporous silica and (b) as-synthesized porous Si/Al₂O₃ composite. In the inset of Figure 6. 2, XRD pattern shows that the porous silica is a crystalline material with a cristobalite structure. Magnified SEM images (inset of Figure 6. 2a and 2b) indicate that the porous structure is still retained after aluminothermic reaction.

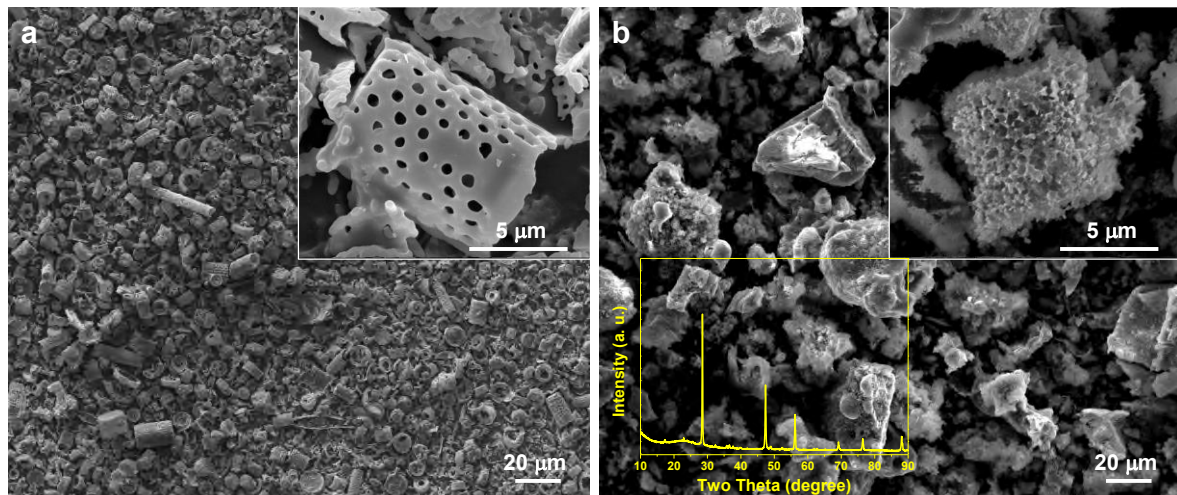


Figure 6. 3 SEM images of (a) macroporous silica and (b) Si particles prepared by magnesiothermic reaction of the porous silica. Magnified SEM images (inset of Figure 6. 3a and 3b) indicate that the original porous structure of silica is not retained after magnesiothermic reaction. In the inset of Figure 6. 3b, XRD patterns show the successful conversion of silica to pure Si.

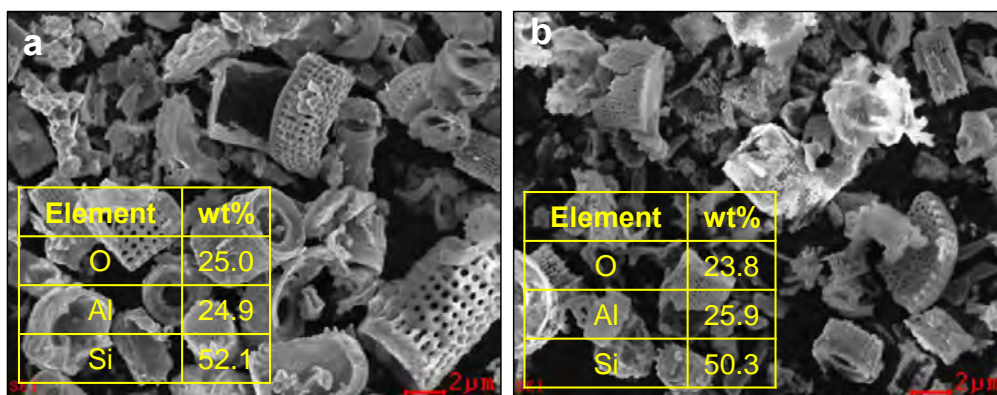


Figure 6. 4 SEM images of as-synthesized porous Si/Al₂O₃ composite materials obtained by two-different etching conditions. (a) 5M HCl and (b) 2M H₃PO₄ were used to remove remaining Al and Al₂O₃ by-products after the aluminothermic reaction between silica and Al. In both conditions, remaining pure Al particles were completely removed, while Al₂O₃ layers were partially removed without destroying the original porous structure.

6.3.2. Two-Step Reduction Process of Macroporous SiO₂ Particles

To reduce the amount of Al₂O₃ in the composite, we employed a magnesiothermic reduction process between Al₂O₃ and Mg in the following equation (2):



According to the Ellingham diagram, Mg vapor is easily oxidized to form MgO and Al mixture which can be successfully removed in a concentrated HCl etchant. When the Si/Al₂O₃ composite reacted with the Mg powder (molar ratio of composite/Mg = 1:0.4) at 700 °C, followed by rinsing with 5M HCl at 50 °C, the morphology of Si/Al₂O₃ (denoted as Si-Al-7-3 for composite with Si of 70wt% and Al₂O₃ of 30wt%) was still retained due to the low exothermic reaction (as indicated in the equation 2), as shown in SEM image (Figure 6. 5a). Interestingly, the EDS analysis of the composite materials suggests that the Al₂O₃ layers were uniformly distributed to the Si phase and significantly reduced to ~30 wt% (Figure 6. 5b-5d). In order to further investigate inner structure of the Si-Al-7-3 composite, a focused-ion-beam (FIB) technique that makes use of Ga-ions was employed to obtain cross-sectioned sample. SEM image of the FIB-sectioned sample shows that the Si-Al-7-3 retains tubular-type cylinder structure of original diatomite (Figure 6. 5e). However, magnified image in the yellow box indicated in Figure 6. 5e shows that the Si-Al-7-3 is composed of mesoporous structure (Figure 6. 5f). The EDS mapping analyses of image seen in Figure 6. 5f indicate spatial locations of Si and Al₂O₃. Si is mainly located to inner region (Figure 6. 5g), while Al₂O₃ takes position in the outer part of frame with an average thickness of 100 nm (Figure 6. 5h). The XRD pattern of the Si-Al-7-3 composite shows a typical crystalline Si structure (Figure 6. 5i). In the similar manner, when a stoichiometric amount of Mg powder relative to Si/Al₂O₃ was varied ranging from 0.2 to 0.7, macroporous Si/Al₂O₃ composites with Al₂O₃ contents of 50 and 10 wt% were obtained (Figure 6. 6).

Since the Si/Al₂O₃ composite has an intrinsically low electrical conductivity, it should be coated with conductive layers, such as carbon, metal coating, or conductive polymers to be used as anode materials in LIBs.¹⁹⁻²¹ We used a thermal decomposition process of acetylene gas (at 900 °C for 10 min) to make a Si/Al₂O₃ composite with uniform carbon-coating layers. The carbon contents of 10 wt% were characterized by elemental analysis. The Raman spectra of the carbon-coated Si/Al₂O₃ composite displays two peaks at ~1360 and ~1580 cm⁻¹ corresponding to the D band and the G band, respectively (Figure 6. 7). The intensity ratio of the D band to the G band was estimated to be 2.6, indicating an amorphous carbon.^{11,17}

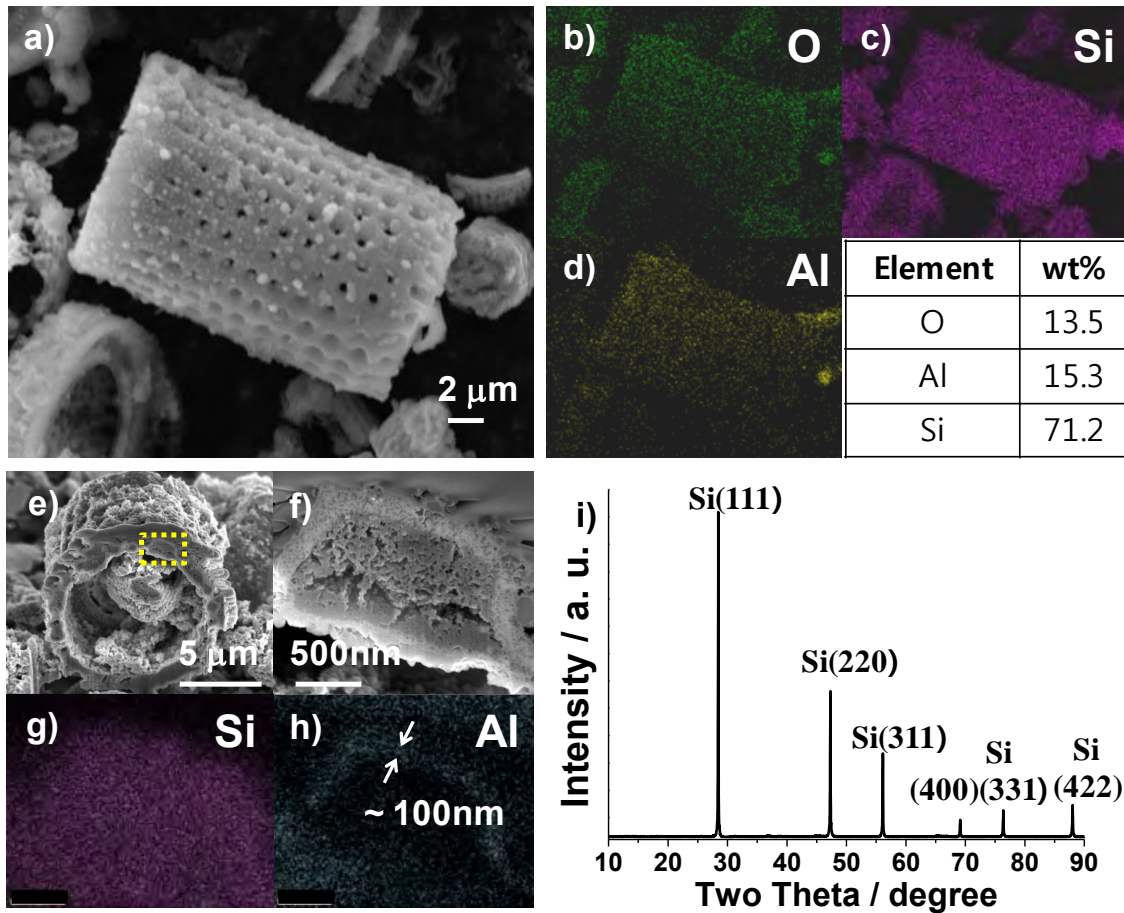


Figure 6. 5 Characterizations of Si/Al₂O₃ composite (Si-Al-7-3) synthesized by two-step metallo-thermic reaction. (a) SEM image of Si-Al-7-3 showing macroporous structure. EDS mapping analyses of the sample (seen in Figure 6. 5a) show uniform distribution of (b) oxygen (green), (c) Si (magenta), and (d) Al (yellow) in the composite, and content of each element was listed. (e) FIB cross-sectioned SEM image of Si-Al-7-3 showing tubular-type cylinder structure. (f) Magnified SEM image in yellow box region seen in Figure 6. 5e shows mesoporous structure. EDS mapping analyses of Figure 6. 5f show spatial distributions of (g) Si part (magenta) and (h) Al part (cyan). (i) XRD pattern of as-synthesized Si-Al-7-3 composite.

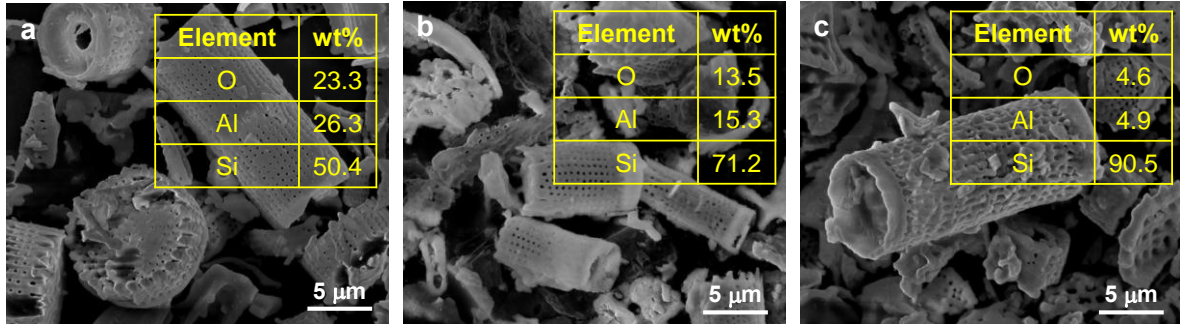


Figure 6. 6 SEM images and elemental analysis of three-different macroporous Si/Al₂O₃ composites ((a) Si-Al-5-5, (b) Si-Al-7-3, and (c) Si-Al-9-1) obtained by two-step metallothermic reaction. All three samples retain the macroporous structure after a chemical reduction process.

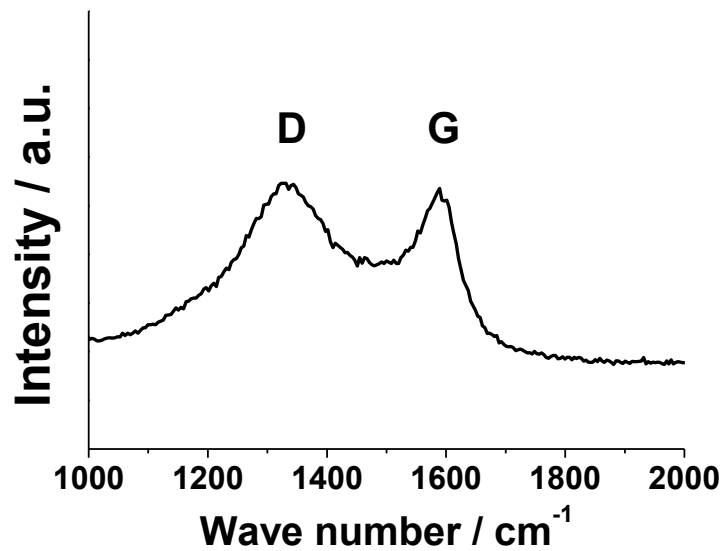


Figure 6. 7 Raman spectrum of carbon-coated Si-Al-7-3 composite indicates characteristic of amorphous carbon layer (with D/G ratio of 2.6).

6.3.3. Electrochemical Properties of Si Anodes Synthesized via Two-Step Reduction Process

Several carbon-coated macroporous Si/Al₂O₃ composites were tested as anode materials in LIBs. Figure 6. 8a shows the first cycle voltage profiles of the discharging (lithiation) and charging (delithiation) of the Si/Al₂O₃ composite electrodes with different amounts of Al₂O₃ at a rate of C/20 in the range of 0.01-1.2 V. The first discharge capacities of Si/ Al₂O₃ (Si-Al-5-5, Si-Al-7-3, and Si-Al-9-1) are 1554, 2445, and 3385 mAh g⁻¹ with a high initial coulombic efficiency of 80.4, 85.5, and 86.7 %, respectively (Figure 6. 8a). Increasing Si contents in the composite electrodes led to an enhancement of the initial coulombic efficiency due to a reduced amount of inactive Al₂O₃ layers. The dQ/dV plots obtained from the voltage profiles (seen in Figure 6. 8a) show typical cathodic and anodic peaks of Si electrodes.⁸⁻¹⁰ As expected, increasing Al₂O₃ contents brought about an increase of ohmic polarization (i.e., IR-drop) during the lithiation and delithiation, since the Al₂O₃ layers act as an insulating material in LIBs (Figure. 6. 9). However, the cycling performances of Si/Al₂O₃ composite anodes exhibit the opposite tendency (Figure 6. 8b). The Si-Al-9-1, Si-Al-7-3, and Si-Al-5-5 anodes showed capacity retentions of 61%, 86%, and 89% at a C/5 rate after 100 cycles, respectively. Excellent cycling performances of Si-Al-5-5 and Si-Al-7-3 electrodes may be explained as follows: (i) a suitable amount of Al₂O₃ layers act as a buffer layer to a large volume change during the lithiation/delithiation process. (ii) tubular and mesoporous structures have many void spaces which can act as buffer layer for a large volume change. (iii) the Al₂O₃ particles can form stable solid-electrolyte-interphase (SEI) layers by forming lithium alumina composite materials in the first cycle,^{23,32,33} and (iv) the good mechanical properties of the Al₂O₃ retains the structural integrity of macroporous Si/Al₂O₃ during cycling. In contrast, a carbon-coated non-porous Si (prepared by a magnesiothermic reduction reaction) electrode showed a poor cycling performance (capacity retention of 18% after 100 cycles at C/5 rate) due to a large volume expansion of Si (Figure. 6. 10).

Figure 6. 8c shows rate capabilities of Si-Al-5-5, Si-Al-7-3 and Si-Al-9-1 electrodes. Both Si-Al-7-3 and Si-Al-5-5 electrodes exhibit superior rate capabilities (capacity retention of >95% at 10 A g⁻¹ compared to 0.5 A g⁻¹), even though composite materials have a large amount of Al₂O₃. It may suggest that Al₂O₃ nanoparticles are not fully covered on the Si surface, but well distributed separately with void spaces that can access Li ions and electrolytes. Moreover, the Si/Al₂O₃ composite electrode shows a significant reduction of open circuit voltage (OCV) in a fully lithiated state after 100 cycles (Figure 6. 8d). Since the Si electrode is extremely reactive in the electrolyte in its fully discharged state, it leads to the loss of Li ions and accompanies an increase of OCV.^{23,35} To investigate the interactions between the anode and electrolyte of the Si-Al-7-3 and pure Si (obtained by magnesiothermic reaction) electrodes, the cells were discharged to 0.005 V and relaxed as a function of time to monitor the increase of OCV. As expected, the Si-Al-7-3 electrode shows a lower OCV increase than the pure Si electrode, indicating the lithiated electrode with a suitable amount of Al₂O₃ layering effectively prevents some side reactions between the Si electrode and the electrolyte.

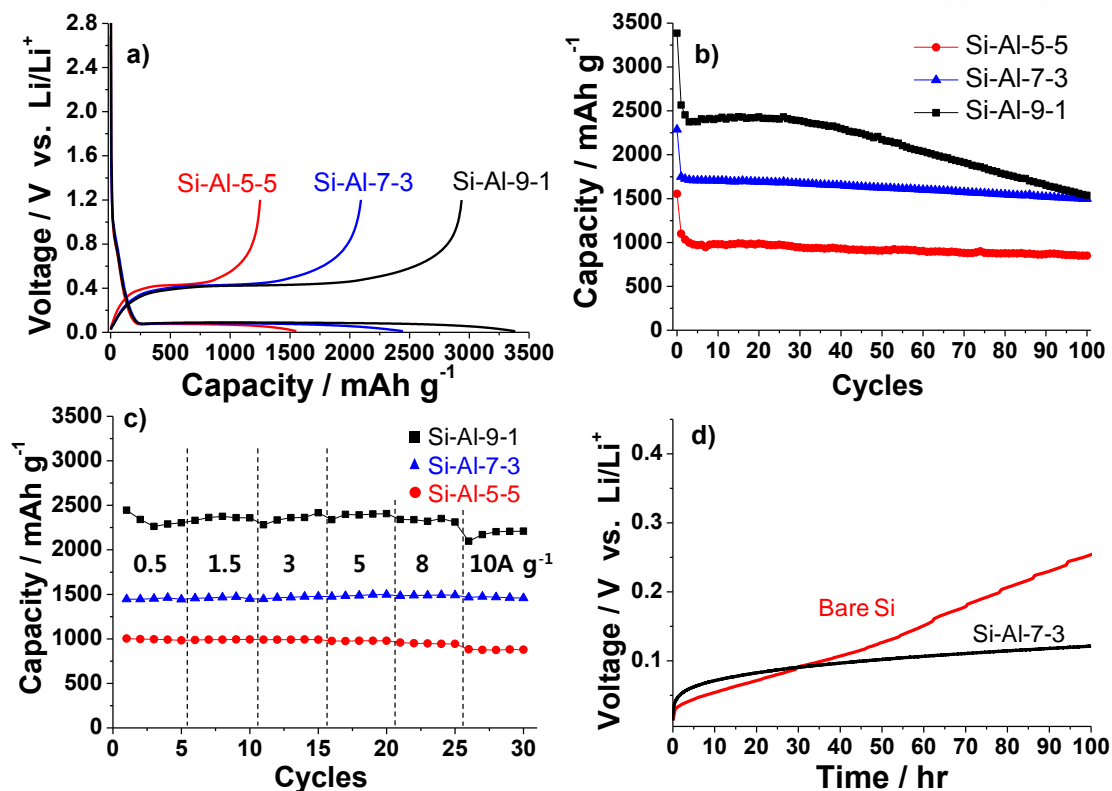


Figure 6. 8 Electrochemical performances of macroporous Si/Al₂O₃ composite electrodes with four different Al₂O₃ contents (Si-Al-5-5: red, Si-Al-7-3: blue, Si-Al-9-1: black). (a) The first cycle voltage profiles of each electrode obtained at a rate of C/20 in the range of 0.01-1.2 V. (b) Cycle performances of three carbon-coated composite electrodes obtained at C/2 rate in the range of 0.01-1.2 V. (c) Rate capabilities of each sample (lithiation rate was fixed to C/5 rate). (d) OCV plots of Si-Al-7-3 (black) and pure Si without Al₂O₃ (red) after 100th cycle.

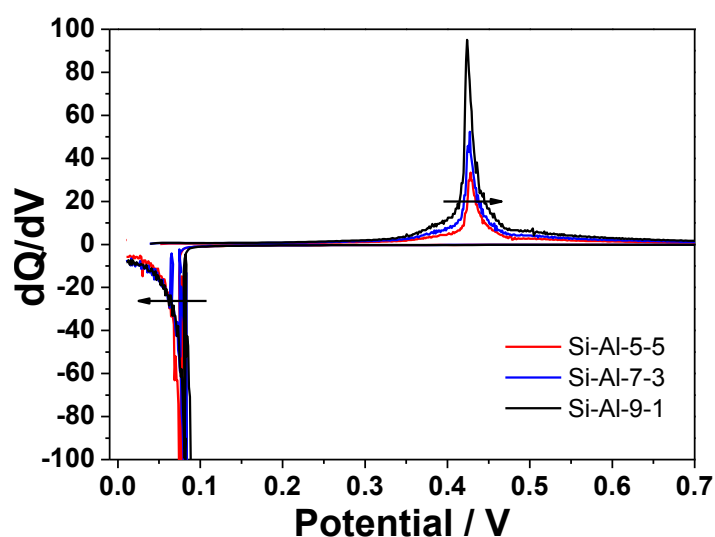


Figure 6. 9 The dQ/dV plots of three composite electrodes at the first cycle. The arrow indicates the increase of ohmic polarization with increasing amount of Al₂O₃

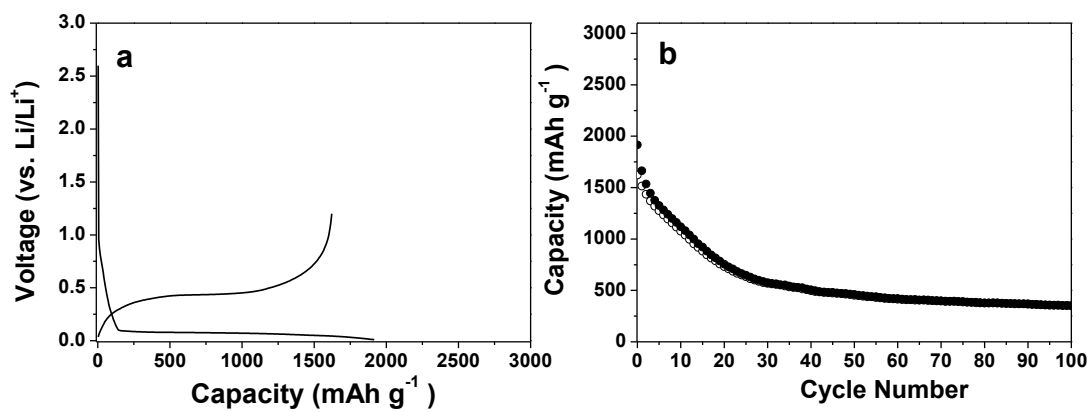


Figure 6. 10 Electrochemical performances of carbon-coated non-porous Si electrodes obtained by magnesiothermic reaction. (a) The first cycle voltage profile was obtained at a rate of C/20 in the range of 0.01-1.2 V. The discharge capacity of the Si electrode was 1900 mAh g⁻¹ with initial coulombic efficiency of 85.3%. (b) Cycle performance (discharge: solid circle, charge: open circle) of the carbon-coated Si electrode was obtained at C/5 rate.

6.3.4. Analysis of Macro Porous Si Electrodes After Cycling

For practical LIB applications, requirements including a high specific capacity, a stable cycling performance, and minimized volume expansion during cycling should be satisfied.¹⁻⁷ Numerous nanostructured Si anodes showing a high capacity and excellent cycling performance have been reported. However, one of the more critical issues in practical LIBs, a volume expansion control of Si-based electrodes, is still a changing issue. There should be a compromise between a high reversible capacity and a volume expansion for use as anode materials in practical LIB applications.

We investigated the effect of Al₂O₃ content in the Si/Al₂O₃ composite on the volume expansion after cycling. Figure 6. 11 presents cross-sectional SEM images of four different Si/Al₂O₃ composite electrodes before and after 100 cycles. Si-Al-9-1, Si-Al-7-3, and Si-Al-5-5 electrodes showed a low volume expansion of 66%, 34%, and 15%, respectively, even after 100 cycles (Figure 6. 11d-f). When Si-Al-7-3 particles were FIB-sectioned after 100 cycles, original tubular-type cylinder structure containing mesopores was clearly observed with remaining mechanically robust Al₂O₃ layers (Figure 6. 12). However, carbon-coated pure Si (without Al₂O₃ layer) electrodes prepared by magnesiothermic reaction showed a large volume expansion of 150%, which is seen in typical carbon-coated Si electrodes (Figure 6. 13).³⁵ These results imply that the volume expansion of a macroporous Si/Al₂O₃ composite electrode is largely accommodated by the void space of the macropores in the composite and the Al₂O₃ buffer layer with a good mechanical property.

The electrochemical performances of the macroporous Si/Al₂O₃ composite were tested in a half-cell. This is not sufficient to claim its relevance as a novel anode material for practical LIB applications. Thus, we tested a full cell (energy density of 2.6 mAh cm⁻²) where the Si-Al-7-3 electrode was coupled with a LiCoO₂ cathode. The electrochemical performance of Si-Al-7-3/LiCoO₂ system was examined at charge/discharge = 0.5C/0.5C at a voltage range of 2.5-4.4 V. The charge/discharge voltage profiles of the full-cell are shown in Figure 5a. The first charge/discharge profile of the Si / LiCoO₂ cell shows a coulombic efficiency of 80% in the pre-cycle at C/10 rate (Figure 6. 14a). Subsequent long-term cycling (up to 40th cycle at C/2 charging-C/2 discharging rate) in a full-cell was evaluated. The good capacity retention of 72% was achieved after 40 cycles with a charge-discharge efficiency of >99.5% (Figure 6. 14b). It suggests that the macroporous Si/Al₂O₃ composite is a promising candidate as anode material for practical LIB applications.

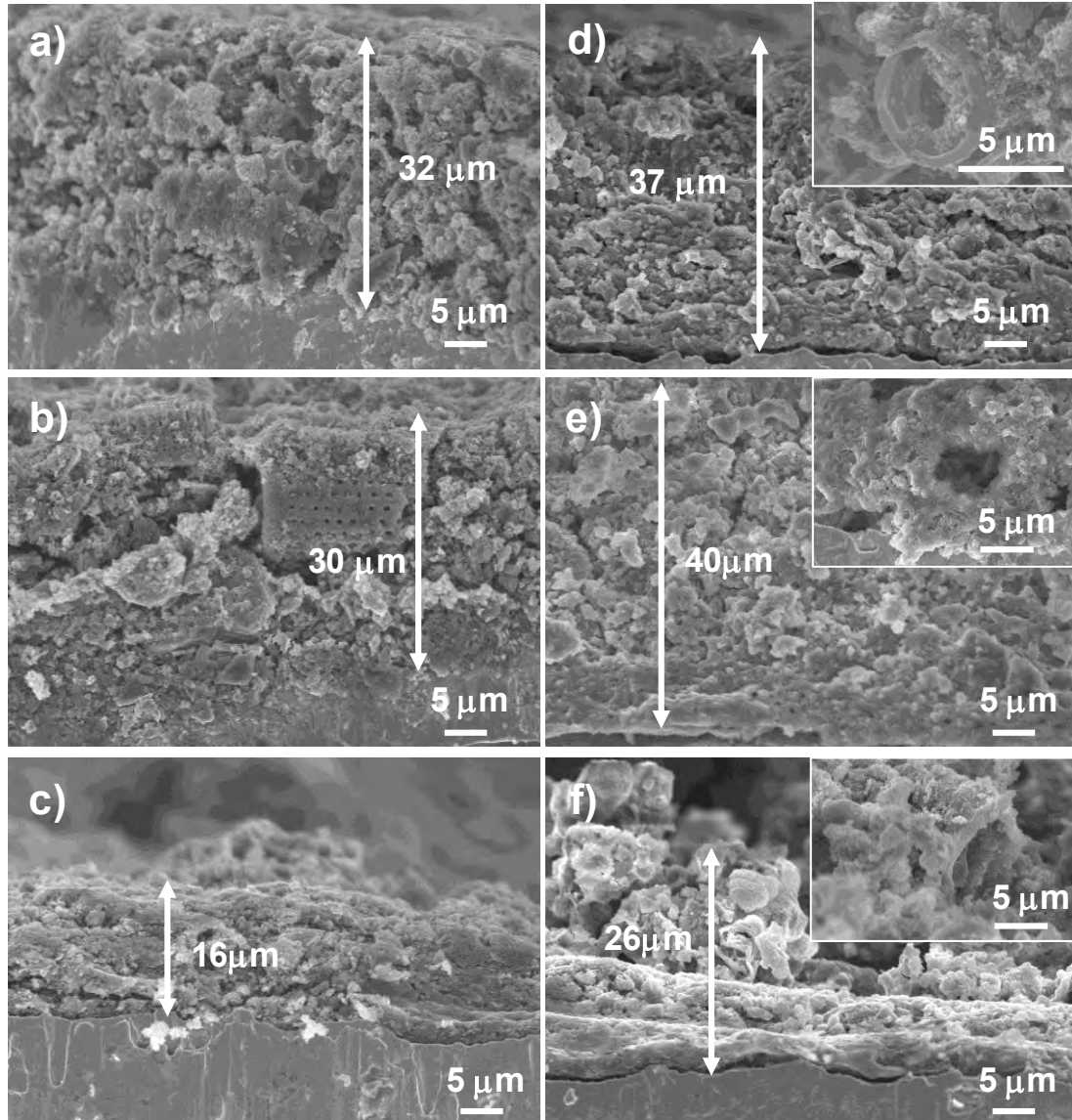


Figure 6. 11 Cross-sectional SEM images of composite electrodes (Si-Al-5-5 (a, d), Si-Al-7-3 (b, e), and Si-Al-9-1 (c, f)) before (a-c) electrochemical test and after 100 cycles (d-f). In the inset, magnified SEM images of composite electrodes after cycling were seen.

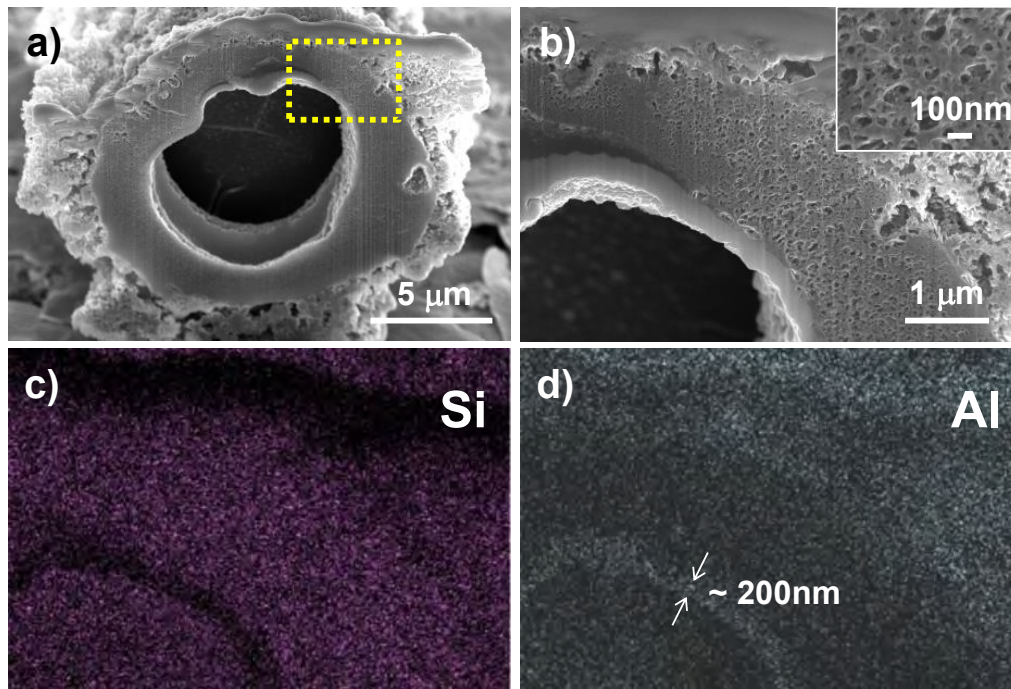


Figure 6. 12 (a) Cross-sectional SEM images of Si-Al-7-3 particles after 100 cycles. (b) Magnified image of Si-Al-7-3 (yellow box seen in Figure 6. 12a) showing mesoporous structure. EDS mapping analyses of sample seen in Figure 6. 12b showing (c) inner Si part (magenta) and (d) outer Al layer (cyan).

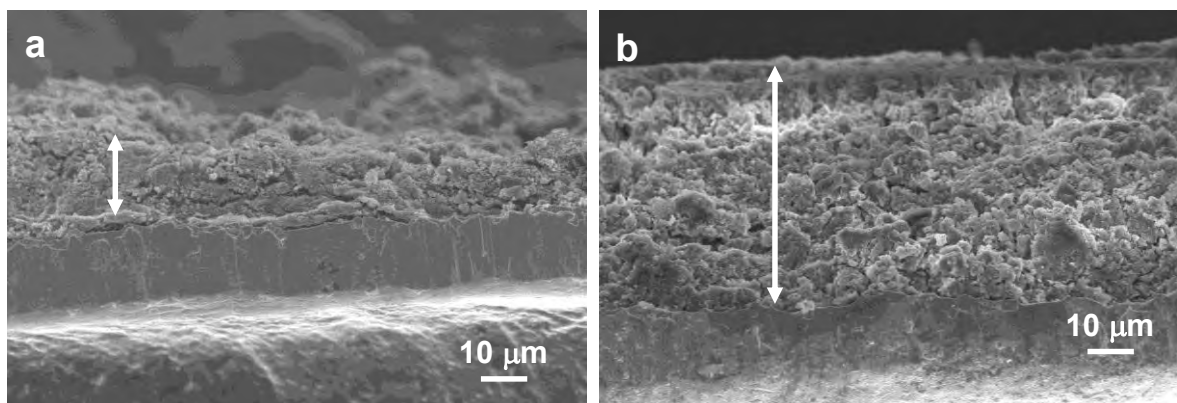


Figure 6. 13 Cross-sectional SEM images of carbon-coated non-porous Si electrode prepared from magnesiothermic reaction (a) before and (b) after 100 cycles. After cycling, a huge volume expansion of 150% occurred due to the absence of porous structure and Al_2O_3 layer.

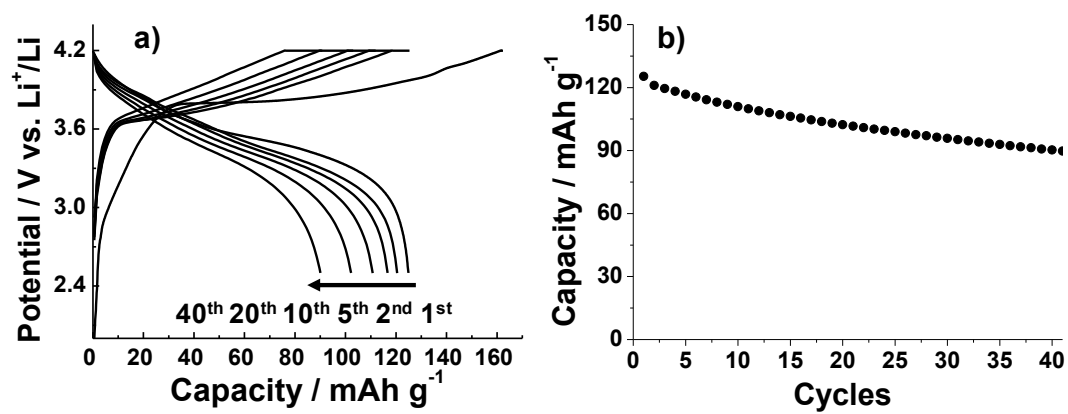


Figure 6. 14 Electrochemical performances of full cell consisting of Si-Al-7-3/LiCoO₂. (a) Voltage profiles of Si-Al-7-3/LiCoO₂ electrode obtained at a rate of C/10 (first cycle) and C/2 (other cycles) in the range of 2.5-4.2 V. (b) Cycle retention of Si-Al-7-3 (anode)-LiCoO₂(cathode) full-cell at C/2(charging)-C/2(discharging) rate.

6.4. Conclusion

We synthesized a shape-preserving macroporous Si/Al₂O₃ composite material via a two-step metallothermic reaction of macroporous silica particles in a large scale. This process enabled us to find a compromise between a reversible gravimetric capacity and a volume expansion of Si-based anode materials by tuning the amount of Al₂O₃ layers. The Si-based anode materials consisting of a macroporous structure and Al₂O₃ with a good mechanical property exhibited excellent electrochemical properties, including a highly stable cycling performance (a high reversible capacity of ~1500 mAh g⁻¹ at C/5 rate after 100 cycles) and a minimized volume expansion of <35% after 100 cycles. This simple synthetic route can be extended to make other high-performance anode materials in lithium ion batteries.

6.5. References

1. Nazri, G. A.; Pistoia, G., *Lithium Batteries: Science and Technology*. Springer: 2004.
2. Song, M.-K.; Park, S.; Alamgir, F. M.; Cho, J.; Liu, M., Nanostructured electrodes for lithium-ion and lithium-air batteries: the latest developments, challenges, and perspectives. *Materials Science and Engineering: R: Reports* **2011**, *72* (11), 203-252.
3. Szczech, J. R.; Jin, S., Nanostructured silicon for high capacity lithium battery anodes. *Energy & Environmental Science* **2011**, *4* (1), 56-72.
4. Kasavajjula, U.; Wang, C.; Appleby, A. J., Nano- and bulk-silicon-based insertion anodes for lithium-ion secondary cells. *Journal of Power Sources* **2007**, *163* (2), 1003-1039.
5. Boukamp, B.; Lesh, G.; Huggins, R., All-solid lithium electrodes with mixed-conductor matrix. *Journal of the Electrochemical Society* **1981**, *128* (4), 725-729.
6. Park, C.-M.; Kim, J.-H.; Kim, H.; Sohn, H.-J., Li-alloy based anode materials for Li secondary batteries. *Chemical Society reviews* **2010**, *39* (8), 3115-3141.
7. Liu, C.; Li, F.; Ma, L. P.; Cheng, H. M., Advanced materials for energy storage. *Advanced materials* **2010**, *22* (8), E28-E62.
8. Xu, K.; von Cresce, A., Interfacing electrolytes with electrodes in Li ion batteries. *Journal of Materials Chemistry* **2011**, *21* (27), 9849-9864.
9. Pan, Q.; Wang, H.; Jiang, Y., Covalent modification of natural graphite with lithium benzoate multilayers via diazonium chemistry and their application in lithium ion batteries. *Electrochemistry communications* **2007**, *9* (4), 754-760.
10. Wu, H.; Cui, Y., Designing nanostructured Si anodes for high energy lithium ion batteries. *Nano Today* **2012**, *7* (5), 414-429.
11. Kim, H.; Han, B.; Choo, J.; Cho, J., Three-dimensional porous silicon particles for use in high-performance lithium secondary batteries. *Angewandte Chemie* **2008**, *120* (52), 10305-10308.
12. Wu, H.; Chan, G.; Choi, J. W.; Yao, Y.; McDowell, M. T.; Lee, S. W.; Jackson, A.; Yang, Y.; Hu, L.; Cui, Y., Stable cycling of double-walled silicon nanotube battery anodes through solid-electrolyte interphase control. *Nature nanotechnology* **2012**, *7* (5), 310-315.
13. Magasinski, A.; Dixon, P.; Hertzberg, B.; Kvit, A.; Ayala, J.; Yushin, G., High-performance lithium-ion anodes using a hierarchical bottom-up approach. *Nature materials* **2010**, *9* (4), 353-358.
14. Chen, D.; Mei, X.; Ji, G.; Lu, M.; Xie, J.; Lu, J.; Lee, J. Y., Reversible Lithium-Ion Storage in Silver-Treated Nanoscale Hollow Porous Silicon Particles. *Angewandte Chemie International Edition* **2012**, *51* (10), 2409-2413.

15. Yoo, J. K.; Kim, J.; Jung, Y. S.; Kang, K., Scalable fabrication of silicon nanotubes and their application to energy storage. *Advanced materials* **2012**, *24* (40), 5452-5456.
16. Lu, Z.; Zhu, J.; Sim, D.; Zhou, W.; Shi, W.; Hng, H. H.; Yan, Q., Synthesis of ultrathin silicon nanosheets by using graphene oxide as template. *Chemistry of Materials* **2011**, *23* (24), 5293-5295.
17. Lee, J. I.; Lee, K. T.; Cho, J.; Kim, J.; Choi, N. S.; Park, S., Chemical-Assisted Thermal Disproportionation of Porous Silicon Monoxide into Silicon-Based Multicomponent Systems. *Angewandte Chemie* **2012**, *124* (11), 2821-2825.
18. Dai, F.; Zai, J.; Yi, R.; Gordin, M. L.; Sohn, H.; Chen, S.; Wang, D., Bottom-up synthesis of high surface area mesoporous crystalline silicon and evaluation of its hydrogen evolution performance. *Nat. Commun.* **2014**, *5*, 3605.
19. Gohier, A.; Laïk, B.; Kim, K. H.; Maurice, J. L.; Pereira-Ramos, J. P.; Cojocar, C. S.; Van, P. T., High-Rate Capability Silicon Decorated Vertically Aligned Carbon Nanotubes for Li-Ion Batteries. *Advanced materials* **2012**, *24* (19), 2592-2597.
20. Murugesan, S.; Harris, J. T.; Korgel, B. A.; Stevenson, K. J., Copper-coated amorphous silicon particles as an anode material for lithium-ion batteries. *Chemistry of Materials* **2012**, *24* (7), 1306-1315.
21. Yu, Y.; Gu, L.; Zhu, C.; Tsukimoto, S.; van Aken, P. A.; Maier, J., Reversible Storage of Lithium in Silver-Coated Three-Dimensional Macroporous Silicon. *Advanced materials* **2010**, *22* (20), 2247-2250.
22. Nguyen, H. T.; Zamfir, M. R.; Duong, L. D.; Lee, Y. H.; Bondavalli, P.; Pribat, D., Alumina-coated silicon-based nanowire arrays for high quality Li-ion battery anodes. *Journal of Materials Chemistry* **2012**, *22* (47), 24618-24626.
23. He, Y.; Yu, X.; Wang, Y.; Li, H.; Huang, X., Alumina-Coated Patterned Amorphous Silicon as the Anode for a Lithium-Ion Battery with High Coulombic Efficiency. *Advanced materials* **2011**, *23* (42), 4938-4941.
24. Bao, Z.; Weatherspoon, M. R.; Shian, S.; Cai, Y.; Graham, P. D.; Allan, S. M.; Ahmad, G.; Dickerson, M. B.; Church, B. C.; Kang, Z.; Abernathy, H. W., 3rd; Summers, C. J.; Liu, M.; Sandhage, K. H., Chemical reduction of three-dimensional silica micro-assemblies into microporous silicon replicas. *Nature* **2007**, *446* (7132), 172-5.
25. Wang, M.-S.; Fan, L.-Z.; Huang, M.; Li, J.; Qu, X., Conversion of diatomite to porous Si/C composites as promising anode materials for lithium-ion batteries. *Journal of Power Sources* **2012**, *219*, 29-35.
26. Jia, H.; Gao, P.; Yang, J.; Wang, J.; Nuli, Y.; Yang, Z., Novel Three-Dimensional Mesoporous Silicon for High Power Lithium-Ion Battery Anode Material. *Advanced Energy*

Materials **2011**, *1* (6), 1036-1039.

27. Ellingham, H., Reducibility of oxides and sulfides in metallurgical processes. *J Soc Chem Ind* **1944**, *63*, 125-133.
28. Loomis, C. C., The Production of Metallic Calcium by Thermal Reduction. *Transactions of The Electrochemical Society* **1946**, *89* (1), 207-216.
29. Banerjee, H.; Sen, S.; Acharya, H., Investigations on the production of silicon from rice husks by the magnesium method. *Materials Science and Engineering* **1982**, *52* (2), 173-179.
30. Jung, D. S.; Ryou, M.-H.; Sung, Y. J.; Park, S. B.; Choi, J. W., Recycling rice husks for high-capacity lithium battery anodes. *Proceedings of the National Academy of Sciences* **2013**, *110* (30), 12229-12234.
31. Luo, W.; Wang, X.; Meyers, C.; Wannemacher, N.; Sirisaksoontorn, W.; Lerner, M. M.; Ji, X., Efficient fabrication of nanoporous Si and Si/Ge enabled by a heat scavenger in magnesiothermic reactions. *Scientific reports* **2013**, *3*, 2222.
32. Liu, Y.; Hudak, N. S.; Huber, D. L.; Limmer, S. J.; Sullivan, J. P.; Huang, J. Y., In situ transmission electron microscopy observation of pulverization of aluminum nanowires and evolution of the thin surface Al₂O₃ layers during lithiation–delithiation cycles. *Nano letters* **2011**, *11* (10), 4188-4194.
33. Xiao, X.; Lu, P.; Ahn, D., Ultrathin multifunctional oxide coatings for lithium ion batteries. *Advanced materials* **2011**, *23* (34), 3911-3915.
34. Key, B.; Morcrette, M.; Tarascon, J. M.; Grey, C. P., Pair distribution function analysis and solid state NMR studies of silicon electrodes for lithium ion batteries: understanding the (de)lithiation mechanisms. *Journal of the American Chemical Society* **2011**, *133* (3), 503-12.
35. Bang, B. M.; Kim, H.; Song, H.-K.; Cho, J.; Park, S., Scalable approach to multi-dimensional bulk Si anodes via metal-assisted chemical etching. *Energy & Environmental Science* **2011**, *4* (12), 5013-5019.

* Chapter VI is reproduced in with a permission of “S. Choi, T. Bok, J. Ryu, J.-I. Lee, J. Cho, S. Park, Revisit of metallothermic reduction for macroporous Si: compromise between capacity and volume expansion for practical Li-ion. *Nano Energy* 2015”. Copyright **2015** Elsevier Ltd.

Chapter VII. Cost-Effective Scalable Synthesis of Mesoporous Germanium Particles *via* Zincothermic Reduction for High-Performance Li-Ion Batteries

7.1. Introduction

Lithium-ion batteries (LIBs), which are essential electrochemical energy storage devices, are being used to power portable electronics such as cell phones, laptops, and digital cameras, because of their advantageous properties, which include a high working voltage, high energy density, long cycling life, and the absence of the memory effect.¹⁻³ However, current LIBs, which consist of a graphite anode and a LiCoO₂ cathode, do not meet the requirements for more advanced applications, such as higher energy and power densities. Thus, it is crucial to develop alternative electrode materials with higher gravimetric and volumetric capacities than those of conventional ones.^{4,5} For example, in the case of a 18650 cell consisting of a graphite anode with a capacity of 372 mA h g⁻¹ and a LiCoO₂ cathode with a capacity of ~137 mA h g⁻¹, if graphite anode is replaced with an anode of a lithium-alloying material having a capacity greater than 1000 mA h g⁻¹, the total battery capacity would increase by more than 20%.^{6,7} For this reason, Si and Ge are attracting increasing attention as promising high-capacity anode materials.

Even though Ge is more expensive than Si and thus has attracted less attention, the fact that Ge is as abundant as Si in the earth's crust suggests that Ge-based materials can be used for LIB anodes.⁸ Furthermore, Ge has several advantages over Si. Although the gravimetric capacity of Ge at room temperature (1384 mA h g⁻¹ in the form of Li₁₅Ge₄) is much lower than that of Si at room temperature (3579 mA h g⁻¹), the volumetric capacity of Ge (7366 A h cm⁻³) is second only to that of Si (8334 A h cm⁻³).⁹ In addition, Ge exhibits high electrical conductivity (10⁴ times higher than that of Si), owing to its small band gap, which is 0.6 eV,^{10,11} and exceptionally high lithium-ion diffusivity (400 times greater than that for Si at room temperature), allowing for high rate capability.¹² Finally, Ge-based anodes show isotropic lithiation behaviour, while Si-based ones exhibit highly anisotropic behaviour, as well as nonhomogeneous alloying pathways for Li ions.⁹ The phenomenon of isotropic lithiation may lead to Ge-based anodes exhibiting highly reversible capacities, as it minimizes fracturing in the anodes.

However, as is the case with Si-based anodes, a critical issue related to Ge-based anodes is that they exhibit a significant volume change (greater than 230%), which may lead to the cracking and pulverization of the Ge particles, resulting in poor cycling life.^{11,13} To overcome this problem, numerous efforts have been made to design Ge-based materials that do not exhibit significant volume changes. These include reducing the particle size¹¹, forming one-dimensional nanostructures^{9,14,15},

dispersing Ge in an inactive/active matrix¹⁶, forming porous structures^{9,17}, and coating shells with the Ge materials¹⁸ in order to improve their electrochemical performances.

For example, Cho and co-workers have reported that the Li-ion storage ability of Ge nanoparticles depends on their morphology and changes when the particles are transformed from zero-dimensional hollow-type ones to three-dimensional porous assemblies.¹⁹ They also demonstrated that Ge nanotubes and graphene-coated Ge nanowires exhibit high rate capabilities and long-term stable cyclability.²⁰ Further, Hand and co-workers have proposed a simple method for synthesizing amorphous, porous, and hierarchically structured GeO_x anodes with a capacity as high as ~1250 mA h g⁻¹ after 600 cycles.²¹ Anodes of other Ge/carbon nanocomposites, including those with surface carbon coatings, also show significantly improved electrochemical performances, as well as controlled volume expansion and stable cyclability over 100 cycles.^{18,22-26} However, these materials are synthesized through complicated multistep processes that involve the use of expensive and hazardous organic-capped Ge precursors (e.g., GeH₄ and GeCl₄).²⁷ In addition, magnesiothermic reduction involving the use of magnesium as a reducing agent can be dangerous owing to the large thermal shock generated during the chemical reaction.¹⁷ Therefore, the development of a simple, safe, cost-effective, and scalable method for synthesizing high-performance Ge-based battery anodes is highly desired but still a challenge.

Herein, we present a simple and cost-effective technique for synthesizing mesoporous Ge particles. Metallic Zn, which has a low melting temperature (420 °C), is used as the reducing agent for the simple conversion of cheap GeO₂ into mesoporous Ge particles *via* a redox-transmetalation reaction²⁸ (*i.e.*, a zincothermic reduction reaction (ZRR)). This strategy has several advantages. To begin with, the reaction temperature for the ZRR is much lower than that for typical metallothermic reactions (e.g., those involving Mg, Al, or Ca); hence, the shape of the original GeO₂ particles is preserved even after they have been converted into metallic Ge particles. Further, the large change in volume exhibited by the Ge particles during the lithiation/delithiation process is accommodated by the mesoporous structure of the particles. Finally, the ZRR process allows one to produce mesoporous Ge materials on a large scale through a one-step synthetic reaction using an environmentally benign and cost-effective approach. Using the ZRR process, it is possible to fabricate an optimized mesoporous Ge anode that exhibits a reversible capacity as high as ~1400 mAh g⁻¹ after 300 cycles at a rate of 0.5 C (corresponding to the capacity retention of 99.5% compared to a capacity in the initial cycle), excellent rate capability, and stable cycling performance in a full cell containing the Ge anode and a LiCoO₂ cathode.

7.2. Experimental

7.2.1. Synthesis of Hollow Germanium Oxide Particles and Ge Materials

Hollow GeO₂ particles were synthesized by the hydrolysis of GeCl₄ and SnCl₄ (Ge/Sn molar ratio = 1 : 1) under ultrasonication. First, 1.635 g of SnCl₄·5H₂O was dissolved in 35 mL of ethanol (99.9%, Sigma Aldrich) under ultrasonication for 10 min. Next, 1 g of GeCl₄ (99.999%, Alfa Aesar) dissolved in 10 mL of ethanol was added to the SnCl₄ solution. Subsequently, 7 mL of deionized water and 1 mL of concentrated NH₄OH were added to the above mixture and the mixture was subjected to ultrasonication for 120 min. The resulting white precipitate was collected by centrifugation (3500 rpm for 10 min) and rinsed several times with ethanol before being dried in vacuum at 80 °C.

Synthesis of mesoporous germanium materials. Commercially available GeO₂ (99.999%, Sigma-Aldrich) was mixed uniformly with a zinc powder (Zn 99.9%, Alfa Aesar) in a mortar. The mixture was placed in a stainless steel vessel, whose cap was then closed in an argon-filled glove box. In a typical process, the furnace was heated to 390–800 °C at a rate of 5 °C min⁻¹ and kept at the target temperature for 3 h. The thus-obtained samples were immersed in a 1 M HCl solution at 30 °C for 1 h to remove the ZnO formed as a by-product. From this synthetic process, Ge particles of >65% were obtained in one batch.

7.2.2. Physical Characterization.

The surface morphologies of the GeO₂ and Ge particles were characterized using field-emission scanning electron microscopy (FESEM, Hitachi S-4800), which was performed at 10 kV. The microstructures of the GeO₂ particles and the as-synthesized Ge particles were investigated using XRD analyses (Bruker D8-Advance), which were performed at 40 kW using Cu-Kα radiation. The Raman spectra to characterise the Ge phase in the Ge and GeO₂ particles were obtained using a JASCO spectrometer (NRS-3000), which was operated at 532 nm.

7.2.3. X-Ray Absorption Spectroscopy.

The temperature-dependent in-situ Ge and Zn K-edge X-ray absorption spectra of the mixture of the Ge and Zn particles were collected at the BL10C beamline of the Pohang light source (PLS-II) in the top-up mode under a ring current of 300 mA at 3.0 GeV. The XANES and EXAFS analyses were also performed under the same conditions. A monochromatic X-ray beam was obtained from high-intensity X-ray photons emitted by a multiple wiggler source using a liquid-nitrogen-cooled Si (111) double crystal monochromator (Bruker ASC). The transmitted XAFS spectra were collected using a laboratory-made heating stage for temperatures ranging from the room temperature to 600 °C for ~4 h (heating rate = 2.5 °C/min).

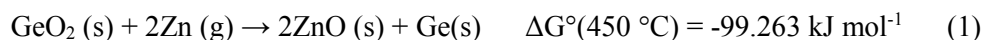
7.2.4. Electrochemical Test.

The electrochemical properties of the Ge-based electrodes were evaluated using coin-type half cells (2016R) at 25 °C. The Ge-based electrodes were composed of the Ge active material, super-P carbon black, and poly(acrylic acid)/sodium carboxymethyl cellulose (1:1, w/w) as binder in a weight ratio of 7:1.5:1.5. The electrolyte used was 1.3 M LiPF_6 containing ethylene carbonate/diethyl carbonate (PANAX Starlyte, Korea, 3/7 (v/v)) and 10 wt% fluoroethylene carbonate as an additive. The half cells were tested galvanostatically between 0.01 and 1.5 V (versus Li/Li+) for C rates of 0.05–7 C. The coin-type full cells consisted of an anode of the synthesized material (z600-Ge) and a LiCoO_2 cathode. The cell performance was examined using a cycle tester (WBCS 3000 battery systems, Wonatech). The full cells were cycled at rates of 0.1–0.5 C between 2.5 and 4.2 V.

7.3. Result and discussion

7.3.1. In-situ Study of Redox-Transmetalation Reaction between GeO₂ and Zn.

A schematic illustration of the process for synthesizing mesoporous Ge materials *via* a redox-transmetalation reaction between Zn⁰ and Ge⁴⁺ (GeO₂) is shown in Figure 7. 1a. Hollow GeO₂ nanoparticles react with Zn vapour at a temperature well above the melting temperature of Zn metal, with Ge and ZnO forming after the ZRR. Subsequently, the by-product ZnO is removed completely using hydrochloric acid, resulting in hollow mesoporous Ge nanoparticles. According to a previous study,²³ we synthesized hollow GeO₂ nanoparticles *via* the hydrolysis of Ge⁴⁺ and Sn⁴⁺ precursors (Ge⁴⁺/Sn⁴⁺ molar ratio = 1 : 1) under basic conditions. This simultaneously generated insoluble GeO₂ and Sn(OH)₄ as white precipitates. The gradual dissolution of Sn(OH)₄ under basic conditions led to the formation of hollow GeO₂ nanoparticles. The surface morphology and microstructure of the as-synthesized GeO₂ nanoparticles were characterized using scanning electron microscopy (SEM) and transmission electron microscopy (TEM), as shown in Figure 7. 1b. It was found that uniform ellipsoidal GeO₂ nanoparticles with sizes of 200–300 nm were synthesized; the void space within the particles was indicative of their hollow structure. The X-ray diffraction (XRD) pattern of the hollow GeO₂ particles suggested that the particles have a crystalline structure and are of trigonal GeO₂ (JCPDS Card No. 36-1463) (Figure 7. 1c). The resulting GeO₂ particles react with Zn metal *via* a ZRR process at a certain temperature range as the following chemical reaction:



That a redox-transmetalation process corresponding to $2\text{Zn}^0 + \text{Ge}^{4+} \rightarrow 2\text{Zn}^{2+} + \text{Ge}^0$ occurs was confirmed by temperature-dependent *in-situ* X-ray absorption fine structure (XAFS) spectroscopy performed during the ZRR process. Since the spectroscopic method yields atomic-selective structural information related to the elements present, Ge and Zn K-edge XAFS measurements can elucidate the thermal dependence of the phase transition for every element on the ZRR.

The variations in the normalized Ge and Zn K-edge X-ray absorption near edge structure (XANES) spectra are shown in Figure 7. 2, while the corresponding radial distribution functions (RDFs) of the extended XAFS (EXAFS) spectra for temperatures of 25–600 °C (heating rate = 2.5 °C/min) are shown in Figures 7. 1d and 7. 1e. The spectral features corresponding to the oxide phase (GeO₂) and metallic Zn at room temperature change abruptly and simultaneously to those corresponding to metallic Ge and ZnO, respectively, at 420 °C. In particular, the Ge-O and Ge-O-Ge peaks of the oxide phase in the RDFs disappear and metallic Ge-Ge peak are observed (Figure 7. 1d), while the Zn-Zn metallic peak transforms into one corresponding to an oxide phase (ZnO) (Figure 7. 1e). The fact that the XANES and EXAFS spectral features remain unchanged up to 600 °C indicates the successful formation of metallic Ge phase from GeO₂ through the redox-transmetalation process.

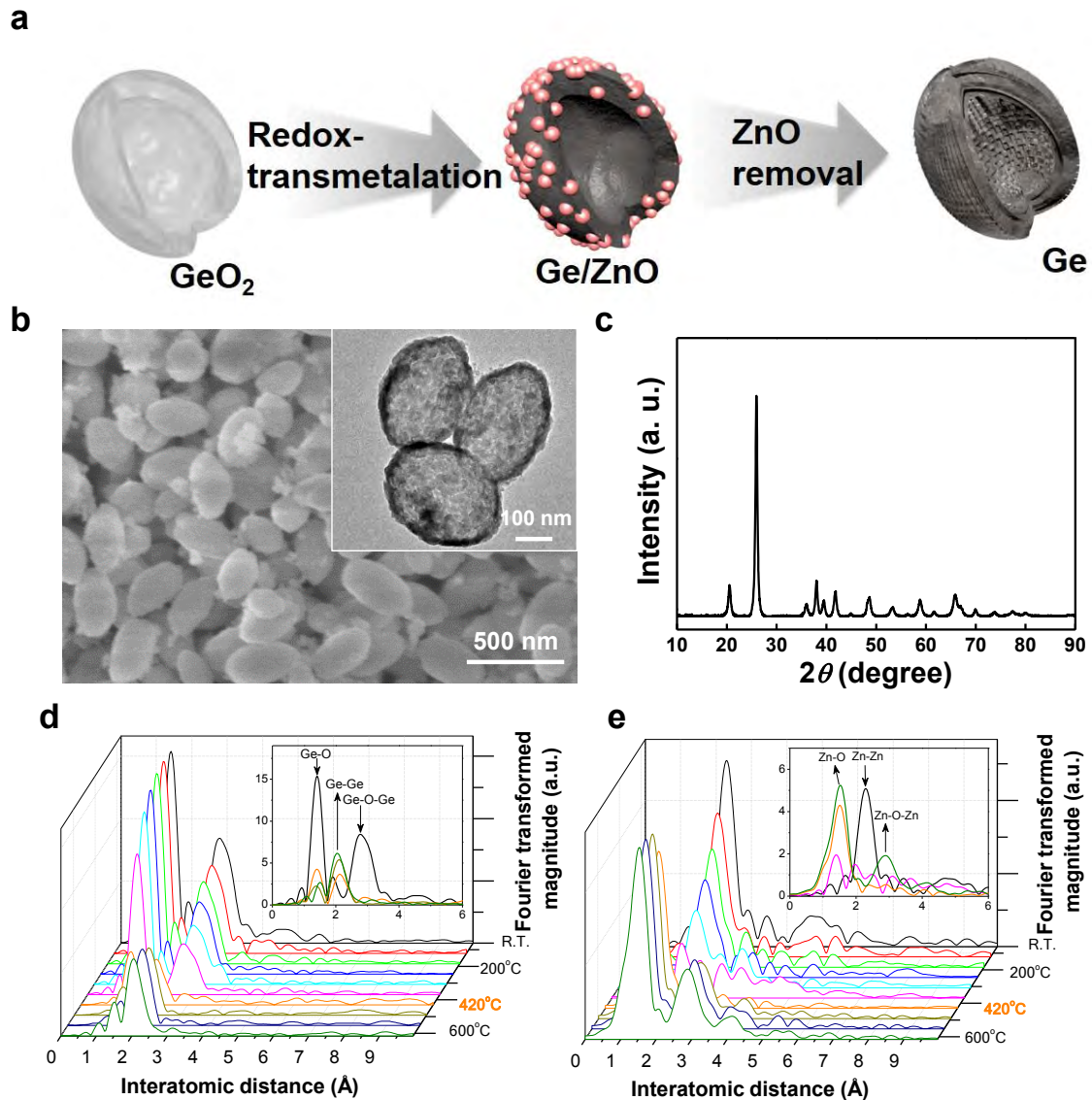


Figure 7. 1 (a) Schematic illustration of the method for synthesizing mesoporous Ge materials via a unique redox-transmetalation process. (b) SEM images of the synthesized GeO_2 particles showing their ellipsoidal structure. Inset is a HRTEM image of GeO_2 particles showing their hollow structure. (c) XRD pattern of the as-synthesized hollow GeO_2 particles. Radial distribution functions of (d) the Ge K-edge k^3 and (e) the Zn K-edge k^3 -weighted XAFS spectra as functions of the temperature.

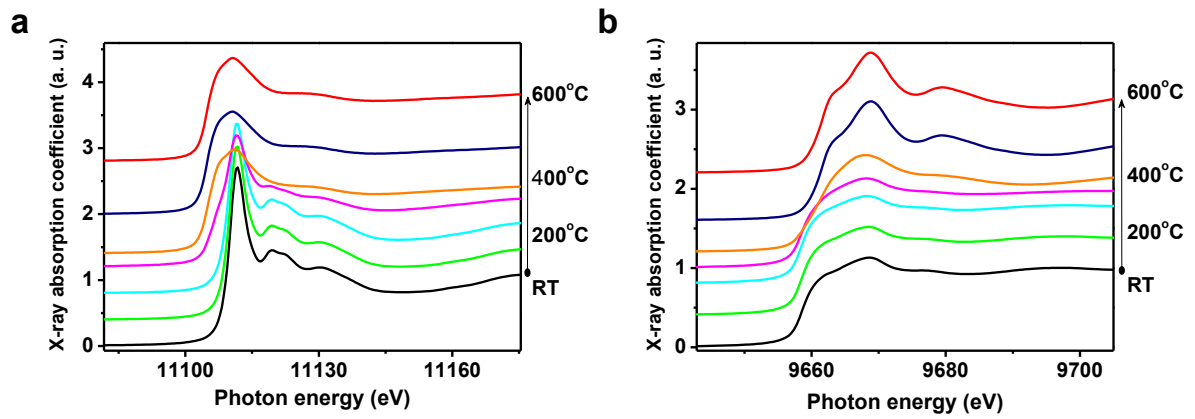


Figure 7. 2 (a) Normalized Ge and (b) Zn K-edge XANES spectra as function of temperature.

On the basis of the *in-situ* XAFS spectroscopy results, we performed a ZRR reaction between hollow GeO₂ particles and Zn metal at several temperatures. A mixture of hollow GeO₂ nanoparticles and Zn (GeO₂/Zn weight ratio = 1:1.25) was heated at 390, 420, and 450 °C for 3 h and subsequently rinsed with 1 M HCl to dissolve the ZnO formed as by-product. Next, the resulting products were characterized by XRD analysis (Figure 7. 3c). The concentration of each component (*i.e.*, the Ge/GeO₂ ratio) was estimated from the areas under the XRD peaks (Figure 7. 3d). Even at temperatures lower than the melting temperature of Zn, a small amount of Ge (14.7%) was produced, owing to the exothermal heat generated during the ZRR process (see top of Figure 7. 3c). When the reaction temperature reached the melting temperature of Zn (420 °C), Ge was formed in a greater amount (41.6%), indicating that a larger portion of GeO₂ was transformed into Ge (see middle of Figure 7. 3c). With a further increase in the reaction temperature to 450 °C, all of the GeO₂ was completely converted into pure metallic Ge (see bottom of Figure 7. 3c). The ZRR (at 450 °C) of the hollow GeO₂ nanoparticles led to the formation of shape-preserving mesoporous Ge nanoparticles, without there being a significant change in the dimensions of the nanoparticles (SEM image in Figure 7. 3a) or a change in the original hollow structure of the GeO₂ nanoparticles (TEM image in Figure 7. 3b). Further, high-resolution TEM confirmed that highly crystalline Ge was obtained after the ZRR process (inset of Figure 7. 3b).

The crystallite sizes of the Ge nanoparticles formed at different temperatures were calculated using the Scherrer formula and the XRD data.²⁹ The average size of the crystalline domains was calculated using the following formula:

$$\tau = K\lambda/\beta\cos\theta \quad (2)$$

where K is a dimensionless shape factor, λ is the X-ray wavelength, β is the degree of line broadening at half the maximum intensity, and θ is the Bragg angle. It was found that the crystallite sizes of the Ge particles synthesized at 390, 420, and 450 °C were 118, 149, and 157 nm, respectively. With an increase in the ZRR temperature, the size of the Ge crystals increased significantly (Figure 7. 3d). A Brunauer-Emmett-Teller (BET) analysis indicated that the hollow GeO₂ nanoparticles had a BET surface area of 37.84 m² g⁻¹, while the hollow Ge nanoparticles had a BET surface area of 80 m² g⁻¹ (Figure 7. 3e), indicating that a number of mesopores were formed during the ZRR process. The pore size distribution, obtained using the Barrett-Joyner-Halenda (BJH) method, suggested that the hollow Ge nanoparticles had a narrower pore size distribution (smaller than 20 nm in diameter) than that of the hollow GeO₂ nanoparticles, which ranged from 10 to 80 nm in diameter (Figure 7. 3f).

However, these nanomaterials have several disadvantages, which include (i) high cost to synthesize due to the complexity of their synthesis processes, (ii) the low volumetric energy density resulting from the lowered tap density of the nanoparticles, and (iii) undesired side reactions between the electrode and electrolyte owing to the large surface areas.⁴

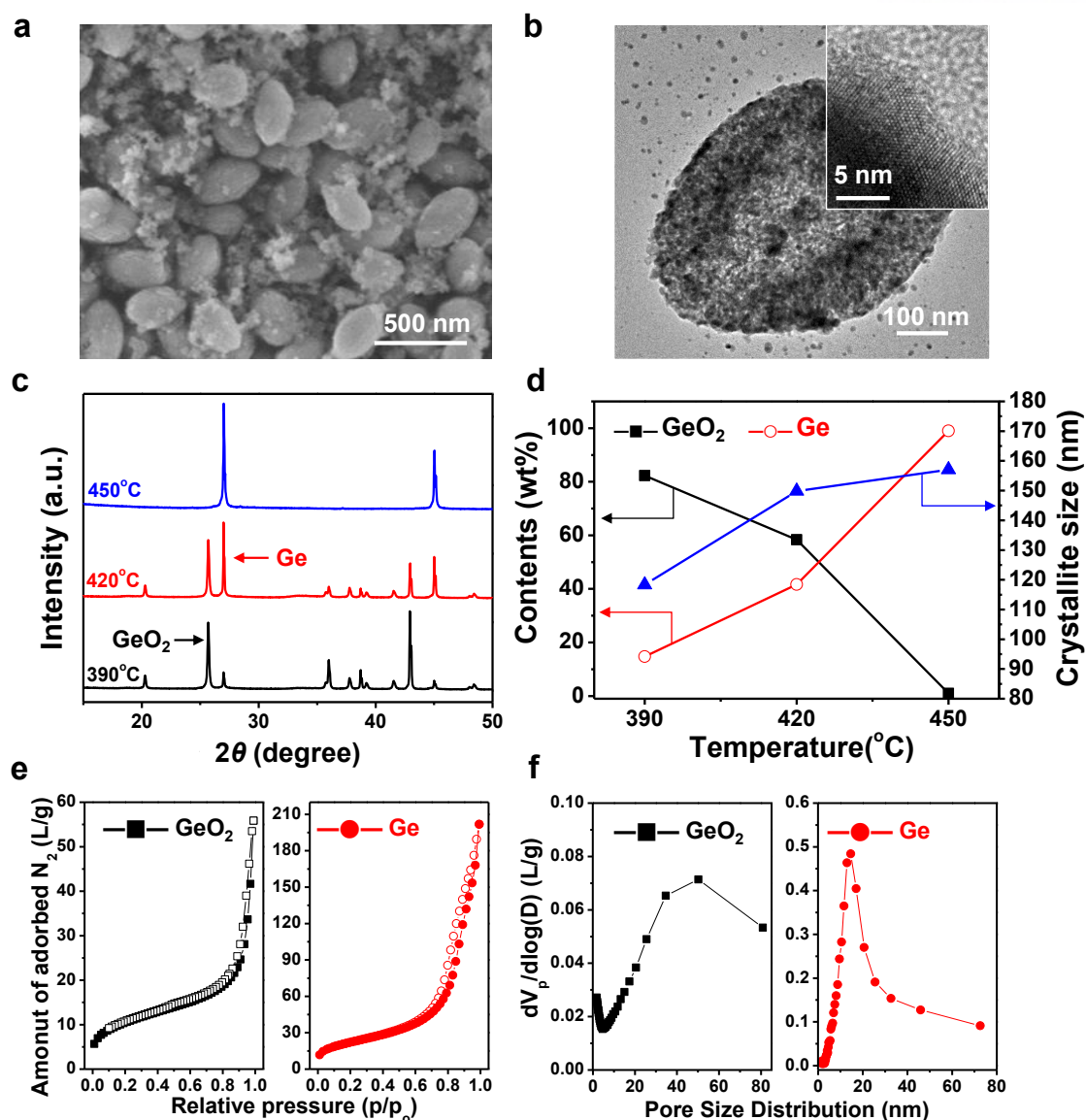


Figure 7. 3 Characterization of hollow Ge particles synthesized by the ZRR process. (a) SEM image of shape-preserving mesoporous Ge particles with a hollow structure. (b) TEM image of the Ge particles showing the presence of mesopores. In the inset, the crystalline structure of the Ge particles can be seen clearly. (c) XRD patterns of hollow Ge particles synthesized from hollow GeO₂ nanoparticles at three different reaction temperatures (390, 420, and 450 °C). (d) Concentration and crystallite size of Ge, as estimated from the XRD pattern shown in Figure 7. 3c. (e) Nitrogen adsorption-desorption plots and (f) pore size distribution plots of the hollow GeO₂ and mesoporous Ge ellipsoidal particles obtained by the ZRR process at 450 °C

7.3.2. Synthesis of Mesoporous Ge Particles from Bulk GeO₂ Particles.

In addition to synthesizing Ge nanomaterials, we employed the ZRR process to fabricate micrometer-sized bulk GeO₂ particles. SEM images of commercially available bulk GeO₂ particles show large secondary particles (10–20 μm), which formed by the irregular stacking of primary particles (200–500 nm). Further, tiny pores are formed in the stacked regions of the primary particles (Supporting Information, Figures 7. 4a and 7. 4b). The XRD pattern of the GeO₂ particles indicates a crystalline structure consisting of a trigonal GeO₂ phase (Figure 7. 4c).³⁰ The ZRR process for synthesizing metallic Ge from bulk GeO₂ particles with a low surface area requires additional heat. When the bulk GeO₂ reacted with Zn vapour at 550 °C for 3 h, most of the GeO₂ was converted into Ge; however, a small amount of GeO₂ remained (Figure 7. 5). It should be noted that the GeO₂ particles, which were initially composed of a trigonal phase, transformed such that they consisted of a tetragonal phase (JCPDS Card No. 35-0729), owing to the additional heat generated during the ZRR process.

When the bulk GeO₂ particles were reacted with Zn vapour in the presence of NaCl (employed as a heat scavenger) at 600 °C for 3 h in an argon atmosphere, they resulted in pure Ge particles (z600-Ge) and ZnO (by-product), with no unreacted GeO₂ being present, as confirmed by the XRD pattern (Figure 7. 6c). During the ZRR process, the secondary GeO₂ particles broke into numerous submicron-sized primary particles and were simultaneously converted into submicron-sized Ge particles. Figures 7. 6a and b show SEM images of the z600-Ge particles of 200–500 nm in size. In general, metallothermic reduction processes generate large amounts of heat, resulting in the collapse of original structure of the metal oxide material.^{31,32} To solve this problem, we employed NaCl as a heat scavenger to preserve the original structure of the GeO₂ particles after the ZRR process. Powders of GeO₂, NaCl, and Zn (GeO₂/Zn/NaCl = 1 : 1.25 : 2.25 by mass) were mixed homogeneously in an argon-filled glove box. After the completion of the chemical reduction process, the NaCl was removed by washing the product several times with deionised water, while the ZnO formed as a by-product was removed with HCl. The XRD pattern of the as-synthesized Ge/ZnO composite indicated that it contained a large amount of ZnO (as a by-product) and the NaCl salt used as a heat scavenger (see bottom of Figure 7. 6c). When the composite material was dissolved in a 1 M HCl solution, the ZnO was completely removed, as indicated by the XRD pattern shown in Figure 7. 6c (see top). After the complete removal of ZnO and NaCl, the XRD pattern of the z600-Ge particles suggested that the particles had a crystalline structure of diamond cubic Ge (JCPDS Card No. 04-0545).

Meanwhile, when the ZRR temperature of the bulk GeO₂ was increased to 700 and 800 °C, a mixture of mesoporous/macroporous particles and micrometer-sized aggregated porous Ge particles were synthesized, respectively, owing to the excessive exothermic heat generated (Figure 7. 7). Using

the Scherrer formula, the crystallite sizes of the Ge particles synthesized at 600, 700, and 800, were found to be 93, 149, and 162 nm, respectively. With an increase in the reduction temperature, the size of the Ge particles increased significantly (Figure 7. 6d). Thus, the reaction temperature affects both the particle size and the crystallite size. Raman spectroscopy is another tool that can yield information on the intrinsic characteristics of GeO₂ and metallic Ge. Figure 7. 6e shows the Raman spectra of z600-Ge and bulk GeO₂. The spectrum of the bulk GeO₂ powder shows a strong peak at 448 cm⁻¹, which corresponds to symmetric Ge-O-Ge stretching, while the bands at 167 and 260 cm⁻¹ correspond to the complex translation and rotation of the GeO₄ tetrahedra (see bottom of Figure 7. 6e).¹⁵ In the Raman spectrum of z600-Ge, two peaks, corresponding to crystalline and amorphous Ge, are observed at 300 cm⁻¹ and 270 cm⁻¹, respectively (inset of Figure 7. 6e).²⁷ In addition, nitrogen adsorption BET measurements indicated that the specific surface area of commercially available bulk GeO₂ is very low (0.01 m² g⁻¹), while that of z600-Ge is significantly higher (~15 m² g⁻¹), owing to the formation of mesopores during the ZRR process (Figure 7. 6f).

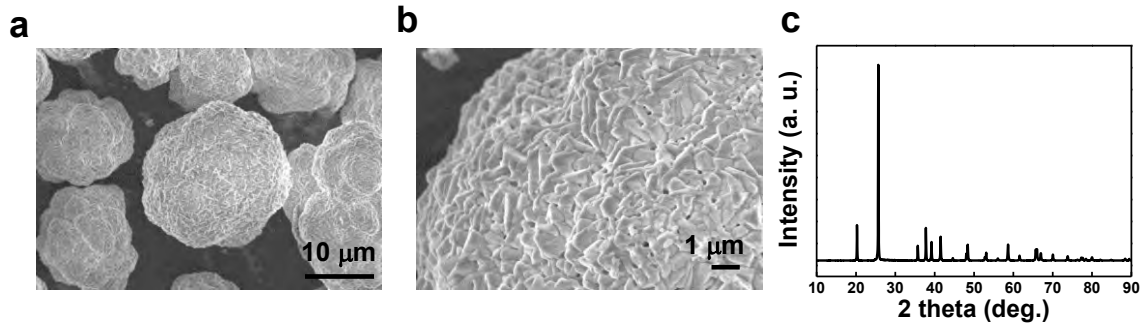


Figure 7. 4 (a) SEM image of bulk GeO_2 powder and (b) its magnification show that large secondary particles (10-20 μm) are irregularly stacked by primary particles (200-500 nm in size) and tiny pores are formed in the stacked regions of primary particles. (c) XRD pattern of the bulk GeO_2 particles shows that the GeO_2 has a trigonal crystalline phase.

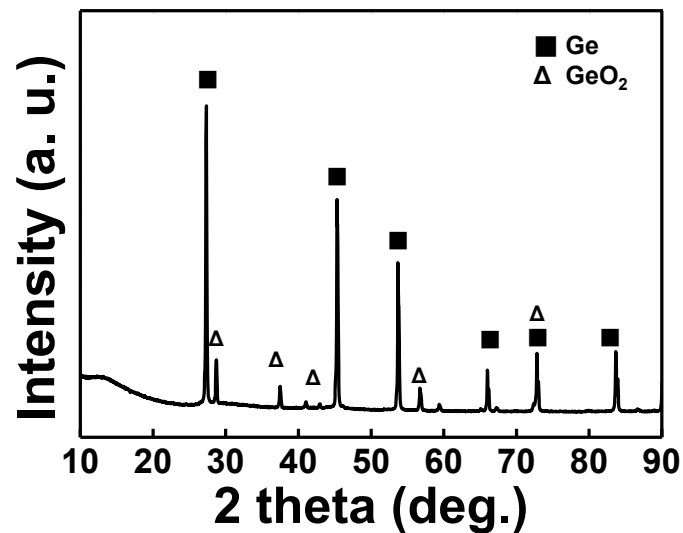


Figure 7. 5 XRD pattern of as-synthesized mesoporous Ge particles synthesized by ZRR reaction of bulk GeO_2 and Zn vapor at 550 $^{\circ}\text{C}$ for 3h. Small portion of GeO_2 with tetragonal crystalline phase are still remained after the chemical reduction reaction.

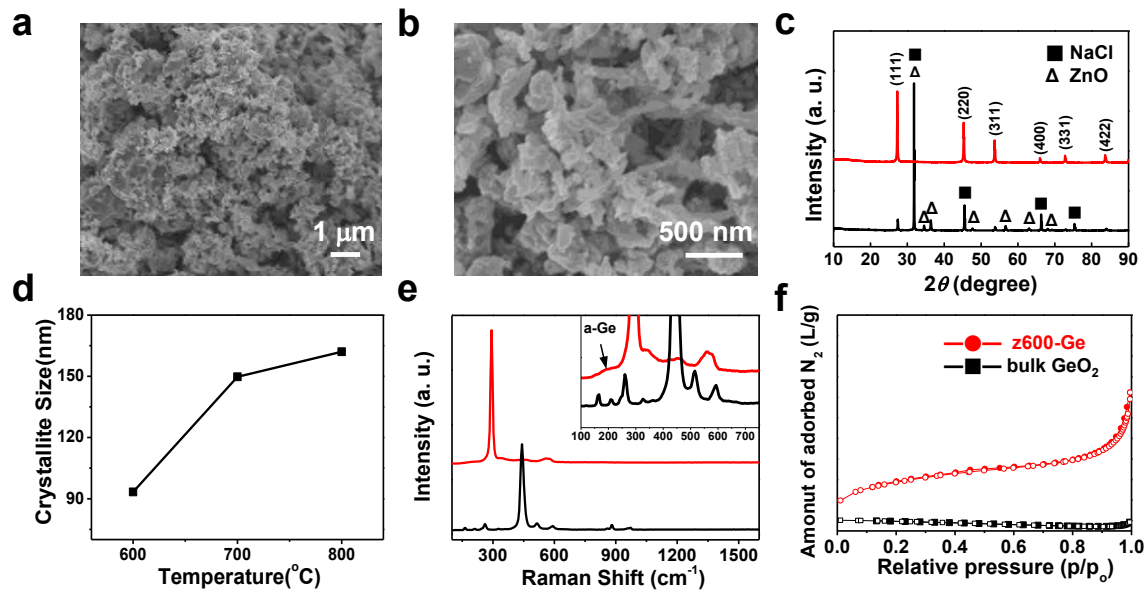


Figure 7. 6 Characterization of the mesoporous Ge particles synthesized from bulk GeO_2 by the ZRR process at 600 °C. (a) Low-magnification and (b) high-magnification SEM images of the as-synthesized z600-Ge. (c) XRD pattern of the sample obtained immediately after the ZRR process (bottom) and that of the HCl-treated sample (top). (d) Crystallite sizes of the zGe samples obtained at three different temperatures. (e) Raman spectra of the z600-Ge particles (red line) and bulk GeO_2 (black line). Inset indicates that the z600-Ge particles contained both crystalline Ge and amorphous Ge. (f) Nitrogen adsorption-desorption plots of bulk GeO_2 and the z600-Ge particles.

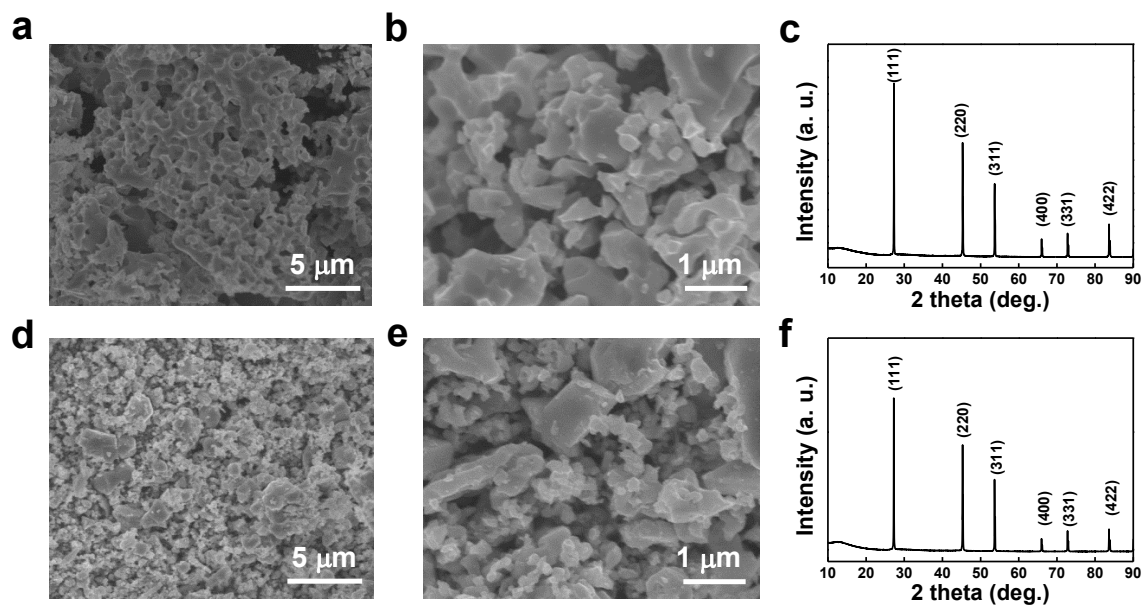


Figure 7. 7 Characterization of mesoporous Ge materials obtained by two different ZRR temperatures. (a) SEM image of z800-Ge particles at 800 °C and (b) its magnification show that macroporous z800-Ge particles are formed. (c) XRD pattern of the z800-Ge particles clearly shows a diamond cubic Ge (JCPDS card no. 04-0545) crystalline structure. (d) SEM image of z700-Ge particles synthesized at 700 °C and (e) its magnification show macro-/mesoporous z700-Ge particles. (f) XRD pattern of the z700-Ge also shows a diamond cubic Ge crystalline structure.

7.3.3. Electrochemical Properties of Mesoporous Ge Anode.

The galvanostatic discharge-charge cycling of the Ge particles was performed for potentials of 0.01–1.5 V at different current densities. Commercially available anodes containing micrometer-sized Ge particles showed a remarkably high initial coulombic efficiency of 93.3%, owing to the good electrical conductivity of single-crystalline Ge (Figure 7. 9).¹⁴ However, an electrode of bulk Ge exhibited a capacity retention rate as low as 17.5% at a 0.2 C rate after 100 cycles; this was because of the large volume change experienced by the Ge particles during battery operation.¹⁴ In contrast, an electrode of the hollow Ge nanoparticles obtained by the ZRR process at 450 °C (seen in Figure 7. 3) showed high cycling stability, exhibiting outstanding capacity retention (91.4%) at 0.5 C after 200 cycles (Figure 7. 8b). This is attributed to the peculiar structure of the anode, which had mesopores in the shell part and nanocavities in the interior; these can provide extra void space and accommodate the large volume changes occurring during the lithiation/delithiation process. However, the initial coulombic efficiency of the anode of mesoporous and hollow Ge particles was 74%, which corresponded to a discharge (lithiation) capacity of 1470 mA h g⁻¹ and a charge (delithiation) capacity of 1086 mA h g⁻¹ (Figure 7. 8a). This was due to a side reaction of the nanoparticles, which had a high surface area.

Given the various advantages and disadvantages of nanomaterials, the z600-Ge particles, which had a lower surface area and a higher crystallinity than those of hollow Ge particles, may be more suitable anodic materials for LIBs. Figure 7. 8c shows the first cycle voltage profile corresponding to the discharge and charge of the z600-Ge electrodes at a rate of 0.05 C when used in a coin-type half-cell. The first discharge and charge capacities of the z600-Ge electrode were 1585 mA h g⁻¹ and 1410 mA h g⁻¹, respectively; these corresponded to an initial coulombic efficiency of 89%. It should be noted that an increase in the ZRR temperature leads to an increase in the initial coulombic efficiency. This suggests that increasing the crystallite and particle sizes of Ge increases its electrical conductivity, resulting in an increase in the kinetics of lithiation and delithiation. The Ge-based electrodes (z700-Ge and z800-Ge) obtained by the ZRR process at 700 and 800 °C showed markedly improved initial coulombic efficiencies of 90 and 92.2%, respectively (Figure 7. 10a and 10 c). However, as expected, the cycling performances of both the electrodes (z700-Ge and z800-Ge) resulted in significant capacity fading, because of the large volume changes occurring owing to the increase in particle size. The z700-Ge and z800-Ge anodes showed capacity retention rates of 59% and 17%, respectively, at a rate of 0.2 C after 100 cycles (Figures 7. 10b and 10d). In contrast, the z600-Ge electrode exhibited outstanding long-term cycling stability, exhibiting a capacity retention rate of more than 99.5% at 0.5 C rate after 300 cycles (Figure 7. 8d). Furthermore, the coulombic efficiency per cycle was more than 99.5%, demonstrating that the mesopores act as effective active sites for reversible electrochemical lithium storage.

The excellent electrochemical performances of the z-Ge series of electrodes can be explained as follows: (i) the crystallite size of the Ge particles depends on the ZRR temperature and affects the initial coulombic efficiency; (ii) decreasing the crystallite size improves the cycling stability, as increasing the amorphous content within the Ge particles improves their electrochemical properties, while also preventing particle fracturing and decreasing the volume change experienced during cycling;³³ and (iii) when mesopores are present within an active material in a suitable number density, they can act as buffer spaces and accommodate the large volume changes experienced during the repeated cycling.

As a control experiment, we synthesized macroporous Ge particles using a well-known metallothermic reduction reaction, namely, a magnesiothermic reaction, which was performed at 700 °C for 1 h. Bulk GeO₂ was successfully converted into Ge particles (denoted as m-Ge) and MgO (by-product) ($\text{GeO}_2 (\text{s}) + 2\text{Mg} (\text{g}) \rightarrow 2\text{MgO} (\text{s}) + \text{Ge} (\text{s})$, $\Delta G^\circ(700 \text{ }^\circ\text{C}) = -599.63 \text{ kJ mol}^{-1}$). However, significantly aggregated Ge particles were obtained, owing to the large amount of heat generated during the chemical reduction process (Figure 7. 11a). An electrode of m-Ge showed an initial coulombic efficiency of 81.9% (Figure 7. 11c). In addition, the m-Ge electrode exhibited a gradual decay in capacity during cycling, showing a capacity retention rate of 73.7% at a rate of 0.2 C after 100 cycles; this was due to the large volume change experienced by the aggregated Ge particles (Figure 7. 11d).

Moreover, the z600-Ge electrode exhibited specific capacities of 1178, 1075, and 804 mA h g⁻¹ at current densities of 2.63 (2 C), 3.89 (3 C), and 6.47 A g⁻¹ (5 C), respectively, even though no coating layer (such as that of carbon, metal, or conductive polymers)³⁴⁻³⁸ was introduced on the Ge surface (Figure 7. 8e). The electrochemical performances of the anodes of the mesoporous Ge nanoparticles were tested in half cells. However, this is not sufficient to determine the suitability of the nanomaterials as anodic materials for LIBs. Thus, we employed a full cell (loading density of ~1 mA h cm⁻²), in which a z600-Ge electrode was coupled with a LiCoO₂ cathode. The first charge/discharge voltage profile of the Ge/LiCoO₂ full cell shows that it had a coulombic efficiency of 80% during precycling at a rate of 0.1 C for voltages of 2.5–4.2 V (see inset of Figure 7. 8f). During subsequent long-term cycling (including a 2nd cycle of charging/discharging, which was performed at 0.5 C), the anode exhibited a capacity retention rate of ~80% after 100 cycles (Figure 7. 8f). This demonstrates that the mesoporous z600-Ge is a promising anodic material for practical LIBs.

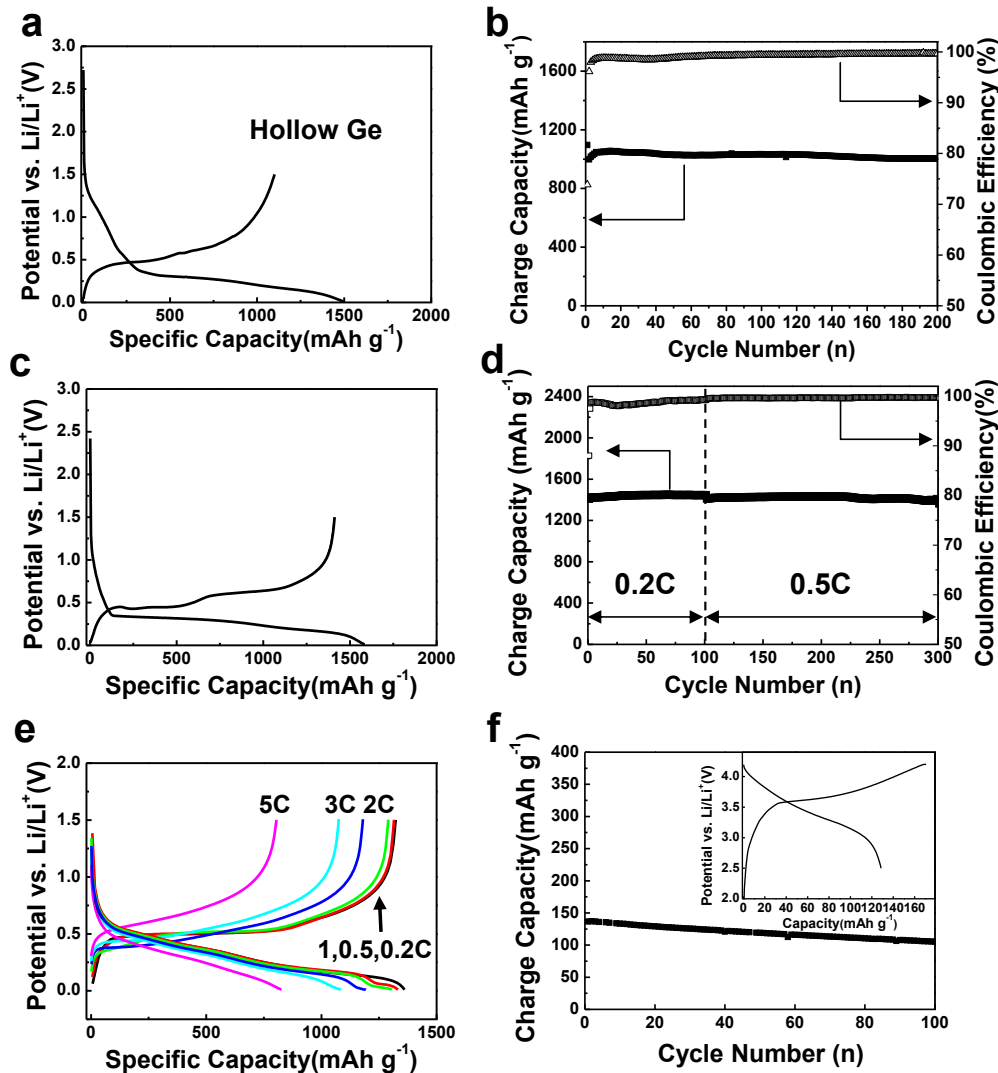


Figure 7. 8 Electrochemical performances of the electrodes formed using the hollow Ge and z600-Ge particles. (a) First-cycle voltage profile of the hollow Ge particles-based electrode obtained at a rate of 0.05 C in the range of 0.005–1.5 V. (b) Cycling performance of the hollow Ge particles-based electrode obtained at a rate of 0.2 C. (c) First-cycle voltage profile of the z600-Ge electrode at 0.05 C in the range of 0.005–1.5 V. (d) Cycling performances of the z-600Ge electrode at 0.2 C (1st to 100th cycles) and 0.5 C (101th to 300th cycles). (e) Rate capabilities of the z600-Ge electrode at the same charge/discharge rates. (f) Cycling performance of a full cell (LiCoO₂ cathode and z600-Ge anode) at 0.5 C in the range of 2.5–4.2 V. The inset shows the first-cycle voltage profile of the full cell.

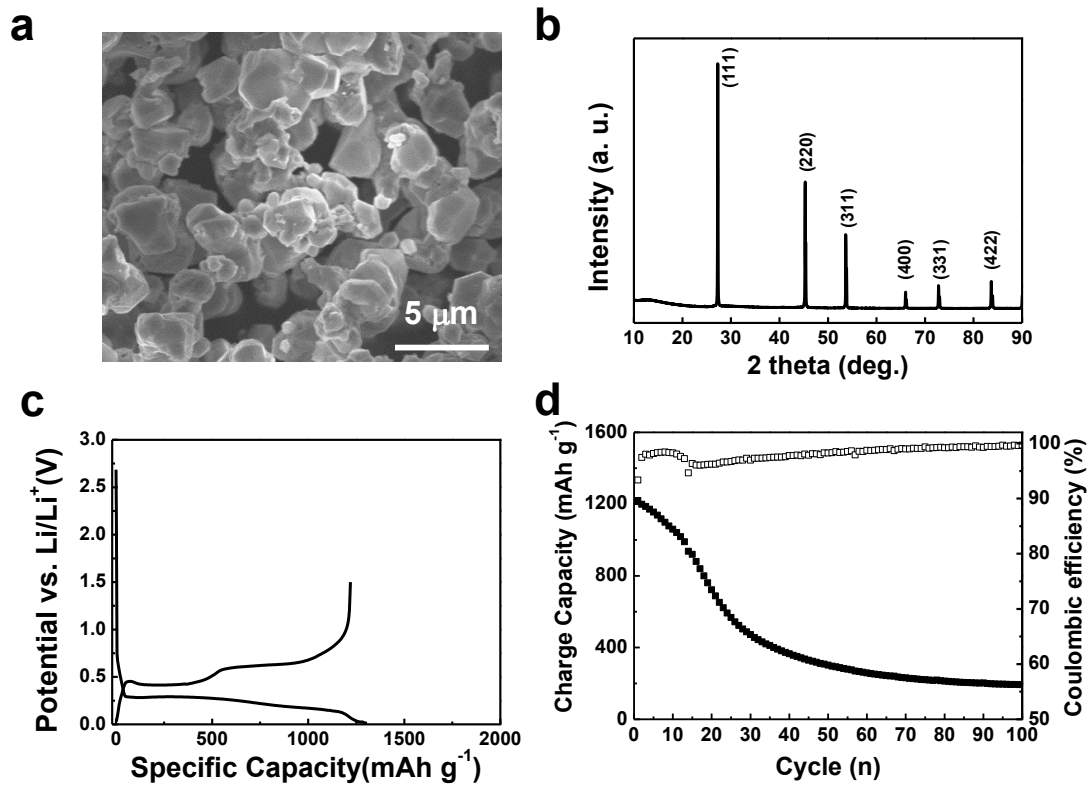


Figure 7. 9 Characterization of commercially available Ge particles (c-Ge). (a) SEM image of c-Ge particles showing an average particle size of 3 μm and (b) XRD pattern of c-Ge showing a diamond cubic Ge crystalline structure. Electrochemical performances of c-Ge electrodes: (c) First cycle voltage profile was obtained at a rate of 0.05C in the range of 0.005-1.5 V. The discharge capacity of the c-Ge electrode was 1306 mAh g⁻¹ with initial coulombic efficiency of 93.3%. (d) Cycle performance of the c-Ge electrode showed the poor capacity retention of 17.5% at 0.2C rate after 100 cycles, compared to initial capacity.

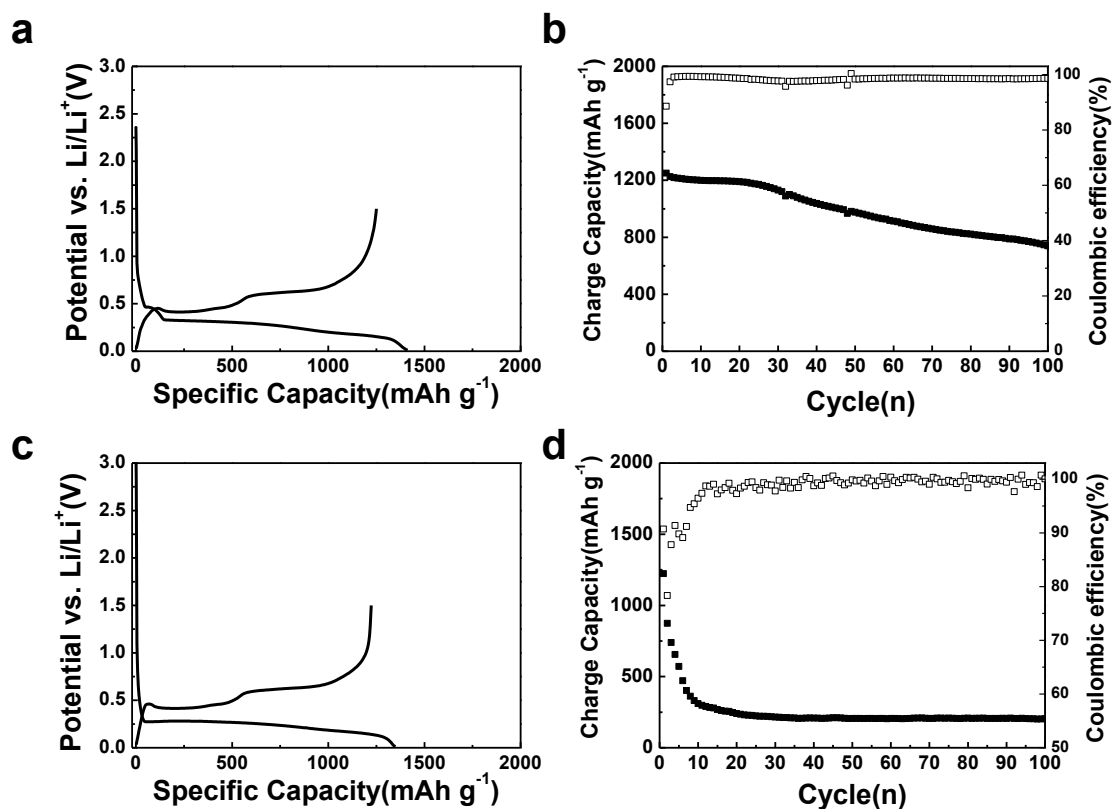


Figure 7. 10 Electrochemical performances of z700-Ge and z800-Ge electrodes. (a) The first cycle voltage profile of the z700-Ge was obtained at a rate of 0.05C in the range of 0.01-1.5 V. The discharge capacity of the z700-Ge electrode was 1411 mAh g⁻¹ with initial coulombic efficiency of 90%. (b) Cycle performance of the z700-Ge electrode was obtained at 0.2 rate. (c) At the same electrochemical test condition, the discharge capacity of the z800-Ge electrode was 1348 mAh g⁻¹ with initial coulombic efficiency of 92.2%. (d) Cycle performance of the z800-Ge electrode was obtained at 0.2 C rate. The z700-Ge and z800-Ge anodes showed capacity retentions of 59% and 17% at a 0.2 C rate after 100 cycles, respectively. With increasing ZRR reaction temperature, initial coulombic efficiency of the resulting Ge particles was increased, but its cycling performance was significantly decayed due to a serious aggregation of Ge particles during the ZRR synthesis.

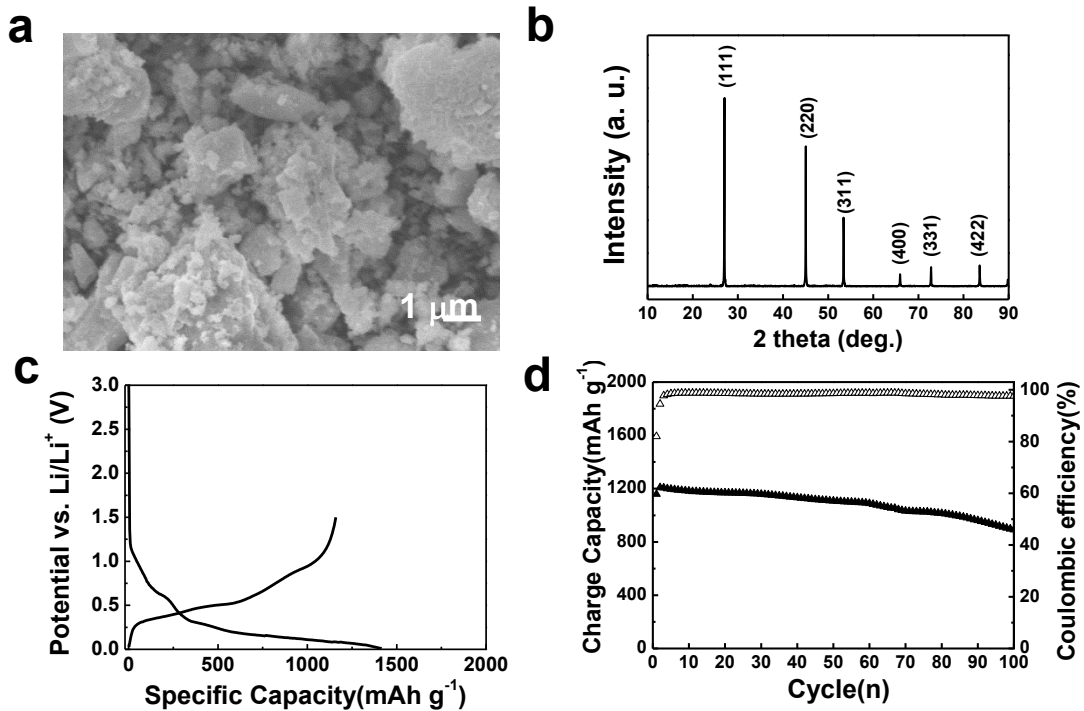


Figure 7. 11 Characterization of Ge particles (m-Ge) obtained by a magnesiothermic reaction of bulk GeO₂ and Mg vapor. (a) SEM image of the m-Ge powders showing a serious aggregated particles and (b) XRD pattern of the m-Ge showing a diamond cubic crystalline Ge structure. Electrochemical performances of the m-Ge electrodes: (c) First cycle voltage profile was obtained at a rate of 0.05C in the range of 0.005-1.5 V. The discharge capacity of the Ge electrode was 1415 mAh g⁻¹ with initial coulombic efficiency of 81.9%. (d) Cycle performance of the m-Ge electrode was obtained at 0.2C rate. The m-Ge electrode exhibited the capacity retention of 73.7% after 100 cycles, compared to initial capacity.

7.3.4. Discussion of Electrochemical Properties of Ge Electrode

Electrodes of mesoporous Ge (fabricated by a ZRR process) showed high specific capacities, outstanding cycling stabilities, and excellent rate capabilities. However, the other critical issue determining the suitability of an anodic material for use in LIBs is whether a stable solid-electrolyte interphase (SEI) layer is formed on the electrode surface during repeated lithiation/delithiation.³⁹

It should be noted that the surface chemistry of metal-based electrodes with high theoretical capacities is a critically important issue that influences the lithiation/delithiation kinetics and the interfacial stability of the electrodes during long-term cycling. To investigate the surface chemistry of the Ge electrodes, ex-situ X-ray photoelectron spectroscopy (XPS) analyses were performed. Figure 7. 12 shows the F 1s and C 1s XPS spectra of a Ge electrode after 300 cycles. Two major peaks were seen in the F 1s XPS spectrum (Figure 7. 12b): one was assignable to the C-F bond (686.3 eV) produced by the decomposition of fluoroethylene carbonate (FEC) ($\text{FEC} + \text{Li}^+ + \text{e}^- \rightarrow \text{CH}_2=\text{CHF} + \text{Li}_2\text{CO}_3$, $\text{CH}_2=\text{CHF} \rightarrow \text{C-F}$ containing polymer species)³⁹ and the other was attributable to LiF (684.5 eV) formed by the reaction of the C-F-containing polymer species $(\text{CH}_2-\text{CHF})_n$ with Li^+ ions and electrons, as described in Figure 7. 12c. This demonstrates that employing FEC as an additive is an efficient means of forming an SEI layer on Ge electrodes and thus preventing unwanted electrolyte decomposition during cycling. The C1s XPS spectrum shows peaks corresponding to four types of carbon: C-H (285.0 eV), C-O-C/ CH_2 -CHF (286.5 eV), O-C=O (carbonate species; 288.0 eV), and $\text{Li}_2\text{CO}_3/\text{C-F}$ (290.5 eV) (Figure 7. 12a). The appearance of two peaks corresponding to carbon bonded to fluorine (C-F and CH_2 -CHF), at 286.5 and 290.5 eV, respectively,⁴⁰ confirms that FEC acts as an SEI-forming agent on the z600-Ge electrode during long-term cycling.

More interestingly, when we investigated the swelling of the z600-Ge electrodes after repeated cycles, we found that the electrode thickness increased significantly by up to 150% during the first cycle, owing to the formation of lithium-alloying products (Fig. 7. 13b). However, during subsequent long-term cycling (*i.e.*, till the 300th cycle), the electrode thickness is quite similar to that after the first cycle (Figures 7.13c-13f), increasing to 157% of the original value. This result once again demonstrates that the stable SEI layer on the z600-Ge electrode surface forms and the mesoporous structure of z600-Ge mitigates the large volume change occurring during long-term cycling, resulting in highly stable cycling performance. In contrast, commercial Ge electrode showed a remarkable increase of electrode thickness as function of cycles. After 300 cycles, the electrode swelling of >350% was observed (Figure 7. 14).

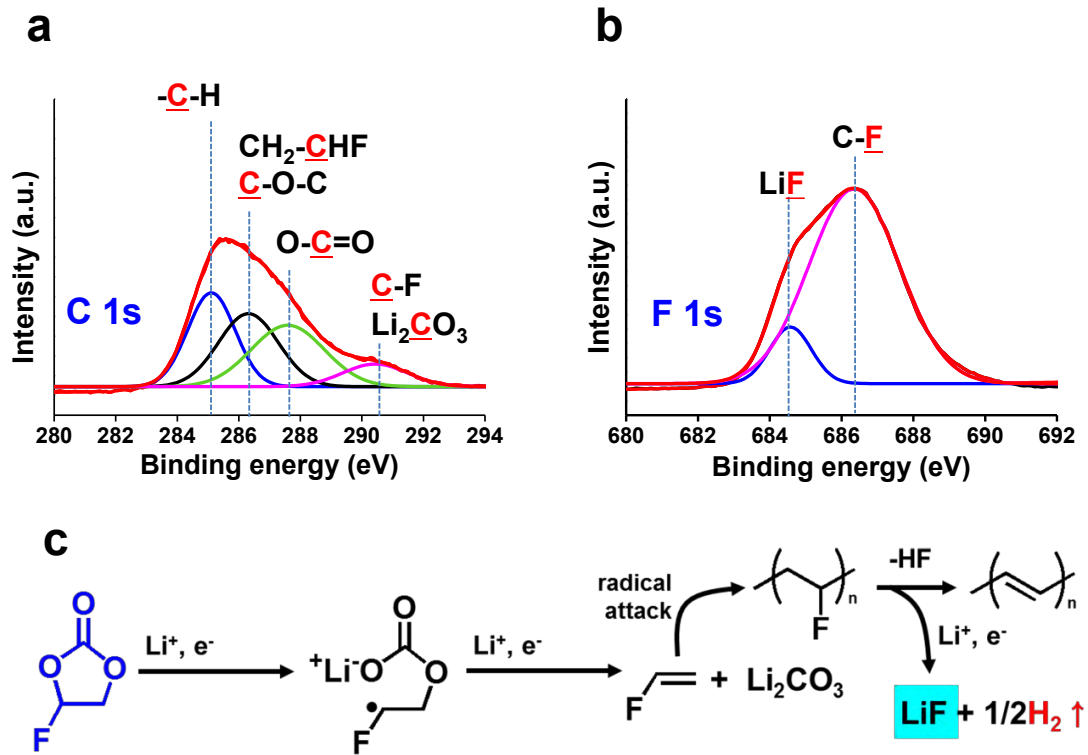


Figure 7. 12 (a) C 1s and F 1s XPS spectra of the mesoporous z-Ge electrode after 300 cycles. (c) Reaction mechanism showing the formation of the C-F bond and LiF.³⁹

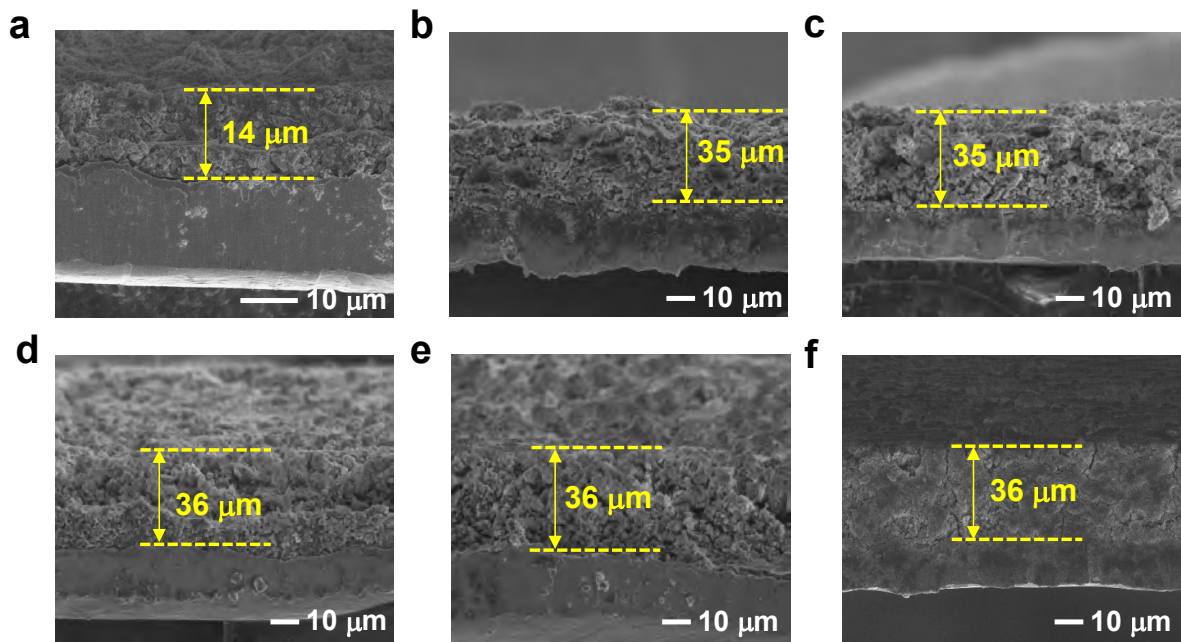


Figure 7. 13 Cross-sectional SEM images of the z600-Ge electrode (a) before and after (b) the 1st cycle, (c) 5th cycle, (d) 10th cycle, (e) 20th cycle, and (f) 300th cycle.

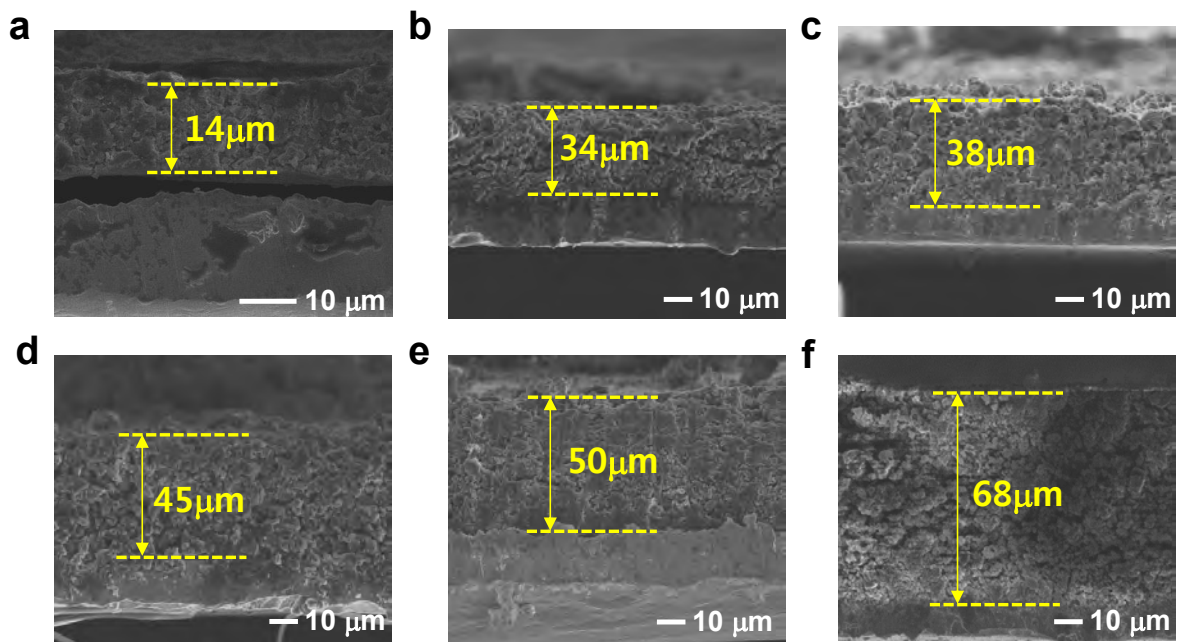


Figure 7. 14 Cross-sectional SEM images of the commercial-Ge electrode (a) before and after (b) the 1st cycle, (c) 5th cycle, (d) 10th cycle, (e) 20th cycle, and (f) 300th cycle.

7.4. Conclusion

In summary, we demonstrated a simple and cost-effective large-scale process for synthesizing mesoporous Ge particles *via* a unique redox-transmetalation reaction between GeO₂ and Zn powders. Using *in-situ* XAFS analyses performed at various temperatures, the redox-transmetalation reaction was monitored. This method allowed us to preserve the shape of the original GeO₂ particles and to form additional mesopores in the resulting Ge particles. There are several other advantages of this technique. The low-temperature reduction process enabled us to synthesize metallic particles from inexpensive metal oxides on a large scale. Next, the resulting mesoporous Ge particles exhibited outstanding electrochemical properties when used as anode materials in LIBs, showing a specific capacity as high as ~1400 mA h g⁻¹, highly stable cycling performance (capacity retention rate of 99.5% after 300 cycles), and excellent rate capability (a specific capacity of 804 mA h g⁻¹ at a rate of 5 C). This simple strategy may open up an effective way for synthesizing mesoporous particles of other metals *via* a one-step synthetic reaction through an environmentally benign and cost-effective approach.

7.5. References

1. Nazri, G.-A.; Pistoia, G. *Lithium Batteries: Science and Technology*. Kluwer Academic/Plenum (2004).
2. Tarascon, J. M.; Armand, M. Issues and Challenges Facing Rechargeable Lithium Batteries. *Nature* **2001**, *414*, 359-367.
3. Ozawa, K. *Lithium Ion Rechargeable Batteries*. Wiley (2009).
4. Song, M.-K.; Park, S.; Alamgir, F. M.; Cho, J.; Liu, M. Nanostructured Electrodes for Lithium-Ion and Lithium-Air Batteries: The Latest Developments, Challenges, and Perspectives. *Mater. Sci. Eng. R* **2011**, *72*, 203-252.
5. Choi, N.-S.; Chen, Z.; Freunberger, S. A.; Ji, X.; Sun, Y.-K.; Amine, K.; Yushin, G.; Nazar, L. F.; Cho, J.; Bruce, P. G. Challenges Facing Lithium Batteries and Electrical Double-Layer Capacitors. *Angew. Chem. Int. Ed.* **2012**, *51*, 9994-10024.
6. Chockla, A. M.; Klavetter, K. C.; Mullins, C. B.; Korgel, B. A. Solution-Grown Germanium Nanowire Anodes for Lithium-Ion Batteries. *ACS Appl. Mater. Interf.* **2012**, *4*, 4658-4664.
7. Yuan, F.-W.; Tuan, H.-Y. Scalable Solution-Grown High-Germanium-Nanoparticle-Loading Graphene Nanocomposites as High-Performance Lithium-Ion Battery Electrodes: An Example of a Graphene-Based Platform toward Practical Full-Cell Applications. *Chem. Mater.* **2014**, *26*, 2172-2179.
8. Graetz, J.; Ahn, C. C.; Yazami, R.; Fultz, B. Nanocrystalline and Thin Film Germanium Electrodes with High Lithium Capacity and High Rate Capabilities. *J. Electrochem. Soc.* **2004**, *151*, A698-A702.
9. Liu, X. H.; Huang, S.; Picraux, S. T.; Li, J.; Zhu, T.; Huang, J. Y. Reversible Nanopore Formation in Ge Nanowires during Lithiation–Delithiation Cycling: An In Situ Transmission Electron Microscopy Study. *Nano Lett.* **2011**, *11*, 3991-3997.
10. Wang, D.; Chang, Y.-L.; Wang, Q.; Cao, J.; Farmer, D.; Gordon, R.; Dai, H. Surface Chemistry and Electrical Properties of Germanium Nanowires. *J. Am. Chem. Soc.* **2004**, *126*, 11602-11611.
11. Fuller, C. S.; Severiens, J. C. Mobility of Impurity Ions in Germanium and Silicon. *Phys. Rev.* **1954**, *96*, 21-24.
12. Liang, W.; Yang, H.; Fan, F.; Liu, Y.; Liu, X. H.; Huang, J. Y.; Zhu, T.; Zhang, S. Tough Germanium Nanoparticles under Electrochemical Cycling. *ACS Nano* **2013**, *7*, 3427-3433.
13. Seo, M.-H.; Park, M.; Lee, K. T.; Kim, K.; Kim, J.; Cho, J. High performance Ge nanowire anode sheathed with carbon for lithium rechargeable batteries. *Energy Environ. Sci.* **2011**, *4*, 425-428.
14. Chan, C. K.; Zhang, X. F.; Cui, Y. High capacity Li ion battery anodes using ge nanowires. *Nano Lett.* **2008**, *8*, 307-309.
15. Seng, K. H.; Park, M.-H.; Guo, Z. P.; Liu, H. K.; Cho, J. Catalytic Role of Ge in Highly Reversible GeO₂/Ge/C Nanocomposite Anode Material for Lithium Batteries. *Nano Lett.* **2013**, *13*, 1230-1236.
16. Yang, L. C.; Gao, Q. S.; Li, L.; Tang, Y.; Wu, Y. P. Mesoporous Germanium as Anode Material of High Capacity and Good Cycling Prepared by a Mechanochemical Reaction. *Electrochem. Commun.* **2010**, *12*, 418-421.
17. Xue, D. J.; Xin, S.; Yan, Y.; Jiang, K. C.; Yin, Y. X.; Guo, Y. G.; Wan, L. J. Improving the electrode performance of Ge through Ge@C core-shell nanoparticles and graphene networks. *J. Am. Chem. Soc.* **2012**, *134*, 2512-2515.

18. Kim, H.; Son, Y.; Park, C.; Cho, J.; Choi, H. C. Catalyst-Free Direct Growth of a Single to A Few Layers of Graphene on a Germanium Nanowire for the Anode Material of a Lithium Battery. *Angew. Chem. Int. Ed.* **2013**, *52*, 5997-6001.
19. Park, M. H.; Kim, K.; Kim, J.; Cho, J. Flexible Dimensional Control of High-Capacity Li-Ion Battery Anodes: From 0D Hollow to 3D Porous Germanium Nanoparticle Assemblies. *Adv. Mater.* **2010**, *22*, 415-418.
20. Wang, X. L.; Han, W. Q.; Chen, H.; Bai, J.; Tyson, T. A.; Yu, X. Q.; Wang, X. J.; Yang, X. Q. Amorphous Hierarchical Porous GeO_(x) as High-Capacity Anodes for Li Ion Batteries with Very Long Cycling Life. *J. Am. Chem. Soc.* **2011**, *133*, 20692-20695.
21. Li, S.; Chen, C.; Fu, K.; White, R.; Zhao, C.; Bradford, P. D.; Zhang, X. Nanosized Ge@CNF, Ge@C@CNF and Ge@CNF@C Composites via Chemical Vapour Deposition Method for Use in Advanced Lithium-Ion Batteries. *J. Power Sources* **2014**, *253*, 366-372.
22. Wei, W.; Guo, L. One-Step In Situ Synthesis of GeO₂/Graphene Composites Anode for High-Performance Li-Ion Batteries. *Part. Part. Syst. Charact.* **2013**, *30*, 658-661.
23. Li, L.; Seng, K. H.; Feng, C.; Liu, H. K.; Guo, Z. Synthesis of Hollow GeO₂ Nanostructures, Transformation into Ge@C, and Lithium Storage Properties. *J. Mater. Chem. A* **2013**, *1*, 7666-7672.
24. Li, D.; Seng, K. H.; Shi, D.; Chen, Z.; Liu, H. K.; Guo, Z. A Unique Sandwich-Structured C/Ge/Graphene Nanocomposite as an Anode Material for High Power Lithium Ion Batteries. *J. Mater. Chem. A* **2013**, *1*, 14115-14121.
25. Seng, K. H.; Park, M. H.; Guo, Z. P.; Liu, H. K.; Cho, J. Self-Assembled Germanium/Carbon Nanostructures as High-Power Anode Material for the Lithium-Ion Battery. *Angew. Chem. Int. Ed.* **2012**, *51*, 5657-5661.
26. Vaughn, D. D. II; Schaak, R. E. Synthesis, Properties and Applications of Colloidal Germanium and Germanium-Based Nanomaterials. *Chem. Soc. Rev.* **2013**, *42*, 2861-2879.
27. Chiasera, A.; Macchi, C.; Mariazzi, S.; Valligatla, S.; Lunelli, L.; Pederzoli, C.; Rao, D. N.; Somoza, A.; Brusa, R. S.; Ferrari, M. CO₂ Laser irradiation of GeO₂ planar waveguide fabricated by rf-sputtering. *Opt. Mater. Express* **2013**, *3*, 1561-1570.
28. Lee, W.-R.; Kim, M. G.; Choi, J. R.; Park, J. I.; Ko, S. J.; Oh, S. J.; Cheon, J. Redox-Transmetalation Process as a Generalized Synthetic Strategy for Core-Shell Magnetic Nanoparticles. *J. Am. Chem. Soc.* **2005**, *127*, 16090-16097.
29. Cullity, B. D. Elements of X-Ray Diffraction, Addison-Wesley (1978).
30. Smith, G. S.; Isaacs, P. B. The Crystal Structure of Quartz-like GeO₂. *Acta Crystallographica* **1964**, *17*, 842-846.
31. Won, C. W.; Nersisyan, H. H.; Won, H. I.; Lee, J. H. Refractory Metal Nanopowders: Synthesis and Characterization. *Curr. Opin. Solid State Mater. Sci.* **2010**, *14*, 53-68.
32. Luo, W.; Wang, X.; Meyers, C.; Wannemacher, N.; Sirisaksoontorn, W.; Lerner, M. M. Ji, X. Efficient Fabrication of Nanoporous Si and Si/Ge Enabled by a Heat Scavenger in Magnesiothermic Reactions. *Sci. Rep.* **2013**, *3*, 2222.
33. Cui, L.-F.; Ruffo, R.; Chan, C. K.; Peng, H.; Cui, Y. Crystalline-Amorphous Core-Shell Silicon Nanowires for High Capacity and High Current Battery Electrodes. *Nano Lett.* **2008**, *9*, 491-495.
34. Yu, Y.; Gu, L.; Zhu, C.; Tsukimoto, S.; van Aken, P. A.; Maier, J. Reversible Storage of Lithium in Silver-Coated Three-Dimensional Macroporous Silicon. *Adv. Mater.* **2010**, *22*, 2247-2250.
35. Yoo, H.; Lee, J.-I.; Kim, H.; Lee, J.-P.; Cho, J.; Park, S. Helical Silicon/Silicon Oxide Core-

- Shell Anodes Grown onto the Surface of Bulk Silicon. *Nano Lett.* **2011**, *11*, 4324-4328.
36. Wu, H.; Chan, G.; Choi, J. W.; Ryu, I.; Yao, Y.; McDowell, M. T.; Lee, S. W.; Jackson, A.; Yang, Y.; Hu, L. *et al.* Stable Cycling of Double-Walled Silicon Nanotube Battery Anodes through Solid-Electrolyte Interphase Control. *Nat. Nanotechnol.* **2012**, *7*, 310-315.
 37. Yao, Y.; Liu, N.; McDowell, M. T.; Pasta, M.; Cui, Y. Improving the Cycling Stability of Silicon Nanowire Anodes with Conducting Polymer Coatings. *Energy Environ. Sci.* **2012**, *5*, 7927-7930.
 38. Park, O.; Lee, J.-I.; Chu, M.-J.; Yeon, J.-T.; Yoo, S.; Choi, S.; Choi, N.-S.; Park, S. High-Performance Si Anodes with a Highly Conductive and Thermally Stable Titanium Silicide Coating Layer. *RSC Adv.* **2013**, *3*, 2538-2542.
 39. Nakai, H.; Kubota, T.; Kita, A.; Kawashima, A. Investigation of the Solid Electrolyte Interphase Formed by Fluoroethylene Carbonate on Si Electrodes. *J. Electrochem. Soc.* **2011**, *158*, A798-A801.
 40. Song, J.; Lee, S. J.; Kim, Y.; Kim, S.-S.; Lee, K. T.; Choi, N.-S. Thermal Reactions of Lithiated and Delithiated Sulfur Electrodes in Lithium-Sulfur Batteries. *ECS Electrochem. Lett.* **2014**, *3*, A26-A29.

* Chapter VII is reproduced in with a permission of “S.Choi, J. Kim, N.-S. Choi, M. G. Kim, S. Park, Cost-Effective Scalable Synthesis of Mesoporous Germanium Particles via a Redox-Transmetalation Reaction for High-Performance Energy Storage Devices. *ACS Nano* 2015”. Copyright **2015** American Chemical Society

Chapter VIII. Redox-Responsive Assembly of Carbon-Sheathed Germanium Coaxial Nanowire Heterostructures

8.1. Introduction

One-dimensional semiconducting nanowires have been demonstrated as building blocks for a rich variety of potential applications, such as field-effect transistors, light-emitting diodes, field emitters, photodetectors, solar cells, and lithium-ion batteries.¹⁻⁷ In particular, germanium nanowires (GeNWs), an especially attractive class of one-dimensional nanostructures, received a great attention due to their large exciton Bohr radius (~24.3 nm) and higher carrier mobility compared with silicon. GeNWs have been synthesized using numerous methods, like electrochemical etching, solvothermal, supercritical fluidic, laser ablation, vapor transport, and chemical vapor deposition (CVD).⁸⁻¹³ In particular, metal-catalyzed nanowire growth using vapor-liquid-solid (VLS) mechanism is the most widely used one for synthesizing GeNWs at relatively low synthetic temperature of 335 °C.^{13,14} Even though significant advances have been done to synthesize GeNWs with controlled dimension and electrical properties, there are still several challenges.¹⁵ First, Ge precursor is highly toxic and flammable.¹⁶ Second, its synthetic yield is extremely low and may not be suitable for commercial production, since the amount of producible nanowires is limited to the amount of metal catalysts that are immobilized on the substrate.¹⁷ Third, during the VLS growth process, unintentional tapering takes place; reaction species from the gas phase are not only impinged onto the molten metal catalyst but also adsorbed on the nanowire sidewalls, giving rise to adverse effects on structural and electrical uniformities of the nanowires.¹⁸ Fourth, a high solubility of semiconductor material in the metal catalyst resulted in detrimental effects on the electrical properties of the nanowires.¹⁹ During the nanowire growth process, metal catalyst can diffuse across the nanowire surface, leading to the tapering of nanowires via the Ostwald ripening process.²⁰ Fifth, thermally and chemically unstable germanium oxide (GeO_x) can be formed on the surface of the as-synthesized GeNWs during synthetic process of sample storage in atmosphere.^{21,22}

A second class of nanowire heterostructures, synthesis of coaxial nanowires, can be one of the good solutions to overcome these obstacles. Coaxial structures can be fabricated by coating nanowires with a conformal layer of a second material (i.e., organic monolayer or carbon).²³ In particular, since GeNWs can be easily oxidized and contaminated due to their high surface chemical reactivity, generation of coaxial nanowire heterostructures is of importance in nanoelectronics and energy storage applications.²⁴ To date, various coaxial metal or semiconductor nanowire heterostructures have been synthesized using metal catalytic growth. Lieber group reported high quality Ge-Si core-sheath nanowires produced by CVD method, in which the nanowire field-effect transistors outperformed their planar counterparts.²⁴ As another example, Whang group reported a catalytic

simultaneous growth of a GeNW core and a very thin amorphous carbon sheath via VLS growth process.²⁵ The resulting carbon-sheathed GeNWs showed excellent performance in field effect transistors even after high temperature annealing in air, compared to pristine nanowires without carbon layers. Crocker group demonstrated a single-step synthesis of GeNW encapsulated within multi-walled carbon nanotubes using a CVD method of solid precursor, phenyltrimethylgermane, having both carbon and Ge source.²⁶ However, for the next generation energy-related applications, costly effective and environmentally benign methods are required to produce Ge-based heterostructured nanowires. A simple strategy that do not use highly toxic and/or high cost germanium precursor but instead generate high quality Ge-carbon core-sheath nanowires through reduction of low cost germanium oxide (GeO_2) and subsequent seedless growth need to be demonstrated. These GeNWs are suitable materials for satisfying increasing of needs of rechargeable high-power energy storage system for portable devices, electric vehicle, and energy storage system.²⁷

Herein, we demonstrate a new bottom-up approach to synthesize hierarchically assembled carbon-sheathed germanium coaxial nanowire (c-GeNW) heterostructures in a large scale, which can enhance chemical and thermal stability of nanowires, using self-catalytic growth process assisted by hydrogen/carbon generated from thermal decomposition of natural gas. In this process, GeNWs are grown via chemical reduction of GeO_2 particles and subsequent self-catalytic growth during thermal decomposition of natural gas. Simultaneously, carbon sheath layers are uniformly covered on the surface of GeNWs to make the resulting hierarchically assembled nanowires, in which the dimensions of carbon layers and GeNWs are easily tunable by controlling flow rate, reaction temperature and reaction time of natural gas. This strategy is large-scale and cost-effective synthetic route which can extend to other metal oxides. As-synthesized c-GeNWs are used as rechargeable lithium-ion battery anode material and show outstanding electrochemical properties including exceptionally stable cycling property (capacity retention of >96% after 1000 cycles at 1 C rate).

8.2. Experimental

8.2.1. Fabrication of germanium oxide film.

Germanium oxide (GeO₂) thin films were deposited within a stainless steel vacuum chamber that was evacuated to a pressure of 1.5×10^{-6} Torr or below. Pumping was accomplished using a turbo-molecular pump in conjunction with a mechanical roughing pump. After reaching the required pressure, research grade O₂ (99.995%) and Ar (99.999%) were introduced into the chamber using mass flow controllers. The working pressure, controlled via an automated gate valve assembly, was maintained at 30 mTorr. The O₂ flow rate was varied between 0.0 and 20.0 sccm at increments of 5.0 sccm, and the argon flow rate was adjusted to keep the net flow rate constant at 20.0 sccm. The plasma was generated using a Dressler CESAR power supply at a power of RF 150W. A shutter was used to shield the substrate from any spurious droplets caused by arcing at the onset of plasma ignition. The shutter was opened upon achieving a steady-state plasma. A 3 inch germanium sputter target (RNDKOREA, 99.999% purity) was used as the source material. The GeO₂ films were deposited on prime grade, p-type (100) oxidized Si wafers (LG Siltron Inc, Korea). The wafers were placed on a rotating sample holder (30 rpm) located at a distance of 90 mm from the surface of the sputtering target.

8.2.2. Synthesis of Carbon sheathed GeNWs heterostructures.

Commercially available GeO₂ powders (99.99%, Germanium Corporation of America Inc.) was uniformly placed inside an alumina boat. In a typical process, the furnace was heated to 700 - 1000 °C with a ramping speed of 5 °C min⁻¹ and kept at target temperature for 10 sec to 60 min (Figure 8. 1A). Subsequently, hydrocarbon gases (acetylene, ethylene, methane, toluene and hydrogen) were introduced inside the furnace by controlling flow rate and exposure time.

8.2.3. Physical Characterization.

Surface morphologies of GeO₂ particles and c-GeNWs were characterized by field emission scanning electron microscopy (FE-SEM, FEI Verios 460 and Hitachi S-4800) operating at 10 kV and high resolution transmission electron microscopy (HR-TEM, JEOL JEM-2100F) operating at 200 kV. And the microstructures of GeO₂ and as-synthesized c-GeNWs were investigated by X-ray diffractometer (XRD, Bruker D8-Advance) operated at 3 kW using CuK α radiation. Raman spectra were obtained from a JASCO spectrometer (NRS-3000) operating at 532 nm to characterize the Ge and GeO₂ phase in the Ge based materials.

8.2.4. Electrochemical Test.

Electrochemical properties of Ge-based electrodes were evaluated using coin-type half-cell (2016R) at 25 °C. The Ge-based electrodes were composed of Ge active materials, super-P carbon black, and poly(acrylic acid)/sodium carboxymethyl cellulose (1:1, w/w) binder in a weight ratio of 8:1:1. The electrolyte was 1.3 M LiPF₆ with ethylene carbonate/diethyl carbonate (PANAX Starlyte, Korea, 3/7 (v/v)) including 10 wt% fluoroethylene carbonate (FEC) additive. The half-cells were tested galvanostatically between 0.01 and 1.5 V (versus Li/Li⁺) in the range of 0.05 C - 5 C rates. The cell performance was examined using a cycle tester (WBCS 3000 battery systems, Wonatech).

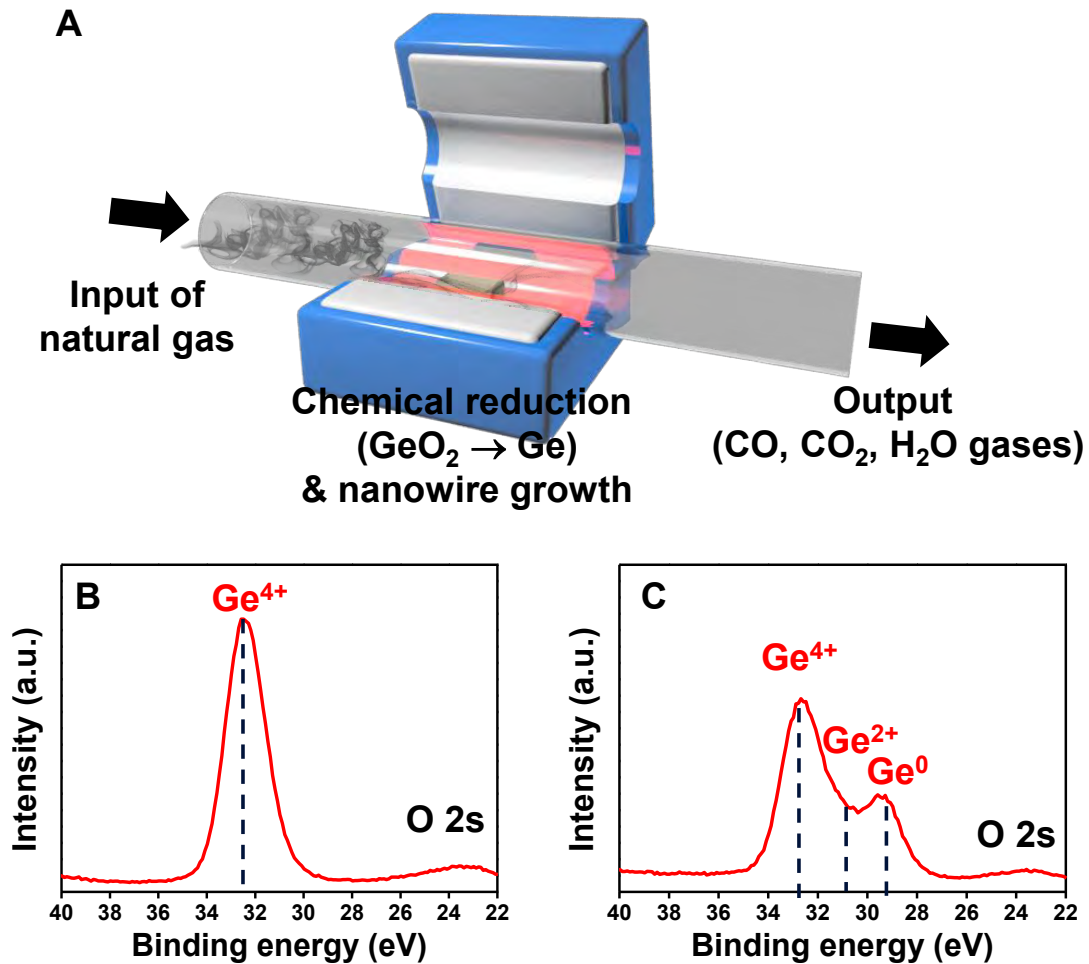


Figure 8. 1 Synthesis process of c-GeNWs and their characterization. (A) Schematic illustration showing synthetic route of c-GeNWs from GeO_2 particles by hydrogen and carbon clusters generated from thermal decomposition of unsaturated natural gas. XPS spectra of (B) Ge^{4+} and O 2s of as-synthesized GeO_2 film on Si wafer and (C) GeO_x film formed after hydrogen/carbon-assisted chemical reduction by thermal decomposition of acetylene gas at 800 °C for 1 min.

8.3. Result and discussion

8.3.1. Redox responsive reaction and nanowire growth process

A schematic illustration shows the synthetic process of c-GeNWs via a redox-responsive self-catalytic growth process between carbon/hydrogen (produced from thermal decomposition of natural gas) and Ge^{4+} (original GeO_2 particles). The surface of GeO_2 reacts with hydrogen and carbon vapor at well above the decomposition temperature of acetylene gas, resulting in a formation of Ge, CO, CO_2 and H_2O by-products via hydrogen/carbon-assisted chemical reduction. (Figure 8. 1A)

According to previous report²⁸, we fabricated 30-nm-thick GeO_2 thin film on silicon wafer (with 300-nm-thick SiO_2 layers) using RF-sputter system. XPS spectrum of as-prepared GeO_2 films shows the peak corresponding to Ge^{4+} binding energy without metallic Ge^0 bonding (Figure 8. 1B). After chemical reduction for a short time (at 800 °C for 1 min), the surface of GeO_2 film was partly converted to GeO_x and was synthesized GeNWs sheathed with carbon layers (Figure 8. 1C). Growth mechanism of c-GeNWs was schematically illustrated in Figure 8. 2A. An unsaturated hydrocarbon (here, acetylene gas) was thermally decomposed into hydrogen and carbon cluster at above 450 °C. Initially, the hydrogen/carbon generated can easily reduce GeO_2 to Ge nanoclusters due to its low activation energy at low temperature. Simultaneously, excess carbon clusters produced by decomposed acetylene gas are uniformly covered on the reduced Ge surface. Subsequently, GeNWs are grown via self-catalytic growth mechanism with carbon-sheathed GeNW heterostructure.

We monitored the growth process of GeNWs at various reaction times at a fixed temperature of 800 °C. First, the reduced Ge vapor made by hydrogen/carbon-assisted chemical reduction of GeO_2 was aggregated with hemispherical dome-shape at reaction time of 10 sec. Simultaneously, carbon clusters were knitted on the Ge-dome surface due to the negligible carbon solubility in bulk Ge (<0.1 atomic%)²⁹. When the reaction temperature was increased to 20 sec, rod-shaped Ge with carbon layers was made by continuous feeding of Ge source according to self-catalytic growth mechanism. Further increase of reaction time (30 sec and 60 sec) led to a successful synthesis of c-Ge NWs (Figure 8. 2B).

We extended this idea to commercially available bulk GeO_2 particles. SEM image of bulk GeO_2 shows large secondary particles (3-5 μm) irregularly stacked by primary particles (200-500 nm in size) as shown in Figure 8. 3A. The XRD pattern and Raman spectrum of the GeO_2 particles show a crystalline structure of trigonal GeO_2 phase (Figure 8. 4)³⁰. When the GeO_2 powder are chemically reduced at 900 °C for 20 min under a 200 sccm C_2H_2 gas, the hierarchically structured c-GeNWs are successfully synthesized without unreacted GeO_2 (Figure 8. 2B), in which the resulting Ge shows diamond cubic structure (JCPDS card no. 04-0545) and Raman spectrum (Figure 8. 5). Chemical reduction of GeO_2 particles by hydrogen/carbon-assisted self-catalytic process leads to a formation of hierarchically assembled c-GeNWs heterostructure. This process can be called a redox-responsive assembly in that the reduction of GeO_2 by hydrogen-carbon induces the growth of c-GeNWs and subsequently, form three-dimensional assembly of one-dimensional heterostructures. TEM image of

c-GeNWs clearly shows that carbon layers are uniformly sheathed on the GeNWs over entire nanowire surface (Figure 8. 3C). The high-resolution TEM (HR-TEM) image shows that the diameter of GeNW is ~ 30 nm, while the thickness of carbon layers is ~ 20 nm (Figure 8. 3D). To further investigate the crystallinity and chemical elements of the as-grown c-GeNWs, the fast Fourier transform (FFT) patterns at four different spots and energy dispersive X-ray spectroscopy (EDS) are obtained (Figure 8. 3D and 3E). The FFT patterns explicitly show the same crystalline lattice of the four different regions (including tip, neck, and body of GeNW) (Figure 8. 3E). Also, the EDS line-scan and mapping results indicate that quasi-graphitic carbon layers are uniformly sheathed on the surface of GeNW without any oxygen contents (Figure 8. 3D and 3F).

We investigated the effect of flow rate of C_2H_2 gas, reaction time, and reaction temperature on the dimension of carbon sheath layer and GeNW (Figure 8. 3G-3I). Increasing flow rate of C_2H_2 gas generates a large amount of carbon clusters which can reduce the nucleation rate of GeNW, resulting in decreasing diameter of NW and increasing thickness of carbon layer (Figure 8. 6). Meanwhile, diameter of GeNWs is not influenced on increasing reaction time because the dimension of Ge nuclei is determined at a very short time (as shown in Figure 8. 2B) (Figure 8. 3H and Figure 8. 7). However, the thickness of carbon layers is significantly increased as a function of reaction time due to exposure of large amount of carbon clusters. Similar results are obtained by variation of reaction temperature. In the range of $800 \sim 950$ °C, dimension of GeNW is a quite similar, but the diameter of GeNW is significantly decreased at 1000 °C due to oversupply of carbon clusters (Fig. 2I and Figure 8. 8). The Ge crystallite size synthesized at each reaction temperature was calculated by Scherrer equation (Figure 8. 5B). The crystallite size was decreased with increasing reaction temperature, because feeding of large amount of carbon clusters at higher temperature interrupt a fast growth of GeNW. Raman spectra of carbon sheath layers in the c-GeNWs (synthesized at 800 and 900 °C) indicate that two peaks of disordered graphitic carbon are observed at $\sim 1,300$ cm^{-1} (D-band) and $\sim 1,600$ cm^{-1} (G-band) peaks, respectively. Also, the Ge peak appearing at 300 cm^{-1} proves that crystallite size of GeNW synthesized at 800 °C is larger than sample obtained at 900 °C (Figure 8. 5C).

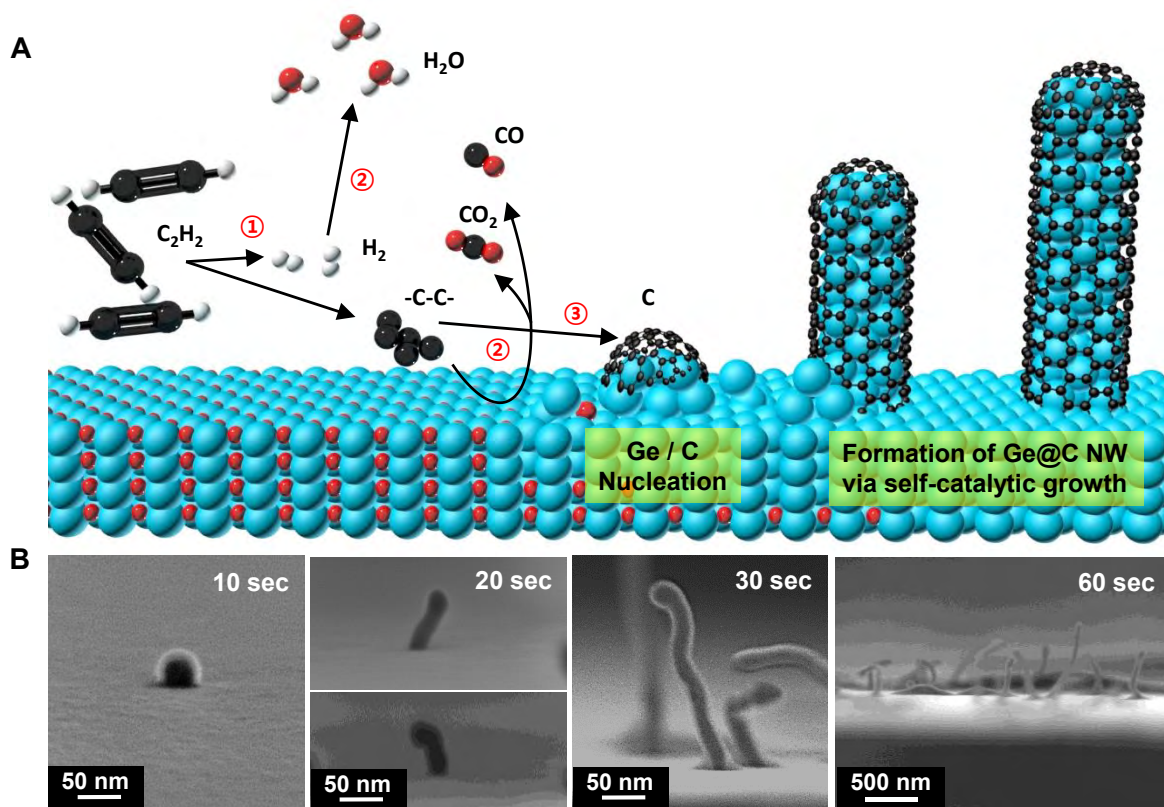


Figure 8. 2 A New class of nanowire growth mechanism. (A) Schematic illustration showing synthetic route of c-GeNW from GeO_2 particles by hydrogen/carbon-assisted chemical reduction. (B) SEM images showing growth mechanism of GeNW as a function of exposure time of GeO_2 to thermally decomposed hydrocarbon gases.

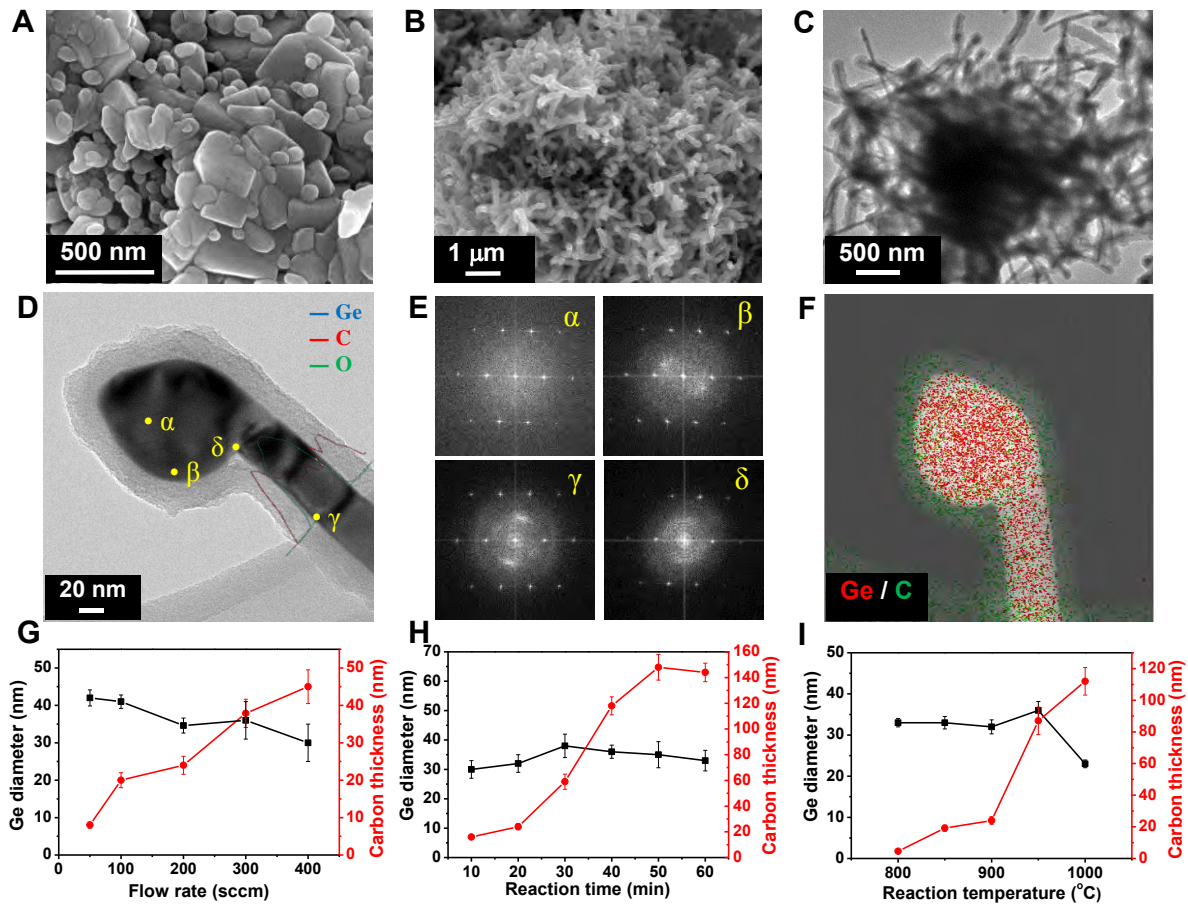


Figure 8. 3 Characterization of c-GeNWs synthesized by hydrogen/carbon-assisted chemical reduction. SEM images of (A) original bulk GeO₂ particles and (B) as-synthesized c-GeNWs. (C) TEM image of c-GeNWs showing hierarchically assembled heterostructure. (D) Magnified TEM image showing tip and body of GeNW and EDS elemental line scan profiles containing O (green), Ge (cyan), C (red). (E) Fast Fourier transform (FFT) pattern showing the same crystal lattice of Ge from each point taken in Fig. 2D. (F) EDS mapping of c-GeNWs showing spatial locations Ge (red) and C (green) elements. Plots of Ge core size and carbon-layer thickness as a function of (G) gas flow rate (fixed temperature of 900 °C and reaction time of 20 min), (H) reaction time (fixed temperature of 900 °C and gas flow rate of 200 sccm) and (I) reaction temperature (fixed gas flow rate at 200 sccm and reaction time of 20 min).

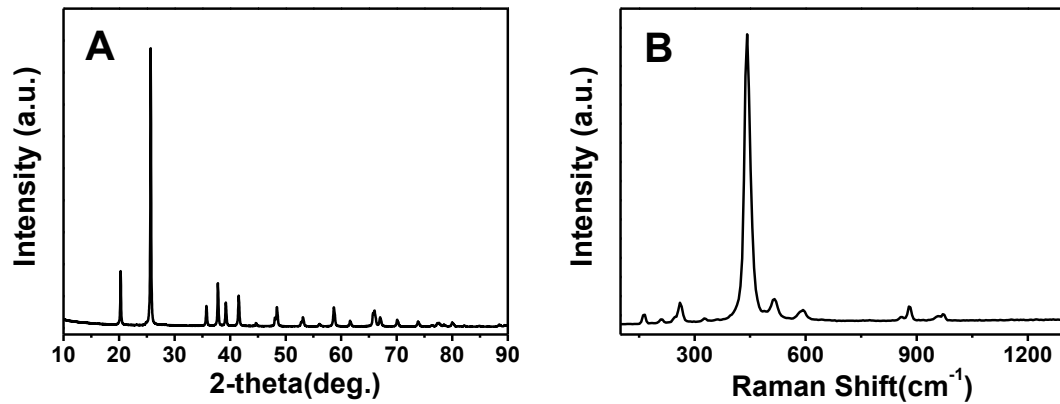


Figure 8. 4 Characterization of the original bulk GeO₂ powder. (A) XRD pattern and (B) Raman spectrum of bulk GeO₂ particles showing pure GeO₂ microstructure.

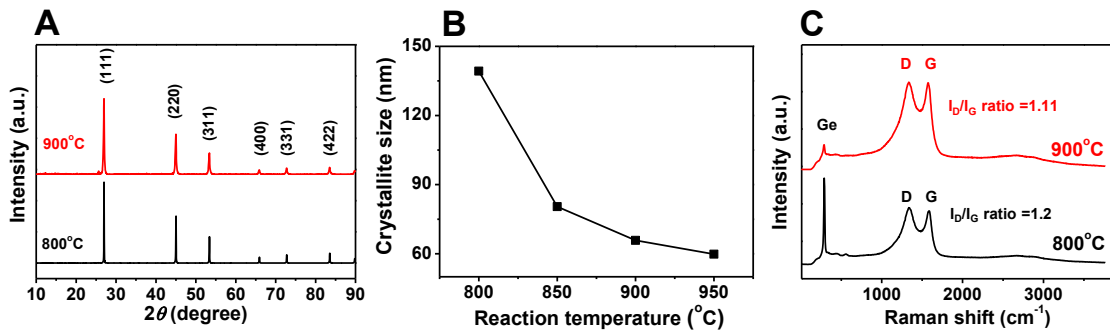


Figure 8. 5 Characterization of as-synthesized c-GeNWs. (A) XRD pattern of c-GeNWs synthesized at 900 °C and at 800 °C. (B) Ge crystal size (estimated using Scherrer equation) of c-GeNWs synthesized as a function of reaction temperature. (C) Raman spectra of c-sheated GeNWs show characteristic of crystallite Ge and a quasi-graphitic carbon layers in each samples.

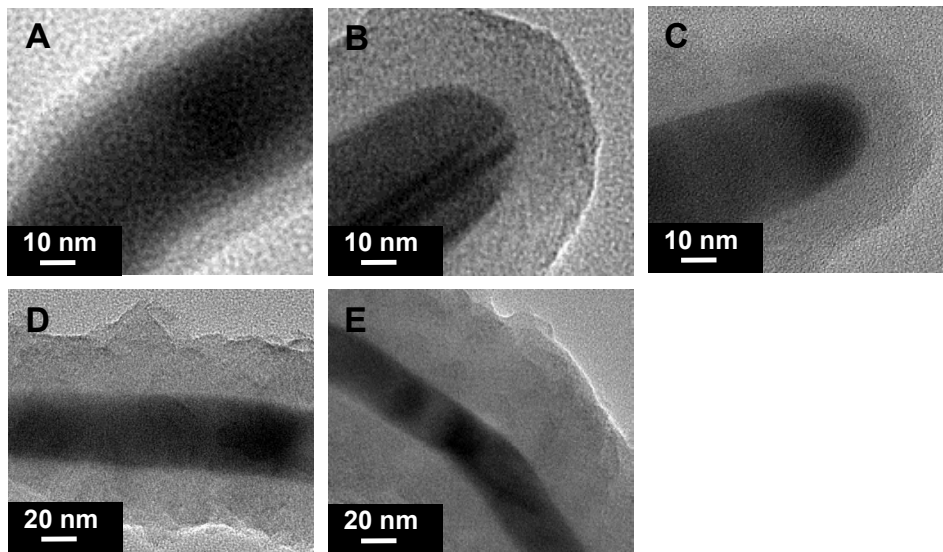


Figure 8. 6 TEM images of Ge nanowires synthesized at various flow rates of acetylene gas at 900 °C for 20 min. (A) 50 sccm, (B) 100 sccm, (C) 200 sccm, (D) 300 sccm, and (E) 400 sccm. When the flow rate of acetylene gas was increased, carbon coating layers became thicker, while the diameter of Ge nanowires was thinner.

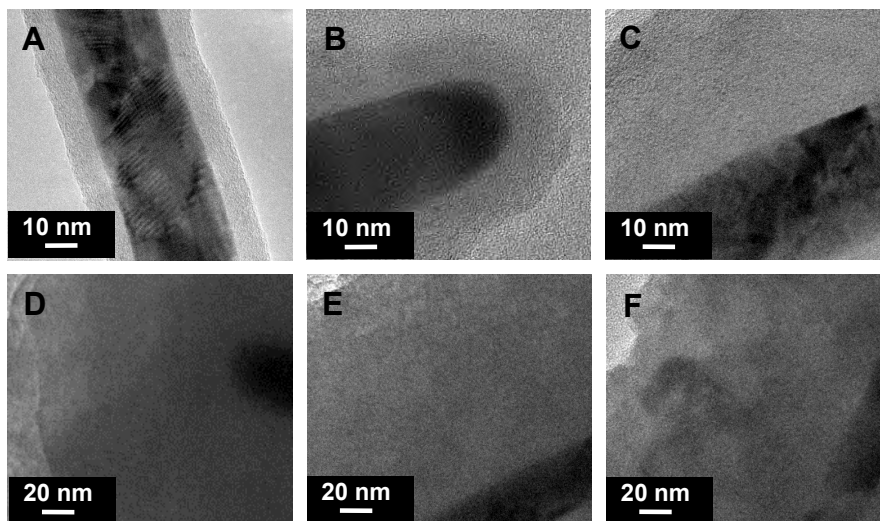


Figure 8. 7 TEM images of Ge nanowires at various reaction times at 900 °C under a fixed flow rate (200 sccm of C_2H_2 gas). (A) 10 min, (B) 20 min, (C) 30 min, (D) 40 min, (E) 50 min and (F) 60 min. The diameter of Ge nanowires was a quite similar, while the thickness of carbon layers was significantly increased.

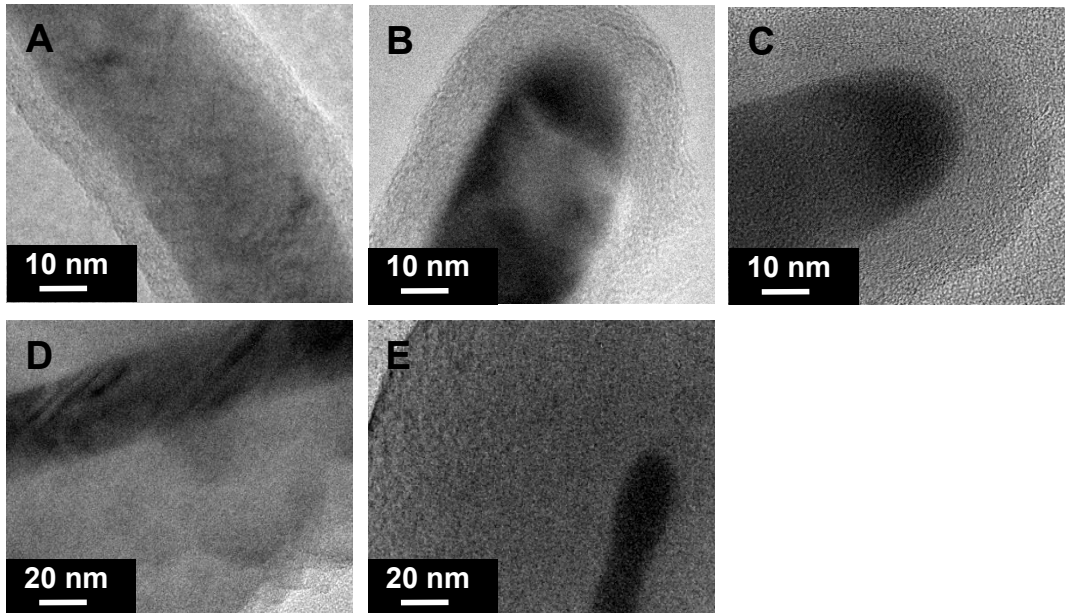


Figure 8. 8 TEM images of Ge nanowires at various reaction temperatures at a fixed flow rate of acetylene gas (200 sccm) for 20 min. (A) 800 °C, (B) 850 °C, (C) 900 °C, (D) 950 °C, and (E) 1000 °C. When the reaction temperature was increased, the diameter of Ge nanowires became thinner, while the carbon coating layers were thicker.

8.3.2. Redox-responsive reaction mechanism using another metal oxide and hydrocarbon gas

In addition to C_2H_2 gas, we investigated the effect of various other natural gases on the chemical reduction of GeO_2 particles. Hydrogen (H_2), methane (CH_4), ethylene (C_2H_4), and toluene ($C_6H_5CH_3$) gases were introduced on the thermal reaction containing GeO_2 particles in a similar manner with that of C_2H_2 gas (Figure 8. 9).

H_2 gas is well-known reducing agent which can convert GeO_2 to pure Ge metal at >500 °C. When the GeO_2 particles are exposed to H_2 gas at 900 °C for 20 min, GeO_2 was partially transformed to Ge and subsequently, pure Ge was evaporated due to the melting temperature depression. The H_2 -treated GeO_2 particles are confirmed as GeO_2 particles with macropores (indicating spatial locations of evaporated Ge) by SEM and XRD (Figure 8. 9A-C). Similar results are obtained by CH_4 gas, because carbon contents produced by thermal decomposition of CH_4 are not enough to wrap the reduced Ge vapor (Figure 8. 9D-F). Meanwhile, C_2H_4 gas which can produce large amount of carbon and hydrogen vapor leads to a successful synthesis of c-GeNWs, similar to that of C_2H_2 system (Figure 8. 9G-I). As another natural gas, we introduced toluene ($C_6H_5CH_3$) gas having large carbon contents, resulting in a formation of carbon-coated GeO_2 particles due to minimized H_2 contents (Figure 8. 9J-L). These results demonstrate that both carbon and hydrogen vapors should provide to synthesize c-GeNWs from GeO_2 particles.

Synthetic process of carbon-sheathed metallic/semiconducting nanowires can be extended to several other metal oxide particles including SnO_2 , In_2O_3 and NiO . Even though these materials have different melting temperature and activation energy for reduction, hydrogen/carbon-assisted chemical reduction process leads to a successful synthesis of carbon-sheathed metallic/semiconducting nanowires at different reaction temperature (Figure 8. 10).

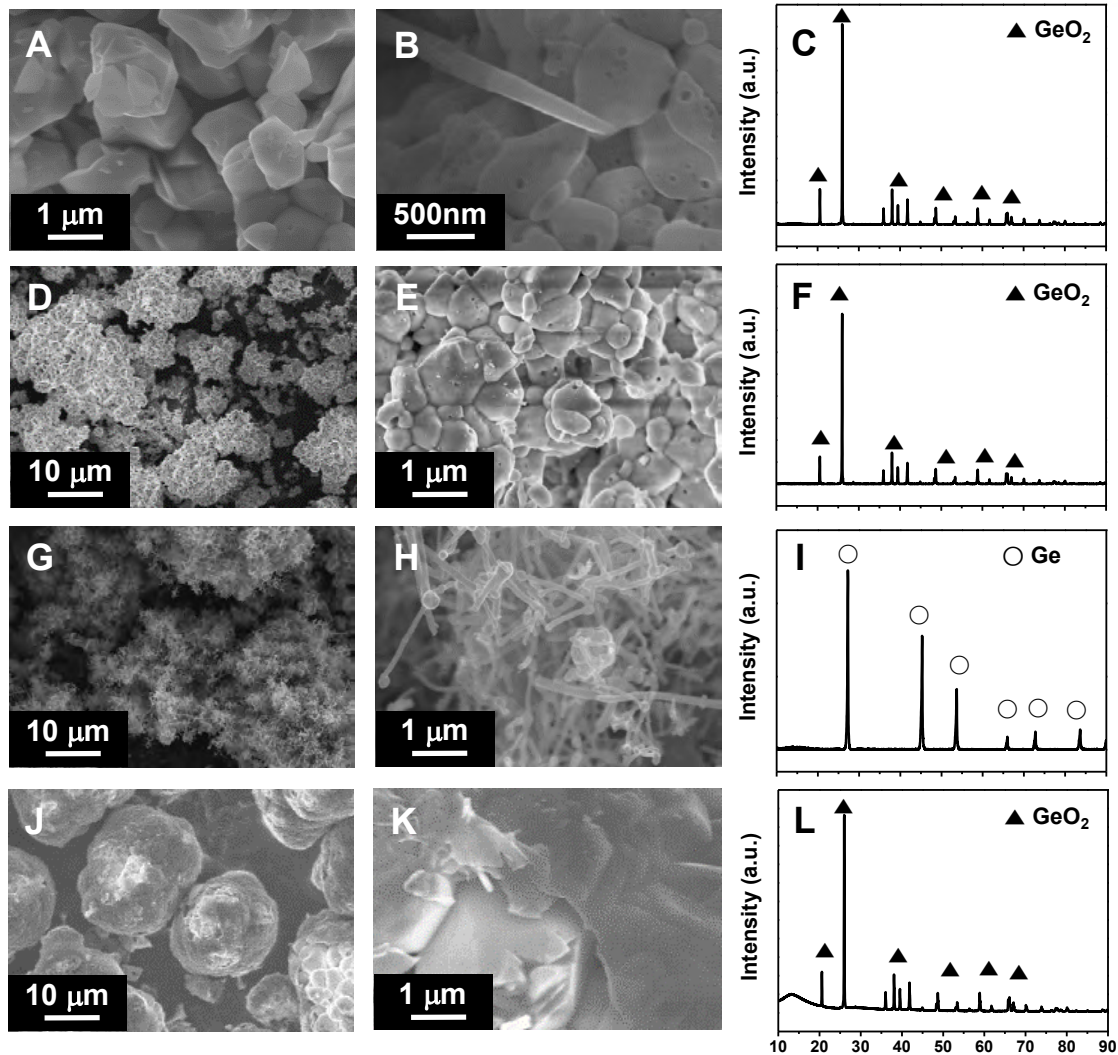


Figure 8. 9 SEM images and XRD patterns of reduced Ge and GeO_2 obtained by thermal decomposition of various nature gases at $900\text{ }^\circ\text{C}$ for 20 min. (A) Porous GeO_2 particles synthesized by H_2 gas and (B) the corresponding magnified SEM images showing macroporous regions. (C) XRD pattern only shows GeO_2 microstructure due to a complete evaporation of Ge reduced by H_2 . (D) Porous GeO_2 particles synthesized by CH_4 gas and (E) the magnified SEM image macroporous regions. (F) XRD pattern only shows GeO_2 microstructure. Both H_2 and CH_4 gases produces hydrogen at $900\text{ }^\circ\text{C}$, in which GeO_2 are partially reduced to Ge, and subsequently the Ge is evaporated to make void space on the surface of GeO_2 particles at this temperature. (G) Carbon-sheathed Ge nanowires synthesized by C_2H_4 gas and (H) the magnified SEM image showing hierarchically assembled nanowires. (I) XRD pattern shows crystalline Ge microstructure in the c-GeNW synthesized by C_2H_4 gas. (J) Carbon-coated GeO_2 particles synthesized by toluene gas and (K) the magnified SEM image showing thick carbon coating layers on the surface of GeO_2 . (L) XRD pattern only shows GeO_2 microstructure. Toluene was thermally decomposed at $900\text{ }^\circ\text{C}$ to produce a large amount of carbon cluster, but it is hard to generate hydrogen gas, resulting in the formation of carbon-coated GeO_2 particles.

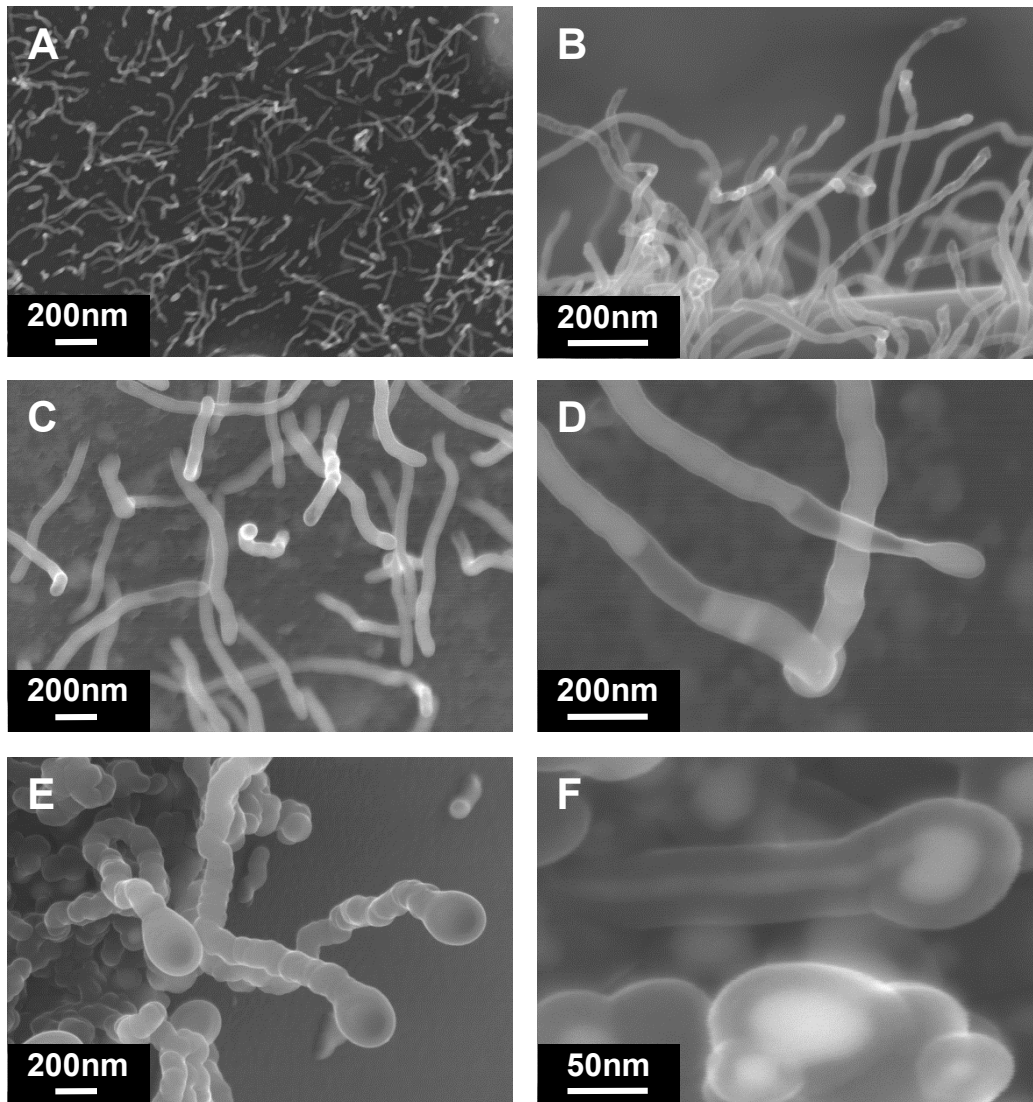


Figure 8. 10 General approach for synthesizing other metal nanowires. (A) SEM image of carbon-sheathed Sn nanowires grown on the surface of SnO₂ films at 700 °C for 2 min under a flow rate of acetylene gas and (B) the magnified SEM image. (C) SEM image of carbon-sheathed In nanowires grown on the surface of In₂O₃ films at 850 °C for 2 min under a flow rate of acetylene gas and (D) the magnified SEM image. (E) SEM image of carbon-sheathed Ni nanowires grown on the surface of NiO films at 900 °C for 2 min under a flow rate of acetylene gas and (F) the magnified SEM image.

8.3.3. Effects of carbon sheathed Ge nanowires in application

Stimulated by the hierarchical c-GeNWs heterostructure, we explored its chemical/thermal stability and electrochemical properties as an anode material for high-performance lithium-ion batteries. Firstly, chemical stability of c-GeNWs was investigated using strong oxidant, H_2O_2 (Figure 8. 11). The c-GeNWs showed significantly suppressed anti-oxidation properties due to efficient protection of carbon-sheath layers to exposure of GeNWs in oxygen, while Ge nanoparticles (GeNPs) without carbon coating layer were quickly transformed to GeO_2 as a function of immersion time in H_2O_2 (Figure 8. 13A and 13B). Secondly, the GeNPs were thermally oxidized at $550\text{ }^\circ\text{C}$ for 2 h, while the c-GeNWs made still unchanged without changing the original morphology after thermal oxidation (Figure 8. 12). These results demonstrate that the carbon-sheath layers effectively protect from a chemical attack and side reaction by oxygen so that this process can be applied to various other applications. Thirdly, we tested electrochemical properties of the c-GeNW anodes in a coin-type half-cell (2016 R-type). The galvanostatic discharge-charge cycling for the c-GeNWs heterostructures (synthesized at $900\text{ }^\circ\text{C}$ for 20 min) was performed in the potential region of 0.01-1.5 V at different current densities. The first discharge and charge capacities of c-GeNWs are 665 and 521 mAh g^{-1} , respectively, at a rate of 0.05 C (Figure 8. 13C). The c-GeNW electrodes exhibit high rate capabilities corresponding to the capacity retention of 40 % at even 5 C rate, compared to Ge without carbon layers (Figure 8. 13D). More outstanding electrochemical property is a long-term cycling stability. The c-GeNW electrode exhibited capacity retention of >99% at 0.5 C rate after 300 cycles and subsequent retention of >96% after 900 cycles at 1 C rate (Figure 8. 13E). These excellent electrochemical performances of the c-GeNW electrodes can be explained as follows: (i) Carbon-sheath layers on the surface of c-GeNWs significantly increase the electrical properties of GeNWs, resulting in enhancement of high rate capability. (ii) The carbon layers of c-GeNWs contribute to the cycling stability by forming stable solid-electrolyte-interphase layers on the electrode surface and by alleviating a large volume change of GeNWs during cycling. And (iii) available void spaces within hierarchical structured c-GeNWs act as a buffer space which can accommodate a large volume change during the battery operation.

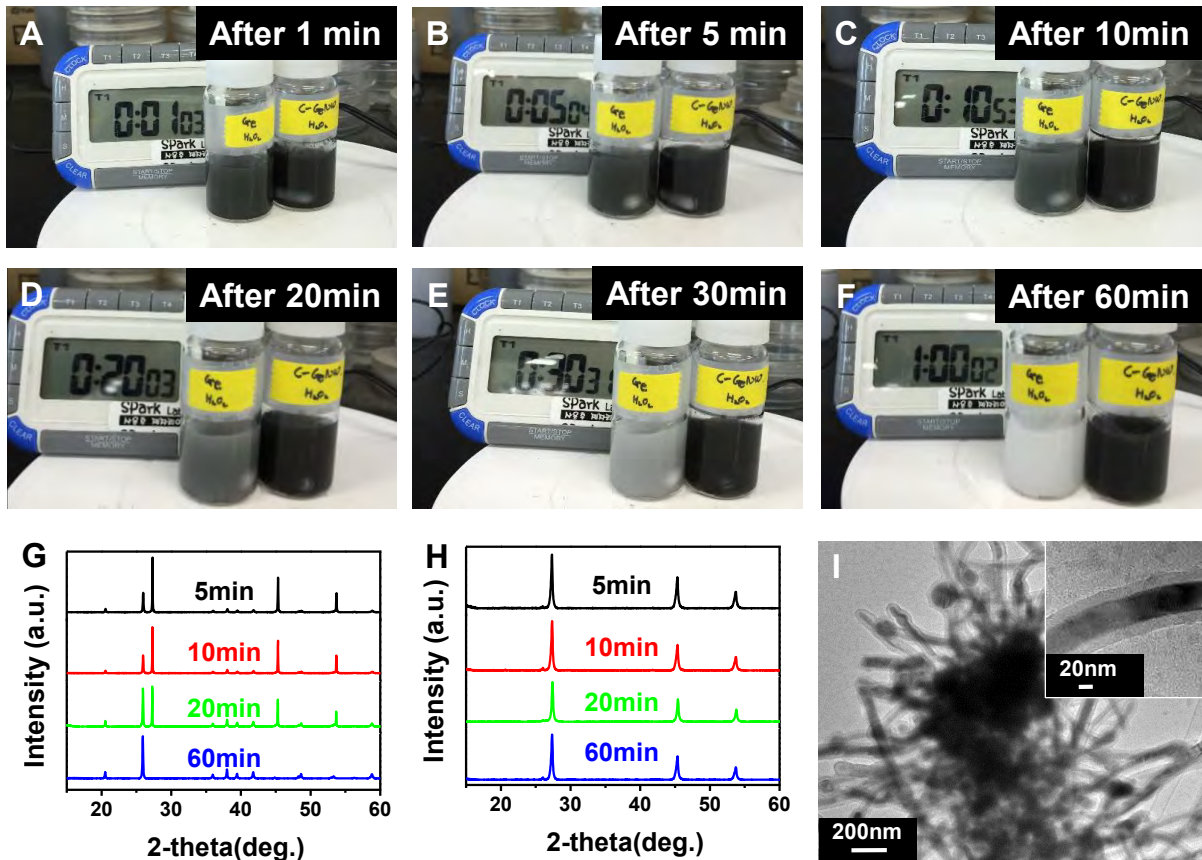


Figure 8. 11 Anti-oxidation test of c-GeNWs and GeNPs in 3wt% H₂O₂ solution for 1h. (A)-(F) Photographs of c-GeNWs and GeNPs in H₂O₂ solution during chemical oxidation process as a function of immersion time. The color of GeNPs solution are changed to bright gray and finally turned to white (indicating the complete oxidation of GeNPs). Meanwhile, c-GeNWs solution did not change from the original color. (G) XRD patterns of (G) GeNPs and (H) c-GeNWs during anti-oxidation test. (I) TEM image of c-GeNWs after anti-oxidation test shows intact morphologies compared to the original c-GeNWs.

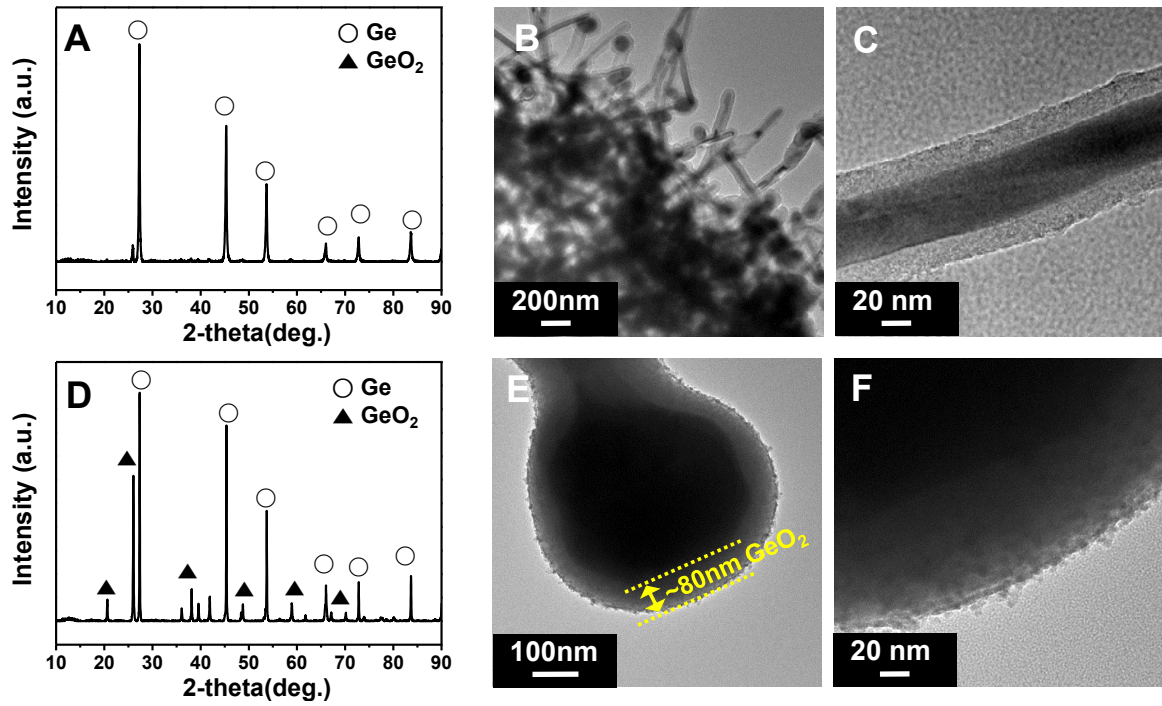


Figure 8. 12 Thermal oxidation tests of c-GeNWs and GeNPs at 550 °C for 2 h in air. (A) XRD pattern, (B) TEM image, and (C) the magnified TEM image of c-GeNWs after thermal oxidation test. These results demonstrate that the c-GeNWs made unchanged after thermal oxidation due to effective protection of carbon-sheathed layers from exposure of Ge to oxygen. (D) XRD pattern, (E) TEM image, and (F) the magnified TEM image of GeNPs after thermal oxidation test. These results show that GeNPs were partially oxidized with thickness of 80 nm.

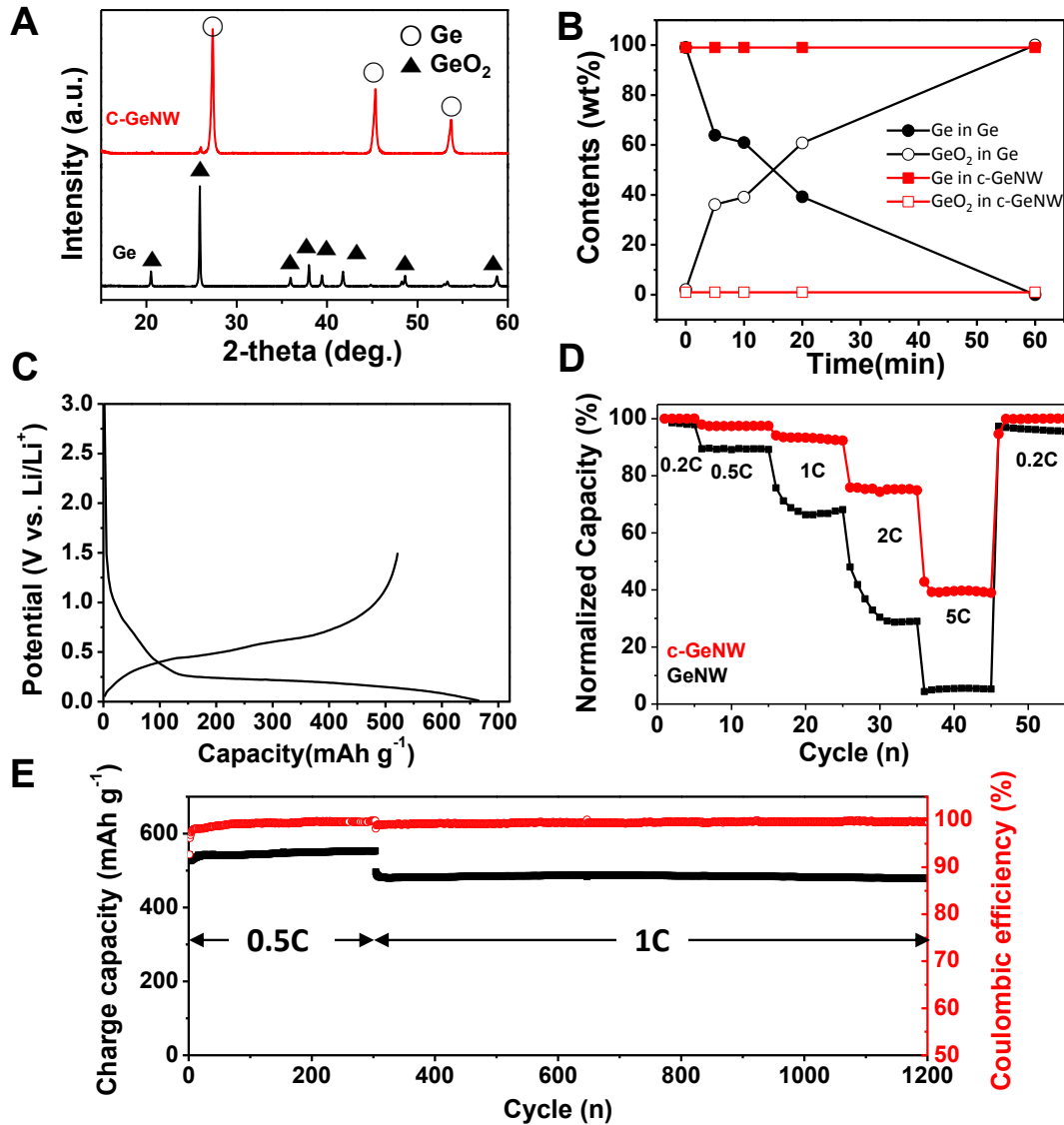


Figure 8.13 Anti-oxidation and electrochemical properties of c-GeNWs and Ge. (A) XRD patterns of c-GeNWs and GeNPs after immersion to H₂O₂ solution for 1 h. (B) Plots of Ge and GeO₂ contents in each Ge sample as a function of immersion time in H₂O₂. (C) The first cycle voltage profile of c-GeNW (synthesized at 900 °C) electrodes obtained at a rate of 0.05 C in the range of 0.01-1.5 V. (D) Rate capabilities of Ge electrodes at the same delithiation and lithiation rate. (E) Outstanding cycling stability of the c-GeNW electrodes obtained at 0.5 C (1st-300th cycle) and at 1 C (301th-1200th) rate.

8.4. Conclusion

In summary, we demonstrated a newly developed synthetic process for c-GeNWs via a unique redox-responsive reaction between GeO_2 and natural gas. We proved the synthetic mechanism of the c-GeNWs by combining experimental results and density functional theory (DFT) calculation. Our synthetic routes for carbon-sheathed metallic/semiconducting nanowire heterostructures have several advantages as follows: (i) A simple hydrogen/carbon-assisted chemical reduction enabled us to synthesize hierarchically assembled heterostructured materials from inexpensive metal oxides in a large scale. (ii) Our synthetic process can be generalized to other metal oxides including SnO_2 , NiO , In_2O_3 , and Bi_2O_3 . And (iii) the resulting c-GeNWs exhibited chemical/thermal stability and outstanding electrochemical properties as lithium-ion battery anodes. This simple strategy may open up an effective way to make other metallic/semiconducting nanomaterials via one-step synthetic reaction through environmentally benign and cost-effective approach.

8.5. References

1. Duan, X., Huang, Y., Cui, Y., Wang, J. & Lieber, C.M. Indium phosphide nanowires as building blocks for nanoscale electronic and optoelectronic devices. *Nature* **409**, 66-69 (2001).
2. McAlpine, M.C., Ahmad, H., Wang, D. & Heath, J.R. Highly ordered nanowire arrays on plastic substrates for ultrasensitive flexible chemical sensors. *Nature materials* **6**, 379-384 (2007).
3. Wang, C. et al. User-interactive electronic skin for instantaneous pressure visualization. *Nature materials* **12**, 899-904 (2013).
4. Li, L. et al. Crystallinity-Controlled Germanium Nanowire Arrays: Potential Field Emitters. *Advanced Functional Materials* **18**, 1080-1088 (2008).
5. Chen, G. et al. Single-Crystalline p-Type Zn₃As₂ Nanowires for Field-Effect Transistors and Visible-Light Photodetectors on Rigid and Flexible Substrates. *Advanced Functional Materials* **23**, 2681-2690 (2013).
6. Yoon, J. et al. Ultrathin silicon solar microcells for semitransparent, mechanically flexible and microconcentrator module designs. *Nature materials* **7**, 907-915 (2008).
7. Lee, S.W. et al. High-power lithium batteries from functionalized carbon-nanotube electrodes. *Nature Nanotechnology* **5**, 531-537 (2010).
8. Fang, C., Föll, H. & Carstensen, J. Long germanium nanowires prepared by electrochemical etching. *Nano letters* **6**, 1578-1580 (2006).
9. Hanrath, T. & Korgel, B.A. Crystallography and surface faceting of germanium nanowires. *Small* **1**, 717-721 (2005).
10. Hobbs, R.G. et al. Seedless growth of sub-10 nm germanium nanowires. *Journal of the American Chemical Society* **132**, 13742-13749 (2010).
11. Morales, A.M. & Lieber, C.M. A laser ablation method for the synthesis of crystalline semiconductor nanowires. *Science* **279**, 208-211 (1998).
12. Wu, Y. & Yang, P. Germanium nanowire growth via simple vapor transport. *Chemistry of Materials* **12**, 605-607 (2000).
13. Kodambaka, S., Tersoff, J., Reuter, M. & Ross, F. Germanium nanowire growth below the eutectic temperature. *Science* **316**, 729-732 (2007).
14. Trentler, T.J. et al. Solution-Liquid-Solid Growth of Crystalline III-V Semiconductors: An Analogy to Vapor-Liquid-Solid Growth. *Science* **270**, 1791-1794 (1995).
15. Ertz, D. et al. High density germanium nanowire assemblies: contact challenges and electrical characterization. *The Journal of Physical Chemistry B* **110**, 820-826 (2006).
16. Woelk, E. et al. Designing novel organogermanium OMVPE precursors for high-purity germanium films. *Journal of crystal growth* **287**, 684-687 (2006).

17. Pan, C. et al. Wafer-Scale High-Throughput Ordered Arrays of Si and Coaxial Si/Si_{1-x}Ge_x Wires: Fabrication, Characterization, and Photovoltaic Application. *ACS nano* **5**, 6629-6636 (2011).
18. Periwal, P., Baron, T., Gentile, P., Salem, B. & Bassani, F. Growth strategies to control tapering in Ge nanowires. *APL Materials* **2**, 046105 (2014).
19. Allen, J.E. et al. High-resolution detection of Au catalyst atoms in Si nanowires. *Nature Nanotechnology* **3**, 168-173 (2008).
20. Wang, Y., Schmidt, V., Senz, S. & Gösele, U. Epitaxial growth of silicon nanowires using an aluminium catalyst. *Nature nanotechnology* **1**, 186-189 (2006).
21. Hannon, J., Kodambaka, S., Ross, F. & Tromp, R. The influence of the surface migration of gold on the growth of silicon nanowires. *Nature* **440**, 69-71 (2006).
22. Hanrath, T. & Korgel, B.A. A comprehensive study of electron energy losses in Ge nanowires. *Nano Letters* **4**, 1455-1461 (2004).
23. Collins, G., Fleming, P., O'Dwyer, C., Morris, M.A. & Holmes, J.D. Organic functionalization of germanium nanowires using arenediazonium salts. *Chemistry of Materials* **23**, 1883-1891 (2011).
24. Lauhon, L.J., Gudiksen, M.S., Wang, D. & Lieber, C.M. Epitaxial core-shell and core-multishell nanowire heterostructures. *Nature* **420**, 57-61 (2002).
25. Kim, B.-S. et al. Control of lateral dimension in metal-catalyzed germanium nanowire growth: Usage of carbon sheath. *Nano letters* **12**, 4007-4012 (2012).
26. Pandurangan, A., Morin, C., Qian, D., Andrews, R. & Crocker, M. Single-step synthesis of germanium nanowires encapsulated within multi-walled carbon nanotubes. *Carbon* **47**, 1708-1714 (2009).
27. Larcher, D. & Tarascon, J. Towards greener and more sustainable batteries for electrical energy storage. *Nature chemistry* (2014).
28. Murphy, N.R. et al. Correlation between optical properties and chemical composition of sputter-deposited germanium oxide (GeO_x) films. *Optical Materials* **36**, 1177-1182 (2014).
29. Lee, Jae-Hyun, et al. Wafer-scale growth of single-crystal monolayer graphene on reusable hydrogen-terminated germanium. *Science* **344**, 286-289, (2014)
30. Choi, S., Kim, J., Choi, N.-S., Kim, M.G. & Park, S. Cost-Effective Scalable Synthesis of Mesoporous Germanium Particles via a Redox-Transmetalation Reaction for High-Performance Energy Storage Devices. *ACS nano* **9**, 2203-2212 (2015).

Publication list

1. J.-P. Lee, **S. Choi**, S. Park*, "Extremely Superhydrophobic Surfaces with Micro- and Nanostructures Fabricated by Copper Catalytic Etching", *Langmuir* (2011).
2. J.-P. Lee, B. M. Bang, **S. Choi**, T. Kim, S. Park*, "Patterning of Various Silicon Structures via Polymer Lithography and Catalytic Chemical Etching", *Nanotechnology* (2011).
3. H. Park, **S. Choi**, J.-P. Lee, S. Park*, "Fabrication of Highly Ordered Silicon Pin-in-a-Hole Nanostructures via Chemical Etching of Nanopatterned Polymer Masks" *J. Mater. Chem.* (2011).
4. H. Cho, **S. Choi**, J. Y. Kim, S. Park*, "Fabrication of gold dot, ring, and corpuscle arrays from block copolymer templates via a simple modification of surface energy", *Nanoscale*, (2011).
5. J.-P. Lee, **S. Choi**, S. Park*, "Preparation of Silica Nanospheres and Porous Polymer Membranes via Phase Separation", *Nanoscale Research Letters*, (2012).
6. **S. Choi**, J.-I. Lee and S. Park*, "Patterning of electrodes for mechanically robust and bendable lithium-ion batteries", *Journal of Materials Chemistry*, (2012).
7. O. Park, J.-I. Lee, M.-J. Chun, J.-T. Yeon, S. Yoo, **S. Choi**, N.-S. Choi*, S. Park*, "High-performance Si anodes with a highly conductive and thermally stable titanium silicide coating layer", *RSC Advances* (2013).
8. J.-I. Lee, **S. Choi**, S. Park*, "A Simple Fabrication of Interconnected CuO Nanotube Electrodes for High Performance Lithium-Ion Batteries", *Chem. Asian J.* (2013).
9. **S. Choi**, J. Lee, O. Park, M.-J. Chun, N.-S. Choi*, S. Park*, "Synthesis of micro-assembled Si/titanium silicide nanotube anodes for high-performance lithium-ion batteries", *J. Mater. Chem. A* (2013).
10. T. Bok, **S. Choi**, J. Lee, S. Park*, "Effective strategies for improving the electrochemical properties of highly porous Si foam anodes in lithium-ion batteries", *J. Mater. Chem. A* (2014).
11. C. Kim, M. Ko, S. Yoo, S. Chae, **S. Choi**, E.-H. Lee, S. Ko, S.-Y. Lee, J. Cho*, S. Park*, "Novel design of ultra-fast Si anodes for Li-ion batteries: crystalline Si@amorphous Si encapsulating hard carbon", *Nanoscale* (2014).
12. M.-H. Park, M. Noh, S. Lee, M. Ko, S. Chae, S. Sim, **S. Choi**, H. Kim, H. Nam, S. Park*, J. Cho*, "Flexible High-Energy Li-Ion Batteries with Fast-Charging Capability", *Nano Lett.* (2014).
13. **S. Choi**, T.-H. Kim, J.-I. Lee, J. Kim, H.-K. Song*, S. Park*, "General Approach for High-Power Li-Ion Batteries: Multiscale Lithographic Patterning of Electrodes", *ChemSusChem.* (2014).

14. H. Park, **S. Choi**, S. Lee, G. Hwang, N.-S. Choi*, S. Park*, "Novel design of silicon-based lithium-ion battery anode for highly stable cycling at elevated temperature", *J. Mater. Chem. A* (2015).
15. **S. Choi**, T. Bok, J. Ryu, J.-I. Lee, J. Cho*, S. Park*, "Revisit of metallothermic reduction for macroporous Si: compromise between capacity and volume expansion for practical Li-ion battery", *Nano Energy* (2015).
16. G. Hwang, H. Park, T. Bok, **S. Choi**, S. Lee, I. Hwang, N.-S. Choi, K. Seo, S. Park*, "A high-performance nanoporous Si/Al₂O₃ foam lithium-ion battery anode fabricated by selective chemical etching of the Al-Si alloy and subsequent thermal oxidation", *Chem. commun.* (2015).
17. **S. Choi**, J. Kim, N.-S. Choi, M. G. Kim*, S. Park*, "Cost-Effective Scalable Synthesis of Mesoporous Germanium Particles via a Redox-Transmetalation Reaction for High-Performance Energy Storage Devices", *ACS Nano* (2015).
18. J. Ryu, **S. Choi**, T. Bok, S. Park*, "Nanotubular structured Si-based multicomponent anodes for high-performance lithium-ion batteries with controllable pore size via coaxial electrospinning", *NanoScale* (2015).
19. C. Kim, **S. Choi**, S. Yoo, D. Kwon, S. Ko, J.-M. Kim, S.-Y. Lee, I.-D. Kim, S. Park*, "A facile route for growth of CNT on Si@hard carbon for conductive agent-free anodes for lithium-ion batteries", *Nanoscale* (2015).
20. J. Ryu, Y. J. Jang, **S. Choi**, H. J. Kang, J. S. Lee*, S. Park*, "All-in-one strategy for large-scale mesoporous silicon nanosheets from natural clay: Their application to hydrogen evolution reaction", (2015). just submitted
21. **S. Choi**, J. Kim, D. Hwang, J. Ryu, D. Kwon, N.-S. Choi, S. K. Kwak*, S. Park*, "Redox-responsive assembly of carbon sheathed germanium coaxial nanowire heterostructure", (2015). Ready to submit

Patent list

1. 국내출원: 10-2012-0134810 (2012. 11. 26) 박수진, 조재필, 최신호, 이정인
국내등록: 10-1453513 (2014. 10. 15)
전극의 제조 방법, 상기 방법에 따라 제조된 전극, 및 상기 전극을 포함하는 리튬 이차 전지
2. PCT 출원: PCT/KR2013/002016 (2013. 03. 13) 박수진, 송현곤, 조재필, 최신호
전극의 제조 방법, 상기 방법에 따라 제조된 전극, 및 상기 전극을 포함하는 리튬 이차 전지
3. 국내출원: 10-2012-0048713 (2012. 05. 08) 박수진, 최신호, 조재필
국내등록: 10-1396489 (2014. 05. 12)
실리콘계 음극 활물질의 제조 방법, 리튬 이차전지용 음극 활물질 및 이를 포함하는 리튬 이차전지
4. PCT 출원: PCT/KR2012/006987 (2012. 08. 31) 박수진, 최신호, 조재필
실리콘계 음극 활물질의 제조 방법, 리튬 이차전지용 음극 활물질 및 이를 포함하는 리튬 이차전지
5. 국내출원: 10-2012-0157544 (2012. 12. 28) 박수진, 최남순, 최신호, 박옥지, 천명진
국내등록: 10-1488483 (2015. 01. 26)
리튬 이차 전지용 음극 활물질, 이의 제조 방법 및 리튬 이차 전지
6. 국내출원: 10-2013-0067917 (2013-06-13) 이상영, 최근호, 김세희, 박수진, 최신호, 이정인
전해질-전극 합체, 이의 제조 방법, 및 이를 포함하는 전기 화학 소자
7. 국내출원: 10-2013-0071793 (2013. 06. 21) 박수진, 최신호
다공성 실리콘계 음극 활물질, 이의 제조 방법, 이를 포함하는 리튬 이차 전지
8. 국내출원: 10-2013-0071115 (2013. 06. 20) 박수진, 최남순, 최신호
리튬 이차 전지용 음극 활물질, 이의 제조 방법 및 리튬 이차 전지
9. 국내출원: 10-2014-0047656 (2014. 04. 21) 박수진, 최신호, 복태수
실리콘 나노 튜브 음극 활물질, 이의 제조 방법, 및 이를 포함하는 리튬 이차전지
10. 국내출원: 10-2014-0055080 (2014. 05. 08) 이상영, 김세희, 최근호, 박수진, 최신호
복합 전극-복합 전해질 합체, 이의 제조 방법, 및 이를 포함하는 전기 화학 소자

11. PCT 출원: PCT/KR2014/004541 (2014. 05. 21) 이상영, 최근호, 김세희, 박수진, 최신희, 이정인
전해질-전극 합체, 이의 제조 방법, 및 이를 포함하는 전기 화학 소자
12. 국외출원: 14/309,945(미국) (2014. 06. 20) 박수진, 최신희
다공성 실리콘계 음극 활물질, 이의 제조 방법, 이를 포함하는 리튬 이차 전지
13. 국외출원: 201410283382.3(중국) (2014. 06. 23) 박수진, 최신희
다공성 실리콘계 음극 활물질, 이의 제조 방법, 이를 포함하는 리튬 이차 전지
14. PCT 출원: PCT/KR2014/004277 (2014. 05. 13) 박수진, 최남순, 최신희
리튬 이차 전지용 음극 활물질, 이의 제조 방법 및 리튬 이차 전지
15. 국내출원: 10-2014-0154762 (2014. 11. 07) 박수진, 최신희, 김지은
리튬 이차 전지용 음극 활물질, 이의 제조 방법, 및 이를 포함하는 리튬 이차 전지
16. 국외출원: 14/399,333(미국) (2014. 11. 06) 박수진, 최신희, 조재필
실리콘계 음극 활물질의 제조 방법, 리튬 이차전지용 음극 활물질 및 이를 포함하는 리튬 이차전지
17. 국외출원: XXXX(일본) (2014. 11. 07) 박수진, 최신희, 조재필
실리콘계 음극 활물질의 제조 방법, 리튬 이차전지용 음극 활물질 및 이를 포함하는 리튬 이차전지
18. 국외출원: XXXX(중국) (2014. 11. 25) 박수진, 최신희, 조재필
실리콘계 음극 활물질의 제조 방법, 리튬 이차전지용 음극 활물질 및 이를 포함하는 리튬 이차전지
19. 국외출원: 12876512(EPO) (2014. 11. 07) 박수진, 최신희, 조재필
실리콘계 음극 활물질의 제조 방법, 리튬 이차전지용 음극 활물질 및 이를 포함하는 리튬 이차전지
20. 국내출원: 10-2015-0018206 (2015. 02. 05) 박수진, 최신희, 김지은
나노 구조체, 및 이의 제조 방법
21. 국내출원: XXXX (2015. 03. 30) 박수진, 최신희, 김지은
리튬 이차 전지용 음극 활물질, 이의 제조 방법, 및 이를 포함하는 리튬 이차 전지

Acknowledgements

본 학위를 받기 전 먼저 모든 것을 행하시고 인도 하신 하나님, 감사합니다.

2009년 겨울 첫 만남부터 오늘까지 제가 항상 믿고 존경하는 지도교수님이신 박수진교수님, 감사합니다. 교수님의 근면성실과 연구자적 자세는 항상 정답이어서 제가 더 의지할 수 있었습니다. 부족하지만 저를 믿고 학위를 주셨기에 앞으로도 감사하는 마음으로 살아가겠습니다. UNIST 이차전지 핵심이신 조재필, 이상영, 최남순 교수님, 교수님들께 학문, 기술을 배울 수 있었다는 것 자체로 영광으로 생각하며, 교수님들의 가르침과 조언을 항상 생각하도록 하겠습니다. 이탈리아에서는 이렇게 인연이 될 줄 몰랐던 장민철 박사님, 박사님의 조언대로 전진하는 삶과 부족한 부분을 채워가도록 하겠습니다. 감사합니다. 이 학위를 받기 전 인제대학교에서 저를 가르쳐주셨던 스승이신 교수님들께 감사합니다. 우선, 실험이 무엇인지 알려주셨던 류혁현교수님, 무에서 유를 창조하라고 아이디어를 강조하셨던 교수님의 조언을 바탕으로 제가 연구를 할 수 있었습니다. 항상 상담하러 가면 저를 믿고 기쁘게 맞이해주신 박원욱 교수님, 교수님의 조언과 가르침이 학위과정 동안 밑거름이 되었습니다. 처음부터 졸업까지 항상 바른길로 인도해주시고 롤모델이 되신 조관식 교수님, 감사합니다.

항상 함께 했던 S.Park 연구실 인원과 동기들, 함께 연구했던 주변사람 모두에게 감사합니다. 항상 편하게 많은 것을 알려주신 권도형 박사님, 다양한 분야에서 경험에 대해 조언들을 수 있어 좋았습니다. 저의 사수이자, 이제는 아이 엄마가 된 이정인 박사님, 누나의 연구적 자세에 있어 많은 도전을 받고 열심히 할 수 있었습니다. 조카 무럭무럭 크게 잘 키우세요. 늘 함께였고, 앞으로도 함께할 박형민 박사님, 박형이 있어 정말 행복했습니다. 항상 형을 응원합니다. 동갑이라 편했고 힘들 때 랩장 시켜서 미안한 우진이, 충분히 잘하고 있으니 더욱 힘내서 좋은 성과 많이 내길, 부사수로 들어와 고생만했던 태수, 때론 화내기도 하고 떠넘기기만 해서 미안했고, 가정과 연구 모두 성공하길 바란다. 알다가도 모를 명수, 승민이형, 정인누나 백업한다고 고생 많았고 이제는 너를 위한 연구를 하길 바란다. 처음 학부생일 때 들어와 고생했지만 묵묵히 잘 따라온 재건이, 미국에서도 돌아와서도 지금처럼만 하면 넌 성공한다. 항상 열심히 해서 좋았다. 수줍은 듯 할말 다 하는 규진이, 항상 밝게 웃고 행동하는 모습이 좋아, 열심히 하길. 동기야 많이 함께 하지 못해 아쉽지만 많은 추억과 연구 하길 바란다. 506호 방장 가은이, 항상 열심히 실험하고 열심히 실패하고 그래도 꾸준하게 해서 보기 좋다. 앞으로 좋은일 만 가득하길 바랄께. 그리고 학부생인 아영이, 꼭 미국 가서 학위 받으세요!

그 동안 함께 했고 지금은 연구실을 떠나 각자의 삶을 열심히 살고 있는 사람들에게도 감사합니다. 먼저 친근하게 다가왔던 이정필 박사님, 형이 있어 실험 기본기를 제대로 배울 수 있었어요. 지금은 나랏일 하는 주란이 동기였지만 반년만 해서 아쉬웠다 그래도

지금 행복하다니 보기 좋아. 삼성맨 유하나님, 아버지가 된 방병만 책임님, 그리고 조희숙 선생님 모두 랩실 꾸러가며 열심히 했던 그때 함께 해서 좋았습니다. 지금 어딘가에서 빵을 생각할 옥지, 그리고 항상 의욕 넘치게 열심히 연구하는 찬훈이, 대전에서도 많은 연구해서 꿈을 이루길 바란다. 저랑 놀러 다닌 기억밖에 없다는 유승민 박사님, 이제 교수님으로 강단에 서있는 형이 자랑스럽네요. 많은 사람들에게 좋은 스승이 되시길 바랍니다. 과감하게 도전했던 그래서 보기 좋았던 승희, 너를 위한 인생을 살길 바랄게. 그리고 마지막 연구를 함께 했던 지은이, 믿고 따라와줘서, 부지런히 실험해줘서 그리고 정말 좋은 결과를 안겨줘서 고맙다.

함께 5년을 생활한 친구, 동기들에게 감사합니다. 고민을 함께 나눈, 지금 미국 가버린 재환이, 올해 꼭 졸업하길. 직설적인 말로 정신차리게 해주는 태희, 많이 그리울 것 같다. 마음이 따뜻한 코코 서진이형, 뭉툭은 된다는 것을 보여주는 효성이, 언제나 투덜거리지만 기쁨이 가득한 정민이, 조용한듯 할 것 다 해버린 시혁이, 웃음 바이러스 동생 동우, 이제는 어엿한 교수님 정수형, 함께 10년을 봐온 효진이형, 태민이, 항상 챙겨주는 자상한 보람이형, 내가 아끼는 동생들 치현이, 윤교, 명진이 모두 함께 할 수 있어 행복했고, 고맙습니다. 그대들은 많이 보고 싶을 것 같습니다.

UCRF 모든 선생님들과 직원 여러분들의 많은 조언과 배려로 학위과정 동안 많은 연구를 할 수 있었습니다. 감사합니다. 특히 번개 같이 나타나 버럭 하시지만 항상 우리를 생각하시는 김영기 선생님, UNFC 수장 그리고 제일 열심히 해서 모범이 되시는 김형일선생님, 선생님의 많은 도움으로 연구를 잘 할 수 있었습니다. 정말 고맙습니다.

항상 기도로 좋은 말씀으로 바른길로 인도해주신 김현규 담임목사님, 항상 저를 자랑스럽게 생각해주신 그리고 존재만으로 위로가 되시는 강용찬 목사님, 올바른 선배의 길을 만들어보자고 하셨던 목사님의 믿음으로 무사히 학위과정을 지날 수 있었습니다. 감사합니다. 그리고 오정 목사님, 정인, 지훈, 보라, 다빈, 성주, 성아, 최전도사 진성이, 김전도사 현기, 모두 고맙습니다. 믿음의 동역자들이 있어서 성숙해지고 더 발전할 수 있었음을 깨닫습니다. 그대들은 하나님의 축복이라 생각합니다.

항상 뒤에서 믿음과 기도로 기다려준 사랑하는 가족들에게 감사드립니다. 아들이 가는 길에 무조건 믿고 기다려주신 그리고 묵묵히 기도로 응원해 주신 사랑하는 부모님, 제 삶의 원동력은 부모님의 기도임을 잊지 않겠습니다. 하나뿐인 동생이라 지극히 챙겨주는 우리 누나, 자형, 늦게 까지 공부하는 동생 뒷바라지 하느라 고생 많았고 고마워요. 고집부리지만 언제나 사랑스런 조카 영준이, 그리고 곧 보게 될 기쁨이, 삼촌이 공부를 오래도록 해서 미안하고, 우리 조카들이 있어 더 행복한 박사 학위 생활이었다.

모두의 도움 없이는 한 순간도 앞으로 진행해 나가기 어려운 인생임을 잘 알기에 정말 고마운 마음을 글로써 표현해봅니다. 모두 고맙습니다. 그리고 사랑합니다. 여러분.

2015년 7월 7일 최신희